Electronic Theses and Dissertations   Theses, Dissertations, and Major Papers

2010

Numerical Simulation of Sheet Metal Forming Using Non-Associated Flow Rule and Mixed Isotropic-Nonlinear Kinematic Hardening Model

Aboozar Taherizadeh
University of Windsor

Follow this and additional works at: https://scholar.uwindsor.ca/etd

Numerical Simulation of Sheet Metal Forming Using

Non-Associated Flow Rule and Mixed Isotropic-

Nonlinear Kinematic Hardening Model

by

Aboozar Taherizadeh

A Dissertation
Submitted to the Faculty of Graduate Studies
through Mechanical Engineering
in Partial Fulfillment of the Requirements for
the Degree of Doctor of Philosophy at
the University of Windsor

Windsor, Ontario, Canada

2009

© 2009 Aboozar Taherizadeh

Numerical Simulation of Sheet Metal Forming Using Non-Associated Flow Rule and
Mixed Isotropic- Nonlinear Kinematic Hardening Model

by

Aboozar Taherizadeh

APPROVED BY:

_____
Dr. P. Wu, External Examiner
Department of Mechanical Engineering, McMaster University

_____
Dr. D. Green, Advisor
Mechanical Engineering (MAME)

_____
Dr. W. Altenhof, Co-advisor
Mechanical Engineering (MAME)

_____
Dr. N. Zamani, Department Reader
Mechanical Engineering (MAME)

_____
Dr. D. Watt, Department Reader
Engineering Materials (MAME)

_____
Dr. S. Das, Outside Reader
Civil and Environmental Engineering

_____
Dr. W. ElMaraghy, Chair of Defense
Industrial and Manufacturing Systems Engineering

September 2, 2009

Declaration of Co-Authorship/Previous Publication

I. Co-Authorship Declaration

I hereby declare that this dissertation incorporates material that is result of joint research, as follows:

- Uniaxial tensile tests for 3 steel sheets used in Chapter 3, 4 and 5 were carried out by Ming Shi from United States Steel and Mai Huang from Mittal Steel.

- Uniaxial tensile tests and biaxial bulge tests for the aluminum alloy used in Chapter 3, 4 and 5 were carried out by J. Brem, F. Barlat, R. Dick and J.W. Yoon from Alcoa.

- Cyclic shear tests used in Chapter 3 and 4 were carried out by Professor S. Thuillier from the Université de Bretagne-Sud in France.

- Hydraulic bulge tests on the steel sheets used in Chapter 3, 4 and 5 were carried out by Dr. J-W Yoon from Alcoa.

- Cyclic tension-compression tests used in Chapter 5 were carried out by Professor Wagoner and Piao Kun from the Ohio State University.

- Measurements of residual stresses used in Chapter 3 were carried out by Dr. T. Gnaeupel-Herold from the NIST.

- Dr. Jean Reid from the IRDI in Midland, Ontario, was responsible for the measurement of friction coefficients used in springback simulations in Chapter 3, 4 and 5.

- Numisheet'05 Benchmark #3 channel draw tests used in Chapter 3, 4 and 5 were performed at the Industrial Research & Development Institute (IRDI) in Midland, Ontario. Also, General Motors of Canada sponsored the Numisheet'05 Benchmark #3 and the A/SP was responsible for building the channel draw die.

I am aware of the University of Windsor Senate Policy on Authorship and I certify that I have properly acknowledged the contribution of other researchers to my dissertation, and have obtained written permission from each of the co-author(s) to include the above material(s) in my dissertation.

I certify that, with the above qualification, this dissertation, and the research to which it refers, is the product of my own work.

II. Declaration of Previous Publication

This dissertation includes 3 original papers that have been previously published/submitted for publication in peer reviewed journals, as follows:

Chapter 3
A. Taherizadeh, A. Ghaei, D.E. Green, W. J. Altenhof. Finite element simulation of springback for a channel draw process with drawbead using different hardening models. Int. J. Mech. Sci., 51 (2009) 314-325.

Chapter 4
A. Taherizadeh, D.E. Green, A. Ghaei, J.W. Yoon. A non-associated constitutive model with mixed iso-kinematic hardening for finite element simulation of sheet metal forming. Int. J. Plasticity, In press (2009), doi: 10.1016/j.ijplas.2009.07.003.

Chapter 5
A. Taherizadeh, D.E. Green, A. Ghaei. Simulation of earing using two anisotropic models: A quadratic non-associated and a non-quadratic associated. IDDRG 2009 International Conference, June 1-3, 2009, Golden, CO, USA, 177-188.

I certify that I have obtained a written permission from the copyright owner(s) to include the above published material(s) in my dissertation. I certify that the above material describes work completed during my registration as graduate student at the University of Windsor.

I declare that, to the best of my knowledge, my dissertation does not infringe upon anyone's copyright nor violate any proprietary rights and that any ideas, techniques, quotations, or any other material from the work of other people included in my dissertation, published or otherwise, are fully acknowledged in accordance with the standard referencing practices. Furthermore, to the extent that I have included copyrighted material that surpasses the bounds of fair dealing within the meaning of the Canada Copyright Act, I certify that I have obtained a written permission from the copyright owner(s) to include such material(s) in my dissertation.

I declare that this is a true copy of my dissertation, including any final revisions, as approved by my dissertation committee and the Graduate Studies office, and that this dissertation has not been submitted for a higher degree to any other University or Institution.

Abstract

This dissertation consists of three major parts. In the first section, the springback simulation of Numisheet'05 Benchmark#3 was investigated with different material models (Hill's 1948 yield with pure isotropic and mixed isotropic-nonlinear kinematic hardening) using the commercial finite element code ABAQUS. Different theoretical and experimental parameters affecting springback were discussed.

In the second section, a new anisotropic material model based on non-associated flow rule (NAFR) and mixed isotropic-nonlinear kinematic hardening was developed and implemented into ABAQUS as a user-defined subroutine. Also, a new direct stress integration formulation applicable to quadratic yield and potential functions (e.g., Hill's 1948 anisotropic function) was developed based on the return mapping algorithm. This model is able to consider different aspects of anisotropy and cyclic hardening while maintaining both theoretical and computational simplicity. The model was validated by comparing numerical predictions of material behaviour under different loading conditions (equibiaxial tension, monotonic and cyclic shear) and of mechanical properties (uniaxial yield stresses, r-values) with experimental data. The model was used to simulate cup drawing and plane-strain channel drawing with drawbeads. The results showed that this non-associated, mixed hardening model significantly improves the prediction of earing and springback, even when a rather simple quadratic constitutive model is used.

In the third section, two different anisotropic models for sheet materials were compared: (*i*) the quadratic NAFR model; (*ii*) a non-quadratic associated model, so-called Yld2000-2d, proposed by Barlat et al. (2003). A new general stress integration scheme applicable to all types of yield and potential functions (quadratic or non-quadratic) and flow rules (associated or non- associated) with mixed hardening, based on the multi-stage backward-Euler return mapping algorithm was developed. Both models were implemented into ABAQUS (for both isotropic and mixed hardening) and used to simulate cup drawing and springback of a plane-strain channel section formed with drawbeads. Cyclic tension-compression tests were performed to determine the mixed hardening parameters. The simulation results predicted with each model were compared and it was shown that both models are able to describe the springback and anisotropic behaviour of sheet materials quite accurately. However, the quadratic NAFR model required significantly less computation time.

To Fatima

`

Acknowledgments

Table of Contents

List of Tables

List of Figures

Chapter 1

Introduction

In recent decades, new materials have been employed in automotive, aerospace and other basic industries to improve safety, fuel efficiency, manufacturability, and environmental issues. For instance, new aluminum alloys and new grades of steel such as ultra-high strength steel, and dual phase and TRIP steels have been developed; pushing the boundaries of what was previously possible with conventional steel grades. The main advantage of using these new materials is that they contribute to reducing weight, while increasing safety. Applying these new materials, the need to investigate the materials behaviour is an emerging field in forming simulations. In sheet metal forming, modelling and simulation can be used for many purposes, for example to predict material flow, to analyze stress-, strain- and temperature-distribution, to determine forming forces, to forecast potential sources of defects and failures, to improve part quality and complexity and to reduce manufacturing costs. Nowadays, modelling and simulation are often integral parts of product and process design in an integrated manufacturing environment. In sheet metal forming simulation, several parameters and influencing factors should be considered. Material properties and constitutive laws, and tribological conditions are of significant importance, but geometrical representations and computational time should also be considered for cost effective and reliable numerical simulation. The focus of the first few decades of finite element method (FEM) analysis by the metal forming industry struggled with the issues of methodology, formulation, and computational efficiency. As these issues are largely resolved and the FEM is applied to a broader range of applications, the question of the validity and limitation of the material model used in the analysis becomes inevitable. This question is especially apparent in the determination of springback and in analyses of secondary forming processes. It is now clear that commonly used

material models cannot reliably predict formability in complex stamping processes and cannot accurately predict springback in general.

Sheet metal forming processes generally involve large deformations and rotations which are both nonlinear with respect to material and geometry positions, respectively. In the analysis and simulation of these processes, usually the logarithmic strain tensor and its conjugate stress tensor (Cauchy stress) are used to form the constitutive equations. All stress, strain, stretches, and state variable components are stored in this local material coordinate system. In fact, it is convenient to use a co-rotational coordinate system in which the reference system rotates with the material. A material model is a vital part of sheet metal forming simulations, since it updates the stress and state variables based on the deformation or deformation rate tensor. Because of the nonlinear and irreversible (or path dependent) nature of plastic deformation it is more convenient to write all elasto-plastic constitutive relations in the incremental or rate-type formulation. Therefore, for any constitutive equation used in the finite element (FE) formulation it is important to derive the relation between the increment of strain (or deformation rate) and increment of stress. The overall response is determined incrementally by integrating the rate-type constitutive and field equations along a given path of loading or deformation (Figure 1.1).
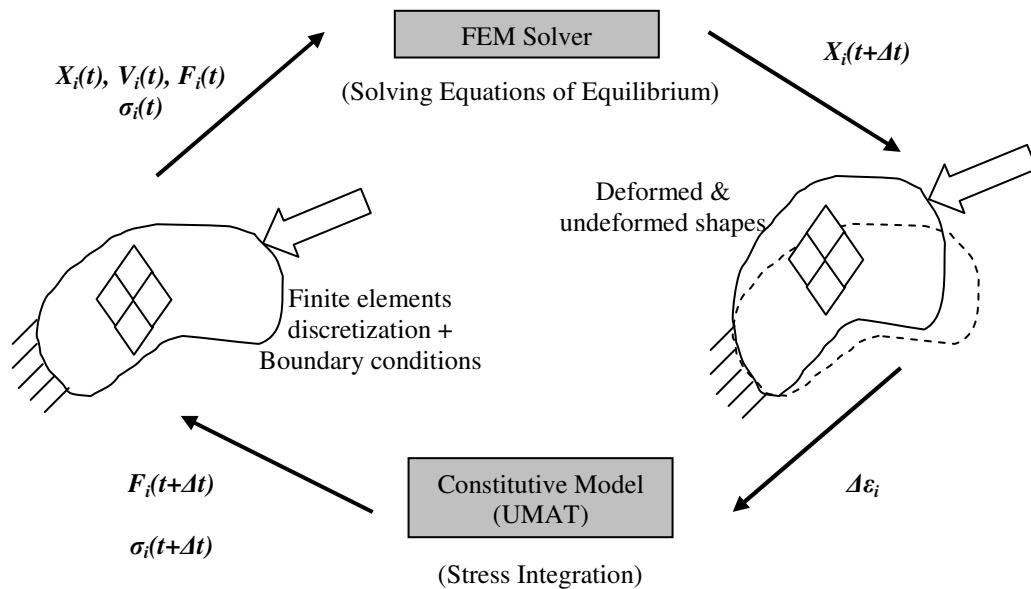
Figure 1.1. Role of constitutive model in nonlinear finite element analysis.

There are many areas in which the simulation results are strongly affected by the material model, such as prediction of springback, formability analysis (FLD), defect analysis like earing and wrinkling, failure analysis and localized deformations etc. An acceptable material model in the

FE simulation of sheet metal forming should be able to capture many different phenomena that occur during plastic deformation, such as the anisotropic yielding behaviour, the proper strain- (or work-) hardening regime, and even cyclic phenomena such as the Bauschinger effect or kinematic hardening etc. Certain factors must be considered when selecting a constitutive model in FE analysis. On one hand, the model should not be so complicated that it requires an excessive number of coefficients, because both the experimental procedure to determine the coefficients and the computational procedure will be expensive. On the other hand, it should provide the best possible fit with actual material properties. For example, texture and microstructure-based constitutive models have also been investigated for the FEM simulation of forming processes. However, these micro-macro models generally require very long computation times and large memory storage, although they often produce accurate results.

It is well-known that plastic deformation of polycrystalline material induces reorientation of individual grains into preferred orientations. This phenomenon, i.e. texture evolution, and the initial texture of the steel sheet are responsible for the mechanical anisotropy of the material, which plays an important role in forming processes. Many phenomenological anisotropic theories have been proposed to take into account different aspects of anisotropy for sheet metal forming. Also, many cyclic plasticity models have been proposed to capture as many phenomena as possible that take place in the cyclic deformation.

After a thorough review of these constitutive models a new material model that is based on a combination of non-associated flow rule theory and mixed isotropic-nonlinear kinematic hardening was developed to predict both anisotropic and cyclic characteristics as accurately as possible. Besides, it was tried to maintain the theoretical simplicity to make the numerical implementation as efficient as possible. Therefore, both the experimental and computational costs were considered in the material development. Comparison between the theoretical predictions by this model and the experimental measurements shows that this model significantly improves the accuracy of the predictions. Also, the developed material model was implemented as user-defined material subroutines (UMAT and VUMAT) to simulate different sheet metal forming processes. Comparison of these simulation results with experimental measurements shows that this model is able to significantly improve the simulation results. Finally, the simulation results obtained using this model were compared with those obtained by a non-quadratic anisotropic associated model. These comparisons show that the proposed non-associated model needs significantly less computation time than the non-quadratic associated model. At the same time, the ability of these two models to predict different aspects of anisotropy are almost equivalent and no significant compromise is made by using this model rather than the non-quadratic associated model.

This dissertation was prepared based on the following publications:

1. A. Taherizadeh, A. Ghaei, D.E. Green, W. J. Altenhof. Finite element simulation of springback for a channel draw process with drawbead using different hardening models. Int. J. Mech. Sci., 51 (2009) 314-325.
2. A. Taherizadeh, D.E. Green, A. Ghaei, J.W. Yoon. A non-associated constitutive model with mixed iso-kinematic hardening for finite element simulation of sheet metal forming. Int. J. Plasticity, In Press, (2009), doi: 10.1016/j.ijplas.2009.07.003.
3. A. Taherizadeh, A. Ghaei, D.E. Green, Prediction of Springback for a Channel Draw Process Using Different Hardening Models, Materials Science and Technology 2007 Conference and Exhibition, September 16-20, 2007, Detroit, MI, USA, 445-456.
4. A. Ghaei, A. Taherizadeh, D.E. Green, The Effect of Hardening Model on Springback Prediction for a Channel Draw Process, ed. P. Hora, Part A, Numisheet 2008 International Conference, September 1-5, 2008, Interlaken, Switzerland, 485-490.
5. A. Taherizadeh, D.E. Green, A. Ghaei. Simulation of earing using two anisotropic models: A quadratic non-associated and a non-quadratic associated. IDDRG 2009 International Conference, June 1-3, 2009, Golden, CO, USA, 177-188.

And the following sections are presented in this dissertation:

- **Chapter 1.** Introduction.
- **Chapter 2.** Literature review.
- **Chapter 3.** Finite element simulation of springback using different hardening models.
- **Chapter 4.** Non-associated constitutive model with mixed isotropic-nonlinear kinematic hardening for simulation of sheet metal forming.
- **Chapter 5.** Comparison of two anisotropic models: quadratic non-associated and non-quadratic associated.
- **Chapter 6.** Conclusions.

Notation: The standard matrix-vector notation (instead of tensorial notation) is employed since it is more convenient for algorithmic description and numerical implementation. Second-order tensors will be replaced by vectors and represented as bold-faced Greek letter and fourth-order tensors replaced by square matrices and shown by ordinary bold-faced capital letter. The symbol "**:**" between two tensors implies double contraction (the trace of their product), and $\otimes$ denotes the tensor or dyadic product of two vectors.

Chapter 2

Literature Review

2.1. Introduction

There are three major concepts in the study of plastic behaviour of materials: the yield function, the flow rule, and the hardening law. Plasticity of the constitutive models for analysis and simulation of sheet metal forming processes will be reviewed in this chapter. To establish the incremental equations for elastic-plastic hardening materials, several conditions are necessary to ensure an appropriate representation of plastic flow: continuity, uniqueness, irreversibility, consistency, and the flow rule. All these conditions, as well as a yield function, are used to determine a general stress-strain relation for plastic deformation.

There are different approaches to evaluate the deformation path of a material element over a small time increment in the finite element formulation. The minimum plastic work path is one of the most accepted ways among different theories. The incremental constitutive equations are obtained based on the minimum plastic work path and is now widely used for advanced computational plasticity formulations (Hill, 1986; Chung and Richmond, 1993; Yoon et al., 1999a, b).

2.2. Anisotropic yield functions

Due to different and complex phenomena occurring during the rolling process the flat rolled products such as sheet metals experience various degrees of anisotropy. Two aspects of the anisotropy are important for sheet metal forming analysis: anisotropy in the yield stress and anisotropy in the plastic flow. The first aspect of the anisotropy is evidenced by a variation of the yield stress in different directions of the sheet metal, and the second aspect is usually defined as a variation of the plastic strain ratio (ratio of width to thickness strain) in different directions. The

ratio of width strain to thickness strain is usually called Lankford coefficient or r-value. There are other matters rather than anisotropy that have been observed in plastic yielding of (sheet) metals such as, Strength Differential Effect (SDE) that is the difference between initial yielding in tension and compression loadings, Bauschinger Effect (BE), hydrostatic stress (pressure) sensitivity, and etc. Several anisotropic yield functions have been proposed for sheet metal forming analysis in order to correlate with the experimental behaviour as accurately as possible. However, for the sake of brevity the most frequently-used and only symmetric pressure-insensitive anisotropic yield functions for sheet metals are reviewed in this section.

2.2.1 Quadratic yield functions

Hill 1948

Hill's (1948) quadratic yield function may be noted as one of the first and most comprehensive yield criteria proposed as a generalization of the von Mises yield function for anisotropic materials. This straightforward function for the plane-stress condition is written as

$$2f = \sqrt{(G+H)\sigma_{xx}^{2} + (F+H)\sigma_{yy}^{2} - 2H\sigma_{xx}\sigma_{yy} + 2N\sigma_{xy}^{2}} - 1 = 0 \qquad (2.1)$$

F, G, H, and *N* are constants that characterize the anisotropy and are simply defined as

$$2G = \frac{1}{(\sigma^{Y}_{x})^{2}} - \frac{1}{(\sigma^{Y}_{y})^{2}} + \frac{1}{(\sigma^{Y}_{B})^{2}}, \qquad 2F = \frac{1}{(\sigma^{Y}_{y})^{2}} - \frac{1}{(\sigma^{Y}_{x})^{2}} + \frac{1}{(\sigma^{Y}_{B})^{2}},$$

$$2H = \frac{1}{(\sigma^{Y}_{x})^{2}} + \frac{1}{(\sigma^{Y}_{y})^{2}} - \frac{1}{(\sigma^{Y}_{B})^{2}}, \qquad 2N = \frac{1}{(\sigma^{Y}_{xy})^{2}} = \frac{1}{(2\sigma^{Y}_{45})^{2}} - \frac{1}{(\sigma^{Y}_{B})^{2}}$$

where σ^{Y}_{x}, σ^{Y}_{y}, and σ^{Y}_{45} are tensile yield stresses in the rolling, transverse and diagonal (45 degrees) directions, σ^{Y}_{xy} is the shear yield stress and σ^{Y}_{B} is the equibiaxial yield stress. It should be noted that the stress transformation in 2-dimensional stress space was used to obtain the second expression of *N*. The above anisotropy coefficients can also be written as functions of the r-values. This formulation will be derived in Chapter 4. It is often assumed that Hill's (1948) suggestion of having the orthotropic directions aligned with the principal plastic stretch directions is valid. This is indeed the case when the principal stress directions remain fixed through out the plastic deformation. However, Dafalias (2000) did investigate how Hill's 1948 yield criterion

could account for a possible re-orientation of principal stress directions with respect to material orthotropic axes during plastic deformation.

2.2.2 Non-quadratic yield functions

Although Hill's 1948 yield function has been widely used for analysis of orthotropic metals, it exhibits some limitations particularly for some aluminum and steel alloys, as highlighted by some researchers (Mellor and Parmer, 1978; Mellor, 1981). It fails to account for materials that display so-called "anomalous behaviour". Therefore in recent decades, much attention has been focused on developing more advanced anisotropic yield criteria. Many researchers (Gotoh, 1977; Hill, 1979, 1990, 1993; Barlat and Lian, 1989; Barlat et al., 1991, 1997, 2003, 2005; Karafillis and Boyce, 1993; Banabic et al., 2005 etc.) have developed different non-quadratic yield functions. Some of these recent anisotropic plasticity models are able to describe the anisotropic behaviour of sheet metals with considerable accuracy, but they necessitate a large number of experiments to define the coefficients.

Hosford 1979

An anisotropic yield function was proposed by Hosford (1979) based on the ideas of Hershey (1954) for using the principal stresses to describe isotropic polycrystalline metals. This function is also a generalization of the non-quadratic isotropic function proposed earlier by Hosford (1972)

$$F|\sigma_1 - \sigma_2|^m + G|\sigma_2 - \sigma_3|^m + H|\sigma_3 - \sigma_1|^m - 1 = 0 \tag{2.2}$$

where *m* is 6 or 8 for BCC or FCC crystal structures, respectively, and σ_1, σ_2 and σ_3 are principal stresses.

Hill 1979

Hill (1979) developed a non-quadratic yield function similar to that of Hosford (1979) as follows

$$F|\sigma_2 - \sigma_3|^m + G|\sigma_3 - \sigma_1|^m + H|\sigma_1 - \sigma_2|^m +$$
$$L|2\sigma_1 - \sigma_2 - \sigma_3|^m + M|2\sigma_2 - \sigma_3 - \sigma_1|^m + N|2\sigma_3 - \sigma_1 - \sigma_2|^m - 1 = 0 \tag{2.3}$$

where *m* (with *m*>1, integer or non-integer) is a material coefficient and is determined by matching the effective stress-strain curves for uniaxial and biaxial tests.

Barlat and Lian 1989

Barlat and Lian (1989) proposed a non-quadratic yield function (so-called *Yld89*) for planar anisotropy of textured polycrystals that is restricted to plane-stress conditions

$$a|K_1 + K_2|^m + a|K_1 - K_2|^m + (2-a)|2K_2|^m - 2\bar{\sigma}^m = 0 \tag{2.4}$$

where K_1 and K_2 are defined as

$$K_1 = \frac{\sigma_{xx} + h\sigma_{yy}}{2}, \text{ and } K_2 = \sqrt{\left(\frac{\sigma_{xx} - h\sigma_{yy}}{2}\right)^2 + (p\sigma_{xy})^2}$$

and a, c, h and p are the anisotropy coefficients.

Hill 1990

Hill (1990) developed another non-quadratic yield function that is also restricted to plane-stress conditions

$$|\sigma_1 + \sigma_2|^m + \left(\frac{\sigma_{EB}}{\tau}\right)^m |\sigma_1 - \sigma_2|^m + |\sigma_1^2 + \sigma_2^2|^{(m/2)-1} \times$$
$$\left\{-2a(\sigma_1^2 - \sigma_2^2) + b(\sigma_1 - \sigma_2)^2 \cos 2\alpha\right\} \cos 2\alpha - (2\sigma_{EB})^m = 0 \tag{2.5}$$

where τ is the shear yield stress, parameter α is the angle between the first principal stress and the axis of orthotropy, and two parameters a, and b are defined as

$$a = \frac{F - G}{F + G}, \text{ and } b = \frac{F + G + 4H - 2N}{F + G}$$

Barlat et al. 1991

A six component non-quadratic yield function (so-called *Yld91*) was developed by Barlat et al. (1991) for orthotropic materials which uses a linear transformation of the stress tensor

$$|S_1 - S_2|^m + |S_2 - S_3|^m + |S_3 - S_1|^m - 2\bar{\sigma}^m = 0 \tag{2.6}$$

where S_i are the principal values of an isotropic plasticity equivalent (IPE) stress tensor defined by

$$S = \mathbf{L}.\sigma \tag{2.7}$$

in which σ is the Cauchy stress tensor and $\mathbf{L}$ is a symmetric and traceless fourth-ranked tensor. Tensor $\mathbf{L}$ introduces the material anisotropy into the formulations and its definition can be found in Barlat et al. (1991).

Hill 1993

Hill (1993) proposed the following non-quadratic yield function to account for the behaviour of the tensile yield to be the same along both rolling and transverse directions, while the associated strain ratios are markedly different

$$\sigma_1^2 - \left(2 - \frac{\sigma_u^2}{\sigma_{EB}^2}\right)\sigma_1\sigma_2 + \sigma_2^2 + \left[(p+q) - \frac{p\sigma_1 + q\sigma_2}{\sigma_{EB}}\right]\sigma_1\sigma_2 - \sigma_u^2 = 0 \tag{2.8}$$

where p and q are non-dimensional anisotropic parameters. This function was proposed with applications to thin sheets and is restricted to the first (tension) quadrant of the (σ_1, σ_2) plane. An additional restriction to this yield function is that the tensile yield stress, denoted by σ_u, is the same in the rolling and transverse directions.

Karafillis and Boyce 1993

Karafillis and Boyce (1993) constructed a non-quadratic anisotropic yield criterion (so-called *K-B*) by mixing two isotropic yield functions

$$(1-c)\left(|S_1 - S_2|^m + |S_2 - S_3|^m + |S_3 - S_1|^m\right) + c\frac{3^m}{2^{m-1}+1}\left(|S_1|^m + |S_2|^m + |S_3|^m\right) - 2\overline{\sigma}^m = 0 \tag{2.9}$$

where c is a material parameter ($0 \leq c \leq 1$), and S_1, S_2 and S_3 are the principal values of the IPE tensor ($\mathbf{L}$) that can be found in Karafillis and Boyce (1993). In this formulation, tensor $\mathbf{L}$ can describe different kinds of material anisotropy (triclinic, monoclinic, orthotropic, etc.). For plane-stress conditions these values can be calculated as

$$S_{1,2} = \frac{S_{xx} + S_{yy}}{2} \pm \sqrt{\left(\frac{S_{xx} - S_{yy}}{2}\right)^2 + S_{xy}^2} \text{ , and } S_3 = S_{zz}$$

If $c=0$ and the **L** component coefficients are considered isotropic, then this yield function represents the Tresca yield criterion when $m\rightarrow\infty$, and the von Mises yield criterion when $m=2$, and of course for orthotropic coefficients the Hill 1948 yield function is restored.

Barlat et al. 1997

Barlat et al. (1997a) proposed the following yield criterion (so-called *Yld94*) based on K-B yield function to capture the experimental and polycrystalline yield surface shapes for alloys with very large amounts of cold reduction

$$\alpha_1 |S_1 - S_2|^m + \alpha_2 |S_2 - S_3|^m + \alpha_3 |S_3 - S_1|^m - 2\bar{\sigma}^m = 0 \qquad (2.10)$$

where S_i are the principal values of the same IPE tensor (**L**) as the K-B yield function. Coefficients α_k are further parameters to describe anisotropy and are defined as

$$\alpha_k = \alpha_x p^2_{1k} + \alpha_y p^2_{2k} + \alpha_z p^2_{3k}$$

where p_{ik} are the components of the transformation matrix **p** between the principal axes of anisotropy to the principal axes of **S** and α_x, α_y and α_z are material coefficients. To overcome some limitations of *Yld94*, Barlat et al. (1997b) further proposed an improved yield criterion (so-called *Yld96*) for plane stress cases. They defined another set of parameters β_j that is chosen to represent the angle between the anisotropy axes and the direction associated with S_1 or S_3 ($S_1 \geq S_2 \geq S_3$), whichever has the highest absolute value. Then the new coefficients α_k are defined as functions of β_j, p_{ik} and other material coefficients. The formulations are rather complex and are not explained here; interested readers are referred to the original paper.

Barlat et al. 2003

There are some problems associated with *Yld96* with respect to FE numerical implementation, such as no proof of convexity that is required to ensure the uniqueness of a solution, first and second derivatives are difficult to obtain, and difficulty to model the general stress states due to

the relative complexity. Therefore, Barlat et al. (2003) developed an incompressible anisotropic yield function (so-called *Yld2000-2d*) that can guarantee convexity, make FE implementation simpler, and for plane stress reduces to

$$\phi = \phi' + \phi'' = \left| X_1' - X_2' \right|^a + \left| 2X_2'' + X_1'' \right|^a + \left| 2X_1'' + X_2'' \right|^a = 2\overline{\sigma}^a \tag{2.11}$$

Components X_i' and X_j'' are the principal values of two linear transformations (X' and X'') of the stress tensor as follows

$$X' = \mathbf{L}' \sigma \quad \text{and} \quad X'' = \mathbf{L}'' \sigma$$

where $\mathbf{L}'$ and $\mathbf{L}''$ are two linear higher-ranked tensors applying the transformations on the stress tensor. The expressions of the anisotropy coefficients of $\mathbf{L}'$ and $\mathbf{L}''$ are given as functions of independent coefficients α_1 to α_8 that are functions of eight uniaxial and biaxial mechanical properties in different directions.

Barlat et al. 2005

Barlat et al. (2005) developed another yield function (so-called *Yld2004-18p*). This is one of the most advanced and accurate anisotropic functions developed yet, and it is useful when a large number of experimental data are available (typically uniaxial tension data for seven directions between 0 and 90 as well as biaxial data). For a full stress state (3D) it is defined as

$$\phi = \phi\left(\tilde{S}', \tilde{S}''\right) = \left| \tilde{S}_1' - \tilde{S}_1'' \right|^a + \left| \tilde{S}_1' - \tilde{S}_2'' \right|^a + \left| \tilde{S}_1' - \tilde{S}_3'' \right|^a + \left| \tilde{S}_2' - \tilde{S}_1'' \right|^a + \left| \tilde{S}_2' - \tilde{S}_2'' \right|^a$$
$$+ \left| \tilde{S}_2' - \tilde{S}_3'' \right|^a + \left| \tilde{S}_3' - \tilde{S}_1'' \right|^a + \left| \tilde{S}_3' - \tilde{S}_2'' \right|^a + \left| \tilde{S}_3' - \tilde{S}_3'' \right|^a = 4\overline{\sigma}^a \tag{2.12}$$

Again, in the above function S_i' and S_j'' are the principal values of two linear transformations (S' and S'') of the stress tensor.

2.3. Flow rule

The *flow rule* specifies the increment of plastic strain once the material has yielded. In classical theory of plasticity the Levy-Mises equations and the Prandtl-Reuss equations are used as specific forms of the plastic constitutive equation or flow rule (Hill, 1950). These equations were

formulated on the assumption that the rate or increment of the (plastic) strain is coaxial with the deviatoric part of the total stress, as observed experimentally. Also these flow rules incorporate the von Mises yield criterion and they can be derived from the plastic potential theory. In an effort to establish the general plastic stress-strain relations for any yield criterion, Drucker (1951) proposed a unified approach based on his stability postulate. One major consequence of Drucker's postulate is that the flow rule for stable materials is associated. Drucker's stability postulate asserts that if a material is stable, the following inequality must be satisfied

$$W = \int_{C_\sigma} \Delta\sigma : d\varepsilon = \int_{C_\sigma} (\sigma - \sigma^0) : d\varepsilon \geq 0 \tag{2.13}$$

where the integral is done over the closed stress cycle, C_σ, a loading-unloading path in stress space (Drucker, 1959). Ilyushin (1961) also defined a class of materials for which the net work in an arbitrary strain cycle is non-negative. It has been shown that Ilyushin's requirement of positive work in every strain cycle is a weaker restriction on the material behaviour than Drucker's requirement of positive work of added stresses in every stress cycle. Hence, the class of materials obeying Ilyushin's postulate is broader than the class of materials obeying Drucker's postulate. These stability postulates are fairly strong requirements that can be satisfied only by hardening materials whose subsequent yield strength increases with the deformation. Some consequences like normality of the plastic strain increment and convexity of the yield surface can also be drawn from these postulates resulting in the associated flow rule.

2.3.1. Associated flow rule

For materials that obey either Drucker's or Ilyushin's postulate, given by the appropriate stress or strain cycle inequalities, it follows that the plastic strain increment must be co-directional with the outward normal to a locally smooth yield surface, while at a vertex it must lie within or on the cone of limiting outward normals. The most widely used theory is to assume that the plastic strain increment can be determined by the following formula (due to the Drucker's stability)

$$d\varepsilon^p = d\lambda \frac{\partial F}{\partial \sigma} \tag{2.14}$$

where F is the yield function and $d\lambda$ is a non-negative parameter called plastic multiplier. From this equation, the plastic strain increment is proportional to the gradient of the yield surface and is, therefore, normal to the yield surface. This is usually referred to as the normality condition. A

flow rule obeying the normality condition is referred to as an *associated flow rule* (AFR). On the other hand, a flow rule in which the plastic strain increment is not normal to the yield surface is known as a *non-associated flow rule* (NAFR). Unfortunately, it is not possible to experimentally confirm that the AFR is true. The reason is that the magnitude of the plastic potential cannot be measured. However, the gradient of the plastic potential can be determined from the ratios of the plastic strain after a finite amount of deformation. But in general it is difficult to maintain constant ratios of biaxial stress to produce sufficient plastic deformation beyond yielding. So the errors associated with measuring the gradient of the plastic potential may be significant. Furthermore, the determination of the gradient of the yield surface to compare to the plastic potential is also a challenge because we cannot precisely measure the yield stress at two nearby points on the yield surface.

2.3.2. Non-associated flow rule

Regardless of the plasticity postulates, it has been experimentally observed that for some materials (e.g. materials which dissipate energy by friction or with internal-microscopic frictional effects) associated flow rules do not accurately predict certain essential features of the mechanical response. For example, they tend to largely overestimate the inelastic volume changes in geomaterials like rocks and soils. Consequently, non-associated flow rules have been employed for such materials. The plastic strain increment is then normal to the plastic potential surface, which is distinct from the yield surface. With regard to plasticity postulates it follows that for materials described by NAFR, there are at least some cycles of stress and strain violating Drucker's and Ilyushin's work inequalities. Hence, neither postulate in general applies to such materials. As noted before, to describe the mechanical response of pressure dependent materials, the non-associated flow rules are commonly employed utilizing the plastic potential function (Q) such that

$$\boldsymbol{d\varepsilon^p} = d\lambda \frac{\partial Q}{\partial \boldsymbol{\sigma}} \tag{2.15}$$

where Q is the plastic potential function and is different from the yield function (F). Historically, the associated flow rule plays an important role in the guarantee of stability. The foundation for the relationship between stability and the AFR was established by Drucker (1959). While the AFR is sufficient to ensure the stability requirements listed above, Mroz, and others argue that the AFR is not necessary for stability (Ruensson and Mroz, 1989; Lubarda et al., 1996). However,

there are many papers concerned with the issue of stability in pressure sensitive materials only, and in particular porous, granular and geomaterials in general, where the AFR is found from experiment to be an invalid constraint. On the other hand, many researchers (for instance see Hill, 1950) strengthened the popularity of the AFR for metals by showing that it can be derived from a model of polycrystals in which plastic deformation occurs when the shear stress on a sufficient number of slip planes reaches a critical value.
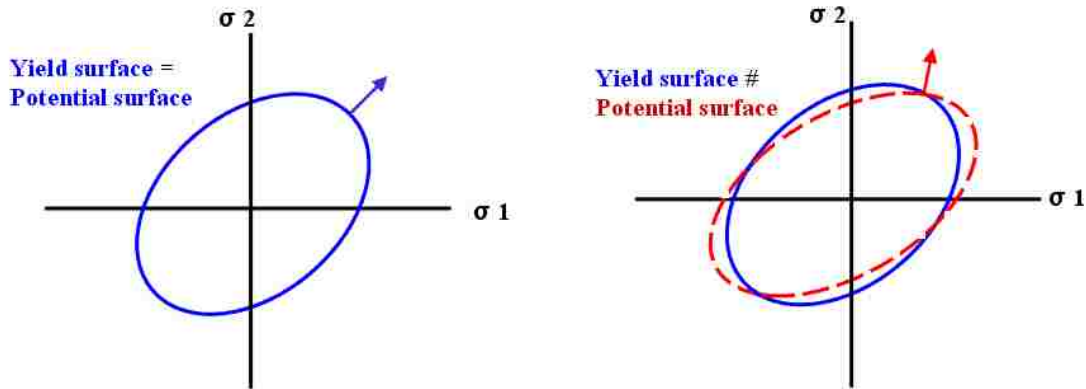
Figure 2.1. Associated (left) and non-associated (right) flow rules in 2D stress space.

The relationship between material stability and plasticity postulates in the case of non-associated flow rule has been studied by many researchers (e.g. Nicholson, 1987; Reunesson and Mroz, 1989; Lubarda et al., 1996; Collins, 2002).

2.3.3. Non-associated flow rule in metal plasticity

Non-associated flow rule (NAFR) has been widely used for analysis and simulation of granular, geotechnical and other pressure sensitive materials for many years. But, there has been a limited application of NAFR in the field of metals plasticity. The main reason for this is the commonly accepted assumption that the plastic behaviour of metals is pressure-insensitive. But Spitzig and Richmond (1984) proposed that plastic yielding of polycrystalline and single crystals of steel and aluminum alloys shows a significant sensitivity to hydrostatic pressure. After their study of the effect of pressure on the flow stress of metals, the issue of using NAFR and pressure-sensitive yield functions for an accurate description of metals behaviour has been an open field for materials and mechanical scientists. Another recent application of NAFR in metals plasticity is to describe the anisotropic yielding and flow in a more convenient way.

Pressure sensitive plastic deformation of metals

While the AFR holds a dominant position in metal plasticity theory, several experiments show that it is violated during metal deformation. Spitzig et al. (1975) first reported a small but measurable pressure sensitivity in the yield stress in tempered martensite without any significant detection of an accompanying plastic dilatancy. This observation implies a possible violation of the AFR because zero plastic dilatancy requires the plastic potential to be a function only of the deviatoric stress, and must therefore be insensitive to pressure. Consequently, it must be different from the yield surface, which is shown in the same experiment to depend on pressure. In fact, this is the same type of study that shows the limitation of the AFR in geomaterials, but the violation in the latter case is more obvious and better known because of the higher pressure-sensitivity in these materials. The study on metals was later expanded to other steel alloys and to at least one aluminum alloy, both in single and polycrystalline forms. All of these tests confirmed a pressure-sensitivity without plastic dilatancy in metals as summarized in a paper by Spitzig and Richmond (1984). Spitzig et al. (1976) and Spitzig (1979) did a series of studies spanning over a decade of research into the yielding of single crystal and polycrystalline aluminum and steel alloys under uniaxial tension with a superimposed hydrostatic pressure. These studies showed a pressure sensitivity that is more than an order of magnitude larger than expected under the AFR and raise a serious challenge to its validity. Noting the mentioned discrepancy the authors proposed a generalization to the von Mises yield theory to account for the effects of the hydrostatic pressure. In further support, the proposed yield function leads to an expected difference in the flow stress under compression and tension. Spitzig and Richmond (1984) defined a strength-differential effect parameter (SDE) to be the difference in the yield stress in uniaxial compression and tension divided by their average, where the yield in compression is defined as a positive number. Then the yield criterion can be used to predict the SDE. Stoughton and Yoon (2004) did a thorough review of the research done by Spitzig and coworkers on the pressure dependency of the metal deformation. They also proposed a generalized non-associated model for anisotropic pressure dependent material and verified their model with experimental work. Also, Aretz (2007) presented a rate-independent non-associated plasticity theory for describing the plastic behaviour of incompressible and hydrostatic pressure-sensitive metals as experimentally observed by Spitzig and Richmond.

Anisotropic plasticity of metals

It has always been a challenge to describe the fully anisotropic plastic strain rates and yield behaviour from a single function, as required by the associated flow rule (AFR). There are several

ways to address this difficulty. The approach widely used by the metal forming industry is to use isotropic or normally anisotropic material models and accept the resulting discrepancies as an approximation to the actual behaviour. A more satisfactory approach in view of the higher degree of accuracy required of material models today, is to propose more complex functions by adding parameters defined by strain ratios and yield stresses measured at additional states of stress (such as the non-quadratic anisotropic functions reviewed in section 2.2.2). A third approach is to question whether these two behaviours, plastic flow and plastic yielding, are in fact described by the same function. Although questioning the AFR is a much simpler solution to the difficulty in defining accurate yield/potential functions since it eliminates the discrepancy by definition, there are a number of theoretical considerations that must be addressed, which are commonly interpreted as validation of the AFR for most metals.

Therefore, in order to improve accuracy without having to define a large number of material parameters, Stoughton (2002) recently proposed an improved model of material behaviour using a non-associated flow rule. This signifies that different yield and plastic potential functions, each with simpler formulations, can be combined to describe plastic behaviour. In this model, Stoughton (2002) assumed that both yield and potential functions were based on Hill's (1948) function with isotropic hardening. Validation of the model showed good agreement with experimental data for both yield and plastic strain ratios in uniaxial, equibiaxial, and plane-strain tension under proportional loading for steel, aluminum and possibly other alloys. The generalization described by Stoughton includes realistic elastic effects and fully anisotropic plastic behaviour under a NAFR, resulting in an accurate simulation of the *r*-value distribution and both uniaxial and biaxial yield behaviour. The latter behaviour is challenging for Hill's quadratic function under the AFR. The model was developed and implemented in FE code that is based on a convected coordinate system. Since the associated flow rule is commonly accepted as a valid law in the theory of plastic deformation of most metals, the arguments for the associated flow rule were also discussed. The material model was assumed to be rate-insensitive, and to have positive work hardening.

Pearce (1968) measured yield and plastic strain ratios in uniaxial and equibiaxial tension for 9 materials with broad range of r-values. Pearce restricted his analysis to address the limitations of Hill's quadratic theory for a material with normal anisotropy, or in-plane isotropy. Analysis of the Pearce data under the proposed NAFR model provides an interesting perspective on the shape of the yield function and plastic potentials for a wide range of materials (Stoughton, 2002). Figure 2.2 plots these shapes for each of the 9 materials, assuming normal anisotropy. All curves are normalized to unity in uniaxial tension. Interestingly, the shapes of the yield surfaces are very

similar for most of the materials, in that they are elongated in the biaxial mode. On the other hand, the plastic potentials are flattened in the biaxial mode for materials with low $\bar{r}$ and elongated as $\bar{r}$ is increased.
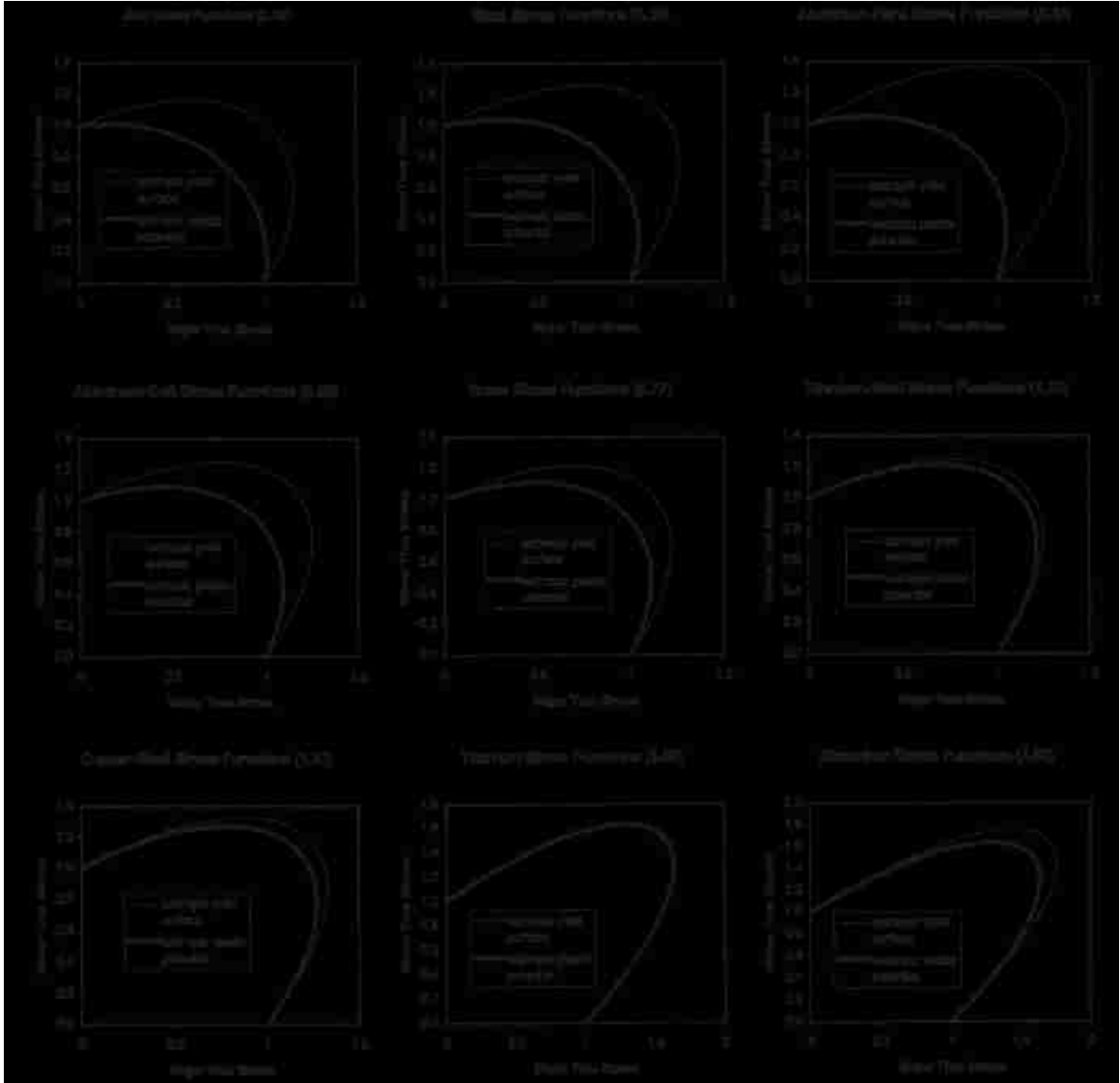
Figure 2.2. Yield stress functions (thin black line) and plastic potentials (heavy gray line) for the 9 materials used in the Pearce study, assuming normal anisotropy and NAFR model (Stoughton, 2002).

In other work, Stoughton and Yoon (2004) proposed a non-associated flow rule based on a pressure-sensitive yield criterion with isotropic hardening that is consistent with the Spitzig and Richmond data and analysis and fully accounts for the strength differential effect (SDE). Again, both functions (the potential function and the pressure insensitive part of the yield function) used in their model were based on Hill's (1948) formulation. Since the compression test results

departed from the experimental results, they suggested using mixed isotropic-kinematic hardening as a possible way to improve the model. As an example of the results presented by Stoughton and Yoon (2004), comparison of the shape of the plastic potential and yield functions of two different aluminum alloys (2090-T3 and 2008-T4) at zero shear stress is shown in Figure 2.3. The difference in shape, and more importantly, the difference in the normals between these two functions shows the degree to which these materials violate the AFR under this model. The violation does not appear to be as significant in the case of the 2008-T4 alloy.
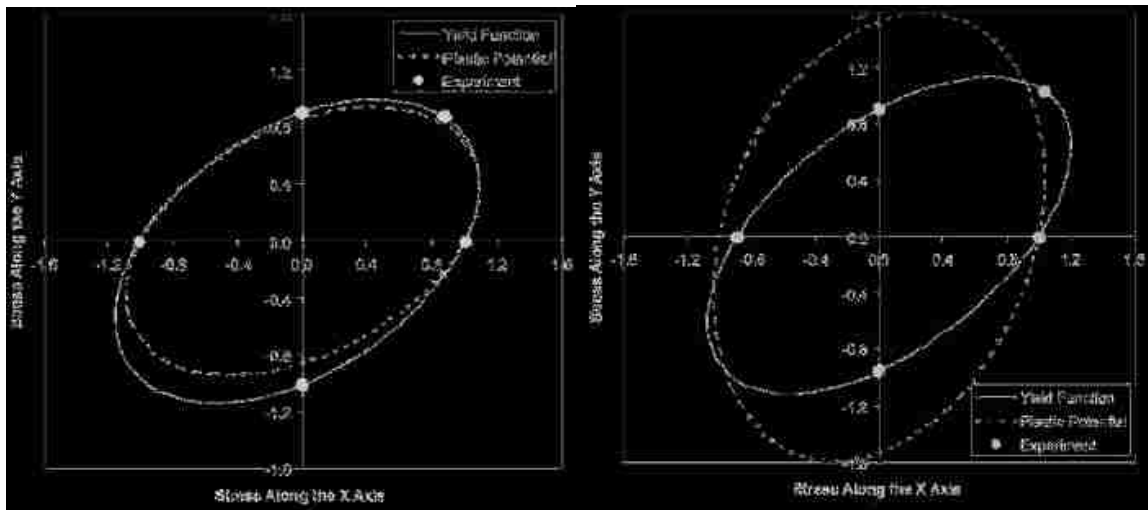
Figure 2.3. Comparison of yield function and plastic potential at zero shear stress for the 2008-T4 (left) and 2090-T3 (right) alloys. Experimental data points used to define the yield function are also shown (Stoughton and Yoon, 2004).

The NAFR models described in this section were based on isotropic hardening. It is natural to extend these concepts to include kinematic or more appropriately a mixture of kinematic and isotropic hardening. Such an extension raises two issues. First, kinematic effects give rise to a strength-differential effect. The standard implementation of kinematic models introduces an SDE in terms of a back-stress that offsets a pressure-insensitive yield criterion. This is mathematically incompatible with the SDE considered in the Stoughton and Yoon (2004) model. Interestingly, both types of SDE may play a role in the evolution of the material behaviour. The second issue concerning the inclusion of kinematic effects in a NAFR is the possibility that the plastic potential and yield functions are offset by different backstress tensors. Although numerical problems will arise if the centres of the two functions are completely independent, there does not appear to be any obvious reason why the centres need to be exactly aligned. Interesting possibilities arise if the centres of the two functions are defined by separate tensors. Numerical

problems can be avoided by suitable definition of a co-dependence in the evolution equations for these two back-stress tensors.

When considering ways to increase accuracy or efficiency for finite element simulation through the use of an improved material model, it is necessary to confirm that the new model satisfies all requirements for intrinsic stability. The relationship between the AFR and stability was briefly explained in section 2.3.1. Stoughton and Yoon (2006) discussed about a specific class of material models based on NAFR for a rate and temperature insensitive, isotropic hardening metal and derived the constraints required to ensure stability for this class of models. The existence of this class of non-associated flow rule models proves that both postulates are a sufficient but not necessary condition for stability. The constraints proved in their paper were derived based on generic yield and potential functions. So that, any NAFR model that does not violate these constraints is guaranteed to be intrinsically stable. The existence of an indeterminate solution has been thought to discourage the use of NAFR for both dynamic and quasi-static analyses theoretically. However, it was shown by Stoughton and Yoon (2008) that the indeterminate solution that may solve the equations of motion is intrinsically dynamic, and it goes to zero in the quasi-static limit regardless of other indeterminate parameters. Consequently, the existence of this indeterminate dynamic solution has no influence on stability and the use of NAFR for analysis of quasi-static problems. So, these common models can be generalized to include non-associated flow for analysis of the dynamic problem without concern that the solution will become indeterminate. In fact, based on these researches it was shown that Drucker's postulate is a sufficient but not necessary condition to ensure stability of plastic flow in metals. While this is well known for non-crystalline materials, the postulate continues to inhibit the consideration of NAFR models, and therefore, at least implicitly, is regarded by some in the metal forming field as effectively a necessary condition for a robust model.

Computational aspects

The use of advanced NAFR models has generally been ignored in computational metal plasticity - possibly due to the difficulties involved in obtaining the necessary material properties as well as to the added complexities in the mechanical model and its numerical implementation. The availability of powerful computers and efficient numerical methods make it possible, however, to carry out extensive numerical simulations and thus render these objections less critical. However, previous finite element analyses on the effect of superimposed hydrostatic pressure on the finite elastic-plastic deformation behaviour of crystalline solids have been presented by Brunig (1998; 1999) and Brunig and Obrecht (1998). Their formulations take into account deviations from the

classical Schmid-rule of the critical resolved shear stress as well as plastic volume changes including a macroscopic non-associated flow rule. Preliminary numerical simulations demonstrate the influence of additional constitutive and kinematic parameters on plastic yielding and permanent volume expansion in tension and compression tests. Most of these papers deal with the numerical simulation of large elastic-plastic deformation and localization behaviour of metals which are plastically dilatant and sensitive to hydrostatic stresses.

In general, efficient and stable iterative techniques are employed to solve the discretized equilibrium equations for each time step in displacement-based finite element procedures for nonlinear problems. Each iteration result may be seen as an estimate of the incremental displacements which are used to compute the current stress state and other field variables in the integration points of the finite elements. In computational plasticity approaches, many research groups employ the radial return technique (elastic predictor-plastic corrector method) to integrate the constitutive rate equations. This procedure works well for smooth yield conditions and associated flow rules as long as time increments remain reasonably small. Since the trade-off between accuracy and computational efficiency is an issue of current interest, Nemat-Nasser (1991) presented an alternative algorithm. His plastic predictor-elastic corrector technique yields nearly the exact solution even in large time steps for elastic-plastic materials.

2.4. Hardening law

During a process of plastic deformation of a hardening (or softening) material, the initial neutral yield surface is subjected to subsequent transformations. Experimental results show that these transformations in stress space consist of the following five elements (Kurtyka and Zyczkowski, 1996)

- Proportional expansion
- Translation
- Affine deformation
- Rotation
- Distortion, exceeding affine deformation.

The simplest case of pure proportional expansion is isotropic hardening and pure translation is called kinematic hardening. The combined case of expansion and translation is called mixed isotropic-kinematic hardening, or briefly mixed hardening and is often sufficiently accurate for

engineering applications. However, a more precise description of plastic hardening requires taking the remaining three of the above-mentioned elements into account. Simple hardening rules such as isotropic or kinematic hardening are based on the assumption that one or two hardening parameters describe the material state with sufficient accuracy. For instance, in the yield condition we have

$$f(\boldsymbol{\sigma} - \boldsymbol{\alpha}) - \sigma^Y(p) = 0 \tag{2.16}$$

This equation describes translation and expansion or contraction of the initial yield surface, and two parameters $\boldsymbol{\alpha}$ and p characterize the hardening state. Here $\boldsymbol{\sigma}$ denotes the stress tensor; $\boldsymbol{\alpha}$ may be interpreted as the backstress tensor whereas p is proportional to the length of plastic strain trajectory. Although, kinematic hardening appears to better represent actual test data, isotropic hardening is still widely used. The reason lies in the ease with which isotropic hardening may be implemented mathematically. It should be noted that neither the isotropic nor the kinematic hardening model is truly representative of the real material hardening behaviour, which can be quite complicated as observed experimentally. In the following, these two general categories will be introduced and explained.

2.4.1. Isotropic hardening

An isotropic hardening model assumes that the subsequent yield surface is a uniform expansion of the initial yield surface. It neglects the anisotropic effect on the subsequent yielding induced by deformation like Bauschinger effect which is observed experimentally. For isotropic, pressure insensitive materials, the yield function is

$$F = f(\boldsymbol{\sigma}') - \sigma^Y(p) = 0 \tag{2.17}$$

where $\boldsymbol{\sigma}'$ is the deviatoric stress tensor. Only one hardening parameter, p, is necessary to characterize isotropic hardening; σ^Y is a monotonically increasing function of p. Function σ^Y is typically taken as uniaxial yield strength that increases with p (usually the effective plastic strain). In fact, this function represents the radius of the yield surface, so, the only parameter which can vary in this model is the size of the yield surface. As the material starts to harden due to plastic work, the yield surface expands in stress space. There are two measures of hardening that can be used to define p: the first one is defined by the effective plastic strain and called the strain

hardening hypothesis. The second measure used as the isotropic hardening parameter is the total plastic work called the work hardening hypothesis. Also, different representation of common functions can be used to provide a best fit the experimental stress-strain curves of different materials. The most common functions are as follows

Isotropic hardening model	Formulation
Power law (Hollomon)	$\sigma^Y(p) = K \cdot p^n$
Power law (Ludwik)	$\sigma^Y(p) = \sigma_0 + B \cdot p^n$
Power law (Swift)	$\sigma^Y(p) = K \cdot (\varepsilon_0 + p)^n$
Exponential law (Voce)	$\sigma^Y(p) = \sigma_0 + Q \cdot (1 - e^{-b \cdot p})$

The applicability of these models in describing the metals hardening behaviour was investigated by Kleemola and Nieminen (1974).

2.4.2. Kinematic hardening

Cyclic material response can vary quite markedly from pure monotonic behaviour. Some early studies were done to describe yield surface evolution due to loading, unloading, and reloading, but their scope was limited to tensile deformation (Phillips and Sierakowski, 1965; Eisenberg and Phillips, 1971). Basically the plastic behaviour of material during reverse loading (as a part of cyclic deformation) is different in many aspects like yielding, hardening, and even elastic recovery. It is difficult to determine the hardening behaviour- or the expansion (contraction), translation and distortion of the yield surface- quantitatively without a knowledge of the stress-strain relation for plastic deformation. The alternation of the yield point observed when a stress reversal occurs after hardening is called "Bauschinger" effect. In classical kinematic hardening models, the yield surface translates freely in any direction but is not permitted to rotate. In the modelling of cyclic deformation of materials, so-called cyclic plasticity, kinematic hardening must be considered because it is able to model different situations in loading and reverse loading conditions more realistically. Ratcheting is another fact that is imperative to the definition of isotropic and kinematic hardening. Ratcheting is the accumulation of plastic strain, cycle-by-cycle, for a stress amplitude with a non-zero mean stress. As loading is repeated, each consecutive hysteresis loop will displace forward in a pertinent rate due to the failure of complete closure of each loop. Ratcheting is generally considered to be dominated by kinematic hardening (Khan and Huang, 1995). Generally, the models to be considered for cyclic plasticity and kinematic hardening include:

1. Prager-Ziegler kinematic hardening
2. Mechanical sub-layer model (Overlay model)
3. Multi-surface model (Mroz model)
4. Two surface model
5. Non-linear kinematic hardening model (Evanescent hardening)
6. Endochronic theory

Some experimental phenomena to be modeled in cyclic plasticity have been given by Drucker and Palgen (1981) and discussed by Dafalias (1984). A list of items applicable to models for large strain should include the following:

1. After deformation in one stress direction an excursion across the yield surface should show a reduced stress magnitude when yielding occurs again.
2. There should be a smooth transition from elastic to elastic-plastic behaviour when crossing the yield surface in the reverse direction from the previous loading.
3. The plastic modulus should gradually decrease as plastic flow recommences and achieves the value it had prior to unloading after 2-10 % subsequent strain.
4. After reverse flow when the plastic modulus achieves the value it had prior to unloading there may be a permanent softening where the flow stress magnitude is less than it would have been in unidirectional loading at the same equivalent strain.
5. Under symmetric stress or strain cycles, metals and alloys will cyclically harden or soften to a stable hysteresis loop.
6. Asymmetric stress cycles will cause cyclic creep (or ratcheting) in the direction of the mean stress.
7. Asymmetric strain cycles will cause progressive relaxation of the mean stress to zero.
8. Multiaxial, proportional, cyclic loading behaves similar to uniaxial cycling when the equivalent stress and equivalent strain are used for comparison.
9. Increased hardening is observed for multiaxial, non-proportional, cycling. Higher saturation stress levels are obtained for cycling to the same maximum strains. The largest increase in hardening is seen for 90° out-of-phase cycling.

A review of these observations shows that the first four items relate to deformation having few changes in loading direction while the next three are observed during cyclic deformation. The last

two items relate specifically to multiaxial cycling. Some of these phenomena are shown in Figure 2.4. for the uniaxial state, since the vast majority of the experiments and modelling have been applied to uniaxial cycling.

Figure 2.4. An example of stress-strain response in a forward-reverse deformation in uniaxial state (Yoshida and Uemori, 2003).

A common feature of all of the models considered is their use of a "backstress" to account for the stress space symmetry. The differences arise from the way the backstress develops. These models can be characterized by evolution laws for the backstress and can be evaluated in terms of how well they can represent the conditions described above. When considering these cyclic plasticity models, attention is given to the backstress evolution, or kinematic portion. In some applications no isotropic hardening is used (Mroz models) but for most of these models a monotonic increase in the yield surface radius is allowed (as explained in the previous subsection). A brief summary of the models listed above is given in the following. The highlights of their suitability to model the above mentioned phenomena are also considered.

2.4.2.1. Prager-Ziegler linear kinematic model

To calculate the Bauschinger effect, Prager (1956) suggested the kinematic hardening model. This model assumes that the yield surface translates as a rigid body in stress space during the plastic deformation. According to this model, the simulation of plastic response of materials is

proportional to the plastic strain. The equation proposed by Prager to describe the evolution of the backstress that represents the centre of the yield surface is

$$d\boldsymbol{\alpha} = C.d\boldsymbol{\varepsilon}^p \qquad (2.18)$$

where C is a material constant derived from a simple monotonic uniaxial curve and $d\varepsilon^p$ is the rate of effective plastic strain. According to Ziegler (1959), one deficiency of Prager's linear kinematic hardening is that it does not give consistent results for 3D and 2D cases. The transverse softening effect introduced by Prager's model as a deficiency for uniaxial tension. To overcome these limitations, Ziegler (1959) proposed the following modification of Prager's model

$$d\boldsymbol{\alpha} = d\mu.(\boldsymbol{\sigma} - \boldsymbol{\alpha}), \quad \text{where} \quad d\mu = C.dp/\overline{\sigma}_e \qquad (2.19)$$

where $d\mu$ is a proportionality scalar constant determined by the yield criterion and dp is the effective plastic strain rate. It should be noted that in the three-dimensional case with von Mises criterion, Prager's model is the same as Ziegler's model. Prager-Ziegler kinematic hardening has the simplest explicit evolution equation for the backstress. This is the most common theory employing a backstress and has been incorporated into most non-linear finite element codes.

The significant shortcomings of this model include its failure to give a smooth elasto-plastic transition during reverse loading, and its failure to develop a stable, symmetric hysteresis loop during cyclic deformation. This model has been applied to large strain deformation, and is often combined with some form of isotropic hardening. For such a model, the permanent softening is a measure of the backstress prior to unloading. However, Wilson and Bate (1986) showed that this is not what occurs physically. The permanent softening is not a good measure of the backstress in the lattice of the material. In fact, the main criticism of this kind of kinematic hardening rule relates to the linearity of the stress-strain behaviour derived from it. Though the model accounts for some Bauschinger effect, difficulties appear when it is applied to model complex loadings. For instance, Eisenberg and Phillips (1968) tried to generalize this model to non-linear hardening. Attempts have also been made to generalize this model by letting C be a function of plastic strain, but this leads to inconsistencies since there is a unique relationship between the backstress and plastic strain (Chaboche, 1986). What is required is for C to be such that it gives the proper backstress increase during monotonic loading (which is a fairly slow increase) and a rapid change in backstress during reversing. As long as this is not the case, the Prager-Ziegler kinematic hardening rule can not be used for a proper modelling of cyclic behaviour.
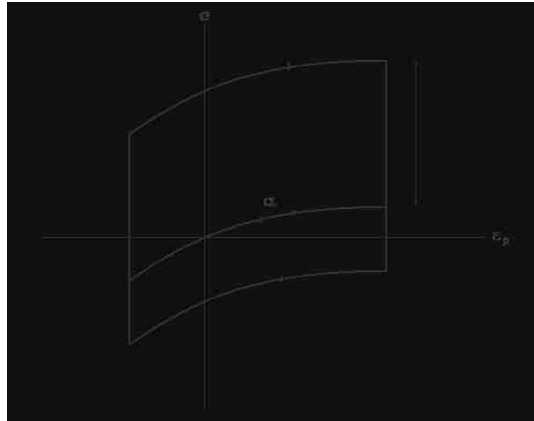
Figure 2.5. Generalized Prager-Ziegler model for nonlinear kinematic behaviour.

2.4.2.2. The overlay model (Mechanical sub-layer model)

The overlay model (also called the distributed-element model or mechanical sub-layer model) was proposed by Besseling (1958) and Iwan (1966) independently and generalized for multiaxial loading by Chiang and Beck (1994) and Bate and Wilson (1986). All these models have been shown to be successful at describing the multiaxial cyclic elastic-plastic behaviour of real materials (Yoon et al., 2004). Among the cyclic plasticity models, the overlay model is considered to be physically motivated, as many real materials or mechanical systems can be thought of as having a similar structure. For instance, most of the materials used in engineering structures have a crystalline structure that is made of a distribution of slip-planes or dislocations of different slip strengths. Moreover, the overlay model has definite advantages compared with classical models in that it can describe qualitatively a variety of effects that the classical models are not able to describe, with a fairly simple description. Schiffner (1995) introduced the four types of sub-element and tried to find the optimal combination of sub-elements for structural analysis under cyclic loading. In the mechanical sub-layer model a number of independent structural elements (so-called Jenkin's elements) are connected and deformed in parallel. Each of the sub-elements represents one of the following idealized material behaviours as shown in Figure 2.6: elastic behaviours (E-sub-element), perfectly elasto-plastic behaviour (P-sub-element), elasto-plastic behaviour with kinematic hardening (K-sub-element) or with isotropic hardening (I-sub-element). Each element undergoes the same deformation but by having different flow strength and hardening properties a composite response is obtained. Physically, these elements might be thought of as representing a slip plane in a solid material. The distribution of yield strength and fraction of elements might be closely related to internal structure, deformation

mechanism, composition, grain size, etc. Chiang et al. (2002) extended this model to account for the deformation-induced anisotropy demonstrated in subsequent yield surfaces.

This modelling concept does not allow the development of permanent softening although it does introduce a more gradual transition from elastic to reverse plastic flow. In order to achieve a good match with experiments many elements are required which adds many variables to the theory and increases the complexity.
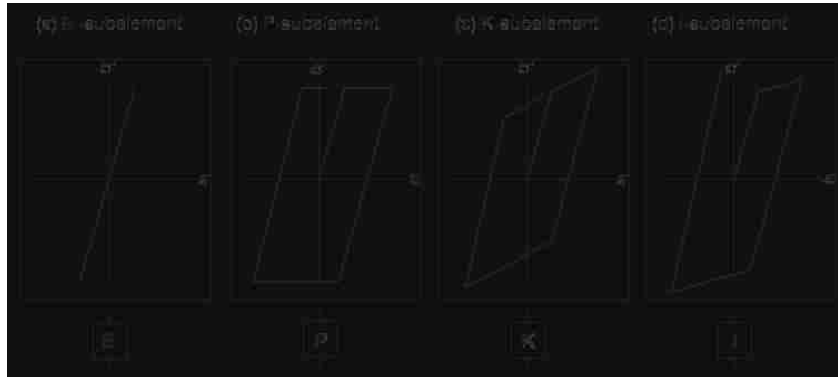
Figure 2.6. Standard models for the description of idealized material behaviour: (a) elastic; (b) perfectly elasto-plastic; (c) elasto-plastic with kinematic hardening; and (d) elasto-plastic with isotropic hardening (Schiffner, 1995).

2.4.2.3. The Mroz model (Multi-surface model)

Mroz (1967; 1969) proposed the multi-yield surface model by introducing the concept of a "field of work hardening moduli" instead of the single modulus *C* used in Prager's model. Clearly the Mroz's model for a one-dimensional case is a simple one. It approximates the nonlinear stress-strain curve for the linear segments and determines the moduli for each segment and initial yield stresses for every adjacent point between any two linear segments. In the multiaxial case, the Mroz model consists of a series of nested surfaces which can translate inside one another. The plastic modulus is given as a function of the size of the active surface. The active surface is the largest surface which the stress point contacts. Once the active surface touches the next larger surface it no longer is active but just translates along with the stress point. The direction in which the active surface translates is given by the vector connecting the stress point with the point on the next larger surface having the same outward normal *n* as the active surface. This is illustrated in Figure 2.7. This leads to a piecewise stress-strain curve with a large number of surfaces required to obtain a good fit to experiment. An important difference between the Mroz and Prager models is the direction of yield surface translation. For multiaxial loading they can be quite different. This is brought out in more detail when considering multiaxial, non-proportional cycling. This

model is useful in generalizing the linear kinematic hardening rule. It also enables the description of the nonlinearity of stress-strain loops under cyclically stable conditions, the Bauschinger effect, and the cyclic hardening and softening of materials with asymptotic plastic shakedown. The shortcoming of this model is its inability to describe ratcheting under asymmetric loading conditions. Another deficiency of this model is that for a smooth nonlinear curve approximation, a large number of yield surfaces are necessary. This disadvantage is more significant if the model is implemented into a numerical FE code. It is computationally expensive because each surface requires the storage of a scalar describing its size, and a tensor value locating its position. Given the large number of surfaces that are required to reasonably approximate the flow curve of a typical material, the number of stored values can rapidly become unwieldy. Choi and Pan (2009) developed a generalized anisotropic hardening rule based on the Mroz multi-surface model for pressure insensitive and sensitive materials.
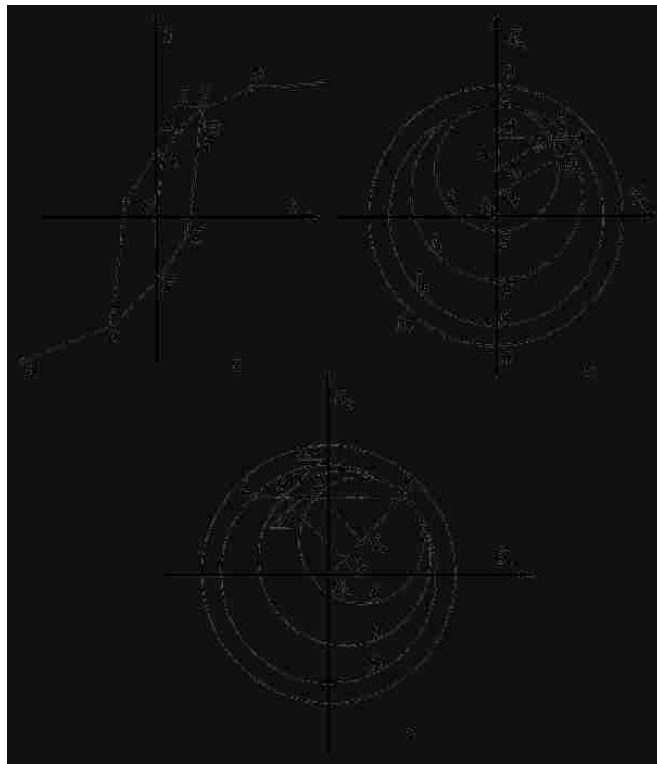
Figure 2.7. Approximation of the stress-strain curve (a) and the corresponding fields of work hardening moduli after reaching point C (b) and for the stress history OCK (c) (Mroz, 1969).

2.4.2.4. Two-surface model (Dafalias and Popov model)

The two-surface model was first introduced by Krieg (1975) and Dafalias and Popov (1975; 1976). Conceptually it is similar to the Mroz model since it contains one surface (the yield or

loading surface) nested inside of another (the bounding surface). In the Mroz model the plastic modulus equals its constant value associated with the outer active surface. In the two-surface model the plastic modulus is given as a function of the distance between the yield and bounding surfaces (so-called plastic internal variable "PIV"). As illustrated in Figure 2.8, when the loading direction is reversed the distance between the two surfaces is measured between points on the corresponding surfaces having the same outward normal n. The magnitude of this distance is given as δ where δ_{in} represents this value when plastic flow is reinitiated. The direction of motion of the yield surface is given by the same rule as that of the Mroz model. That is, the direction of motion is given by the vector connecting the corresponding points on the two surfaces having the same n. Both Krieg's and Dafalias and Popov's models enable the yield and bounding surfaces to experience both isotropic and kinematic transformations. One possible drawback of two-surface models is they require some search algorithm to find the common normal on the bounding surface. While this search is a straightforward operation, it is often preferable to reformulate the problem in terms of differential equations governing the evolution of the yield surface. Recasting these equations can enable the use of more efficient computational algorithms. In this model a small partial reverse load followed by reloading can cause a significant stress overshoot. The updating procedure chosen by Dafalias and Popov leads to this overshoot but it is not a necessary consequence of two-surface models.
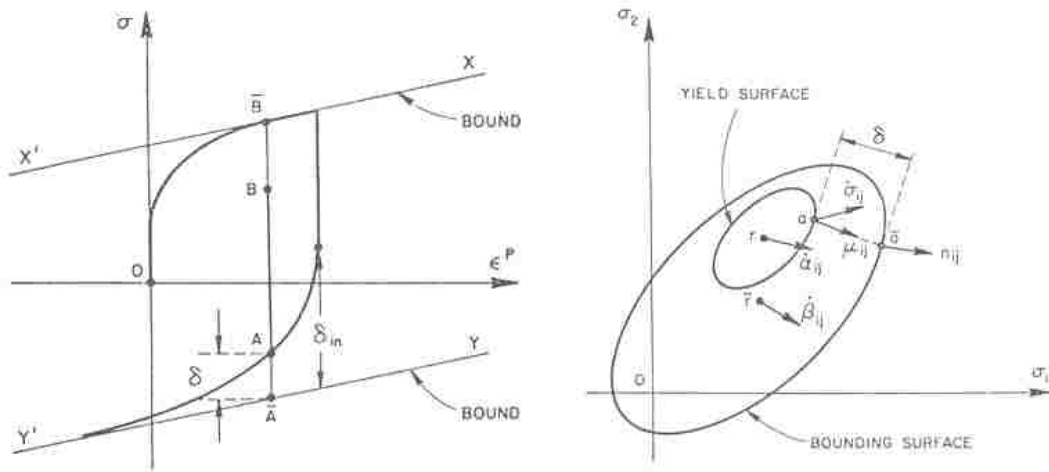
Figure 2.8. Illustration of the two-surface plasticity model (a) one dimensional and (b) multiaxial representation (Dafalias and Popov, 1976).

Within the two-surface concept, attempts were made to solve the problem with the updating procedure of the initial distance δ_{in} and thereby of the rules on how δ, the current distance, should be measured (Petersson and Popov, 1977; Tseng and Lee, 1983; Bruhns and Muller, 1984).

Voyiadjis and Kattan (1990; 1991) proposed a cyclic theory of plasticity for finite deformation in the Eulerian reference system. A new kinematic hardening rule was proposed based on several experimental observations (Philips et al., 1974; Philips and Weng, 1975; Philips and Moon, 1977; Philips and Lee, 1979; Philips and Das, 1985). This model was shown to be more in line with experimental observations than the Tseng-Lee model. This model uses the minimum distance between the yield surface and the bounding surface as a key parameter. Voyiadjis and Sivakumar (1991; 1994) did further modifications on these cyclic models to take other aspects into account.

2.4.2.5. Nonlinear kinematic hardening model (Armstrong-Frederick-Chaboche model)

Proposed by Armstrong and Frederick (1966), this model simulates the multiaxial Bauschinger effect (movement of the yield surface in the stress space). When compared to the previously existing models, this one predicts Bauschinger effect where intuitively one would be expected, for example, the uniaxial cyclic loading test. When compared to experimental results, this model's predictions were more accurate than linear kinematic or isotropic hardening models for cyclic loadings. This model also proposed some advancement in terms of simplicity for computational purposes. The A-F model is based on the assumption that the most recent part of the strain history of a material dictates its mechanical behaviour. They proposed an evanescent strain memory effect (evanescent along the plastic strain path). Its kinematic hardening rule in the simplest form is written by the following differential equation

$$\boldsymbol{d\alpha} = \frac{2}{3}C_1.\boldsymbol{d\varepsilon^p} - C_2.\boldsymbol{\alpha}.dp \qquad (2.20)$$

The constants C_1 and C_2 are determined from uniaxial tests. The key of this simple model is the recall term, the second term on the right hand side whose direction depends on the current value of the backstress and provides the strain path dependence. The nonlinearity introduced by the recall term is thus not the same during a flow under tensile or under compressive loading. Here the backstress is removed more quickly during reverse flow than it builds up during monotonic loading. The plastic modulus is larger when plastic flow commences in the reverse direction than it had been during forward loading but there is not a smooth elasto-plastic transition. Also the theory predicts a saturation of the backstress to a value of ($2C_1/3C_2$) during a long proportional path and no permanent softening. This model has been used to simulate the shape of cyclic curves at one strain range, but often fails when the strain range is changed. The constant C_2 determines both how quickly the backstress builds up during monotonic loading and the degree of rounding

of the stress-strain curve during reversing. A large value of C_2 is needed to adequately model the large stiffness during reversing but a small C_2 is required for the correct build up of backstress. Chaboche (1986) accommodated this to increase the range of validity of the original model and improve the quantitative description of the ratcheting effect and degree of freedom available by superimposing several models of the same type as follows

$$\boldsymbol{\alpha} = \sum_{k=1}^{m} \boldsymbol{\alpha}_k, \text{ where } \quad d\boldsymbol{\alpha}_k = \frac{2}{3}(C_1)_k \, d\boldsymbol{\varepsilon}^p - (C_2)_k (\boldsymbol{\alpha})_k \, dp \qquad (2.21)$$

Each of the variables $\boldsymbol{\alpha}_k$ then works independently with the same kind of nonlinear rule (A-F). One of them can be linear, with the recall term omitted ($C_2=0$), e.g. $d\boldsymbol{\alpha}_m = \frac{2}{3}(C_1)_m \, d\boldsymbol{\varepsilon}^p$.

Adding an additional linear backstress changes the "implied" two-surface model to allow kinematic hardening of the bounding surface in this case. In the original paper by Chaboche, three kinematic variables were suggested and then additional variables were denoted as primary (appearing in the yield surface expression), secondary and tertiary kinematic variables. This was done to construct descriptive relations between this nonlinear kinematic model and other classical models like Mroz or two surface or other nonlinear models.

Superposition of Isotropic Hardening:

Independently of kinematic effect, accumulation of dislocations can be represented by accumulated plastic strain. The corresponding strength modification can be introduced in the modelling through a change in the width of the elastic domain: this change is given by the isotropic internal stress (or the size of the yield surface). To introduce the evolution of isotropic hardening one can use any function of accumulated plastic strain as explained in section 2.4.1.

Characteristics of the Model:

Jiang and Kurath (1996) examined the characteristics of a category of Armstrong-Frederick hardening rules, invoking both theoretical and experimental considerations. Due to the degree of insensitivity and decoupling of many model parameters, it is possible to formulate a straightforward method to fit the basic material properties from a simple uniaxial experiment. Chelminski (2003) analyzed the system of equations proposed by Armstrong and Frederick from the mathematical point of view. Auricchio and Taylor (1995) presented a comparative study between nonlinear kinematic hardening model and a generalized plasticity model as a new model.

The two models were reviewed and discussed from both continuous and discrete time points of view. Broggiato et al. (2008) studied the proper identification processes of the Chaboche model based on an inverse method. Yoshida et al. (2003) presented a novel approach to identification of the mechanical properties of sheet metals for Chaboche model based on optimization of an inverse method.

Other Modifications:

The ability and simplicity of the Armstrong-Frederick model indicates the engineering potential of this type of nonlinear kinematic model. Many researchers have made significant enhancements to this model for different applications. The thermodynamic framework was developed by Chaboche et al. (1989; 1997; 1998) to account for varying temperature effects. There have been many significant modifications to this model which will not be mentioned in detail for the sake of brevity, e.g. (Chaboche, 1991; Wang and Ohno, 1991; Ohno and Wang, 1993a, b; Ohno, 1998; Chen et al., 2005; Yoshida, 2000; Voyiadjis and Basuroychowdhary, 1998; Basuroychowdhary and Voyiadjis, 1998). Furthermore, a number of researchers proposed modifications to the Ohno-Wang model, e.g. (McDowell, 1995; Jiang and Sehitoglu, 1996a, b; AbdelKarim and Ohno, 2000; Chen and Jiao, 2004).

2.4.2.6. Endochronic theory

The endochronic theory uses an internal time variable as a measure of the history of deformation (Khan and Huang, 1995). Many engineers have avoided the endochronic theory because it does not resemble the classical formulations. Plasticity laws have historically been formulated in terms of incremental of flow relationships due to the nature of deformation processes. The endochronic theory has been constructed using integrals over the deformation history. It has received some attention because of its success in modelling some of the phenomena of cyclic plasticity. Its success was derived from its flexibility to include many parameters to match experiments.

2.4.3. Other aspects of hardening

Yield Surface Distortion
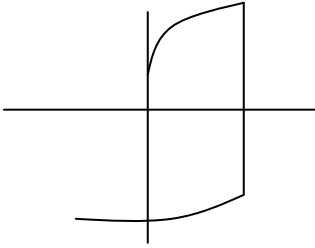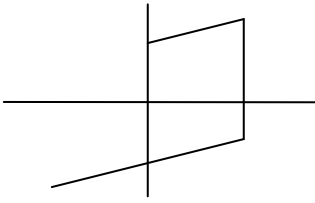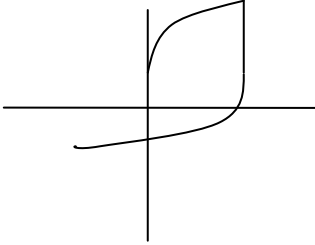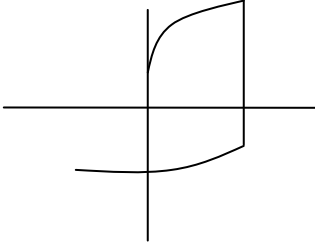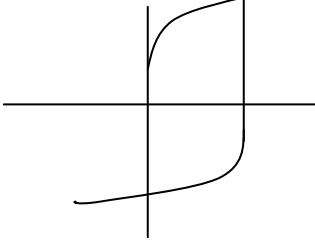
General transformations of the von Mises yield condition, mentioned by Edelman and Drucker, were investigated in detail by Baltov and Sawczuk (1965) and others. Numerous experimental investigations were gathered and discussed by Michno and Findley (1976) and others. Most of them show remarkable distortion of subsequent yield surfaces, connected with increase of their

curvature in the vicinity of the control point (generic stress point), and flattening on the opposite side. Many researchers have proposed different theories to describe these behaviours, e.g. (Freudenthal and Gou, 1969; Williams and Svensson, 1971; Phillips and Weng, 1975; Shiratori et al., 1979; Rees, 1982; Ortiz and Popov, 1983). A relatively simple geometric description of distortional plastic hardening was given by Kurtyka and Zyczkowski (1985) and Zyczkowski and Kurtyka (1984). Other studies have been performed on distortion of isotropic and anisotropic yield surfaces by many researchers, e.g. (Helling and Miller, 1987; 1988; Voyiadjis and Foroozesh, 1990; Kurtyka and Zyczkowski, 1996; Kowalsky et al., 1999; Francois, 2001; Vincent et al., 2002; 2004; Aretz, 2008).

2.4.4. Comparative study

As discussed above, each of these cyclic plasticity models has certain strengths and weaknesses. The choice of a model depends in part upon the phenomena most important for a given application. The Mroz, two-surface, and nonlinear models give qualitatively similar modelling capabilities. The two-surface model has the advantage of specifying a smooth elasto-plastic transition and a better simulation of random-type loadings and ratcheting effects (Chaboche, 1986). One of the disadvantages of the Mroz and two-surface models is that they need significant memory capability for updating procedures in the computational code. Also the updating procedure can fail in the special case of out-of-phase multiaxial loading because no unloading takes place although cycling (the reverse loading) is evident. Another inconsistency of this model that occurs in uniaxial load-unload-reload situations where plastic flow is very small during unloading was pointed out by Chaboche (1986). This leads to the overshooting of the new tensile curve. The nonlinear kinematic models are characterized by difficulties in modelling the smooth elasto-plastic transition, which requires superposition of several nonlinear rules (Chaboche, 1986). Also, they all have a common characteristic of generating reversal flow stress curves that saturate to the monotonic loading curve, thereby having difficulties to model a possible offset in flow stress when the load is reversed. The enforcement of a smooth transition will, in turn, overestimate the ratcheting effect. Because nonlinear models always result in ratcheting this problem appears to be a topic for further investigations. On the other hand, these models have the advantage of easier numerical implementation and connection with internal variable theories. Table 2.1 shows the basic hardening models, all among single-surface plasticity, their characteristics, formulations and uniaxial stress-strain behaviours.

Table 2.1. Different basic hardening models, characteristics, formulations, and behaviours in uniaxial stress-strain shape.

Material Model	Formulation	Stress-Strain behaviour
Isotropic Hardening -No Bauschinger effect -No transient behaviour for reverse loading -High level of stress for reverse loading -No work hardening stagnation -No permanent softening	$f(\boldsymbol{\sigma}) - \sigma^Y = 0$ $\sigma^Y = k(\bar{\varepsilon}^p)$	
Linear Kinematic Hardening -No nonlinearity of stress-strain -No transient behaviour for reverse loading -No work hardening saturation -Quite inaccurate for large strains -No work hardening stagnation -No permanent softening	$f(\boldsymbol{\sigma} - \boldsymbol{\alpha}) - \sigma_0^{\,Y} = 0$ $\sigma_0^{\,Y} = Cte.$ $d\boldsymbol{\alpha} = \dfrac{C}{\sigma^Y}(\boldsymbol{\sigma} - \boldsymbol{\alpha})d\bar{\varepsilon}^p$	
Nonlinear Kinematic Hardening -Early reverse yielding -Severe work hardening saturation -Low level of stress for reverse loading -Problematic fitting for multiple cycles -No work hardening stagnation -No permanent softening	$f(\boldsymbol{\sigma} - \boldsymbol{\alpha}) - \sigma_0^{\,Y} = 0$ $\sigma_0^{\,Y} = Cte.$ $d\boldsymbol{\alpha} = \left[\dfrac{C}{\sigma^Y}(\boldsymbol{\sigma} - \boldsymbol{\alpha}) - \gamma\boldsymbol{\alpha}\right]d\bar{\varepsilon}^p$	
Mixed Isotropic-Linear Kinematic Hardening -No transient behaviour for reverse loading -Problematic fitting for multiple cycles -No work hardening stagnation -No permanent softening	$f(\boldsymbol{\sigma} - \boldsymbol{\alpha}) - \sigma^Y = 0$ $\sigma^Y = k(\bar{\varepsilon}^p)$ $d\boldsymbol{\alpha} = \dfrac{C}{\sigma^Y}(\boldsymbol{\sigma} - \boldsymbol{\alpha})d\bar{\varepsilon}^p$	
Mixed Isotropic- Nonlinear Kinematic Hardening -No work hardening stagnation -No permanent softening	$f(\boldsymbol{\sigma} - \boldsymbol{\alpha}) - \sigma^Y = 0$ $\sigma^Y = k(\bar{\varepsilon}^p)$ $d\boldsymbol{\alpha} = \left[\dfrac{C}{\sigma^Y}(\boldsymbol{\sigma} - \boldsymbol{\alpha}) - \gamma\boldsymbol{\alpha}\right]d\bar{\varepsilon}^p$	

2.5. Cyclic plasticity models for sheet metal forming

In many sheet forming processes, especially those that include drawbeads, the sheet metal undergoes cyclic bending. Particularly for springback analysis, modelling of the Bauschinger effect and cyclic hardening characteristics of materials is of vital importance. Cyclic effects caused by this type of deformation cannot be predicted with the common isotropic hardening law, and a suitable kinematic hardening law is therefore required. Recently, some constitutive models have been proposed for sheet metal forming simulations that endeavour to consider anisotropic properties and cyclic deformation effects and kinematic hardening at the same time.

Tang et al. (2001) used the anisotropic hardening rule proposed by Mroz to calculate the springback of sheet metal after the forming process. For an accurate computation of the stress increment for a given strain increment by using Mroz's rule, they proposed the radial return method to compute such stress increment to save computing time. Gau and Kinzel (2001; 2005) proposed a new incremental method based on the isotropic and kinematic hardening (Mroz multiple surface model) and plane strain assumption. This model compares well with the experimental results for aluminum sheet metal undergoing multiple-bending processes. They used Hill's (1948) yield criterion and implemented it into a series of analytical equations based on incremental deformation to find the internal stress equation for both elastic and plastic deformation of each fibre layer in the sheet thickness. Wu (2002) extended Hill's (1948) anisotropic theory of plasticity to include the concept of combined isotropic-kinematic hardening for sheet metals. A single exponential term was used to describe isotropic hardening and Prager's linear kinematic hardening rule was applied for simplicity.

Geng and Wagoner (2002a; b) generalized the nonlinear kinematic hardening model proposed by Armstrong and Frederick by introducing an independent evolution of the bounding surface to capture a permanent offset. To model the permanent softening the bounding surface translates and expands concurrently according to a mixed hardening rule. In their work, the Geng-Wagoner hardening law was implemented in conjunction with three anisotropic yield functions (Hill's 1948 quadratic yield function, Barlat's three-parameter yield function, Barlat Yld89, and Barlat's seven-parameter yield function, Barlat Yld96) for 6022-T4 aluminum alloy. They used their models to simulate the springback angle and anticlastic curvature of sheet deformed by the draw-bend test. As an alternative to the Geng-Wagoner model, a reasonably simple anisotropic nonlinear kinematic hardening model (ANK model) was proposed by Chun et al. (2002a; b). In their work, the combined nonlinear hardening model for time independent cyclic plasticity, proposed by

Chaboche and co-workers, was examined and a simple modification was suggested for the isotropic part of hardening rule to utilize the conventional tensile test data directly.

Chung et al. (2005) and Lee et al. (2005a; b) formulated the non-quadratic anisotropic plane stress yield function (Yld2000-2d) with modified Chaboche-type combined isotropic-kinematic hardening law to account for the Bauschinger effect and transient behaviour, in order to improve the prediction capability of springback in automotive sheet forming processes. The modified Chaboche model was confirmed to well represent the measured hardening behaviour including the Bauschinger and transient behaviour. Chow and Yang (2004) proposed a generalized mixed isotropic-kinematic hardening plastic model coupled with anisotropic damage for sheet metal forming. They developed a nonlinear anisotropic kinematic hardening rule (in the form of A-F model) for plane stress Hill's (1948) yield criterion for sheet metal forming. In another work, Chow et al. (2002) developed an anisotropic damage coupled mixed isotropic-kinematic hardening for the prediction of forming limit diagrams (FLD).

Yoshida and Uemori (2002; 2003) proposed a framework of constitutive modelling of large-strain cyclic plasticity which describes both the deformation- and texture-induced anisotropies of materials. In this model, the transient Bauschinger effect is described accurately by a new equation of the backstress evolution, and the strain-range and mean-strain dependencies of cyclic strain hardening are expressed by a model of work hardening stagnation. They demonstrate the advantage of their model in the springback analysis over other classical models by comparing the FE simulations of draw bending with the corresponding experimental results. Cardoso et al. (2005) implemented the non-quadratic yield function "Yld2000-2d" with the two-surface Dafalias and Popov kinematic hardening model that is suitable for the treatment of the Bauschinger effect in aluminum alloys sheet forming.

Choi et al. (2006a; b) proposed a new anisotropic elasto-plastic material formulation (rotational-isotropic-kinematic- RIK hardening) to reduce the drawbacks of phenomenological material models under multi-path loadings. The model enables the anisotropic yield surface to grow (isotropic hardening), translate (kinematic hardening) and rotate (rotation of the anisotropy axes) with respect to the deformation, while the shape of the yield surface remains unchanged. The model was formulated on the basis of an Armstrong–Frederick type kinematic hardening, the plastic spin theory for the reorientation of the symmetry axes of the anisotropic yield function, and additional terms coupling these expressions. Barthel et al. (2008) presented a phenomenological material model to take into account the distortional hardening (as well as isotropic and kinematic) and used it to simulate springback. Recently, Cardoso and Yoon (2008) successfully obtained the Bauschinger ratio from a crystal plasticity-based simulation replacing

an experimental approach and implemented the backward-Euler method for Yld2000-2d function (Barlat al, 2003) based on the two-surface Dafalias and Popov kinematic hardening model.

A more advanced hardening model was proposed by Teodosiu and Hu (1998) based on the microstructural evolutions that accurately described the non-proportional loading situation and cyclic effects such as the Bauschinger effect, the work hardening stagnation, and the permanent softening. Haddadi et al. (2006) discussed a detailed description of that (T-H) model and also performed several rheological tests, and carried out numerical simulations on different materials, in order to evaluate the accuracy and the efficiency of this model. A strategy for the identification of material parameters was also discussed. Of course, this model requires a large number of parameters to be identified, so it is an expensive model both experimentally and numerically. Haddag et al. (2007) compared two mixed isotropic-kinematic hardening models: the T-H microstructural model and the classical Chaboche model to investigate the springback behaviour of a drawing process. They concluded that, for more complex processes involving multi-step operations and abrupt strain path changes, further improvement can be expected by using more physically-based models such as the T-H model.

2.6. Experimental determination of cyclic stress-strain curves for sheet metals

Cyclic stress-strain curves can be obtained precisely by the torsion of a metal bar or tube. It is difficult to achieve the cyclic path of deformation in flat sheet metals. The planar simple shear test (Miyauchi, 1977; 1992) makes it possible to measure the Bauschinger effect quantitatively. Figure 2.9 shows the principle of planar shear test. However, pure shear hardly exists in reality and principal stresses are major interests in sheet metal forming. Out-of-plane buckling will occur due to severe shearing. Therefore, the planar simple shear test is easy to analyze but difficult to perform. Kuwabara et al. (1995) presented an in-plane compression test in which the specimen, a piece of sheet metal, is sandwiched between a couple of comb-shaped dies as shown in Figure 2.10. Teflon films were placed between the dies and the specimen in order to reduce the friction forces as much as possible. According to Balakrishnan (1998) in-plane buckling of sheet metals was frequently seen even though out-of-phase buckling was circumvented by transverse clamping forces. The stress is not simply uniaxial due to the clamping force and friction.
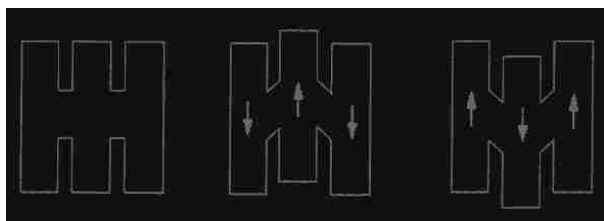
Figure 2.9. Principle of planar simple shear test (Miyauchi, 1977).
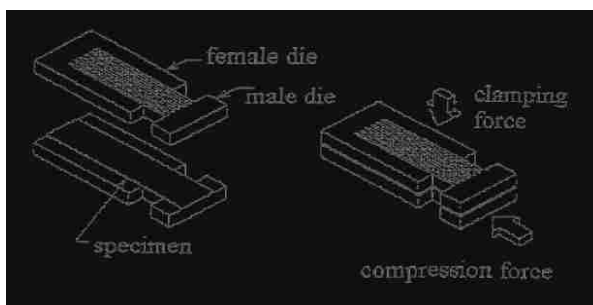
Figure 2.10. Principle of in-plane compression test (Kuwabara et al., 1995).

Another practical type of experiment is the cyclic bending of the metal sheets. Jiang (1997) performed three-point bending tests for springback investigation. The experiment is not quite stable upon reverse loading and the measured punch load versus punch stroke curve is not continuous due to the simple bending apparatus. Shen (1999) carried out similar work with a modified equivalent three-point bending apparatus and thus improved the results. Yoshida et al. (1998) designed a uniform bending machine as illustrated in Figure 2.11. In the test, one end of a specimen is clamped and is rotated by a step-motor, and during the bending process the other end moves freely in x-y directions without rotating. In this method, the noise becomes significant when the thickness of the sheet specimen exceeds 1.0 mm. In the automobile industry, sheet metal with a thickness greater than1.0 mm is quite often utilized.
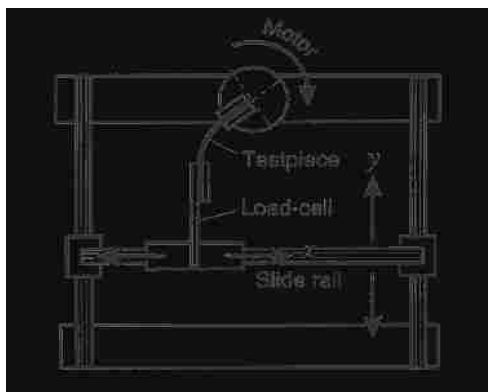
Figure 2.11. Schematic of cyclic pure bending test (Yoshida et al., 1998).

Yoshida and coworkers (2002), in other work, designed an in-plane cyclic tension-compression test for sheet metals. They studied the deformation characteristics of large-strain cyclic elasto-plasticity on steel sheets under in-plane tension-compression and evaluated the performance of some typical existing constitutive models in describing such large-strain cyclic plasticity. In-plane tension-compression tests became possible by employing adhesively bonded sheet laminate specimens, as well as a special device for preventing the buckling of specimens (Figure 2.12 and 2.13). A special device (specimen holder) for preventing buckling was attached to the specimen by coil-springs.
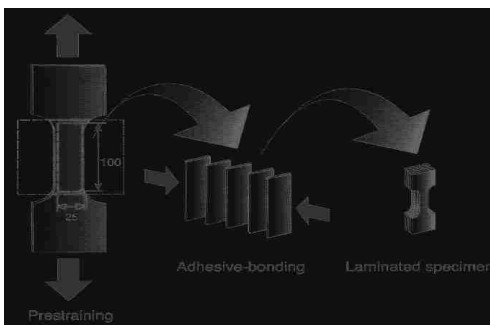
Figure 2.12. Preparation of the laminated specimen with pieces of sheets cut from a uniaxially prestrained sheet (Yoshida et al., 2002).
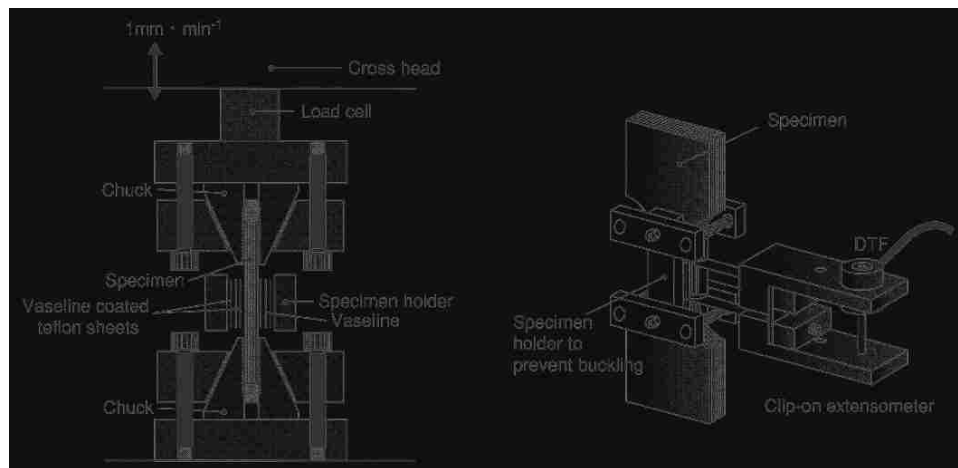
Figure 2.13. Schematic illustrations of in-plane cyclic tension-compression tests of sheet metals (Yoshida et al., 2002).

An equivalent three-point bending test, as illustrated in Figure 2.14, was proposed by Zhao and Lee (2001; 2002). The major advantages of this kind of bending include small capacity requirement, ease of control, and stable transition from unloading to reverse loading. A typical

specimen has a rectangular geometry of 203 mm length and 25 mm width. A load cell is mounted above the punch to record the punch load. All the tests are displacement controlled at punch speed of 0.5 mm/sec so that strain-rate effects can be neglected. The stroke and load of the punch, the strains on both surfaces of the specimen, and the rotation angle at one end of the specimen are recorded simultaneously.
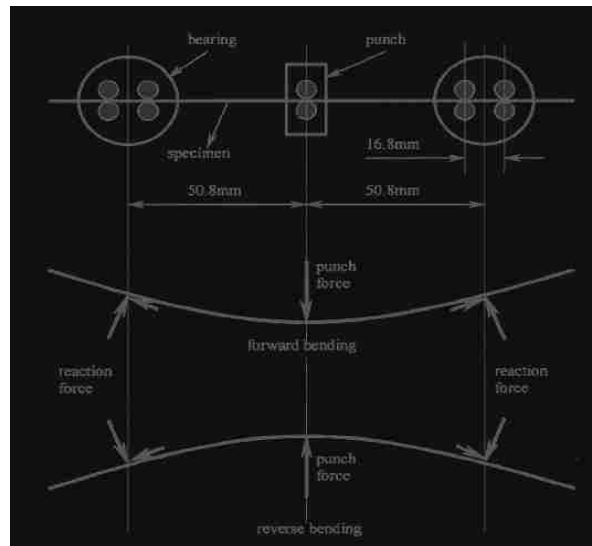
Figure 2.14. Schematics of cyclic three-point bending test (Zhao and Lee, 2001).

Brunet et al. (2001) proposed an inverse identification technique based on bending-unbending experiments for anisotropic sheet-metal strips. The initial anisotropy theory of plasticity was extended to include the concept of combined isotropic and nonlinear kinematic hardening. To this end, a specific bending-unbending apparatus was built to provide experimental moment-curvature curves. The constant bending moment applied over the length of the specimen allows one to determine numerically the strain-stress behaviour but without finite element analysis.
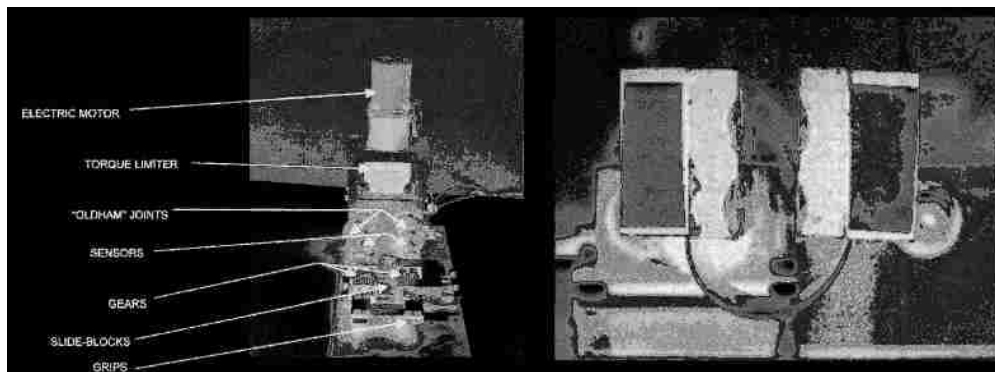
Figure 2.15. Bending-unbending test equipment and strip at imposed curvature (Brunet et al., 2001).

Boger et al. (2005) developed and optimized a new method for in-plane tension-compression testing of sheet materials employing a simple device, special specimen geometry, and corrections for friction and off-axis loading. They carried out continuous strain reversal to compressive strains greater than 0.20 following the guidelines provided for optimizing the test. Because of the restraining force of the side-supports, corrections due to friction and the biaxial state of stress need to be made to obtain the optimum results in terms of a uniaxial stress state.

For 6022-T4 (thickness = 2.5 mm):
G = 36.8 mm, W = 15.2 mm
B = 50.8 mm, L > 3 mm
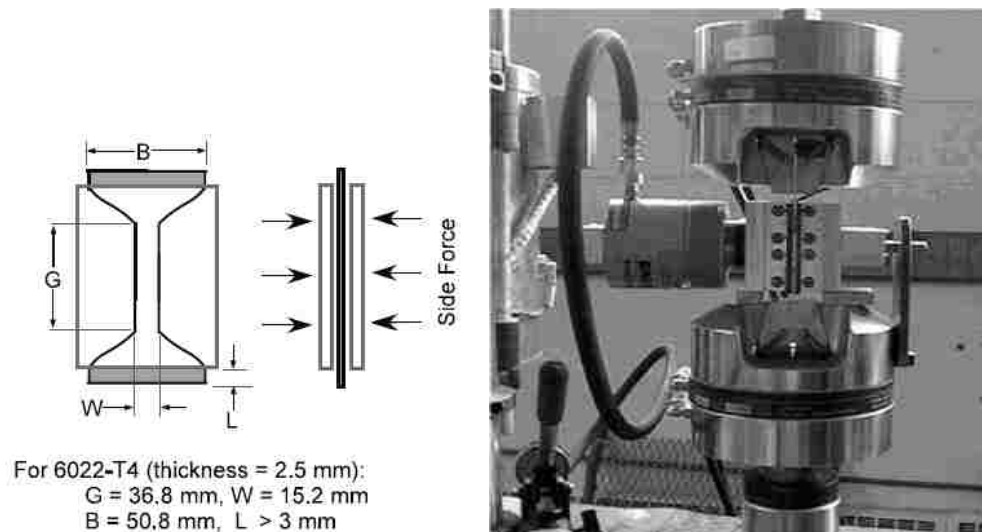
Figure 2.16. Schematic of the flat plate supports and sample dimensions (left) and assembly of new plate test (right) (Boger et al., 2005).

Thuillier and Manach (2009) designed a shear test device and used it to characterize the cyclic hardening of sheet metals. The main reason for special attentions to the cyclic shear tests is that this test is rather simple in performance and also larger compressive strain can be achieved without buckling of the sheet specimen. In their tests, the measurement of the shear strain was performed by the use of digital image correlation technology.
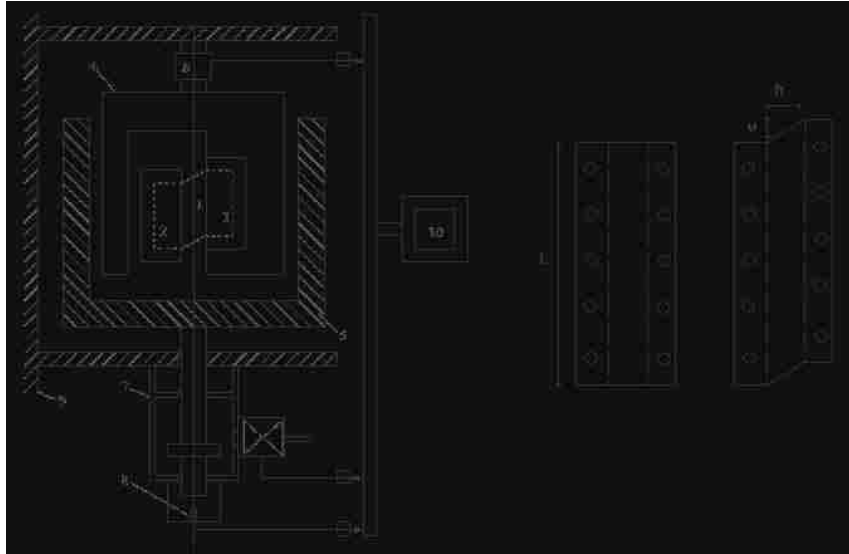
Figure 2.17. Schematic overview of the simple shear test apparatus: 1. sample; 2. movable grip; 3. fixed grip; 4. upper frame part; 5. lower frame part; 6. load cell; 7. hydraulic actuator; 8. actuator displacement sensor; 9. frame and 10. computer (left) and the gauge area (right) (Thuillier and Manach, 2009).

To prevent a sheet specimen from buckling subjected to a tension-compression cyclic loading, Cao et al. (2009) developed a new fixture to use with a regular tensile-compression machine. The novelty of this device lies in a 4-block wedge design with pre-loaded springs. This design allows blocks to freely move in the vertical direction while providing the normal support to the entire length of the specimen during the tension-compression cycle. In order to measure the strain accurately, the transmission type laser extensometer was utilized together with the implementation of double-side fins in the specimen.
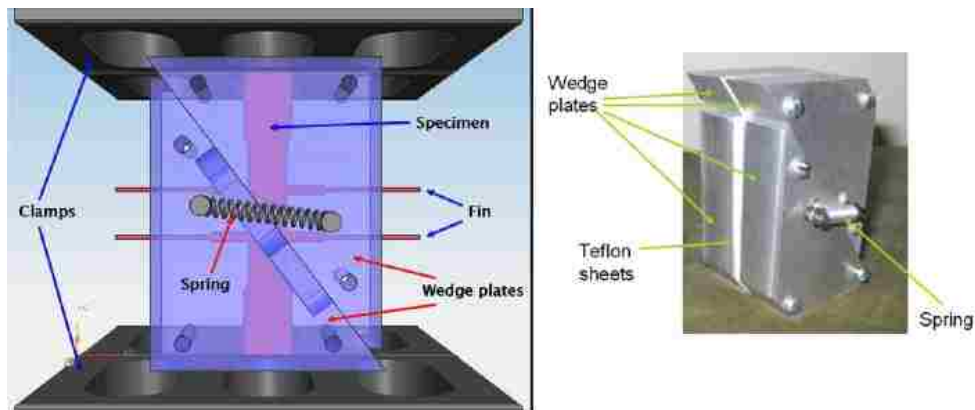
Figure 2.18. Schematic of the double wedge in-plane tension-compression device (left) and the real fixture (right) (Cao et al., 2009).

42

2.7. Bibliography

Abdel Karim, M., Ohno, N., 2000. Kinematic hardening model suitable for ratcheting with steady-state. Int. J. Plasticity 16, 225-240.

Aretz, H., 2007. A consistent plasticity theory of incompressible and hydrostatic pressure sensitive metals. Mech. Research Communications 34, 344-351.

Aretz H., 2008. A simple isotropic-distortional hardening model and its application in elastic–plastic analysis of localized necking in orthotropic sheet metals. Int. J. Plasticity 24, 1457-1480.

Armstrong, P.J., Frederick, C.O., 1966. A Mathematical Representation of the Multiaxial Bauschinger Effect. Central Electricity Generating Board Report, RD/B/N 731.

Auricchio F., Taylor R.L., 1995. Two Material Models for Cyclic Plasticity: Nonlinear Kinematic Hardening and Generalized Plasticity. Int. J. Plasticity 11, 65-98.

Balakrishnan V., 1999. Measurement of In-Plane Bauschinger Effect in Sheet Metals. M.S. Thesis, The Ohio State University.

Baltov A., Sawczuk A., 1965. A Rule of anisotropic hardening. Acta Mechanica 1, 81-92.

Banabic, D., Aretz, H., Comsa, D.S., Paraianu, L., 2005. An improved analytical description of orthotropy in metallic sheets. Int. J. Plasticity 21, 493-512.

Barlat, F., Lian, J. 1989. Plastic behaviour and stretchability of sheet metals. Part I, A yield function for orthotropic sheet under plane stress conditions. Int. J. Plasticity 5, 51-66.

Barlat, F., Lege, D.J., Brem, J.C., 1991. A six-component yield function for anisotropic materials. Int. J. Plasticity 7, 693.

Barlat, F., Becker, R.C., Hayashida, Y., Maeda, Y., Yanagawa, M., Chung, K., Brem, J.C., Lege, D.J., Matsui, K., Murtha, S.J., Hattori, S., 1997. Yielding description for solution strengthened aluminum alloys. Int. J. Plasticity 13, 385.

Barlat, F., Brem, J.C., Yoon, J.W., Chung, K., Dick, R.E., Lege, D.J., Pourboghrat, F., Choi, S.H., Chu, E., 2003. Plane stress yield function for aluminum alloy sheet - Part I: theory. Int. J. Plasticity 19, 1297-1319.

Barlat, F., Aretz, H., Yoon, J.W., Karabin, M.E., Brem, J.C., Dick, R.E., 2005. Linear transformation-based anisotropic yield functions. Int. J. Plasticity 21, 1009-1039.

Barthel C., Levkovitch V., Svendsen B., 2008. Modelling of sheet metal forming processes taking into account distortional hardening. Int. J. Mater. Form. 1, 105-108.

Basuroychowdhury I.N., Voyiadjis G.Z., 1998. A multiaxial cyclic plasticity model for non-proportional loading cases. Int. J. Plasticity, 14, 855-870.

Bate P. S., Wilson D. V., 1986. Analysis of the Bauschinger effect. Acta Mettalurgica 34, 1097-1105.

Besseling J.F., 1958. A Theory of Elastic, Plastic and Creep Deformation of an Initially Isotropic Material Showing Anisotropic Strain Hardening, Creep Recovery and Secondary Creep. ASME J. Applied Mech. 25, 529-536.

Boger, R.K., Wagoner, R.H., Barlat, F., Lee, M.G., Chung, K., 2005. Continuous, large strain, tension/compression testing of sheet material. Int. J. Plasticity 21, 2319-2343.

Broggiato G. B., Campana F., Cortese L., 2008. The Chaboche nonlinear kinematic hardening model: calibration methodology and validation. Meccanica 43, 115-124.

Bruhns O. T., Muller R., 1984. Some Remarks on the Application of a Two-Surface Model in Plasticity. Acta Mechanica 53, 81-100.

Brunet M., Morestin F., Godereaux S., 2001. Nonlinear Kinematic Hardening Identification for Anisotropic Sheet Metals With Bending- Unbending Tests. ASME J. Eng. Mater. Tech. 123, 378-383.

Brunig, M., 1998. Microscopic modelling of volume expansion and pressure dependence of plastic yielding in crystalline solids. Archive Appl. Mech. 68, 71-84.

Brunig, M., Obrecht, H., 1998. Finite elastic-plastic deformation behaviour of crystalline solids based on a non-associated macroscopic flow rule. Int. J. Plasticity 14, 1189-1208.

Brunig, M., 1999. Numerical simulation of the large elastic-plastic deformation behaviour of hydrostatic stress-sensitive solids. Int. J. Plasticity 15, 1237-1264.

Cao J., Lee W., Cheng H.S., Seniw M., Wang H-P., Chung K., 2009. Experimental and numerical investigation of combined isotropic-kinematic hardening behaviour of sheet metals. Int. J. Plasticity 25, 942-972.

Cardoso, R.P.R., Yoon, J.W., Valente, R.A.F., Gracio J.J., Simoes, F., Alves de Sousa, R.J., 2005. A nonlinear kinematic hardening model for the simulation of cyclic loading paths in anisotropic aluminum alloy sheets. In: Onate, E., Owen, D.R.J., (Eds.), VIII International Conference on Computational Plasticity, CIMNE, Barcelona.

Cardoso, R.P.R., Yoon, J.W., 2009. Stress integration method for a nonlinear kinematic/isotropic hardening model and its characterization based on polycrystal plasticity. Int. J. of Plasticity 25, 1684-1710.

Chaboche J. L., 1986. Time-Independent Constitutive Theories for Cyclic Plasticity. Int. J. Plasticity 2, 149-188.

Chaboche J. L., 1989. Constitutive Equations for Cyclic Plasticity and Cyclic Viscoplasticity. Int. J. Plasticity 5, 247-302.

Chaboche, J.L., 1991. On some modifications of kinematic hardening to improve the description of ratcheting effects. Int. J. Plasticity 7, 661-678.

Chaboche J. L., 1997. Thermodynamic formulation of constitutive equations and application to the viscoplasticity and viscoelasticity of metals and polymers. Int. J. Solids Structures 34, 2239-2254.

Chaboche J. L., Jung O., 1998. Application of a kinematic hardening viscoplasticity model with thresholds to the residual stress relaxation. Int. J. of Plasticity 13, 785-807.

Chelminski K., 2003. Mathematical Analysis of the Armstrong-Frederick Model from the Theory of Inelastic Deformations of Metals; First Results and Open Problems. Continuum Mech. Thermodyn. 15, 221-245.

Chen, X., Jiao, R., 2004. Modified kinematic hardening rule for multiaxial ratcheting prediction. Int. J. Plasticity 20, 871-898.

Chen X., Rong J., Kim K-S, 2005. On the Ohno–Wang Kinematic Hardening Rules for Multiaxial Ratcheting Modelling of Medium Carbon Steel. Int. J. Plasticity 21, 161-184.

Chiang D.Y., Beck J.L., 1994. A new class of distributed element models for cyclic plasticity-I. Theory and applications. Int. J. Solids Structures 31, 469-484.

Chiang D.Y., Su K.H., Liao C.H, 2002. A study on subsequent yield surface based on the distributed-element model. Int. J. Plasticity 18, 51-70.

Choi Y., Han C-S., Lee J. K., Wagoner R. H., 2006a. Modelling Multi-axial Deformation of Planar Anisotropic Elasto-plastic Materials, part I: Theory. Int. J. Plasticity 22, 1745-1764.

Choi Y., Han C-S., Lee J. K., Wagoner R. H., 2006b. Modelling Multi-axial Deformation of Planar Anisotropic Elasto-plastic Materials, part II: Applications. Int. J. Plasticity 22, 1765-1783.

Choi K.S., Pan J., 2009. A generalized anisotropic hardening rule based on the Mroz multi-yield-surface model for pressure insensitive and sensitive materials. Int. J. Plasticity 25, 1325-1358.

Chow C. L., Yang X. J., Chu E., 2002. Prediction of Forming Limit Diagram Based on Damage Coupled Kinematic-Isotropic Hardening Model under non-Proportional Loading. ASME J. Eng. Mater. Tech. 124, 259-265.

Chow C. L., Yang X. J., 2004. A Generalized Mixed Isotropic-kinematic Hardening Plastic Model Coupled with Anisotropic Damage for Sheet Metal Forming. Int. J. Damage Mech. 13, 81-101.

Chun B. K., Jinn J. T., Lee J. K., 2002a. Modelling the Bauschinger effect for sheet metals, part I: theory. Int. J. Plasticity 18, 571-595.

Chun B. K., Jinn J. T., Lee J. K., 2002b. Modelling the Bauschinger effect for sheet metals, part II: applications. Int. J. Plasticity 18, 597-616.

Chung, K., Richmond, O., 1993. A deformation theory of plasticity based on minimum work paths. Int. J. Plasticity 9, 907-920.

Chung K., Lee M.-G., Kim D., Kim C., Wenner M. L., Barlat F., 2005. Spring-back evaluation of automotive sheets based on isotropic-kinematic hardening laws and non-quadratic anisotropic yield functions Part I: theory and formulation. Int. J. Plasticity 21, 861-882.

Collins, I.F., 2002. Associated and non-associated aspects of the constitutive laws for coupled elastic/plastic materials. Int. J. Geomechanics 2, 259-267.

Dafalias Y. F., Popov E. P., 1975. A Model of Non-linearly Hardening Materials for Complex Loading. Acta Mechanica 21, 173-192.

Dafalias Y. F., Popov E. P., 1976. Plastic Internal Variables Formalism of Cyclic Plasticity. ASME J. Applied Mech. 98, 645-651.

Dafalias Y. F., 1984. Modelling Cyclic Plasticity: Simplicity versus Sophistication, Mechanics of Engineering Materials. C. S. Desai and R. H. Gallagher, eds., Wiley.

Dafalias, Y.F., 2000. Orientational evolution of plastic orthotropy in sheet metals. J. Mech. Phys. Solids 48, 2231-2255.

Drucker D. C., 1951. A more fundamental approach to plastic stress-strata relations. Proceedings of the First U.S. National Congress of Applied Mechanics, ASME, 487.

Drucker D. C., 1959. A Definition of Stable Inelastic Material. ASME J. Applied Mech. March, 101-106.

Drucker D. C., Palgen L., 1981. On Stress-Strain Relations Suitable for Cyclic and Other Loading. ASME J. Applied Mech. 48, 479-485.

Eisenberg M. A., A. Phillips, 1968. On non-linear kinematic hardening. Acta Mechanica 5, 1-13.

Eisenbeg M. A., Phillips A., 1971. A Theory of Plasticity with Non-Coincident Yield and Loading Surfaces. Acta Mechanica 11, 247-260.

François M., 2001. A plasticity model with yield surface distortion for non proportional loading. Int. J. Plasticity 17, 703-717.

Freudenthal A.M., Gou P.F., 1969. Second Order Effects in the Theory of Plasticity. Acta Mechanica 8, 34-52.

Gau J.-T., Kinzel G. L., 2001. A New Model for Springback Prediction in Which the Bauschinger Effect is Considered. Int. J. Mech. Sci. 43, 1813-1832.

Gau J.-T., Kinzel G. L., 2005. A New Model for Springback Prediction for Aluminum Sheet Forming. ASME J. Eng. Mater. Tech. 127, 279-288.

Geng, L., Shen, Y., Wagoner, R.H., 2002. Anisotropic hardening equations derived from reverse-bend testing. Int. J. Plasticity 18, 743-767.

Geng, L., Wagoner, R.H., 2002. Role of plastic anisotropy and its evolution on springback. Int. J. Mech. Sci. 44, 123-148.

Gotoh, M., 1977. A theory of plastic anisotropy based on a yield function of fourth order. Int. J. Mech. Sci. 19, 505.

Haddadi, H., Bouvier, S., Banu, M., Maier, C., Teodosiu, C., 2006. Towards an accurate description of the anisotropic behaviour of sheet metals under large plastic deformations: Modelling, numerical analysis and identification. Int. J. Plasticity 22, 2226-2271.

Haddag, B., Balan, T., Abed-Meraim, F., 2007. Investigation of advanced strain-path dependent material models for sheet metal forming simulations. Int. J. Plasticity 23, 951-979.

Helling D.E., Miller A.K., 1987. The Incorporation of Yield Surface Distortion into a Unified Constitutive Model, Part I: Equation Development. Acta Mechanica 69, 9-23.

Helling D.E., Miller A.K., 1988. The Incorporation of Yield Surface Distortion into a Unified Constitutive Model, Part II: Predictive Capabilities. Acta Mechanica 72, 39-53.

Hershey, A. V., 1954. The plasticity of an isotropic aggregate of anisotropic face centered cubic crystals. ASME J. Appl. Mech. 21, 241-249.

Hill, R., 1948. A theory of yielding and plastic flow of anisotropic metals. Proc. Roy. Soc. London A193, 281.

Hill R., 1950. The Mathematical Theory of Plasticity. Oxford University Press, Oxford.

Hill, R., 1979. Theoretical Plasticity of textured aggregates. Proc. Camb. Phil. Soc. 85, 179.

Hill, R., 1986. Extremal paths of plastic work and deformation. J. Mech. Phys. Solids 34, 511-523.

Hill, R., 1990. Constitutive modelling of orthotropic plasticity in sheet metal. J. Mech. Phys. Solids 38, 405.

Hill, R., 1993. A user-friendly theory of orthotropic plasticity in sheet metals. Int. J. Mech. Sci. 35, 19.

Hosford, W.F., 1972. A generalized isotropic yield criterion. ASME J. Appt. Mech. 39, 607-609.

Hosford, W.F., 1979. On yield loci of anisotropic cubic metals, 7th North Am. Metalworking Conf. SME, Dearborn, MI, 191.

Ilyushin A. A., 1961. On the postulate of plasticity. Prikl. Mat, Mekh. 25, 503.

Iwan W. D., 1966. Distributed-element model for hysteresis and its steady-state dynamic response. ASME J. Applied Mech. 33, 893-900.

Jiang Y., Kurath P., 1996. Characteristics of the Armstrong-Frederick Type Plasticity Model. Int. J. Plasticity 12, 387-415.

Jiang, Y.Y., Sehitoglu, H., 1996a. Modelling of cyclic ratcheting plasticity, part I: Development of constitutive relations. ASME J. Applied Mech. 63, 720-725.

Jiang, Y.Y., Sehitoglu, H., 1996b. Modelling of cyclic ratcheting plasticity, part II: comparison of model simulations with experiments. ASME J. Applied Mech. 63, 726-733.

Jiang, S., 1997. Springback Investigations. M.S. Thesis, The Ohio State University.

Karafillis, A.P., Boyce, M.C., 1993. A general anisotropic yield criterion using bounds and a transformation weighting tensor. J. Mech. Phys. Solids 41, 1859.

Khan A.S., Huang S., 1995. Continuum Theory of Plasticity. John Wiley & Sons, Inc.

Kleemola HJ, Nieminen MA, 1974. On the strain hardening parameters of metals. Metallurgical Transactions 5, 1863-1866.

Kowalsky U., Ahrens H., Dinkler D., 1999. Distorted yield surfaces - modelling by higher order anisotropic hardening tensors. Computational Materials Science 16, 81-88.

Krieg R. D., 1975. A Practical Two Surface Plasticity Theory. ASME J. Applied Mech. 47, 641-646.

Kurtyka T., Zyczkowski M., 1985. A Geometric Description of Distortional Plastic Hardening of Deviatoric Materials. Archives of Mechanics 37, 383-395.

Kurtyka T., Zyczkowski M., 1996. Evolution Equations for Distortional Plastic Hardening. Int. J. Plasticity 12, 191-213.

Kuwabara T., Morita Y., Miyashita Y., Takahashi S., 1995. Elastic-Plastic Behaviour of Sheet Metal Subjected to In-Plane Reverse Loading. Proceedings of Plasticity'95: Dynamic Plasticity and Structural Behaviours, Gordon and Branch Publishers, 841-844.

Lee M.-G., Kim D., Kim C., Wenner M. L., Wagoner R. H., Chung K., 2005. Spring-back evaluation of automotive sheets based on isotropic-kinematic hardening laws and non-quadratic anisotropic yield functions Part II: characterization of material properties. Int. J. Plasticity 21, 883-914.

Lee M.-G., Kim D., Kim C., Wenner M. L., Chung K., 2005. Spring-back evaluation of automotive sheets based on isotropic-kinematic hardening laws and non-quadratic anisotropic yield functions Part III: applications. Int. J. Plasticity 21, 915-953.

Lubarda, V.A., Mastilovic, S., Knap, J., 1996. Some comments on plasticity postulates and non-associative flow rules. Int. J. Mech. Sci. 38, 247-258.

McDowell, D.L., 1995. Stress state dependence of cyclic ratcheting behaviour of two rail steels. Int. J. Plasticity 11, 397-421.

Michno M. J., Findley W. N., 1976. An Historical Perspective of Yield Surface Investigations for Metals. Int. J. Non-Linear Mech. 11, 59-82.

Miyauchi, K., 1977. A proposal of a planar simple shear. J. Mater. Sci. 18, 903-918.

Miyauchi K., 1992. Deformation Path Effect on Stress-Strain Relation in Sheet Metals. J. Mater. Proc. Tech. 34, 195-200.

Mroz Z., 1967. On the Description of Anisotropic Workhardening. J. Mech. Phys. Solids 15, 163-175.

Mroz Z., 1969. An Attempt to Describe the Behaviour of Metals under Cyclic Loads Using a More General Workhardening Model. Acta Mechanica 7, 199-212.

Nemat-Nasser, S., 1991. Rate-independent finite-deformation elastoplasticity: a new explicit constitutive algorithm. Mech. Mater. 11, 235-249.

Nicholson, D.W., 1987. On a stability criterion in non-associated viscoplasticity. Acta Mech. 69, 167-175.

Ohno N., Wang J.-D., 1993a. Kinematic Hardening Rules with Critical State of Dynamic Recovery- Part I: Formulation and Basic Features for Ratchetting Behaviour. Int. J. Plasticity 9, 375-390.

Ohno N., Wang J.-D., 1993b. Kinematic Hardening Rules with Critical State of Dynamic Recovery- Part II: Application to Experiments of Ratchetting Behaviour. Int. J. Plasticity 9, 391-403.

Ohno N., 1998. Constitutive Modelling of Cyclic Plasticity with Emphasis on Ratchetting. Int. J. Mech. Sci. 40, 251-261.

Ortiz M., Popov E.P., 1983. Distortional Hardening Rules for Metal Plasticity. ASCE J. Eng. Mech. 109, 1042-1057.

Pearce, R., 1968. Some aspects of anisotropic plasticity in sheet metals. Int. J. of Mech. Sci. 10, 995-1005.

Petersson H., Popov E. P., 1977. Constitutive Equations for Generalized Loading. ASCE J. Eng. Mech. 103, 611-627.

Phillips A., Sierakowski R. L., 1965. On the Concept of the Yield Surface. Acta Mechanica 1, 29-35.

Phillips A., Tang J. L., Ricciuti M., 1974. Some New Observations on Yield Surfaces. Acta Mechanica 20, 23-29.

Phillips A., Weng F. J., 1975. An Analytical Study of an Experimentally Verified Hardening Law. ASME J. Appl. Mech. 42, 375-378.

Phillips A., Moon H., 1977. An Experimental Investigation Concerning Yield Surfaces and Loading Surfaces. Acta Mechaninca 27, 91-102.

Phillips A., Lee C. W., 1979. Yield Surfaces and Loading Surfaces Experiments and Recommendations. Int. J. Solids Structures 15, 715-729.

Phillips A., Das P. K., 1985. Yield Surfaces and Loading Surfaces of Aluminum and Brass: An Experimental Investigation at Room and Elevated Temperatures. Int. J. Plasticity 1, 1985, 89-109.

Prager W., 1956. A New Method of Analyzing Stresses and Strains in Work-Hardening Plastic Solids. ASME J. Appl. Mech. 23, 493-496.

Rees D.W.A., 1982. Yield Functions that Account for the Effects of Initial and Subsequent Plastic Anisotropy. Acta Mechanica 43, 223-241.

Runesson, K., Mroz, Z., 1989. A note on non-associated plastic flow rules. Int. J. Plasticity 5, 639-658.

Schiffner K., 1995. Overlay Models for Structural Analysis under Cyclic Hardening. Computers and Structures 56, 321-328.

Shen Y., 1999. Simple/Reverse Bend Test for Measurement of Bauschinger Effect in Sheet Materials. M.S. Thesis, The Ohio State University.

Shiratori E., Ikegami K., Yoshida F., 1979. Analysis of Stress-Strain Relations by Use of an Anisotropic Hardening Plastic Potential. J. Mech. Phys. Solids 27, 213-229.

Spitzig W.A., Sober R. J., Richmond O., 1975. Pressure dependence of yielding and associated volume expansion in tempered martensite. Acta. Metall. 23, 885-893.

Spitzig W.A., Sober R.J., Richmond O., 1976. The effect of hydrostatic pressure on the deformation behaviour of Maraging and HY-80 Steels and its implications for plasticity theory. Metall. Trans. A 7A, 1703-1710.

Spitzig, W.A., 1979. The effect of hydrostatic pressure on plastic-flow properties of iron single crystals. Acta Metall. 27, 523-534.

Spitzig W.A., Richmond O., 1984. The effect of pressure on the flow stress of metals. Acta. Metall. 32, 457-463.

Stoughton T. B., 2002. A non-Associated Flow Rule for Sheet Metal Forming. Int. J. Plasticity 18, 687-714.

Stoughton T.B., Yoon J-W., 2004. A Pressure-Sensitive Yield Criterion Under a non-Associated Flow Rule for Sheet Metal Forming. Int. J. Plasticity 20, 705-731.

Stoughton, T.B., Yoon, J.W., 2006. Review of Ducker's postulate and the issue of plastic stability in metal forming. Int. J. Plasticity 22, 391-433.

Stoughton, T.B., Yoon, J.W., 2008. On the existence of indeterminate solutions to the equations of motion under non-associated flow. Int. J. Plasticity 24, 583-613.

Tang S. C., Xia Z. C., Feng R., 2001. Application of the Radial Return Method to Compute Stress Increments from Mroz's Hardening Rule. ASME J. Eng. Mater. Tech. 123, 398-402.

Teodosiu, C., Hu, H.C., 1998. Microstructure in the continuum modelling of plastic anisotropy. In: 19th Riso International Symposium on Materials Science, 445-455.

Thuillier S, Manach PY. 2009. Comparison of the work-hardening of metallic sheets using tensile and shear strain paths. Int. J. Plasticity 25, 733-751.

Tseng N.T., Lee G.C., 1983. Simple Plasticity Model of Two-Surface Type. ASCE J. Eng. Mech. 109, 795-810.

Vincent L., Calloch S., Kurtyka T., Marquis D., 2002. An Improvement of Multiaxial Ratchetting Modelling Via Yield Surface Distortion. ASME J. Eng. Mater. Tech. 124, 402-411.

Vincent L., Calloch S., Marquis D., 2004. A general cyclic plasticity model taking into account yield surface distortion for multiaxial ratchetting. Int. J. Plasticity 20, 1817-1850.

Voyiadjis G.Z., Foroozesh M., 1990. Anisotropic Distortional Yield Model. ASME J. Appl. Mech. 57, 537-547.

Voyiadjis G.Z., Kattan P.I., 1990. A Generalized Eulerian Two-Surface Cyclic Plasticity Model for Finite Strains. Acta Mechanica 81, 143-162.

Voyiadjis G.Z., Kattan P.I., 1991. Phenomenological Evolution Equations for the Backstress and Spin Tensors. Acta Mechanica 91, 91-111.

Voyiadjis G.Z., Sivakumar S.M., 1991. A Robust Kinematic Hardening Rule for Cyclic Plasticity with Ratchetting Effects: Part I. Theoretical Formulation. Acta Mechanica 90, 105-123.

Voyiadjis G.Z., Sivakumar S.M., 1994. A Robust Kinematic Hardening Rule for Cyclic Plasticity with Ratchetting Effects: Part II. Application to Non-Proportional Loading Cases. Acta Mechanica 107, 117-136.

Voyiadjis G.Z., Basuroychowdhury I.N., 1998. A Plasticity Model for Multiaxial Cyclic Loading and Ratchetting. Acta Mechanica 126, 19-35.

Wang J.-D., Ohno N., 1991. Two equivalent forms of nonlinear kinematic hardening: application to non-isothermal plasticity. Int. J. Plasticity 7, 637-650.

Williams J.F., Svensson N.L., 1971. A Rationally Based Yield Criterion for Work Hardening Materials. Meccanica 6, 104-l 14.

Wilson D.V., Bate P.S., 1986. Reversibility in the Work Hardening of Spheroidised Steels. Acta Mettalurgica 34, 1107-1120.

Wu H-C., 2002. Anisotropic Plasticity for Sheet Metals Using the Concept of Combined Isotropic-Kinematic Hardening. Int. J. Plasticity 18, 1661-1682.

Yoon, J.W., Yang, D.Y., Chung, K., 1999a. Elasto-plastic finite element method based on incremental deformation theory and continuum based shell elements for planar anisotropic sheet materials. Comput. Methods Appl. Mech. Eng. 174, 23-56.

Yoon, J.W., Yang, D.Y., Chung, K., Barlat, F., 1999b. A general elasto-plastic finite element formulation based on incremental deformation theory for planar anisotropy and its application to sheet metal forming. Int. J. of Plasticity 15, 35-68.

Yoon S., Hong S-G, Lee S-B, 2002. Phenomenological description of cyclic deformation using the overlay model. Mater. Sci. Eng. A364, 17-26.

Yoshida F, Urabe M., Toropov V. V., 1998. Identification of Material Parameters in Constitutive Model for Sheet Metals from Cyclic Bending Tests. Int. J. Mech. Sci. 40, 237-249.

Yoshida F., 2000. A Constitutive Model of Cyclic Plasticity. Int. J. Plasticity 16, 359-380.

Yoshida F., Uemori T., Fujiwara K., 2002. Elastic-Plastic Behaviour of Steel Sheets Under in-Plane Cyclic Tension-Compression at Large-Strain. Int. J. Plasticity 18, 633-659.

Yoshida F., Uemori T., 2002. A Model of Large-Strain Cyclic Plasticity Describing the Bauschinger Effect and Work Hardening Stagnation. Int. J. Plasticity 18, 661-686.

Yoshida F., Uemori T., 2003. A Model of Large-Strain Cyclic Plasticity and Its Application to Springback Simulation. Int. J. Mech. Sci. 45, 1687-1702.

Yoshida F, Urabe M., Hino R., Toropov V. V., 2003. Inverse approach to identification of material parameters of cyclic elasto-plasticity for component layers of a bimetallic sheet. Int. J. Plasticity 19, 2149-2170.

Zhao K., Lee J.K., 2001. Generation of Cyclic Stress-Strain Curves for Sheet Metals. ASME J. Eng. Mater. Tech. 123, 391-397.

Zhao K., Lee J.K., 2002. Finite Element Analysis of the Three-Point Bending of sheet Metals. J. Mater. Proc. Tech. 122, 6-11.

Ziegler H., 1959. A Modification of Prager's Hardening Rule. Quarterly of Applied Mathematics 17, 55-60.

Zyczkowski M., Kurtyka T., 1984. Generalized Ilyushin's Spaces for a More Adequate Description of Plastic Hardening. Acta Mechanica 52, 1-13.

Chapter 3

Finite Element Simulation of Springback for a Channel Draw Process with Drawbead Using Different Hardening Models

3.1. Introduction

Springback is defined as the geometrical change of a part after forming, when the forces from forming tools are removed. Since springback affects the final shape of the product, it can lead to significant problems during assembly if the phenomenon is not well controlled. Therefore, it is an important issue in sheet metal forming and consequently has received attention by many researchers (Li et al., 2002; Song et al., 2001; Gan and Wagoner, 2004; Garden et al., 2002). It is very important for the designer to quantitatively predict springback and compensate it by die design techniques such as over-crowning, under-crowning, over-bending, or under-bending. The accuracy of sheet metal forming and springback simulation depends not only on the forming conditions (contact, friction, tool and binder geometry etc.), but also on the choice of the material constitutive model and its numerical implementation into finite element programs. The material constitutive law plays a crucial role in describing the mechanical behaviour of sheet metals because it determines the stress distribution in the formed part, and the shape of the part after springback depends directly on the predicted stress distribution. Thus, a great deal of research has been dedicated to developing new constitutive models that will improve the results of springback simulation (Chung et al., 2005; Choi et al., 2006; Yoshida and Uemori, 2002; Chun et al., 2002;

Gau and Kinzel, 2001). Recently, Oliveira et al. (2007) studied the influence of work-hardening models in springback simulation of Numisheet'05 Benchmark #3 using an implicit in-house code, considering one material (DP600) and one drawbead penetration. They did not compare their simulation results with experimental springback profiles, rather, they compared the different springback profiles predicted by FEM using various hardening models with each other. Assessment of the robustness of the numerical models is best completed with a thorough comparison to experimental findings. In addition, Oliveira et al. (2007) did not perform any cyclic hardening tests to identify the material cyclic hardening behaviour of the benchmark sheet materials. Also, the effect of different drawbead penetrations was not studied in their work. Therefore, to the best of the authors' knowledge, a comprehensive study to evaluate the influence of these constitutive models on the prediction of springback in the presence of drawbeads where cyclic deformation is imposed on the material has not been completed to date.

In this chapter, both forming and subsequent springback stages of the Numisheet'05 Benchmark #3 were simulated for different drawbead penetrations using the commercial code ABAQUS. Four different sheet materials (AKDQ-HDG, HSLA-HDG, DP600-HDG and AA6022-T43) were used to evaluate the ability of material models to predict the springback in the drawn channel section. This benchmark considers four different drawbead penetrations of 25%, 50%, 75% and 100%, but for the sake of brevity, only the results for the deepest and shallowest penetrations will be presented: i.e. 25 & 75% for DP600 and 25 & 100% for the other materials (Stoughton et al., 2005; Green, 2005; Green et al., 2005; Shi and Huang, 2005). Details of these tests are given later in section 3.4. To model the material behaviour, Hill's 1948 yield function was used with two different hardening models, i.e. isotropic hardening (IH) and a combined isotropic-nonlinear kinematic hardening (NKH). A user-defined material subroutine based on Hill and NKH for both ABAQUS-Explicit (VUMAT) and ABAQUS-Standard (UMAT) were developed. Also, cyclic simple shear tests were carried out to generate the cyclic stress-strain curves and in order to study the Bauschinger effect. Further details of the numerical models are described in the next section, and this is followed by a presentation and discussion of the numerical results.

3.2. Material Model

Two hardening models were used to define the behaviour of materials during plastic deformation: (i) isotropic hardening, and (ii) mixed isotropic nonlinear kinematic hardening. In the first case, it is assumed that the yield surface only expands during plastic deformation. This evolution can be defined by using various equations determining the characteristics of the current size of the yield

surface (for example the radius of the yield surface in the π-plane for simple von-Mises type yield functions). In the second case (the mixed hardening model), the evolution of the yield surface is modeled by assuming both expansion and translation. Kinematic hardening is defined based on the motion of yield surface centre (the so-called backstress tensor). The numerical stress integration algorithm for the anisotropic mixed hardening model is now briefly presented.

Hill's (1948) quadratic function is used to describe the anisotropic yield criterion.

$$F = \frac{3}{2}\boldsymbol{\eta}^t \mathbf{N}\boldsymbol{\eta} - \sigma_y^2 = 0 \tag{3.1}$$

In the above equation $\mathbf{N}$ is the anisotropic matrix, tensor $\boldsymbol{\eta}$ is defined as $\boldsymbol{\eta} = \boldsymbol{\sigma} - \boldsymbol{\alpha}$, where $\boldsymbol{\alpha}$ is the backstress tensor, and σ_y is the quasi-static yield stress. The anisotropic matrix for a plane-strain condition is defined as follows:

$$\mathbf{N} = \begin{bmatrix} N_1 + N_2 & -N_1 & -N_2 & 0 \\ -N_1 & N_1 + N_3 & -N_3 & 0 \\ -N_2 & -N_3 & N_2 + N_3 & 0 \\ 0 & 0 & 0 & N_4 \end{bmatrix} \tag{3.2}$$

N_1, N_2, N_3, and N_4 are functions of yield stress ratios (planar anisotropy is assumed and σ_0, σ_{45}, σ_{90} and σ_{EB} are used to define the components of anisotropic matrix). The evolution of the backstress tensor ($\boldsymbol{\alpha}$) is modeled based on the nonlinear kinematic hardening model, so-called Armstrong-Frederick (1966) formulation

$$\boldsymbol{d\alpha} = C\frac{dp}{\sigma_y}\boldsymbol{\eta} - \gamma\boldsymbol{\alpha}\,dp \tag{3.3}$$

where C and γ are material constants associated with nonlinear kinematic hardening and obtained from cyclic stress-strain data. The yield surface size (isotropic hardening or σ_y in the above equations) can be represented by either an exponential or power law function:

$$\sigma_y = \sigma_0 + Q(1 - e^{-b\cdot p}) \tag{3.4a}$$

$$\sigma_y = K(\varepsilon_0^{\,p} + p)^n \tag{3.4b}$$

Q and b or K and n are material constants associated with isotropic hardening. The flow rule is used to determine the plastic part of the strain increment as expressed in equation (3.5).

$$d\boldsymbol{\varepsilon}^p = \frac{3}{2}\frac{dp}{\sigma_y}\mathbf{N}\boldsymbol{\eta} \tag{3.5}$$

The term dp is the effective plastic strain rate (which is equal to the plastic multiplier based on the principle of plastic work equivalence) and is defined by the following equation:

$$dp = d\bar{\varepsilon}^p = (\tfrac{2}{3}d\boldsymbol{\varepsilon}^p : d\boldsymbol{\varepsilon}^p)^{1/2} \tag{3.6}$$

Using elastic stress-strain equilibrium, the flow rule, kinematic hardening formulation and applying the consistency condition for the yield function, the elasto-plastic tangent modulus for calculating the stress increment is derived as:

$$\mathbf{D}^{ep} = \mathbf{D} - \frac{(\mathbf{DN}\boldsymbol{\eta}) \otimes (\mathbf{DN}\boldsymbol{\eta})}{\boldsymbol{\eta}'\,\mathbf{NDN}\boldsymbol{\eta} + \frac{2}{3}C\boldsymbol{\eta}'\,\mathbf{N}\boldsymbol{\eta} - \gamma\boldsymbol{\eta}'\,\mathbf{N}\boldsymbol{\alpha} + \frac{2}{3}h\sigma_y} \tag{3.7}$$

where $\mathbf{D}$ is the elasticity tensor and h is the derivative of yield stress function $d\sigma_y/dp$.

From a numerical viewpoint the implementation of a constitutive model involves the integration of the state of the material at an integration point over a time increment during a nonlinear analysis (Simo and Taylor, 1986; Simo and Hughes, 1998). The return-mapping stress integration algorithm is used to derive the numerically updated stress at the end of each increment as expressed in equation (3.8).

$$\boldsymbol{\eta}_{n+1} = \frac{1}{1 + C\dfrac{dp}{\sigma_y}\theta}\,\boldsymbol{\Xi}\mathbf{D}^{-1}\left[\boldsymbol{\eta}^E + (1-\theta)\boldsymbol{\alpha}_n\right] \tag{3.8}$$

In equation (3.8), $\boldsymbol{\eta}^E$ (called the trial stress tensor or elastic predictor), $\boldsymbol{\Xi}$ (called the modified or algorithmic elastic tangent matrix) and the other terms in the above equation are written as:

$$\boldsymbol{\eta}^E = \mathbf{D}(\boldsymbol{\varepsilon}_{n+1} - \boldsymbol{\varepsilon}^p{}_n) - \boldsymbol{\alpha}_n \tag{3.9a}$$

$$\Xi = \left[\mathbf{D^{-1}} + \frac{\dfrac{3}{2}\dfrac{dp}{\sigma_y}}{1 + C\dfrac{dp}{\sigma_y}\theta} \mathbf{N} \right]^{-1}$$ (3.9b)

$$\theta = \frac{1}{1 + \gamma dp}$$ (3.9c)

In each increment a Newton iteration method is used to solve the yield equation for dp. In fact, the derivative of the yield function is needed in the consistency condition so that the final value of the governing parameter (here, the effective plastic strain) will converge. At each iteration, the yield condition is checked for the updated value and if it is satisfied within a specified user tolerance, the governing parameter is used as a reference for the increment. After obtaining convergence for the effective plastic strain rate, the stress tensor and other state variables are updated. In order to preserve the quadratic rate of asymptotic convergence for the Newton-Raphson method to solve the global finite element equilibrium equation it is necessary to derive the consistent elasto-plastic tangent modulus (Simo and Taylor, 1985). For the described material constitutive model, the consistent or algorithmic tangent modulus is obtained by using the return-mapping algorithm:

$$\frac{d\boldsymbol{\sigma}}{d\boldsymbol{\varepsilon}} = \tilde{\mathbf{D}}^{ep} = \Xi - \frac{(\Xi \mathbf{N}\boldsymbol{\eta}) \otimes (\Xi \mathbf{N}\boldsymbol{\eta})}{\boldsymbol{\eta}^t \mathbf{N}\Xi\Xi\,\boldsymbol{\eta} + \dfrac{2}{3}C\boldsymbol{\eta}^t \mathbf{N}\boldsymbol{\eta} - \gamma\boldsymbol{\eta}^t \mathbf{N}\boldsymbol{\alpha} + \dfrac{2}{3}h\sigma_y}$$ (3.10)

3.3. Material Parameter Identification

Although it is difficult to achieve cyclic deformation in flat sheet metals, several test methods have been proposed to generate experimental cyclic stress-strain curves. For example the in-plane simple shear test, in-plane cyclic tension-compression test, uniform bending-unbending test, three-point bending test, and others are among the most popular methods found in the literature (Yoshida et al., 1998; Zhao and Lee, 2001; Yoshida et al., 2002; Brunet et al., 2001; Boger et al., 2005). Simple shear tests were carried out to obtain the cyclic stress-strain behaviour of the different steel sheets (DP600, AKDQ and HSLA). The shear test device was especially designed for the study of metallic sheets as described in section 2.6 and Figure 2.17 (Thuillier and Manach, 2009). The sample was rectangular in geometry and was clamped at a fixed grip and at a movable grip. The movable grip was displaced at a constant speed. The shear stress is equal to the force

recorded by the load cell, divided by the gauge section. The parameter γ that describes the simple shear strain is defined by the ratio of the longitudinal displacement over the gauge width. In this method, the strain was measured with a commercial, non-contacting optical strain measurement system, ARAMIS (manufactured by G.O.M.). The obtained value was averaged over the central part of the gauge area in order not to take into account any free end effect. This measurement used the notion of a convected material frame. Since the test is controlled by the grip displacement, which can integrate a sliding of the sample under the grips, the value of γ is not controlled, particularly in the case of the Bauschinger type test. The relative accuracy of the stress level is of the order of 1.5 %. Further details about the test procedure and parameters can be found in the following paper (Thuillier and Manach, 2009).

There are 5 plastic material constants to be identified from the cyclic stress-strain curves: σ_0 (the initial yield stress), Q and b isotropic hardening coefficients, and C and γ nonlinear kinematic hardening coefficients. After analytical stress integration, the above constitutive model reduced for the uniaxial condition can be rewritten as:

$$\sigma_t^{\,1} = \sigma_0 + Q(1 - e^{-b.p}) + \frac{C}{\gamma}(1 - e^{-\gamma.p}) \tag{3.11a}$$

$$\sigma_c^{\,1} = -\sigma_0 - Q(1 - e^{-b.p}) - 2\frac{C}{\gamma}(1 - e^{-\gamma.(p-p1)}) + \frac{C}{\gamma}(1 - e^{-\gamma.p1}) \tag{3.11b}$$

$$\sigma_t^{\,2} = \sigma_0 + Q(1 - e^{-b.p}) + 2\frac{C}{\gamma}(1 - e^{-\gamma.(p-p2)}) + \frac{C}{\gamma}(1 - e^{-\gamma.p1}) - 2\frac{C}{\gamma}(1 - e^{-\gamma.(p2-p1)}) \tag{3.11c}$$

where subscripts t and c stand for tensile and compressive loading and $\sigma_t^{\,1}$, $\sigma_c^{\,1}$, and $\sigma_t^{\,2}$ are the stress in the loading, reverse loading, and reloading paths, respectively. The values $p1$ and $p2$ are the levels of plastic strain at the end of loading and subsequent reverse loading, respectively. This is shown schematically in Figure 3.1. The shear stress-strain curves obtained experimentally were converted to equivalent uniaxial stress-strain curves for each material using Hill's 1948 yield function. Then the least-squares method was used to fit the curves to the converted experimental data points. In the tests carried out to determine the Bauschinger effect, specimens were subjected to a single tension-compression cycle during which the stress reversal was effected at two different levels of shear strain (at approximately 10, and 20 % shear strain). This experimental process was adopted to demonstrate the ability of the model to correlate with the experimental data at different levels of strain. For each material, the optimum combination of hardening parameters was found for the two different cyclic curves and one tensile curve were fitted to the

experimental data points so as to obtain the best agreement for all curves. The cyclic stress-strain data obtained experimentally and converted to uniaxial condition was compared with that obtained by two different material models (IH and NKH) and is shown in Figure 3.2. It is evident that the NKH model can capture the cyclic effects due to consecutive reverse loadings, such as transient Bauschinger effect, better than the IH model. However, the current model (NKH) is not able to take the work hardening stagnation effect into account, which is particularly more substantial in the cyclic curves at larger levels of strains (denoted by "Cycle 2" for all figures). Also, for the HSLA steel the NKH model is not able to predict the Yield Point Elongation (YPE) effect. The cyclic material parameters of the AA6022-T43 were calculated based on the offset of the parameters presented by Zhao and Lee (2001) that is applicable for the AA6022-T4 and is very similar to the current aluminum grade. Table 3.1 shows the summary of mechanical properties and hardening parameters used in the simulations.
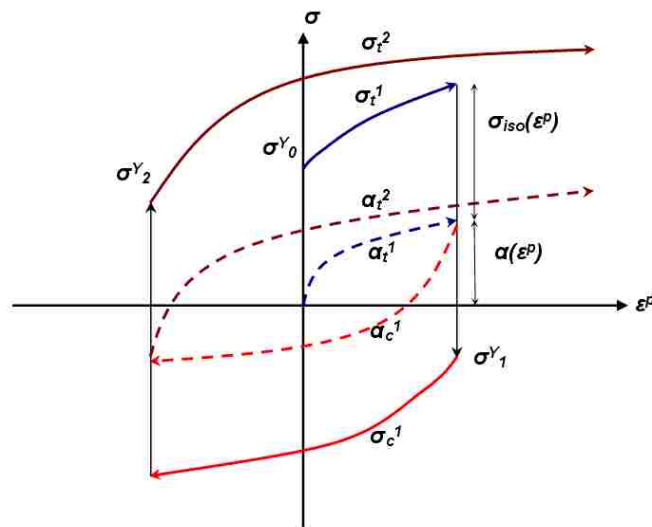
Figure 3.1. Illustration of cyclic hardening behaviour in different cycles using the mixed NKH model.

The pure isotropic hardening behaviour, elastic modulus and anisotropic coefficients (yield stress ratios) were obtained by carrying out quasi-static tensile tests (ASTM E8 standard test method) at different orientations (0, 45, and 90 degrees) with respect to the rolling direction with three replicates for each orientation. Furthermore, in order to assess the equal biaxial stress-strain behaviours, duplicate hydraulic bulge tests were conducted for each material.

56

Table 3.1. Summary of mechanical properties of the materials.

Material	Thickness (mm)	σ_0 (MPa)	Hill's 1948 Coefficients				Mixed Nonlinear Hardening			
			F	G	H	N	C (MPa)	γ	Q (MPa)	b
AA6022	1.00	136	0.63	0.49	0.5	1.58	1400	20	110	7.5
AKDQ	1.00	158.5	0.33	0.42	0.58	1.78	2500	50	210	8
HSLA	0.80	394.5	0.42	0.57	0.43	1.98	5000	140	180	7
DP600	1.00	420	0.44	0.46	0.53	1.82	9500	40	190	8
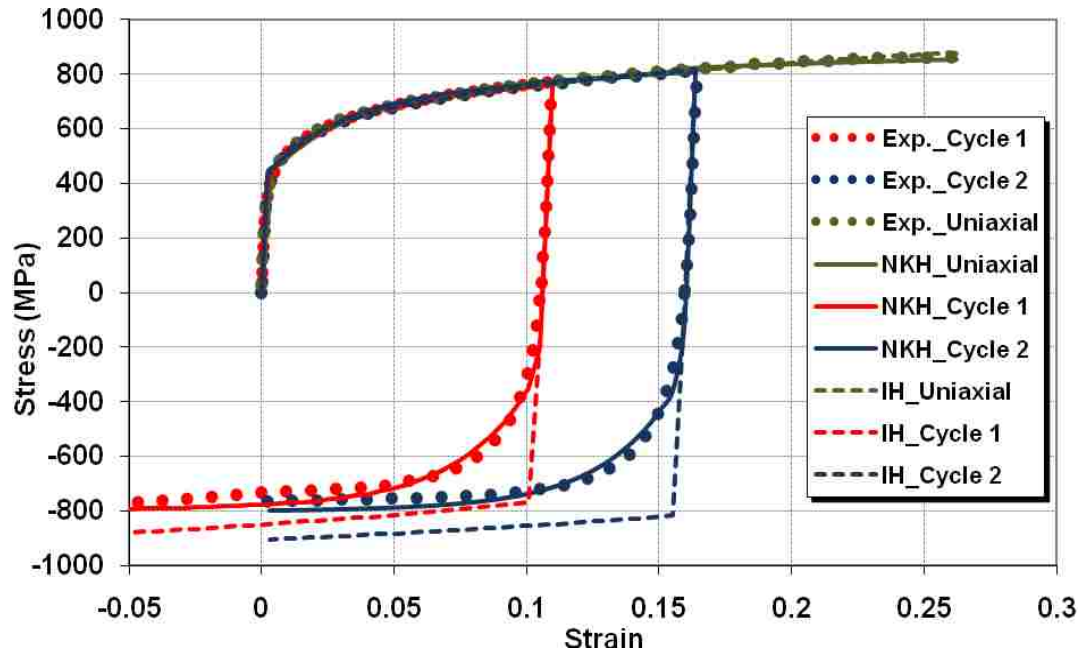
(3.2. a)
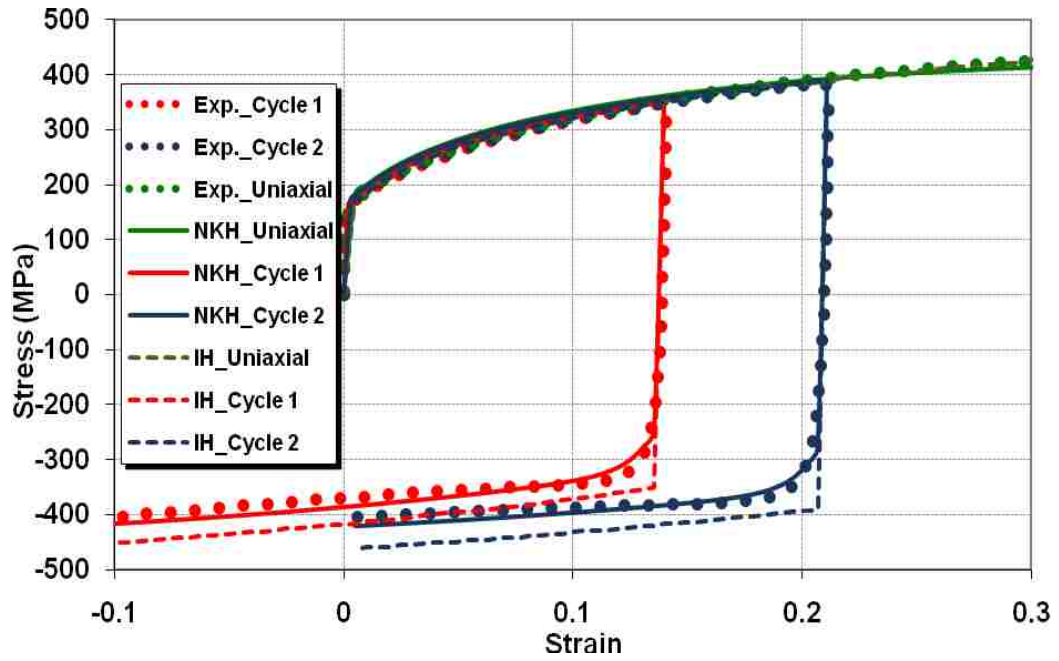
(3.2. b)
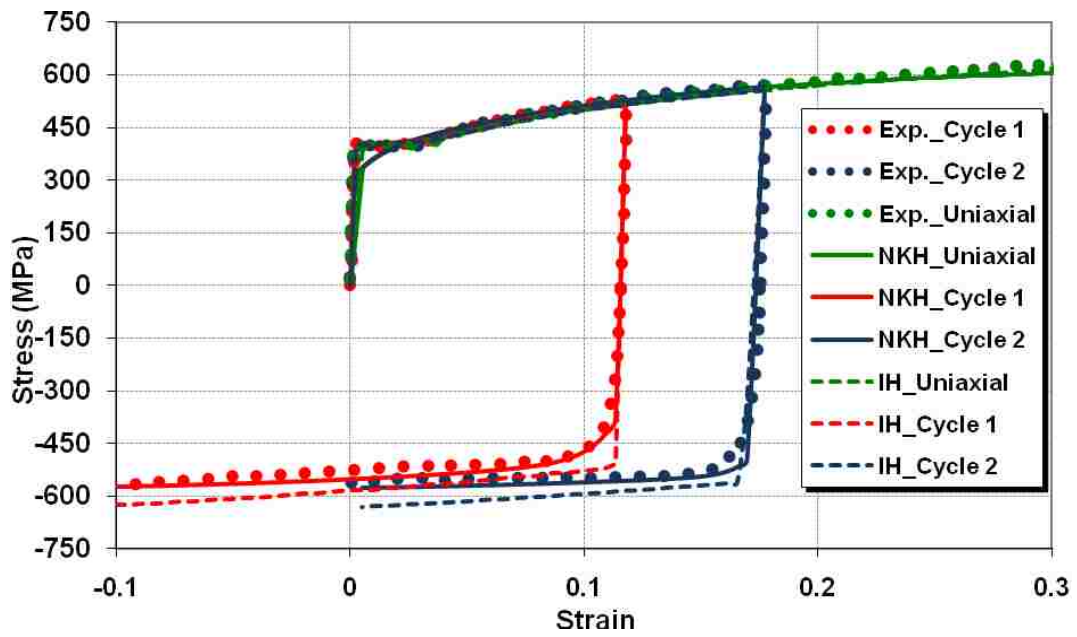
(3.2. c)
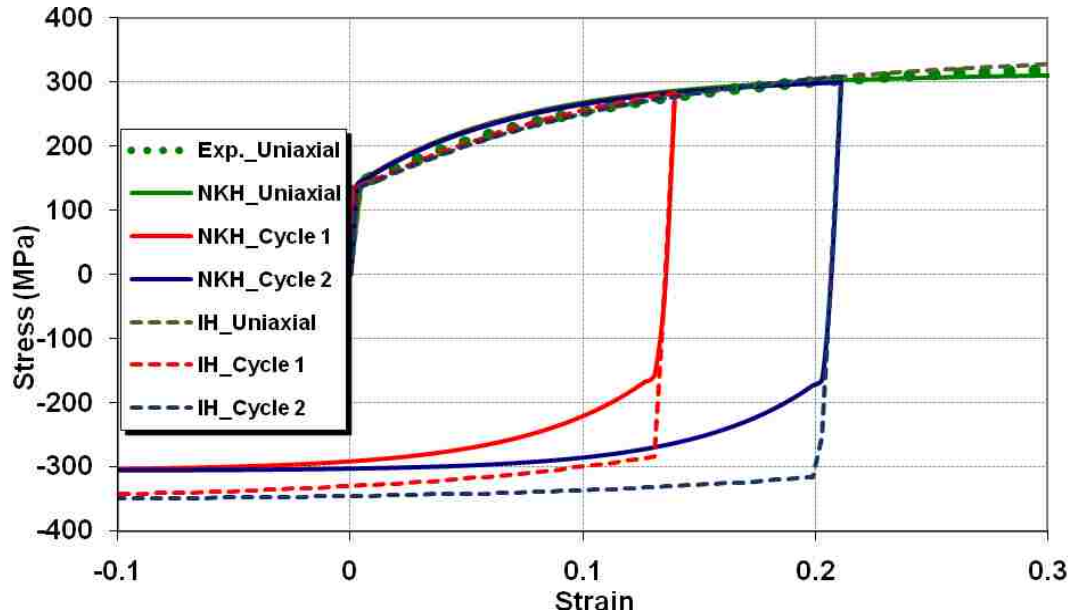
(d)

Figure 3.2. Experimental cyclic stress-strain data compared with the NKH and IH models for three steel sheets: (a) DP600, (b) AKDQ, (c) HSLA, and aluminum alloy (d) AA6022-T43.

3.4. Experimental Setup

A brief description of Numisheet 2005 Benchmark #3 Stage-1: "Channel Drawing with drawbead" will be presented in this section. The objective of this first stage is to document the forming characteristics of metals in a deformation process dominated by cyclic bending. Each of the four sheet materials was formed in a channel draw die at the Industrial Research and Development Institute (IRDI) in Midland, Canada. The draw die, provided by the Auto/Steel Partnership (A/SP) was constructed in such a way that the material in the channel sidewalls was formed over a drawbead and a die entry radius, thus work hardening the material by cyclic bending (Figure 3.3). Spacer blocks were used to hold the binder and upper die to a fixed clearance after binder closure was 0.42 mm larger than the nominal sheet thickness for each material. A blankholder force of 637 KN was generated by four 140 mm diameter cylindrical cushions set at 10.3 MPa. This was sufficient to set the beads and maintain a fixed clearance between the upper die and binder throughout the forming process. Sketches of all major tooling and blank size, location and dimensions are shown in Figure 3.3. Also, the value of tooling dimensions, drawbead and processing parameters in Figure 3.3 are presented in Table 3.2. Drawbeads are often used in stamping and deep drawing processes in order to provide better control of material flow into the die cavity. Experimentally, it is well known that drawbeads play

a very important role in many complex forming operations. However, there are still numerous difficulties to accurately model the geometry of drawbeads and numerically simulate their influence on the work piece (Alves et al., 2005). The channel draw die tests were carried out with four different sheet materials: AA6022-T43, AKDQ-HDG, HSLA-HDG and DP600-HDG. By using variable penetration drawbead inserts, a range of prestrain conditions was achieved in the channel sidewalls for each sheet material. The target, or nominal, drawbead penetrations were 25%, 50%, 75% and 100% penetration. The actual drawbead penetrations were recorded for each material and each prestrain condition according to the procedure described by Green (2005). The influence of drawbead penetration on the forming and springback behaviour of plane-strain channel sections was analyzed by Green et al. (2005). Several parameters were measured and recorded including the punch force, the principal strains in the channel sidewalls, the profile of channel sidewalls after springback, and even residual stresses in the sidewalls. The channel draw die was instrumented with load cells in order to record the punch force during each test. The ram displacement, ram pressure and the cushion pressure in the floating binder were also recorded in real time for each material, each drawbead penetration and for each channel that was formed. After forming plane-strain channel sections using blanks with electro-etched markings, the principal surface strains were measured in the centre of the channel sidewall where deformation was uniform using a steel rule. The initial gauge length for these strain measurements was 127 mm. The thickness strains were measured with an ultrasonic thickness tester. All strain measurements were made on the convex face of the sidewall after the channel had sprung back and reached its natural equilibrium. Strain measurements were recorded for each sheet material and for each prestrain condition (i.e. for each drawbead penetration). The sidewall curl after springback was recorded for each sheet material and for each prestrain condition, using a 2D laser scanner (LaserQC™). The only condition that led to severe metal pick-up on the drawbead inserts and scoring of the channel pieces was with the DP600-HDG at 100% penetration; therefore no data were recorded for this condition. A typical formed channel after springback is shown in Figure 3.4. The residual stresses in the channel sidewalls (after springback) were measured at the National Institute for Standards and Technology (NIST). Stresses were directly measured at the outer (convex) and inner (concave) surfaces of the sidewalls using X-ray diffraction to determine the change in the spacing between atomic planes. The residual stresses were determined from the lattice strains (in terms of the inter-planar spacing) assuming the material has an isotropic, elastic behaviour. A detailed description of the X-ray diffraction procedure and the corresponding stress analysis is provided by Iadicola et al. (2005). The measurements of residual stresses through the thickness of the sheet were carried out by neutron-diffraction at the NIST Center for Neutron

Research. Similar to X-ray diffraction, neutron diffraction permits measurement of inter-planar spacing of the atoms away from the surface of the material. The measurements and the data analysis (stress calculation) are described in detail in Gnaeupel-Herold et al. (2004; 2005).

Table 3.2. Tooling, Drawbead and Processing Parameters in Figure 3.3 (Stoughton et al., 2005).

Description	Symbol	Value (mm)
Upper Die		
Width of Die Cavity	Wd	319.90
Radius of Die Profile	Rd	12.00
Punch		
Width of Punch	Wp	224.00
Radius of Punch Profile	Rp	12.00
Binder		
Binder Gap	Bg	Thickness+0.42
Drawbead		
Bead Position	Bp	31.05
Depth of Bead*	Db	2.34
Radius of Bead	Rb	4.00
Width of Channel	Wc	10.80
Radius of Channel	Rc	4.00
BLANK		
Width	BW	254.00
Length	BL	1066.80

* Depth of bead in the table corresponds to the 25% penetration for other penetrations the bead depths are: 4.75 mm for 50%, 6.85 mm for 75% and 9.09 mm for 100%

(3.3. a)

61
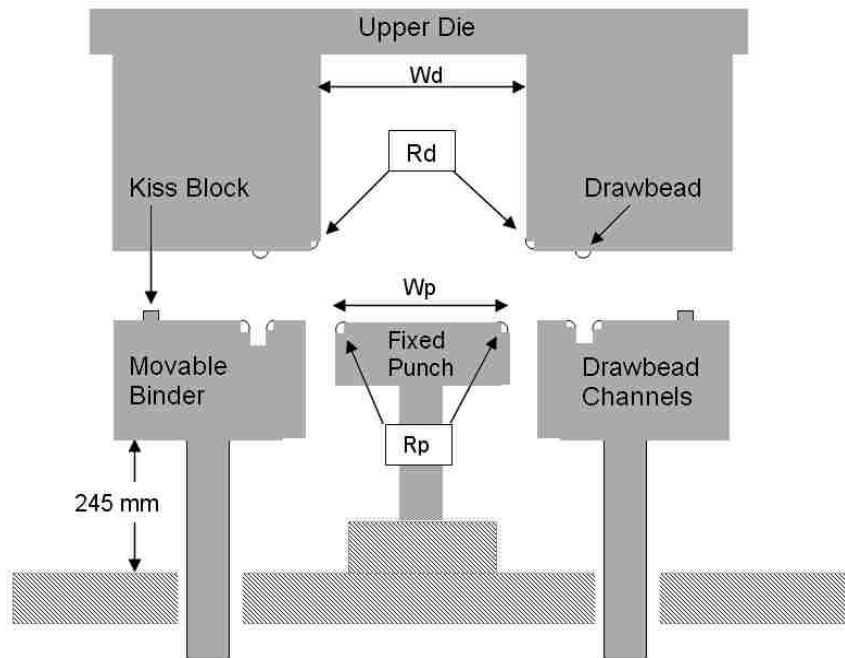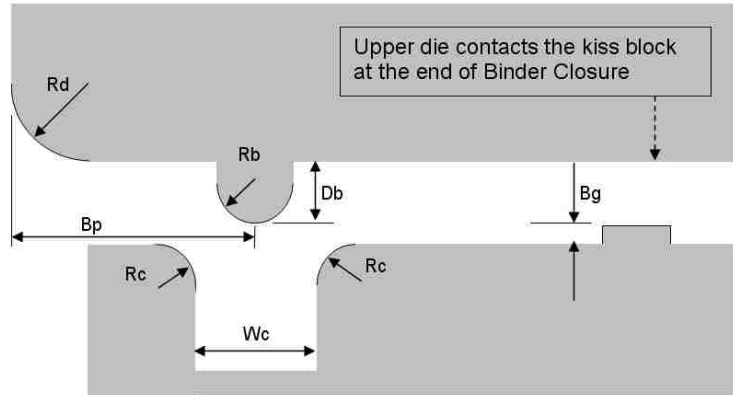
(b)
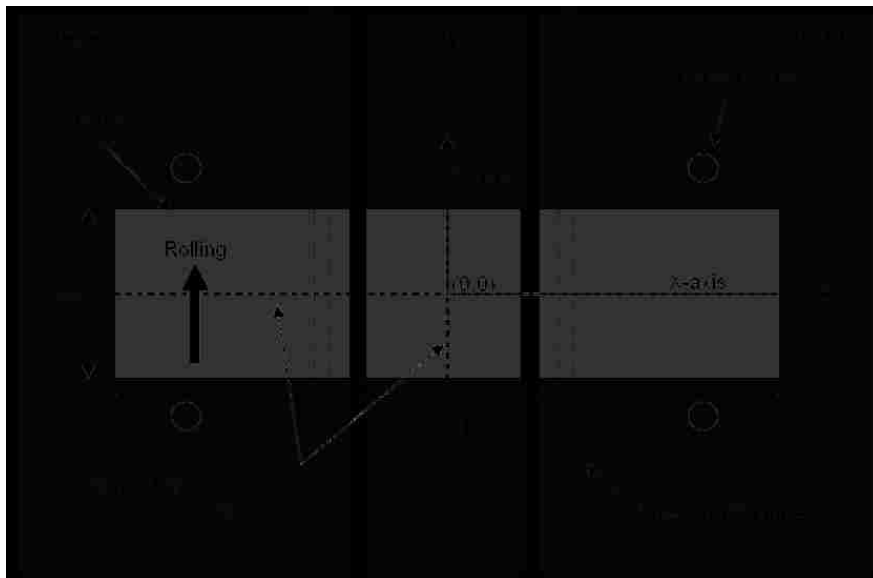
(c)

Figure 3.3. Sketches of the Numisheet 05 Benchmark 3 channel draw: (a) major tooling dimensions, die with location of drawbead inserts. (b) kiss block and drawbead dimensions and location (open position). (c) blank size and location, rolling (0 degree) direction of sheet, and XY coordinate system in plan-view. If symmetry is used, the analysis is restricted to the upper-right quadrant (Stoughton et al., 2005).
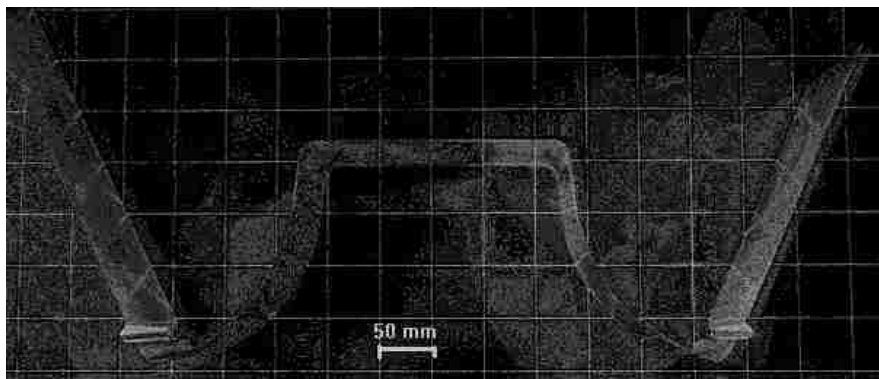
Figure 3.4. A channel formed in the A/SP channel draw die after springback.

3.5. Finite Element Model

There are several critical factors that influence the simulation of springback in sheet metal forming. A detailed study of numerical issues associated with springback prediction was carried out by Li et al. (2002). However, the parameters affecting the numerical simulation of springback are specific to each problem. Therefore, a careful investigation was carried out to evaluate the effect of element type (shell, solid), mesh size and the integration scheme. Based on the authors' investigations it was found that the following conditions yield the best results:

- Solid plane-strain first order elements with reduced integration mode (denoted by CPE4R in ABAQUS)

- A mesh consisting of 4 elements through the sheet thickness and 800-1200 elements along the length (only one half of the channel section was modeled due to symmetry). The numbers and arrangements of the meshes along the length for each case is a very important factor affecting both the amount of springback and the convergence of the solution. Therefore, a study of mesh sensitivity was conducted for different combinations of materials, penetrations, and constitutive models to find the best mesh in each case.

- An explicit-implicit scheme for forming and springback stages, respectively.

For processes in which the sheet metal is subjected to relatively linear loading paths (such as hemispherical punch stretching or cup-drawing), the simple assumption of isotropic hardening may provide good springback predictions. However, the results of simulations for processes in which sheet metal undergoes cyclic loading (such as alternative tension-compression or bending-unbending stresses in deep drawing processes including drawbeads), this assumption should be relaxed to account for the kinematic hardening effects associated with stress reversal. Especially for springback analysis, modelling of the Bauschinger effect and cyclic hardening characteristics of materials is of vital importance (it is well-known that high strength steel and aluminum sheets exhibit more springback than ordinary mild steel sheets) (Moreira and Ferron, 2004). In an experimental study, Gau and Kinzel investigated the influence of the Bauschinger effect on springback prediction of four different materials (three steels: HS, AKDQ, BK and an aluminum alloy AA6111-T4) (Gau and Kinzel, 2001). They concluded that the influence of the Bauschinger effect on internal stresses and springback of the aluminum alloy sheet is more significant than that of the steel sheets. Friction measurements were provided by IRDI using the Twist Compression Test (Reid, 2002). The coefficient of friction based on these tests was 0.12 for all steels and 0.16

for the aluminum alloy. The classical Coulomb friction law in a contact model utilizing a penalty based algorithm was implemented. Preliminary simulations indicated that the coefficient of friction had a much stronger influence on the punch force predictions and a negligible effect on the predicted springback.

The forming stage was first analyzed using ABAQUS-Explicit and then the results were imported to ABAQUS-Standard to simulate the springback stage and obtain the final configuration of the part at equilibrium. Since, ABAQUS-Standard does not support the combined use of Hill and NKH models in its library of material models, a user-defined subroutine material model based on Hill's anisotropic yield function and mixed isotropic nonlinear kinematic hardening for both ABAQUS-Explicit (VUMAT) and ABAQUS-Standard (UMAT) was developed (details of formulations were presented in section 2).

3.6. Results

A series of 16 simulations, each including separate explicit and implicit stages, were carried out: 8 with isotropic hardening (IH) and 8 with nonlinear kinematic hardening (NKH). Simulation and experimental results are compared in this section. It was observed, both experimentally and numerically, that the amount of springback decreased when the drawbead penetration depth increased. Although the absolute value of the through-thickness residual stress increased with drawbead penetration because of additional hardening that occurred, the amount of springback increased for shallower drawbead penetrations. This is no doubt because, for deeper drawbead penetrations the restraining force is higher therefore, the sheet metal is stretched to a greater extent in the sidewall region after passing over the die shoulder. The higher tensile stresses help to decrease the residual stress gradient through the sheet thickness.

It is important to remember that the amount and the nature of the springback are directly affected by the simulation of the prior forming process. In other words, all modelling and material conditions that result from the simulation of the forming process determine the distribution of stress and of state variables throughout the channel sidewall, which in turn determine the subsequent springback.

In order to assess the reliability of the simulations of the forming stage, the experimentally measured punch force and both the major and thickness strains measured in the central zone of the side wall were compared to numerically predicted results. Figure 3.5 shows the experimentally measured punch force versus punch displacement curves for all materials with both shallow and deep drawbead penetrations, compared with the force-displacement curves

calculated by the FEM using two material models: IH and NKH. As it can be seen, all the predicted force-displacement curves tend to oscillate near the experimental curves because of the dynamic nature of the explicit solution scheme used to simulate the forming stage. There is some discrepancy between the predicted and experimental curves in the initial transient region for all cases. The difference in this transient region may be due to various numerical parameters such as the discrete character of the contact, friction, mesh sensitivity, and even material behaviour extrapolated by different models. However, the comparisons between predicted and experimental force-displacement curves can be adequately made in the steady-state region. In the cases associated with the IH model (Figures 3.5a and 3.5c) the simulation overestimated the experimental steady-state punch force for all materials and drawbead penetrations. The overestimation was more evident for the DP600 and AKDQ steels than for the HSLA and AA6022. This signifies that the flow stress predicted with the IH model is greater than the actual values for the former two materials. On the other hand, for the cases predicted with the NKH model (Figures 3.5b and 3.5d) the steady-state punch forces were in better agreement with the experimental forces for all materials compared to those predicted with the IH model. It was observed, however, that for the AKDQ steel, the force-displacement curves predicted with the NKH model for both the shallow and deep drawbead cases slightly overestimated the experimental findings. The reason may be explained as either overestimation of the extrapolated values due to the hardening parameters or overestimation due to the yield function and anisotropic coefficients.

(3.5. a)

(3.5. b)

66
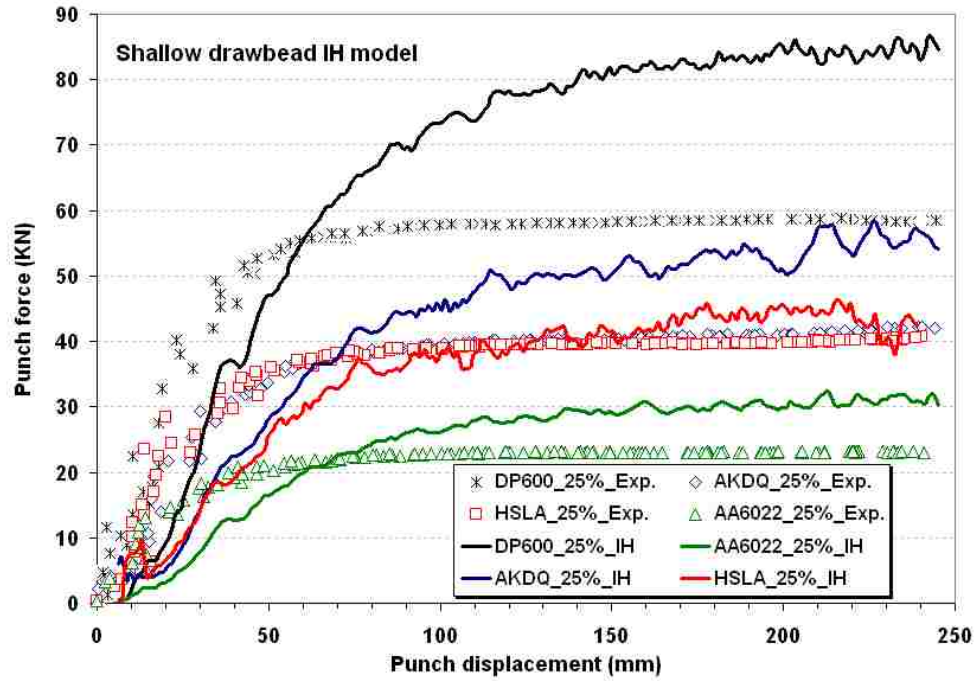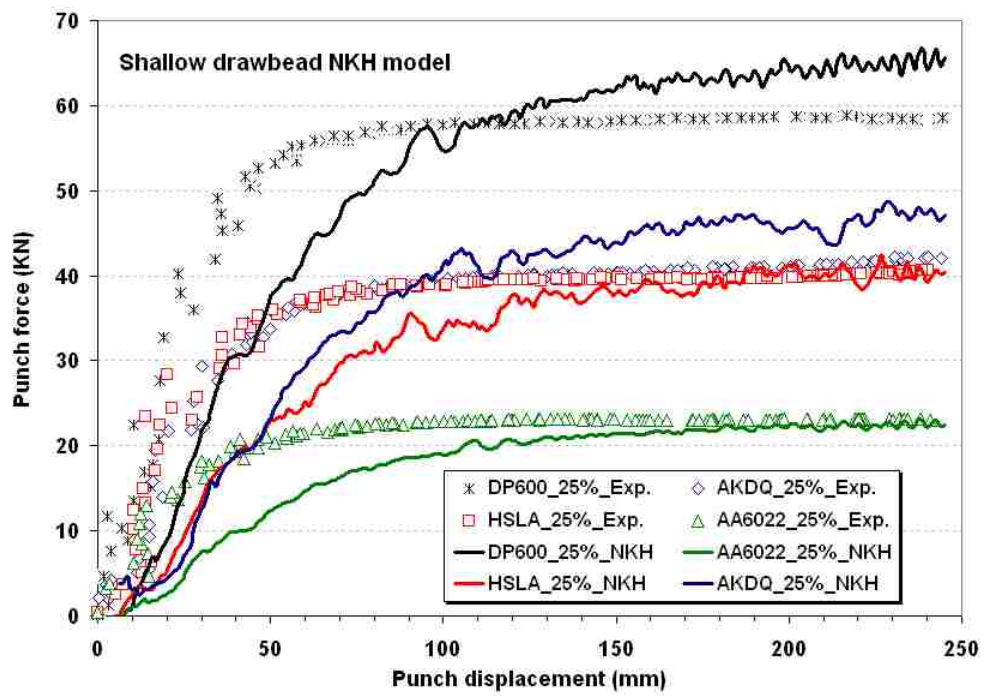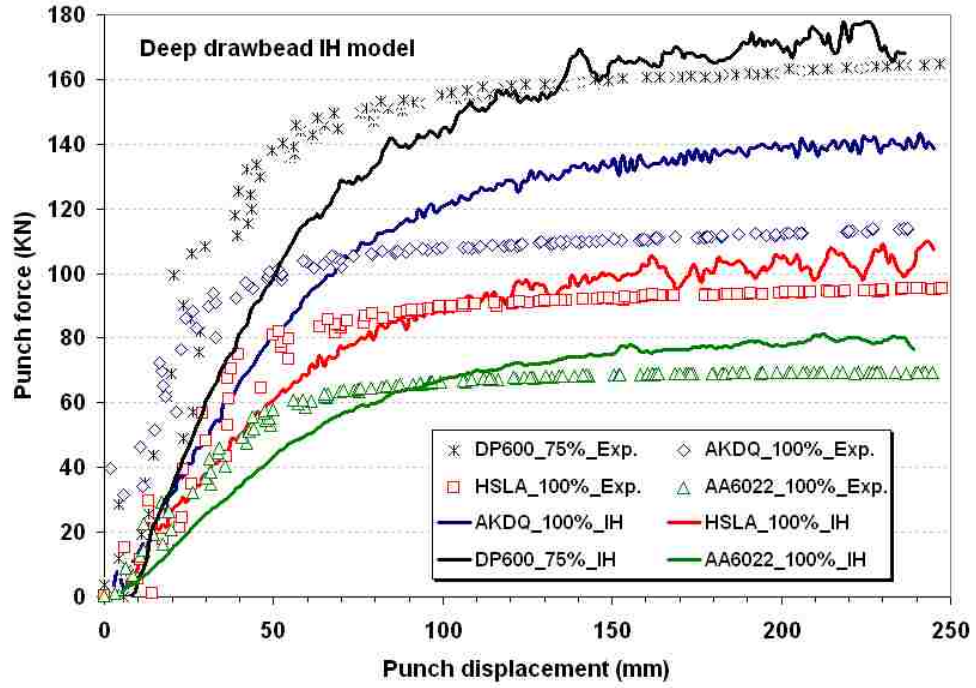
(c)
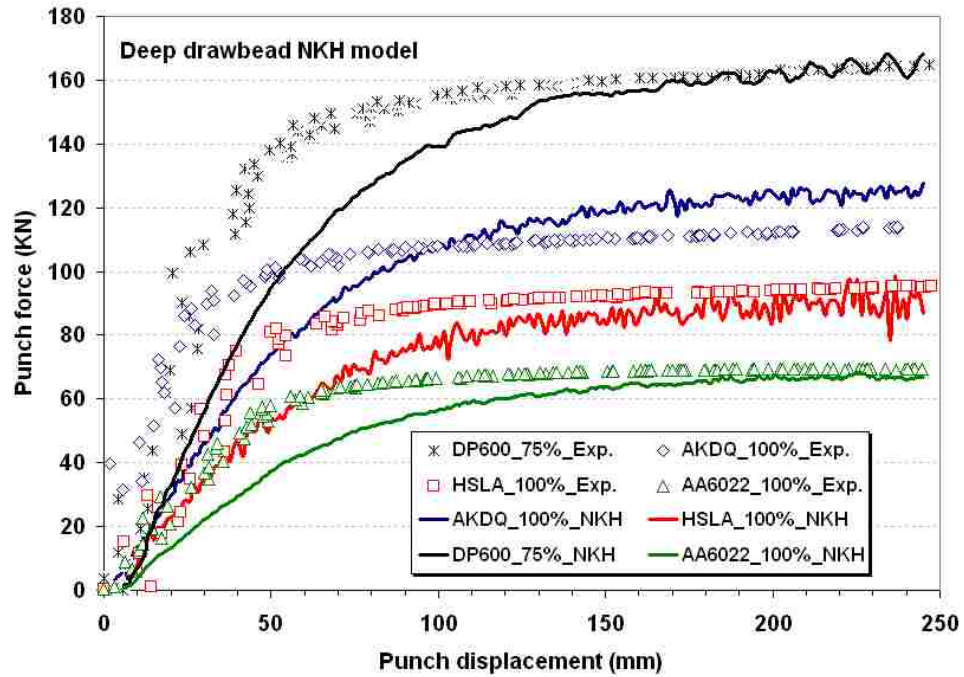
(d)

Figure 3.5. Comparison of experimentally measured punch force versus punch displacement curves with those obtained with the IH and NKH models for all four materials: (a) for shallow drawbead cases with IH model, (b) for shallow drawbead cases with NKH model, (c) for deep drawbead cases with IH model, (d) for deep drawbead cases with NKH model.

67

Both major and minor strains were measured in the side wall after the forming process. Because the plane-strain condition was dominant in the forming process, the minor strain (perpendicular to the drawing direction) was close to zero. Moreover, since 2D plane-strain elements were used to model the sheet in the FE analysis, the theoretical out-of-plane strain (or minor strain in experiments) was zero. Therefore, the minor strain is not compared here. Comparisons of experimental and predicted major strain for all materials and for shallow and deep drawbead cases are shown in Figure 3.6. For shallow drawbead cases the major strains predicted by the IH model overestimated the experimental values on the order of 1-3 % (Figure 3.6a), while the major strains predicted by the NKH model are in better agreement with measurements when the differences vary on the order of 0.2-0.8%. For deep drawbead cases almost all the major strains predicted by either model underestimated the experimental measurements on the order of 0.5-5 % (Figure 3.6b), however, the predicted results are quite close to each other.
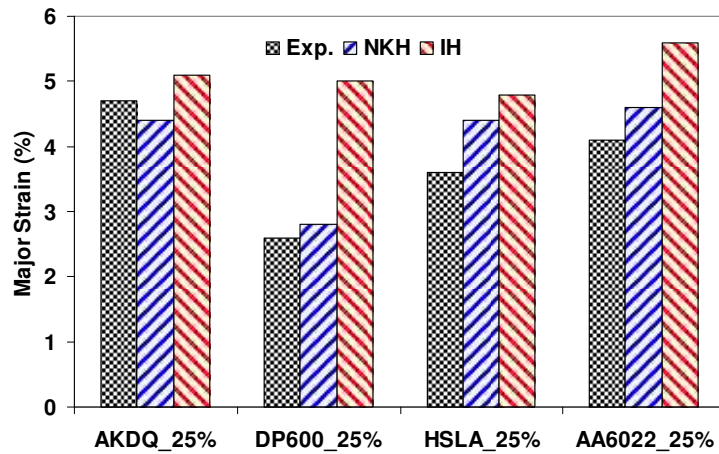
(a)
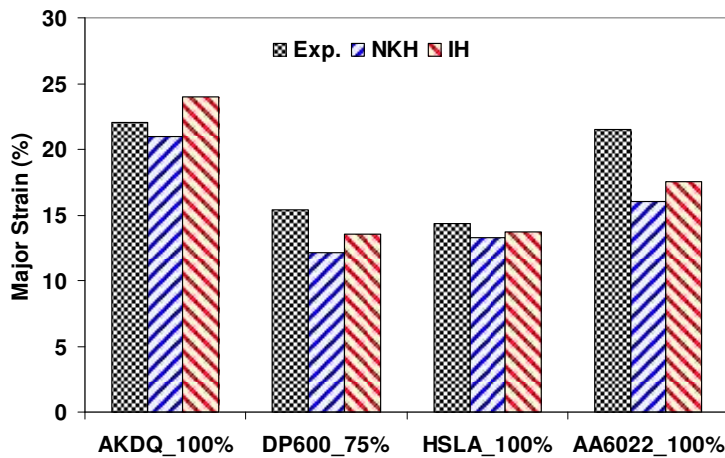
(b)

Figure 3.6. Comparison between experimentally measured and numerically predicted major strain with IH and NKH models for: (a) shallow drawbead cases (b) deep drawbead cases.

Similarly, comparisons of experimental and predicted thickness strain for all materials and for shallow and deep drawbead cases are shown in Figure 3.7. For most of the simulation results in both shallow and deep drawbead cases, the thickness strains predicted by the IH model overestimated the experiments on the order of 0.5-4 %, when the results predicted by the NKH model differ slightly from the measurements on the order of 0.1-2.5%. Accordingly, by comparing the punch force and strain results predicted by the finite element analysis with the experimental values the reliability of simulations of the forming stage was verified.
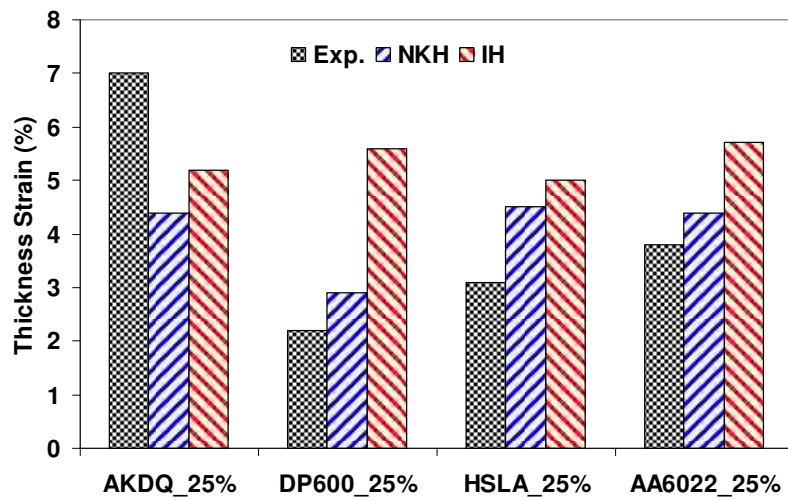
(a)
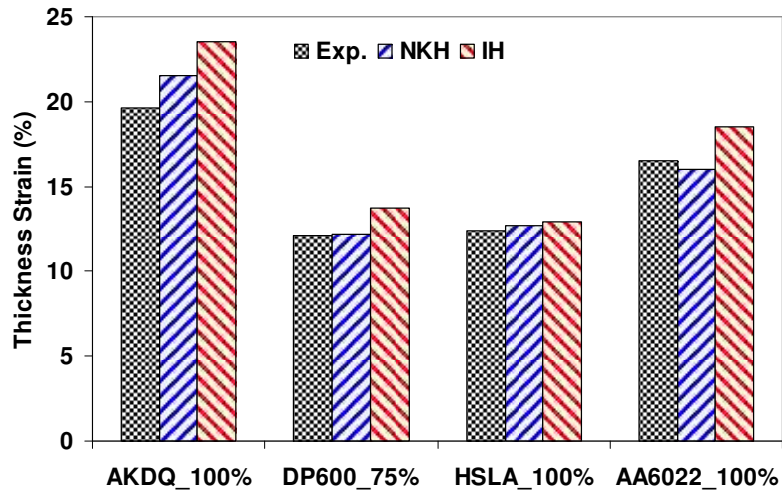
(b)

Figure 3.7. Comparison between experimentally measured and numerically predicted thickness strain with IH and NKH models for: (a) shallow drawbead cases (b) deep drawbead cases.

Before discussing the springback results, a brief explanation is given regarding the effect of plastic deformation on the unloading elastic modulus. Some researchers have recently indicated that the unloading modulus decreases with plastic deformation and they have shown that this effect must be taken into account for a thorough simulation of springback (Yoshida and Uemori, 2002; Morestin and Boivin, 1996; Levy et al., 2006; Yang et al., 2004; Cleveland and Ghosh, 2002; Lou and Ghosh, 2003). Therefore, the decrease in the unloading elastic modulus was implemented into the UMATs to improve the accuracy of the model. According to Levy et al. (2006), the unloading modulus decreases as a function of plastic strain according to the following equation:

$$E_u = E - A(1 - e^{-B.p})$$

(3.12)

where E_u is the effective unloading modulus, E is the elastic modulus during loading, p is the effective plastic strain and A and B are material constants. Based on the experimental data provided by Levy et al. (2006) the values of the constants for the non-DP steels determined by nonlinear regression are A = 29.8 GPa and B = 1.66. For the DP steel, these values are A = 46.3 GPa and B = 1.18. These experimental data are in agreement with those presented by Luo and Ghosh (2003) and Cleveland and Ghosh (2002). Cleveland and Ghosh (2002) also provided experimental data for the change in unloading modulus of AA6022-T4, and these data were used for the current simulations. According to this data, the unloading modulus of this alloy (whose properties are very similar to those of AA6022-T43) was shown to decrease by 11% before reaching a saturation level. As a consequence of these experimental data and of the form of Equation (3.12), it can be shown that for plastic strains greater than 5% the effective unloading modulus reaches a plateau, and there is little subsequent decrease in its value. Figure 3.8 shows the effective plastic strain distribution through the thickness in four different sections of the sidewall at the end of the forming stage for the DP600 drawn with 25% drawbead penetration. As can be seen, the plastic strain is larger than 7.5% at all nodes for this shallow drawbead penetration. This means that material in the sidewall that has passed through the drawbead has reached a constant unloading modulus. The distribution for all other materials with 25% drawbead penetration is very similar to Figure 3.8. For deeper drawbead penetrations, the minimum plastic strain in the middle of the thickness is even greater than 7.5%. Nevertheless, the evolution of the unloading modulus was implemented into the numerical code based on Equation (3.12), so that a more realistic value of the unloading modulus would be used for regions where the plastic strain is less than 5%, such as transition areas.
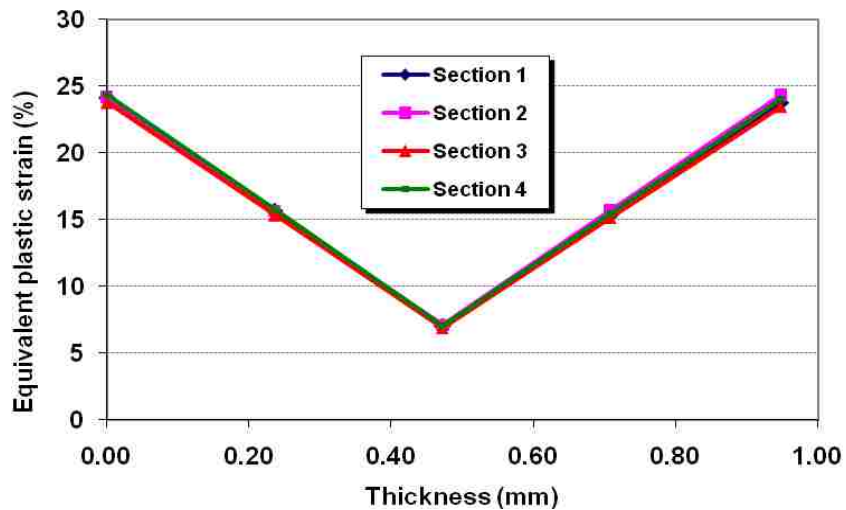
Figure 3.8. The plastic strain distribution at four different sections in the sidewall at the end of the forming stage for the DP600 with 25% drawbead penetration.

Figures 3.9 and 3.10 show a comparison between the experimental profiles of the AKDQ channel sidewalls after springback with those predicted with the IH and NKH models at different drawbead penetrations. It is apparent from these figures that NKH predicts the sidewall profile better than the IH, especially at 25% drawbead penetration where the range of cyclic strain is smaller than for 100% penetration. The NKH model divides the work hardening of the material into expansion and translation of the yield surface in stress space. However, the IH model assumes only an expansion of the yield surface due to global work hardening of the material. Consequently, it does not take the Bauschinger effect into account and is expected to overestimate springback. The overestimated stress obtained by the IH model for the uniaxial condition is also evident in Figure 3.2. However, in both cases the NKH model also overestimates the springback compared to the actual profile. This discrepancy is particularly more significant for the 100% penetration case. Referring to Figures 3.5b and 3.5d the punch force predicted by the NKH model also slightly overestimates the experimental steady-state force and is therefore consistent with the springback overestimation. The final value of the stress predicted by the NKH model at the end of the forming stage is still higher than actual. Again, the reason is the significant difference between the equal-biaxial yield stress and the uniaxial yield stresses for the case of AKDQ. This difference results in higher anisotropic coefficients and therefore will cause an increase in stress levels. To resolve this discrepancy, a more advanced yield or potential function would be required in the simulations, such as the yield criteria proposed by Barlat et al. (1997; 2003).

71

Figure 3.9. Springback profile of the AKDQ channel sidewall for 25% drawbead penetration.
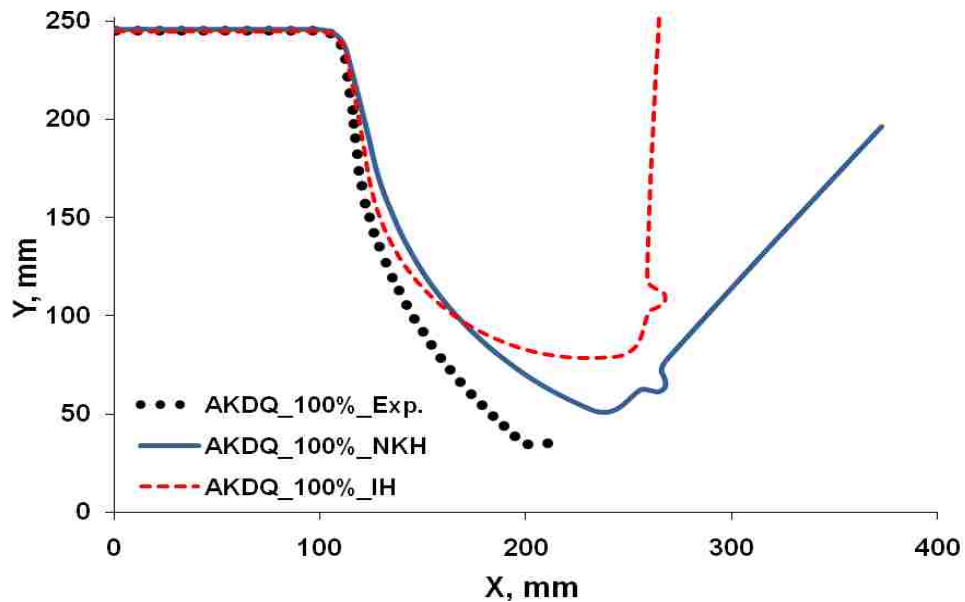
Figure 3.10. Springback profile of the AKDQ channel sidewall for 100% drawbead penetration.

Figure 3.11 shows the predicted through-thickness longitudinal stress distribution for a typical section in the sidewall of the formed AKDQ channel before and after springback. These stress distributions are shown for both 25 % and 100 % drawbead penetration using both the IH and NKH material models. It appears from Figure 3.11 that the maximum tensile and compressive

longitudinal stresses (on the inner and outer surfaces of the sidewall) predicted by the IH model are larger than those predicted by the NKH model. This through-thickness stress gradient after the forming stage is the main cause of springback, and it is evident that the IH model overestimates the amount of springback because the residual stress gradient after forming is greater. Also, the stress gradients for different drawbead penetrations before springback can be compared (Figures 3.11a and 3.11b), and it can be seen that, although the absolute value of stress difference between outer and inner surfaces is greater for the deep drawbead case, the stress gradient is more significant (steeper) for the shallow drawbead case. As a result, the bending moment that causes springback is greater for the shallower case despite the fact that the absolute value of the stress is smaller.

(a)

(b)
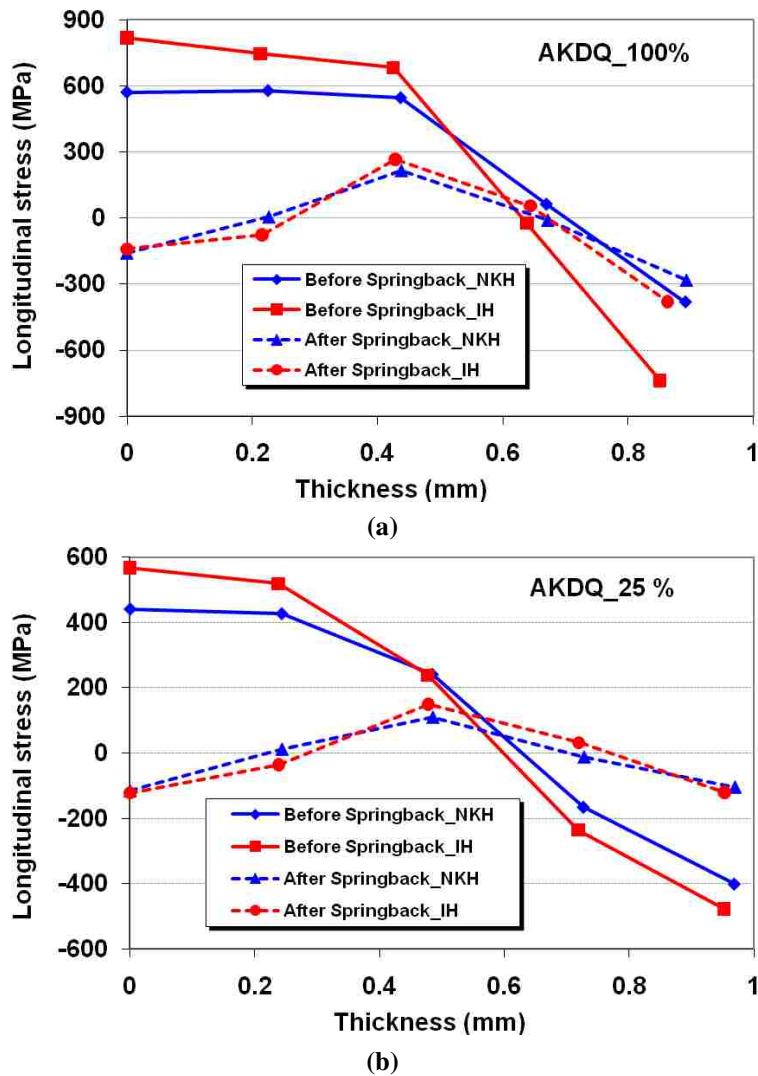
Figure 3.11. Through-thickness longitudinal stress distribution in a sidewall section for AKDQ steel before and after springback predicted by IH and NKH models: (a) 25% penetration, (b) 100% penetration.

Figures 3.12 and 3.13 show the profiles of the HSLA channel sidewalls after springback for the 25% and 100% drawbead penetration cases. Again, the IH model assumption overestimates the springback: this is to be expected considering the over-prediction in both the stress-strain curve and the punch force curve. In contrast, the NKH model is capable of more accurately predicting springback both in the general shape of sidewall and the amount of springback, although a slight overestimation is seen for the case of 100% drawbead penetration. The difference between the springback predictions with the two models is more significant in the 100% penetration case. The reason for this is either that the anisotropic function is inaccurate or the errors in stress prediction introduced by extrapolating the work-hardening curve increase for the deeper drawbead cases. It should be noted that through-thickness longitudinal stress distribution in the HSLA channel sidewall follows the same trend as the curves in Figure 3.11, but is not shown here for the sake of brevity.
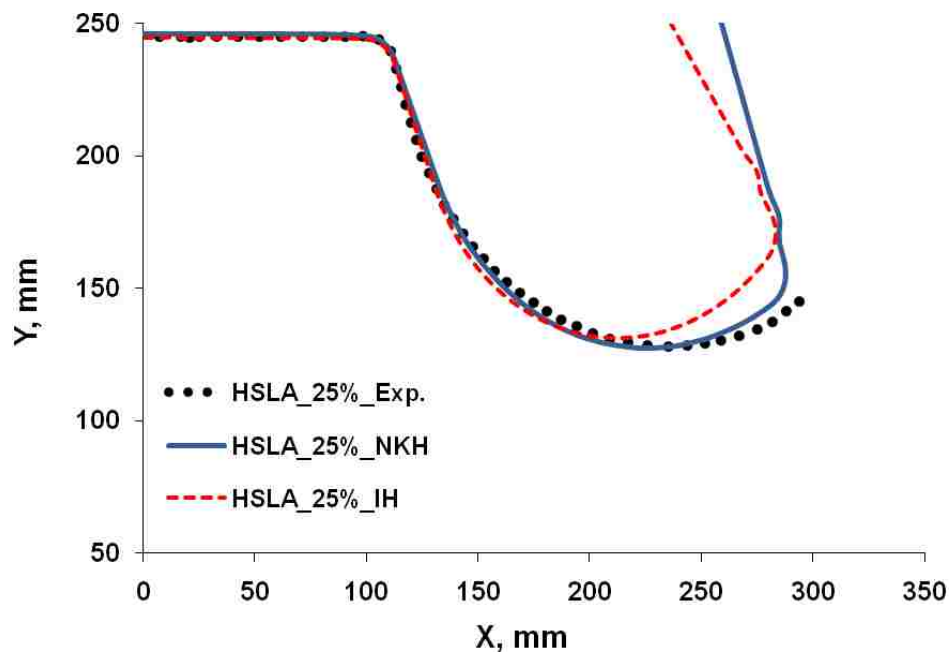
Figure 3.12. Springback profile of the HSLA channel sidewall for 25% drawbead penetration.
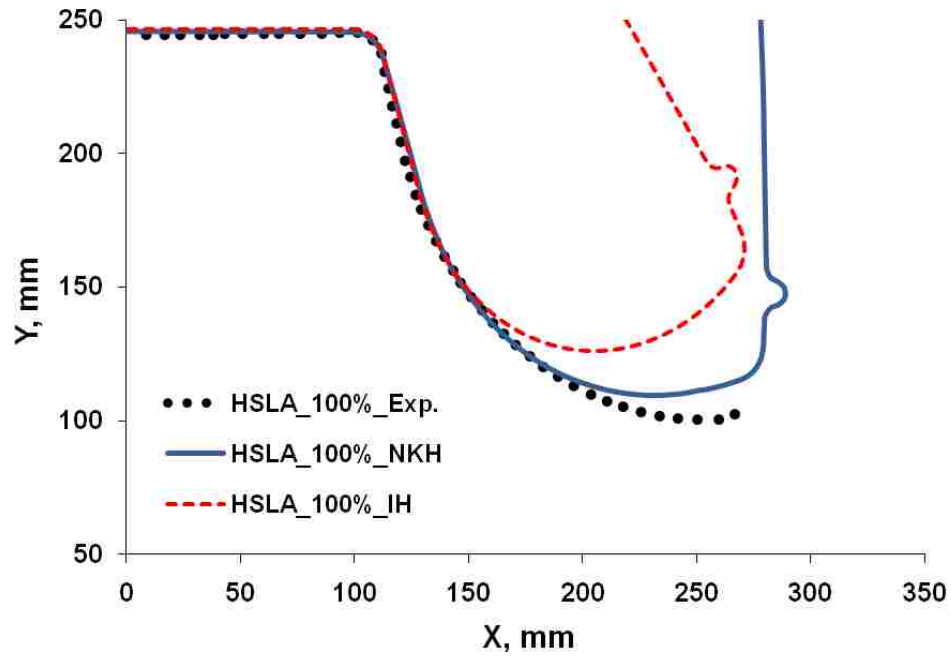
Figure 3.13. Springback profile of the HSLA channel sidewall for 100% drawbead penetration.

A comparison between the experimental sidewall profiles with those obtained by simulation at different drawbead penetrations for DP600 channel sections is shown in Figures 3.14 and 3.15. For both penetration cases the springback profiles predicted by the IH model significantly overestimate the experimental profile. The reason can be explained by referring to Figure (3.2a), where the difference between the IH and NKH models is quite large compared to the other grades of steel. Therefore, the level of stress calculated with the IH model is distinctly greater than the actual stress, and consequently, the predicted profile after springback is also far from the experimental sidewall profile. The NKH model slightly underestimates the springback in the middle of the sidewall for the case of 25% penetration but generally predicts the sidewall curl more accurately than the IH model. The springback in the sidewall for the 75% drawbead penetration case is quite well predicted with the NKH model although, as seen previously, a slight overestimation is seen towards the lower end of the sidewall.
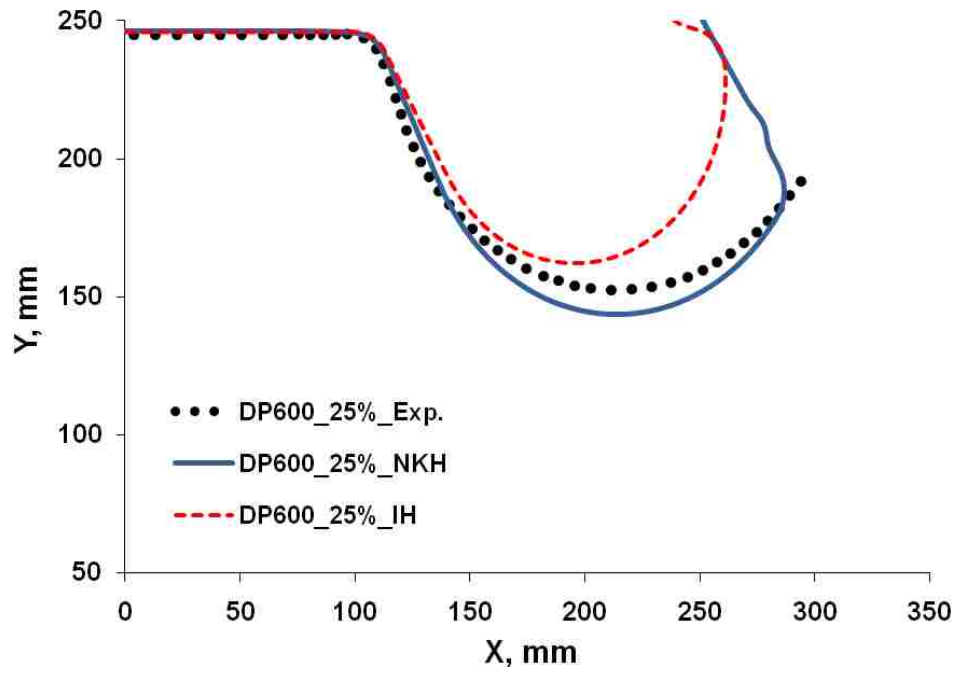
Figure 3.14. Springback profile of the DP600 channel sidewall for 25% drawbead penetration.
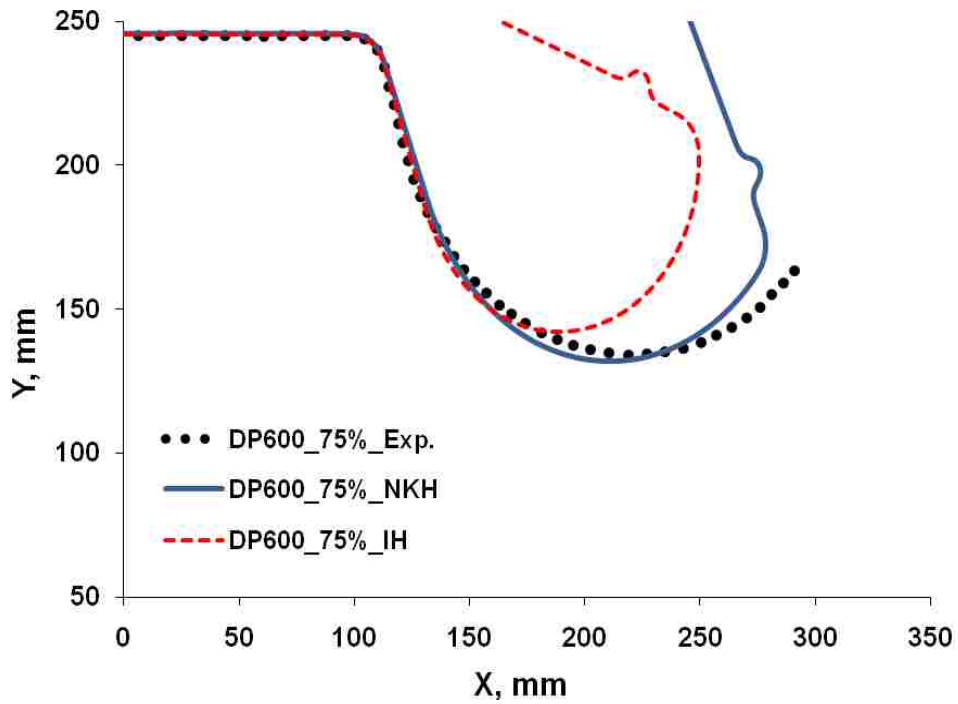
Figure 3.15. Springback profile of the DP600 channel sidewall for 75% drawbead penetration.

Figure 3.16 shows the through-thickness residual longitudinal and transverse stress distributions in the sidewall of the DP600 channel section after springback. These stress distributions are shown for both cases of 25% and 75% drawbead penetrations using two different material models: IH and NKH. It appears that the through-thickness residual stress distributions predicted by the IH and NKH models have very similar trends. Although the FEM results are not in very close agreement with the experimental measurements, the residual stresses predicted by the NKH model still correlate better with the experimental data than those predicted by the IH model.
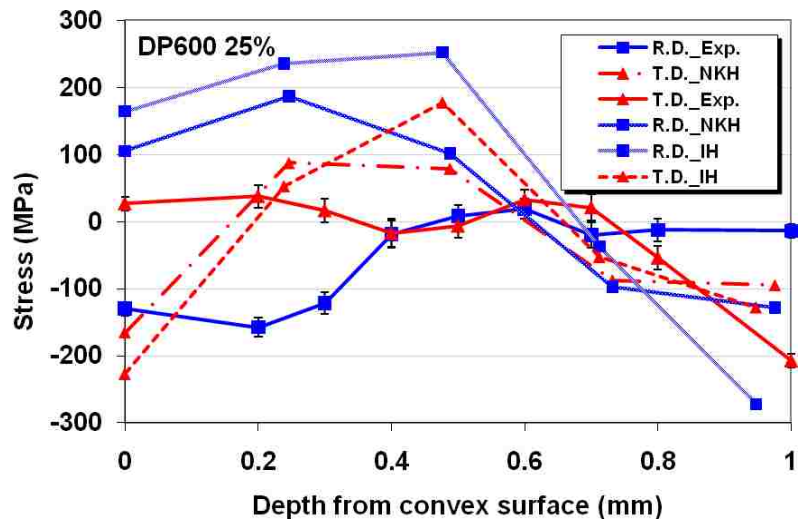
(a)
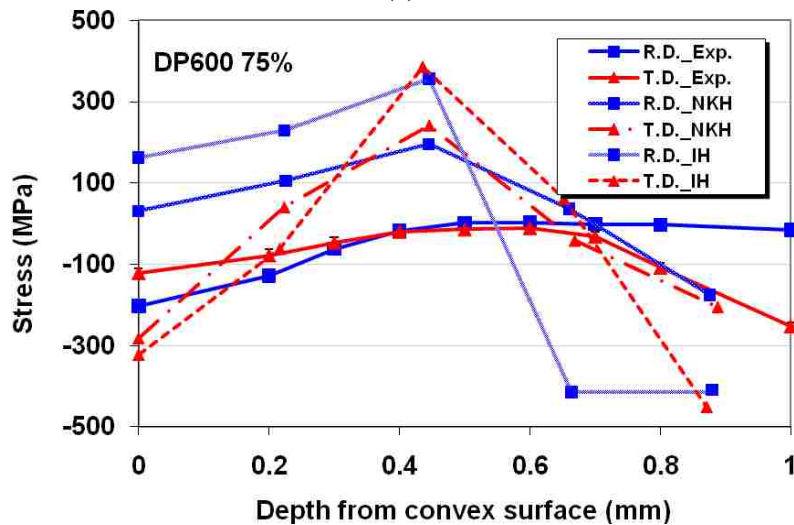
(b)

Figure 3.16. Through-thickness residual stress (Rolling Direction -R.D. and Transverse Direction-T.D.) distribution in a sidewall section for DP600 steel after springback predicted by the IH and NKH models compared with experimental measurements (experimental measurements from Green et al., 2006): (a) 25% penetration, (b) 75% penetration.

The profile of the channel sidewall after springback for AA6022-T43 at 25% and 100% drawbead penetration is shown in Figures 3.17 and 3.18, respectively. In the case of 25% drawbead penetration, the IH model slightly overestimates the springback whereas the NKH slightly underestimates the springback. However, the profile shape predicted by the NKH model is much more similar to the experimental profile than the one predicted by the IH model. With 100% drawbead penetration, the shape of the sidewall profile predicted with the NKH model is in very good agreement with the profile measured experimentally, while that obtained with the IH model overestimates the actual springback. As it was noted previously, the coefficients in the NKH model for the aluminum alloy were obtained from the uniaxial offset of the three-point bending test as explained by Zhao and Lee (2001). Moreover, it has often been pointed out that Hill's quadratic yield function is not able to represent the anisotropic behaviour of most aluminum alloys. As a consequence, numerous non-quadratic anisotropic yield functions have been proposed for aluminum alloys (Barlat et al., 1997; 2003). The effect of plastic anisotropy and its evolution on springback was studied by some researchers. For example Geng and Wagoner (2002) studied the influence of the yield function on the springback of a draw-bend process that does not include drawbeads. It will therefore be interesting to investigate the effect of different yield criteria on the springback behaviour of aluminum alloys for forming processes that do lead to cyclic deformation due to the presence of drawbeads.
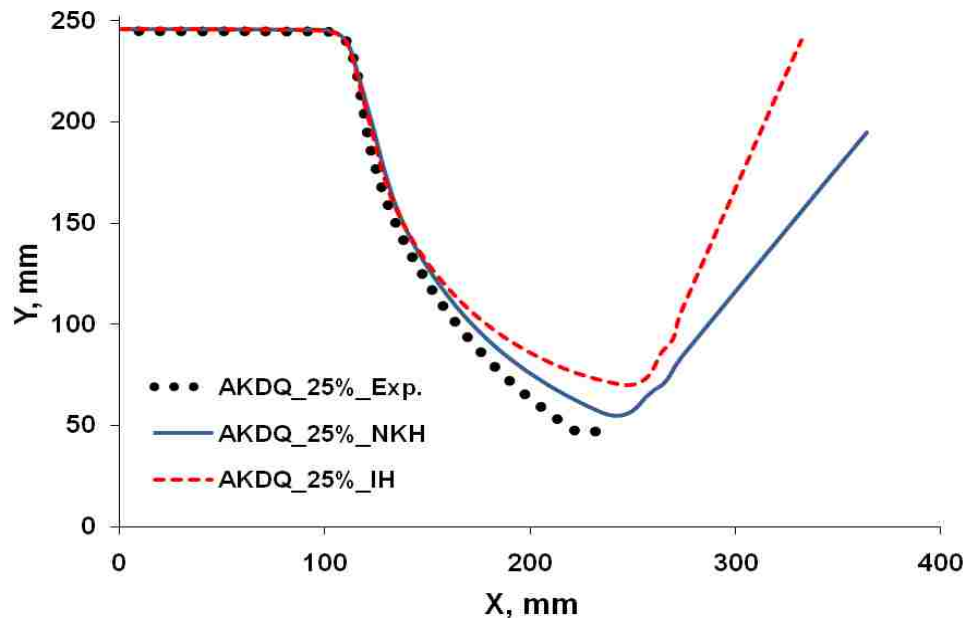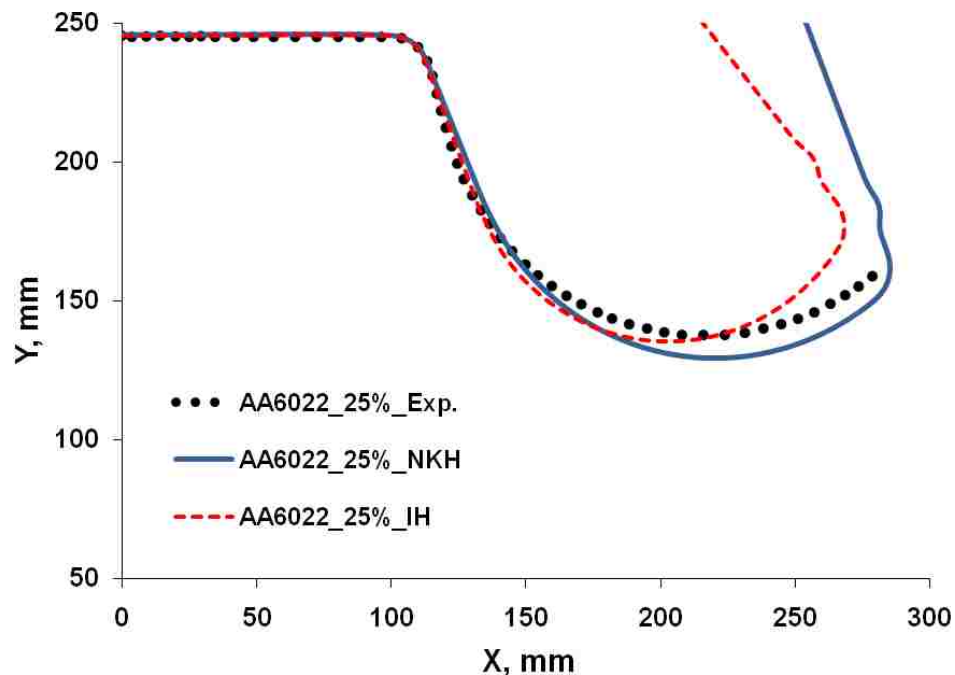

Figure 3.17. Springback profile of the AA6022 channel sidewall for 25% drawbead penetration.
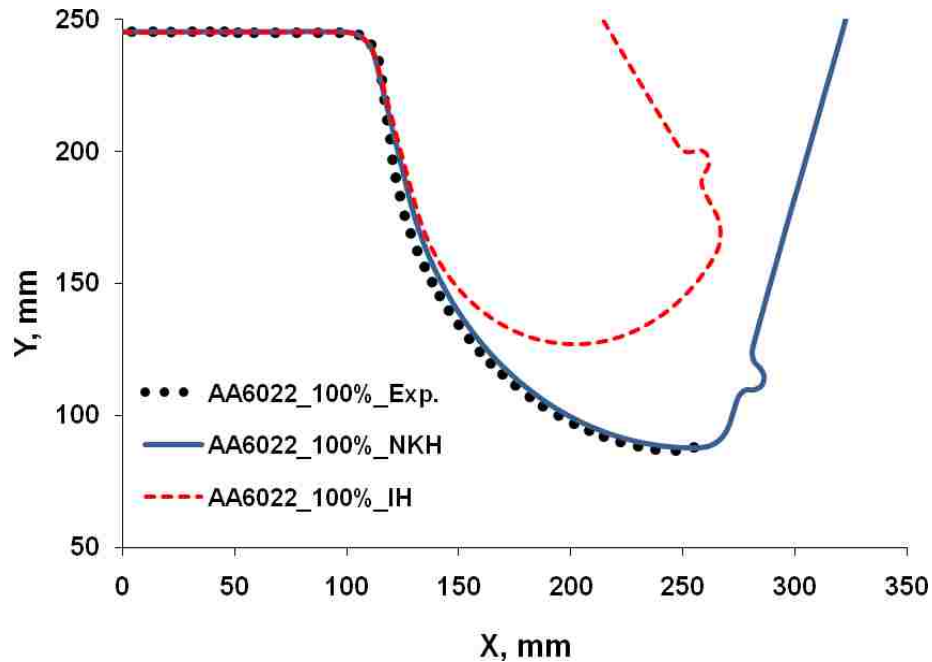
Figure 3.18. Springback profile of the AA6022 channel sidewall for 100% drawbead penetration.

3.7. Conclusions

Numisheet'05 Benchmark #3 was simulated using the nonlinear finite element analysis code ABAQUS. The channel draw tests were conducted with four different sheet materials (3 grades of steel and an aluminum alloy). The drawing of channel sections was simulated using two different drawbead penetrations, and simulations were carried out using two hardening models (isotropic-IH and combined isotropic-nonlinear kinematic-NKH). Hill's 1948 anisotropic yield function was used for all four sheet materials. Also, as an effective parameter in springback simulation, the decrease in unloading [elastic] modulus was taken into account. The material model for the Hill's 1948 yield function and mixed isotropic-nonlinear kinematic hardening was implemented as a user-defined material subroutine in the finite element code ABAQUS for both explicit and implicit time integration schemes, based on return mapping stress integration algorithm. Cyclic simple shear tests with different cycles at different strain levels were conducted to extract the NKH material model coefficients. The cyclic stress-strain curves were compared with the curves predicted by both IH and NKH models and it was seen that the NKH model was significantly closer to the experimental values in the reverse cycles due to its ability to model the Bauschinger effect. Experimental punch force recorded by a load cell during the forming stage was compared

with the punch force predicted by the FEM using different material models. Also, measured major and thickness strains in the uniformly deformed side wall zone were compared to the strains predicted by the FEM using different models. A comparison between predicted and experimental sidewall profiles after springback for all cases was presented. Numerical results were generally consistent with experimental data. For almost all cases the simulation results utilizing the IH model overestimate the experimental data as it was expected. The NKH model, however, is able to predict both the sidewall curl and the sidewall angle significantly more accurately. Finally, it appears that the simulated sidewall profiles for channel sections drawn with shallower drawbead penetration are more accurate than those with deeper drawbead penetration, except for the aluminum alloy.

In summary, it can be concluded that the isotropic hardening model cannot accurately predict springback of sheet metal parts when the forming process leads to cyclic deformations. This is especially true for drawing processes in which the sheet metal is formed through drawbeads. Howbeit, the mixed isotropic-nonlinear kinematic hardening model is able to capture the main cyclic hardening phenomena and therefore is more appropriate for simulating the springback. Nevertheless, it would appear that the prediction of springback can be further improved by accounting for observed material behaviour such as the work hardening stagnation, and by implementing more advanced constitutive models into the numerical simulation code.

3.8. References

Alves JL, Bouvier S, Oliveira MC, Menezes LF, 2005. Drawbeads: to Be or Not to Be. In: Smith L M, Pourboghrat F, Yoon JW, Stoughton TB. Proceedings of Numisheet'05, CP778 Volume A, American Institute of Physics. 655-660.

Armstrong PJ, Frederick CO, 1966. A mathematical representation of the multiaxial Bauschinger effect. Technical Report RD/B/N 731, Central Electricity Generating Board.

Barlat F, Maeda Y, Chung K, Yanagawa M, Brem JC, Hayashida Y, Lege DJ, Matsui K, Murtha SJ, Hattori S, Becker RC, Makosey S, 1997. Yield function development for aluminum alloy sheets. J. Mech. Phys. Solids 45, 1727-1763.

Barlat F, Brem JC, Yoon JW, Chung K, Dick RE, Lege DJ, Pourboghrat F, Choi SH, Chu E, 2003. Plane stress yield function for aluminum alloy sheets part I: theory. Int. J. Plasticity 19, 1297-1319.

Boger RK, Wagoner RH, Barlat F, Lee MG, Chung K, 2005. Continuous large strain tension/compression testing of sheet material. Int. J. Plasticity 21, 2319-2343.

Brunet M, Morestin F, Godereaux S, 2001. Nonlinear Kinematic Hardening Identification for Anisotropic Sheet Metals with Bending-Unbending Tests. ASME J. Eng. Mater. Tech. 123, 378-383.

Carden WD, Geng LM, Matlock DK, Wagoner RH, 2002. Measurement of springback. Int. J. Mech. Sci. 44, 79-101.

Choi Y, Han C, Lee JK, Wagoner RH, 2006. Modelling multi-axial deformation of planar anisotropic elasto-plastic materials part I: Theory. Int. J. Plasticity 22, 1745-1764.

Chun BK, Kim HY, Lee JK, 2002. Modelling the Bauschinger effect for sheet metals part I: theory. Int. J. Plasticity 18, 571-595.

Chung K, Lee M, Kim D, Kim C, Wenner ML, Barlat F, 2005. Springback evaluation of automotive sheets based on isotropic-kinematic hardening laws and non-quadratic anisotropic yield functions Part I: theory and formulation. Int. J. Plasticity 21, 861-882.

Cleveland RM, Ghosh AK, 2002. Inelastic effects on springback in metals. Int. J. Plasticity 18, 769-785.

Gan W, Wagoner RH, 2004. Die design method for sheet springback. Int. J. Mech. Sci. 46, 1097-1113.

Gau J, Kinzel GL, 2001. A new model for springback prediction in which the Bauschinger effect is considered. Int. J. Mech. Sci. 43, 1813-1832.

Gau JT, Kinzel GL, 2001. An Experimental Investigation of the Influence of the Bauschinger Effect on Springback Predictions. J. Mater. Proc. Tech. 108, 369-375.

Geng L, Wagoner RH, 2002. Role of plastic anisotropy and its evolution on springback. Int. J. Mech. Sci. 44, 123-148.

Gnaeupel-Herold T, Prask HJ, Fields RJ, Foecke TJ, Xia ZC, Lienert U, 2004. A Synchrotron Study of Residual Stresses in an Al6022 Deep Drawn Cup. Mat. Sci. Eng. A366, 104-113.

Gnaeupel-Herold T, Foecke TJ, Prask HJ, Fields RJ, 2005. An Investigation of Springback Stresses in an AISI-1010 Deep Drawn Cup. Mat. Sci. Eng. A399, 26-32.

Green DE, 2005. Description of Numisheet 2005 Benchmark #3 Stage-1: Channel Draw with 75% Drawbead Penetration. In: Cao J, Shi MF, Stoughton TB, Wang CT, Zhang L. Proceedings of Numisheet'05, CP778 Volume B, American Institute of Physics. 894-904.

Green DE, Stoughton TB, Gnaeupel-Herold T, Iadicola MA, Foecke T, 2006. Influence of drawbeads in deep drawing of plane-strain channel sections. In: Santos AD, Barata da Rocha A. Proceedings of IDDRG'06, INEGI, Porto. 559-566.

Iadicola MA, Foecke T, Stoughton TB, 2005. Experimental Procedures and Results for Benchmark 3: Stage 2 Forming Process. In: Cao J, Shi MF, Stoughton TB, Wang CT, Zhang L. Proceedings of Numisheet'05, CP778 Volume B, American Institute of Physics. 905-915.

Levy BS, Van Tyne CJ, Moon YH, Mikalsen C, 2006. The Effective Unloading Modulus for Automotive Sheet Steels. In: SAE 2006 World Congress & Exhibition, April '06, Detroit, MI, USA.

Li KP, Carden WP, Wagoner RH, 2002. Simulation of springback. Int. J. Mech. Sci. 44, 103-122.

Luo L, Ghosh AK., 2003. Elastic and inelastic recovery after plastic deformation of DQSK steel sheet. ASME J. Eng. Mater. Tech. 125, 237-246.

Moreira LP, Ferron G, 2004. Influence of the plasticity model in sheet metal forming simulations. J. Mater. Proc. Tech. 156, 1596-1603.

Morestin F, Boivin M, 1996. On the necessity of taking into account the variation in the Young modulus with plastic strain in elastic-plastic software. Nuclear Eng. Design 162, 107-116.

Oliveira MC, Alves JL, Chaparro BM, Menezes LF, 2007. Study on the influence of work hardening modelling in springback prediction. Int. J. Plasticity 23, 516-543.

Reid, JV, 2002. Twist compression evaluation of Numisheet'05 Benchmark lubricants. Industrial report submitted to GM R&D; IRDI, Midland, Canada.

Shi MF, Huang M, 2005. Specification for Benchmark Materials. In: Cao J, Shi MF, Stoughton TB, Wang CT, Zhang L. Proceedings of Numisheet'05, CP778 Volume B, American Institute of Physics. 1173-1178.

Simo JC, Taylor RL, 1985. Consistent Tangent Operators for Rate Independent Elasto-Plasticity. Comput. Meth. Appl. Mech. Eng. 48, 101-118.

Simo JC, Taylor RL, 1986. Return Mapping Algorithm for Plane Stress Elastoplasticity. Int. J. Numer. Meth. Eng. 22, 649-670.

Simo JC, Hughes TJR, 1998. Computational Inelasticity. Volume 7 of Interdisciplinary Applied Mathematics. Springer-Verlag, Berlin.

Song N, Qian D, Cao J, Liu WK, Li S, 2001. Effective Models for Prediction of Springback In Flanging. ASME J. Eng. Mater. Tech. 123, 456-461.

Stoughton TB, Green DE, Iadicola M, 2005. Specification for BM3: Two-stage Channel/Cup Draw. In: Cao J, Shi MF, Stoughton TB, Wang CT, Zhang L. Proceedings of Numisheet'05, CP778 Volume B, American Institute of Physics. 1157-1172.

Thuillier S, Manach PY, 2009. Comparison of the work-hardening of metallic sheets using tensile and shear strain paths. Int. J. Plasticity 25, 733-751.

Yang M, Akiyama Y, Sasaki T, 2004. Evaluation of change in material properties due to plastic deformation. J. Mater. Proc. Tech. 151, 232-236.

Yoshida F, Urabe M, Toropov VV, 1998. Identification of Material Parameters in Constitutive Model for Sheet Metals from Cyclic Bending Tests. Int. J. Mech. Sci. 40, 237-249.

Yoshida F, Uemori T, 2002. A model of large-strain cyclic plasticity describing the Bauschinger effect and workhardening stagnation. Int. J. Plasticity 18, 661-686.

Yoshida F, Uemori T, Fujiwara K, 2002. Elastic-Plastic Behaviour of Steel Sheets Under in-Plane Cyclic Tension-Compression at Large-Strain. Int. J. Plasticity 18, 633-659.

Zhao K, Lee JK, 2001. Generation of Cyclic Stress-Strain Curves for Sheet Metals. ASME J. Eng. Mater. Tech. 123, 391-397.

Chapter 4

A Non-associated Constitutive Model with Mixed Isotropic-Kinematic Hardening for Finite Element Simulation of Sheet Metal Forming

4.1. Introduction

One of the benefits of the non-associated flow rule (NAFR) to describe the plasticity of metals is its convenient description of anisotropic yielding and flow. For instance, in order to improve computation accuracy without having to define a large number of material parameters, Stoughton (2002) proposed a NAFR model which combined different yield and plastic potential functions, each with simple formulations, to describe plastic behaviour. In the first model, Stoughton (2002) assumed that both yield and potential functions were based on Hill's (1948) function with isotropic hardening. The generalization described by Stoughton includes realistic elastic effects and fully anisotropic plastic behaviour under a NAFR, resulting in an accurate simulation of the r-value distribution and both uniaxial and biaxial yield behaviour. The latter behaviour is challenging for Hill's quadratic function under the associated flow rule (AFR). The NAFR models proposed for sheet metal forming so far (they were reviewed in section 2.3.3), have been formulated based on the pure isotropic hardening. So that, in order to improve the ability of these types of models to apply for a broader range of sheet metal forming simulations (such as springback simulation), developing the anisotropic NAFR constitutive models with mixed isotropic-kinematic hardening was recommended.

From a computational point of view, there have been a number of studies concerning numerical stress integration of material models with combination of NAFR and mixed isotropic kinematic hardening. One of the early works was done by Aravas (1987) and is a continuation of Simo and Taylor's (1985; 1986) return mapping algorithm. Simo and Meschke (1993) proposed a methodology for computational plasticity at finite strain within the context of geomechanical applications and the general format of multi-surface plasticity. Zeng et al. (1996) and Kojic (2002) reviewed some numerical procedures for stress integration of inelastic material models that also included NAFR and basic hardening rules. Almost all the numerical techniques presented for the NAFR were concerned with pressure-sensitive isotropic yield and are mainly used for geomechanical analysis (e.g. Ahadi and Krenk, 2003; Hjiaj et al., 2003; Foster et al. 2005; Clausen et al., 2007). Also, there has been some work on the derivation of a numerical model for hydrostatic sensitive metals and localization behaviour that mostly used J_2 yield criterion and isotropic hardening (e.g. Brunig et al., 1998, 1999, 2000; Mahnken, 2001). Lei and Lissenden (2007) implemented a pressure-sensitive non-associated model with nonlinear kinematic hardening law that was used to simulate the behaviour of DRA (Discontinuously Reinforced Aluminum) composites. Recently, Cvitanic et al. (2008) implemented a non-associated based anisotropic material model for simulation of sheet forming processes that was an adaptation of the work done by Yoon et al. (1999) for the associated formulation. They considered two different yield and potential functions: Hill's (1948) and Karafillis and Boyce (1993) with only isotropic hardening; and also derived the algorithmic numerical formulations of the constitutive model.

In this chapter, a phenomenological plane stress elasto-plastic constitutive model based on Hill's (1948) quadratic anisotropic yield function and non-associated flow rule with combined isotropic-nonlinear kinematic hardening is presented. In the first section, elasto-plastic formulation for generic yield and potential functions with mixed hardening rule was developed and solved explicitly (analytically). The kinematic hardening was defined by the nonlinear Armstrong-Frederick model and isotropic hardening by either a power law or exponential law. The model employs two quadratic anisotropic functions in the form of Hill's (1948) yield function, in which anisotropy is defined with the yield stress ratios and the r-values in different orientations with respect to the rolling direction for the yield and potential functions, respectively. The model was then applied for numerical implicit stress integration algorithm using radial return mapping method and the algorithmic consistent elasto-plastic modulus was also derived.

Model verification was demonstrated for both the flow rule and the hardening behaviours. For verification of the mixed hardening model the experimental, cyclic stress-strain curves at different levels of inverse strain were compared with the non-associated model with different isotropic and

mixed hardening regimes. For flow rule verification the distribution of yield stress ratios and r-values at different angles was compared with the experiments. Yield surfaces and plastic potential surfaces were also compared to determine what the differences are. Also, equibiaxial and shear stress-strain curves were predicted with the proposed model and compared to the experimental curves. Finally, the material model was implemented to a user-defined (UMAT) subroutine and used to simulate different sheet metal forming processes to assess its ability to improve the results of finite element simulations. Earing prediction of a cylindrical cup drawing process and springback prediction of a channel draw process with drawbead were simulated. Simulation results showed that this non-associated mixed hardening material model improves the prediction of both anisotropy and hardening behaviour, even though a rather simple quadratic constitutive model was used.

4.2. Constitutive model: non-associated flow rule with mixed hardening

The plane-stress condition was adopted because sheet metal forming analyses usually assume that the sheet thickness is small compared to the other dimensions. However, the formulation was written in such a way that it can be easily modified or converted to the plane-strain or 3-D conditions by replacing the appropriate elastic and anisotropic matrices. All stresses, strains, stretches, and state variables were represented in the local material coordination. Also, it is convenient to use a co-rotational coordinate system in which the basis system rotates with the material (Yoon et al, 1999a).

4.2.1. Basic equations

Assuming additive decomposition of the strain tensor, total strain is decomposed into an elastic part and a plastic part

$$\boldsymbol{\varepsilon} = \boldsymbol{\varepsilon}^e + \boldsymbol{\varepsilon}^p \tag{4.1}$$

By obvious equilibrium considerations, Hooke's law in tensor form can be written for a linear and isotropic elastic material

$$\boldsymbol{\sigma} = \mathbf{D}(\boldsymbol{\varepsilon} - \boldsymbol{\varepsilon}^p) \tag{4.2}$$

where $\mathbf{D}$ is the elastic stiffness tensor and for the plane stress condition is written as

$$\mathbf{D} = \frac{E}{1-v^2} \begin{bmatrix} 1 & v & 0 \\ v & 1 & 0 \\ 0 & 0 & \frac{1-v}{2} \end{bmatrix} \qquad (4.3)$$

where E is the elastic modulus and v is Poisson's ratio. Stress and strain tensors ($\boldsymbol{\sigma}$ and $\boldsymbol{\varepsilon}$) are stored in vector form here for the sake of simplicity and efficiency in the numerical procedures

$$\boldsymbol{\sigma} = \left\{ \begin{array}{c} \sigma_{11} \\ \sigma_{22} \\ \sigma_{12} \end{array} \right\} \quad \text{and,} \quad \boldsymbol{\varepsilon} = \left\{ \begin{array}{c} \varepsilon_{11} \\ \varepsilon_{22} \\ \gamma_{xy}(=2\varepsilon_{12}) \end{array} \right\} \qquad (4.4)$$

For the plane-stress condition, the out-of-plane normal is zero ($\sigma_{33} = 0$). However, when a shell element is used, ABAQUS generates the transverse stress components (σ_{13} and σ_{23}) outside the UMAT based on Mindline assumption with elasticity theory. So, it is not necessary to include the terms during the elasto-plastic stress integration procedure. The static assumption of ($\sigma_{33} = 0$) defines constraints for the resulting boundary-value problem, which are incorporated in advance in the representation of the tensors in the constitutive equations. The constraint $\sigma_{33} = 0$ and the evolution equation for the plastic strains lead to

$$\varepsilon^e{}_{33} = -v/(1-v)(\varepsilon^e{}_{11} + \varepsilon^e{}_{22}) \qquad (4.5a)$$

$$\varepsilon^P{}_{33} = -(\varepsilon^P{}_{11} + \varepsilon^P{}_{22}) \qquad (4.5a)$$

Therefore, the strain $\varepsilon_{33} = \varepsilon^e{}_{33} + \varepsilon^P{}_{33}$ is obtained if the plastic strains $\varepsilon^P{}_{11}, \varepsilon^P{}_{22}$ and the stresses σ_{11}, σ_{22} are known

$$\varepsilon_{33} = (-v/(\varepsilon_{11} + \varepsilon_{22}) - (1-2v)(\varepsilon^P{}_{11} + \varepsilon^P{}_{22}))/(1-v) \qquad (4.6)$$

It should be noted that the strain components $\varepsilon_{33}, \varepsilon^e{}_{33}, \varepsilon^P{}_{33}$ do not enter the formulation explicitly. For a shell element, the thickness is updated based on Equation (4.6) as a post-processing fashion after the stress integration procedure. So, the equilibrium equation is still

solved under a rigid-normal assumption of a shell element (no thickness change). Moreover, for most shell elements, ABAQUS will calculate the transverse shear stiffness values required in the element formulation. ABAQUS computes the transverse shear stiffness by matching the shear response for the case of the shell bending about one axis, using a parabolic variation of transverse shear stress in each layer. However, the default shear stiffness values are not calculated when the material behaviour is computed by a user-defined subroutine. For a homogeneous shell made of a linear, orthotropic elastic material, the transverse shear stiffness terms are given by (ABAQUS, 2007):

$$K^{ts}_{11} = \frac{5}{6}G_{13}t, \qquad K^{ts}_{22} = \frac{5}{6}G_{23}t, \qquad K^{ts}_{12} = 0 \tag{4.7}$$

G_{13} and G_{23} are the material's shear moduli in the out-of-plane direction and t is the average thickness.

4.2.2. Plasticity equations

The yield criterion, as a function of all state variables, can be written in a generic form as

$$F(\boldsymbol{\sigma}, \boldsymbol{\alpha}, \sigma^Y) = f_y(\boldsymbol{\sigma} - \boldsymbol{\alpha}) - \sigma^Y(p) = 0 \tag{4.8}$$

where $f_y(\boldsymbol{\sigma} - \boldsymbol{\alpha})$ is a continuously differentiable yield function, $\boldsymbol{\alpha}$ is a backstress tensor (that is used to describe the evolution of the center of the yield surface in stress space as a kinematic hardening behaviour), scalar p is a hardening parameter (or equivalent plastic strain), and $\sigma^Y(p)$ is a scalar function representing the stress-strain hardening behaviour (so-called isotropic or work hardening rule). The isotropic hardening or σ^Y, that determines the size of the yield surface, is generally represented by either an exponential or power law function

$$\sigma^Y(p) = \sigma_0 + Q(1 - e^{-b.p}) \tag{4.9a}$$

$$\sigma^Y(p) = K(\varepsilon_0^P + p)^n \tag{4.9b}$$

where Q and b, or K and n, are material constants associated with isotropic hardening. Because of the incremental formulation of plasticity, parameter p is generally defined by the rate equation. In

its most general form of a quadratic strain-rate potential, the equivalent plastic strain increment can be expressed as

$$dp = (\frac{2}{3} d\boldsymbol{\varepsilon}^p : \mathbf{A} : d\boldsymbol{\varepsilon}^p)^{1/2} \text{ or } \dot{p} = (\frac{2}{3} \dot{\boldsymbol{\varepsilon}}^p : \mathbf{A} : \dot{\boldsymbol{\varepsilon}}^p)^{1/2}$$

(4.10)

where $\mathbf{A}$ is a fourth order compliance tensor, which represents anisotropy for a quadratic strain-rate potential. In the case of von Mises function, it becomes the identity tensor. The *flow rule* is used to determine the plastic part of the strain increment

$$d\boldsymbol{\varepsilon}^p = d\lambda \frac{\partial f_p}{\partial \boldsymbol{\sigma}}$$

(4.11)

where f_p, a continuously differentiable function, is called a plastic potential, and $d\lambda$ is a non-negative scalar called the plastic multiplier or consistency parameter. Equation (4.11) states that the direction of the plastic strain increment is determined by the normal of the plastic potential surface at the loading point and its magnitude is calculated by the parameter $d\lambda$. In most cases of classical plasticity, and particularly in metals plasticity, it is assumed that the potential function is identical to the yield function, which is called *associated flow rule* (AFR) or normality rule.

Using the principle of plastic work equivalence (or dissipated plastic work) for the incremental deformation theory and with restriction of the plastic potential to first order homogeneous functions, Euler's following identity applies (Cvitanic et al., 2008)

$$dp = d\lambda \frac{\boldsymbol{\sigma} : \dfrac{\partial f_p}{\partial \boldsymbol{\sigma}}}{f_y} = d\lambda \frac{f_p}{f_y}$$

(4.12)

It is obvious that parameters dp and $d\lambda$ are equal if both the yield and plastic potential functions are identical (AFR case). But for the NAFR models the effective plastic strain should be constantly scaled with the factor f_p / f_y. However, in a more convenient approach, these two functions can be matched for the reference direction initially as they have equal magnitude of the stress under that direction (the reference direction that is used to define the stress-strain relation such as uniaxial tension test). Therefore in this paper, the equality of these two parameters is assumed for the sake of brevity and simplicity (i.e. $dp=d\lambda$, Stoughton (2002)).

Yield, loading and unloading conditions for a hardening material are usually defined as

$$F < 0 \qquad\qquad\qquad \text{elastic deformation}$$

$$F = 0 \;\; \text{and} \;\; dF\big|_{dp=0} > 0 \qquad \text{plastic loading}$$

$$F = 0 \;\; \text{and} \;\; dF\big|_{dp=0} = 0 \qquad \text{neutral loading} \tag{4.13}$$

$$F = 0 \;\; \text{and} \;\; dF\big|_{dp=0} < 0 \qquad \text{elastic unloading}$$

where $dF\big|_{dp=0}$ defines the time derivative of the yield functional F at constant internal variables. Since all evolution equations depend on the plastic strain rate, $\dot{\varepsilon}^{p}$ or more simply its scalar equivalent, it is equivalent to demand $dp=0$ i.e. $dF\big|_{dp=0} = \dfrac{\partial f_{y}}{\partial \boldsymbol{\sigma}} : d\boldsymbol{\sigma}$. It will be seen that, these conditions are very important in the computational formulation, where the consistency of the yield function is used to determine the equivalent plastic strain. The above conditions can be described more briefly as the Kuhn-Tucker conditions for the restriction of plastic multiplier (that is a generalization of the theory of Lagrange multiplier)

$$F \le 0, \qquad d\lambda \ge 0, \qquad d\lambda F \equiv 0 \tag{4.14}$$

The consistency condition is used to find the plastic multiplier that determines the magnitude of the plastic flow increment. By applying the consistency condition to Equation (4.8) it is assured that the stress state remains on the yield surface during plastic deformation.

$$dF = \frac{\partial f_{y}}{\partial \boldsymbol{\sigma}} : d\boldsymbol{\sigma} + \frac{\partial f_{y}}{\partial \boldsymbol{\alpha}} : d\boldsymbol{\alpha} - \frac{\partial \sigma^{Y}}{\partial p} dp = 0 \tag{4.15}$$

As noted before, the backstress tensor or kinematic hardening parameter describes the translation of the yield surface in stress space. When modelling the cyclic deformation of materials, or so-called cyclic plasticity, kinematic hardening must be considered because it is able to model different behaviour in loading and reverse loading conditions more realistically. However, isotropic hardening is a non-directional component of hardening that can be thought of as giving the size of the yield surface.

The evolution of the backstress tensor in this paper is modeled based on the nonlinear kinematic hardening theory or so-called AF formulation (Armstrong and Frederick, 1966)

$$d\boldsymbol{\alpha} = (\frac{C}{f_p}\boldsymbol{\eta} - \gamma\boldsymbol{\alpha})dp \qquad (4.16)$$

where parameters C and γ are material constants and tensor $\boldsymbol{\eta}$ was defined as $\boldsymbol{\eta} = \boldsymbol{\sigma} - \boldsymbol{\alpha}$ for convenience. The first part of the backstress tensor increment in Equation (4.16) was written based on Ziegler's method (1959) that is itself a modification to the classical linear kinematic hardening model introduced by Prager (1956). Two possibilities immediately become evident: using the plastic potential function, f_p, in the above expression defines a non-associated hardening whereas the classical form (using f_y) would give an associated hardening (Zienkiewicz and Taylor, 2005). Thus, for a fully associated model we require that f_y be used to define both the plastic potential and the hardening. In such a case the relations of plasticity also may be deduced by using the *principle of maximum plastic dissipation*. However, in this paper the plastic potential function is used to present the *fully non-associated* model.

Armstrong and Frederick (1966) proposed the nonlinear part of the backstress increment, the so-called *recall term*, to provide a means of retaining smoother transitions from elastic to inelastic and the strain path dependency. What is required for the backstress is to give the proper increase during monotonic loading (which is a fairly slow increase) and a rapid change in backstress during reversing. Applications of this approach were presented by Chaboche (1986; 1989) to increase the range of validity of the original model and to improve the quantitative description of the ratcheting effect and degree of freedom. The theory predicts a saturation of the backstress to a value of (C/γ) during long proportional path (such as uniaxial loading) and no permanent softening. Constant γ determines both how quickly the backstress builds up during monotonic loading and the degree of rounding of the stress-strain curve during reversing.

Using the above notation, the consistency condition is written to determine the plastic multiplier

$$\frac{\partial f_y}{\partial \boldsymbol{\eta}} : d\boldsymbol{\eta} = hdp \qquad (4.17)$$

where $h = \dfrac{d\sigma^Y}{dp}$. By differentiating Equation (4.2) and by using the flow rule, it follows that

$$d\,\boldsymbol{\sigma} = \mathbf{D}(\,d\,\boldsymbol{\varepsilon} - dp\,\frac{\partial f_p}{\partial\,\boldsymbol{\sigma}}\,) \tag{4.18}$$

and

$$d\,\boldsymbol{\eta} = d\,\boldsymbol{\sigma} - (\,\frac{C\,\boldsymbol{\eta}}{f_p} - \gamma\,\boldsymbol{\alpha}\,)dp \tag{4.19}$$

Substitution of Equations (4.19) and (4.18) into Equation (4.17) yields

$$dp = \frac{\dfrac{\partial f_y}{\partial\,\boldsymbol{\sigma}} : \mathbf{D} : d\,\boldsymbol{\varepsilon}}{\dfrac{\partial f_y}{\partial\,\boldsymbol{\sigma}} : \mathbf{D} : \dfrac{\partial f_p}{\partial\,\boldsymbol{\sigma}} + \dfrac{C}{f_p}(\dfrac{\partial f_y}{\partial\,\boldsymbol{\sigma}} : \boldsymbol{\eta}) - \gamma(\dfrac{\partial f_y}{\partial\,\boldsymbol{\sigma}} : \boldsymbol{\alpha}) + h} \tag{4.20}$$

By substituting the calculated plastic multiplier into Equation (4.18), the following relation between the total strain and stress increments is derived

$$\frac{d\,\boldsymbol{\sigma}}{d\,\boldsymbol{\varepsilon}} = \mathbf{D}^{ep} = \mathbf{D} - \frac{\left(\mathbf{D} : \dfrac{\partial f_p}{\partial\,\boldsymbol{\sigma}}\right) \otimes \left(\dfrac{\partial f_y}{\partial\,\boldsymbol{\sigma}} : \mathbf{D}\right)}{\dfrac{\partial f_y}{\partial\,\boldsymbol{\sigma}} : \mathbf{D} : \dfrac{\partial f_p}{\partial\,\boldsymbol{\sigma}} + \dfrac{C}{f_p}(\dfrac{\partial f_y}{\partial\,\boldsymbol{\sigma}} : \boldsymbol{\eta}) - \gamma(\dfrac{\partial f_y}{\partial\,\boldsymbol{\sigma}} : \boldsymbol{\alpha}) + h} \tag{4.21}$$

where $\mathbf{D}^{ep}$, a non-symmetric matrix for the non-associated model, is called the *elasto-plastic tangent modulus*. Again, the above formulations can be simply derived for associated plasticity by replacing $f_p = f_y$ and in this case the $\mathbf{D}^{ep}$ matrix will be symmetric.

One of the most important consequences of the non-associated behaviour is that the instantaneous stiffness matrix in the resulting rate formulation is not symmetric. This is a very important issue in the numerical analysis including non-associated materials because non-symmetrical matrices, which reflect underlying physical instabilities, lead to numerical instabilities. The elasto-plastic tensor is a function of plastic multiplier dp, which is calculated by using the consistency condition, yield function f_y, plastic potential function f_p, and other state variables. In the general form of the non-associated model, because $f_p \neq f_y$, their interaction in the derivation of the elasto-plastic stiffness matrix is the reason for the non-symmetry.

4.2.3. Application to Hill's 1948 anisotropic function

In this section the proposed non-associated model is derived for the specific case of Hill's 1948 quadratic function. Hill's 1948 anisotropic yield criterion has the following form in the plane stress condition

$$2F = f_y - \sigma^Y = \tilde{f}_y - 1 = \sqrt{(G+H)\eta_x^2 + (F+H)\eta_y^2 - 2H\eta_x\eta_y + 2N\eta_{xy}^2} - 1 = 0 \qquad (4.22)$$

As before, σ^Y is the yield stress in the reference direction and F, G, H, and N are constant characteristics of the anisotropy and for this anisotropic yield function are simply defined as

$$2G = \frac{1}{(\sigma^Y_x)^2} - \frac{1}{(\sigma^Y_y)^2} + \frac{1}{(\sigma^Y_B)^2} \qquad (4.23a)$$

$$2F = \frac{1}{(\sigma^Y_y)^2} - \frac{1}{(\sigma^Y_x)^2} + \frac{1}{(\sigma^Y_B)^2} \qquad (4.23b)$$

$$2H = \frac{1}{(\sigma^Y_x)^2} + \frac{1}{(\sigma^Y_y)^2} - \frac{1}{(\sigma^Y_B)^2} \qquad (4.23c)$$

$$2N = \frac{1}{(\sigma^Y_{xy})^2} = \frac{1}{(2\sigma^Y_{45})^2} - \frac{1}{(\sigma^Y_B)^2} \qquad (4.23d)$$

where σ^Y_x, σ^Y_y, and σ^Y_{45} are tensile yield stresses in the rolling, transverse and diagonal (45 degree) directions, σ^Y_{xy} is the shear yield stress and σ^Y_B is the equi-biaxial yield stress. It should be noted that the stress transformation in 2D stress space was used to obtain Equation (4.23d). For convenience, function f_y in Equation (4.22) can be written in tensor form as follows

$$f_y = \left(\frac{3}{2}\eta^T \mathbf{M}\,\eta\right)^{\frac{1}{2}} \qquad (4.24)$$

where $\mathbf{M}$ is the yield function anisotropic tensor. The dimensionless coefficients of $\mathbf{M}$ are related to the coefficients of F, G, H, and N according to the following tensor

$$\mathbf{M} = \begin{bmatrix} M_1 + M_2 & -M_1 & 0 \\ -M_1 & M_1 + M_3 & 0 \\ 0 & 0 & 2M_4 \end{bmatrix}$$

where $M_1 = \dfrac{2}{3} H \sigma^{Y2}$, $M_2 = \dfrac{2}{3} G \sigma^{Y2}$, $M_3 = \dfrac{2}{3} F \sigma^{Y2}$, and $M_4 = \dfrac{2}{3} N \sigma^{Y2}$.

However, in the case of sheet metal forming the coefficients of anisotropy are generally defined based on r-value (also called Lankford coefficients), that is the ratio of width to thickness strain. By using the flow rule, taking the derivative of Equation (4.22), the increments of plastic strain components are

$$d\varepsilon^P{}_x = d\lambda \left[(G+H)\eta_x - H\eta_y \right] \tag{4.25a}$$
$$d\varepsilon^P{}_y = d\lambda \left[(H+F)\eta_y - H\eta_x \right] \tag{4.25b}$$
$$d\varepsilon^P{}_{xy} = d\lambda N\eta_{xy} \tag{4.25c}$$

By using the ratio of plastic strain increments to define the three r-values in different orientations relative to the rolling direction (r_0, r_{45}, and r_{90}), we have

$$r_0 = \frac{H}{G} \tag{4.26a}$$

$$r_{90} = \frac{H}{F} \tag{4.26b}$$

$$r_{45} = \frac{1}{2}\left(\frac{2N}{G+F} - 1 \right) \tag{4.26c}$$

Now, the plastic potential function can be defined in the form of Hill's 1948 anisotropic function as follows

$$f_p = \sqrt{(G' + H')\eta_x^2 + (F' + H')\eta_y^2 - 2H'\eta_x\eta_y + 2N'\eta_{xy}^2} \tag{4.27}$$

in which the new set of anisotropy coefficients, F', G', H', and N', are dimensionless functions of the plastic strain ratios defined as follows

$$G' = \frac{1}{1+r_0} \tag{4.28a}$$

$$H' = \frac{r_0}{1+r_0} \tag{4.28b}$$

$$F' = \frac{r_0}{(1+r_0)r_{90}} \tag{4.28c}$$

$$N' = \frac{(1+2r_{45})(r_0+r_{90})}{2(1+r_0)r_{90}} \tag{4.28d}$$

In order to remain consistent with the yield function in the computational procedure for numerical implementation the plastic potential function is also written in tensor form

$$f_p = \left(\frac{3}{2}\boldsymbol{\eta}^T \mathbf{P}\boldsymbol{\eta}\right)^{\frac{1}{2}} \tag{4.29}$$

where $\mathbf{P}$ is the plastic potential function anisotropic tensor and is defined as

$$\mathbf{P} = \begin{bmatrix} P_1 + P_2 & -P_1 & 0 \\ -P_1 & P_1 + P_3 & 0 \\ 0 & 0 & 2P_4 \end{bmatrix}$$

where $P_1 = \frac{2}{3}H'$, $P_2 = \frac{2}{3}G'$, $P_3 = \frac{2}{3}F'$, and $P_4 = \frac{2}{3}N'$.

So far, it can be seen that this model has the capability to describe both experimental aspects of anisotropy: yield stresses and plastic strain ratios. At the same time, the yield and plastic potential functions were defined in the simplest form: as quadratic functions based on Hill's (1948) theory, to reduce the experimental and computational costs. Using the nonlinear definition of backstress tensor for kinematic hardening, Equation (4.16), and also the yield and potential functions as defined by Equations (4.24) and (4.29), the plastic multiplier or the equivalent plastic strain is obtained by substituting the above-mentioned functionals into Equation (4.20)

$$dp = \frac{\frac{3}{2}\boldsymbol{\eta}^T \mathbf{M}\mathbf{D}d\varepsilon}{\left(\frac{3}{2}\right)^2 \frac{1}{f_p}\boldsymbol{\eta}^T \mathbf{M}\mathbf{D}\mathbf{P}\boldsymbol{\eta} + \frac{3}{2}\frac{C}{f_p}\boldsymbol{\eta}^T \mathbf{M}\boldsymbol{\eta} - \frac{3}{2}\gamma\boldsymbol{\eta}^T \mathbf{M}\boldsymbol{\alpha} + \sigma^Y h} \tag{4.30}$$

The elasto-plastic tangent modulus, also called *continuum tangent modulus*, can be determined for this case by implementing the current plastic multiplier

$$\frac{d\boldsymbol{\sigma}}{d\boldsymbol{\varepsilon}} = \mathbf{D}^{ep} = \mathbf{D} - \frac{\frac{3}{2}\boldsymbol{\eta}^T\,\mathbf{MD}\otimes\mathbf{DP}\,\boldsymbol{\eta}}{\frac{3}{2}\boldsymbol{\eta}^T\,\mathbf{MDP}\,\boldsymbol{\eta} + C\,\boldsymbol{\eta}^T\,\mathbf{M}\,\boldsymbol{\eta} - f_p\gamma\boldsymbol{\eta}^T\,\mathbf{M}\,\boldsymbol{\alpha} + \frac{2}{3}f_p\sigma^Y h}$$ (4.31)

In fact, this straightforward formulation might be used in the numerical procedure to integrate the stress over the time increment as *first-order forward Euler* integration scheme, also called the explicit stress integration because the stress at the end of time step t_{n+1} is calculated as a function of all variables at the beginning of time step t_n:

$$\boldsymbol{\sigma}_{n+1} = \boldsymbol{\sigma}_n + \mathbf{D}_n^{ep}\Delta\boldsymbol{\varepsilon}$$ (4.32)

However, it has been shown that this method has significant disadvantages when compared to the implicit integration scheme (Kojic, 2002), primarily because it is conditionally stable and only accurate for small time steps (Cardoso and Yoon, 2009). In the next section, the implicit stress integration procedure is developed based on the so-called return mapping algorithm.

4.2.4. Stress integration algorithm

From a numerical viewpoint the implementation of a constitutive model involves the integration of the state of the material at an integration point over a time increment during a nonlinear analysis. Different approaches have been proposed in order to numerically integrate the stress and other state variables over an increment. The radial return mapping method is no doubt the most popular integration method. The *radial return-mapping algorithm* is a particular case of elastic predictor-plastic corrector algorithms when a purely elastic *trial stress* is followed by a plastic corrector phase (Simo and Hughes, 1998). The purpose of the latter is to enforce consistency at the end of a step in a manner consistent with the prescribed flow rule. It is assumed that the stresses and all state variables are known at the beginning of the time step based on the converged values of the last time increment and the system is in the global equilibrium. In the following formulation, subscript n represents values at the beginning of the time step and subscript $n+1$ is omitted for the sake of simplicity. First, the trial stress is computed based on the gradient of the displacement field increment (or total strain increment tensor) over the time increment $[t_n, t_{n+1}]$

$$\varepsilon = \varepsilon_n + \Delta\varepsilon \tag{4.33}$$

$$\sigma^E = \mathbf{D}\left[\varepsilon - \varepsilon^P{}_n\right] \tag{4.34}$$

$$\sigma = \sigma^E - \mathbf{D}\Delta\varepsilon^P = \mathbf{D}\left[\varepsilon - \varepsilon^P{}_n - \Delta\varepsilon^P\right] \tag{4.35}$$

$$\alpha = \alpha_n + \Delta\alpha \tag{4.36}$$

$$\eta^E = \sigma^E - \alpha_n \tag{4.37}$$

It should be noted that the superscript E indicates that the trial stress is a purely elastic deformation, and is also called the *elastic predictor*. This trial stress is theoretically outside the yield surface, but based on the following procedure, it will be forced to satisfy the yield condition. By using the flow rule and kinematic hardening definition the increment of the plastic strain tensor and the backstress tensor are written as

$$\Delta\varepsilon^P = \frac{3}{2}\Delta p\,\frac{\mathbf{P}\eta}{f_p} \tag{4.38}$$

$$\alpha = \frac{1}{1+\gamma\Delta p}\left(\alpha_n + \frac{C\Delta p}{f_p}\eta\right) \tag{4.39}$$

Substituting the above relations into Equations (4.35-4.37) and knowing that $\eta = \sigma - \alpha$, we have

$$\eta = \eta^E - \frac{3}{2}\frac{\Delta p}{f_p}\mathbf{DP}\,\eta - \frac{1}{1+\gamma\Delta p}\frac{C\Delta p}{f_p}\eta + \frac{\gamma\Delta p}{1+\gamma\Delta p}\alpha_n \tag{4.40}$$

Rearranging the formulation

$$\eta = \frac{1}{1+\dfrac{C}{1+\gamma\Delta p}\dfrac{\Delta p}{f_p}}\,\mathbf{\Xi D}^{-1}\left[\eta^E + \frac{\gamma\Delta p}{1+\gamma\Delta p}\alpha_n\right] \tag{4.41}$$

where $\mathbf{\Xi,}$ called modified or algorithmic elastic tangent matrix, is written as

$$\Xi = \left[\mathbf{D}^{-1} + \frac{\dfrac{3}{2}\dfrac{\varDelta p}{f_p}}{1 + \dfrac{C}{1+\gamma\varDelta p}\dfrac{\varDelta p}{f_p}} \mathbf{P} \right]^{-1}$$

(4.42)

Then, $\boldsymbol{\eta}$ from Equation (4.41) is substituted into the yield function

$$\left(\frac{3}{2}\boldsymbol{\eta}^{T}\,\mathbf{M}\boldsymbol{\eta}\right)^{\frac{1}{2}} - \sigma^{Y}\left(p + \varDelta p\right) = 0$$

(4.43)

As a result, this is a closed-form nonlinear function of $\varDelta p$ that might be solved by any efficient numerical method (typically one of Newton's methods). In short, in each increment the *Newton iteration method* is used to solve the yield equation (for the updated values) to find the governing parameter $\varDelta p$ that is used as a reference for the increment. Thus, the derivative of the yield function is needed in the consistency condition to get the convergence for the final value of the governing parameter. Once the converged value of the effective plastic strain rate is known, Equation (4.41) is used to update tensor $\boldsymbol{\eta}$, and Equation (4.39) is used to update the backstress tensor. Finally, the plastic strain increment and stress tensors are obtained. To preserve the quadratic rate of asymptotic convergence for the *Newton-Raphson* method to solve the global finite element equilibrium equation, it is necessary to derive the *consistent elasto-plastic tangent modulus* (Simo and Hughes, 1998). For the described constitutive model, the consistent or algorithmic tangent modulus was derived using the above mentioned return-mapping algorithm

$$\frac{d\varDelta\boldsymbol{\sigma}}{d\varDelta\boldsymbol{\varepsilon}} = \widetilde{\mathbf{D}}^{ep} = \Xi - \frac{\dfrac{3}{2}\boldsymbol{\eta}^{T}\,\mathbf{M}\Xi\otimes\Xi\mathbf{P}\boldsymbol{\eta}}{\dfrac{3}{2}\boldsymbol{\eta}^{T}\,\mathbf{M}.\Xi.\mathbf{P}\boldsymbol{\eta}+C\boldsymbol{\eta}^{T}\,\mathbf{M}\boldsymbol{\eta}-f_{p}\gamma\boldsymbol{\eta}^{T}\,\mathbf{M}\boldsymbol{\alpha}+\dfrac{2}{3}f_{p}\sigma^{Y}h}$$

(4.44)

Figure 4.1 shows a schematic representation of the return mapping algorithm used for the non-associated model with mixed hardening (both translation and expansion of the yield and potential surfaces are shown). The material model presented in this section was implemented in a user-defined material subroutine (UMAT) for ABAQUS and used to simulate different sheet metal forming processes.
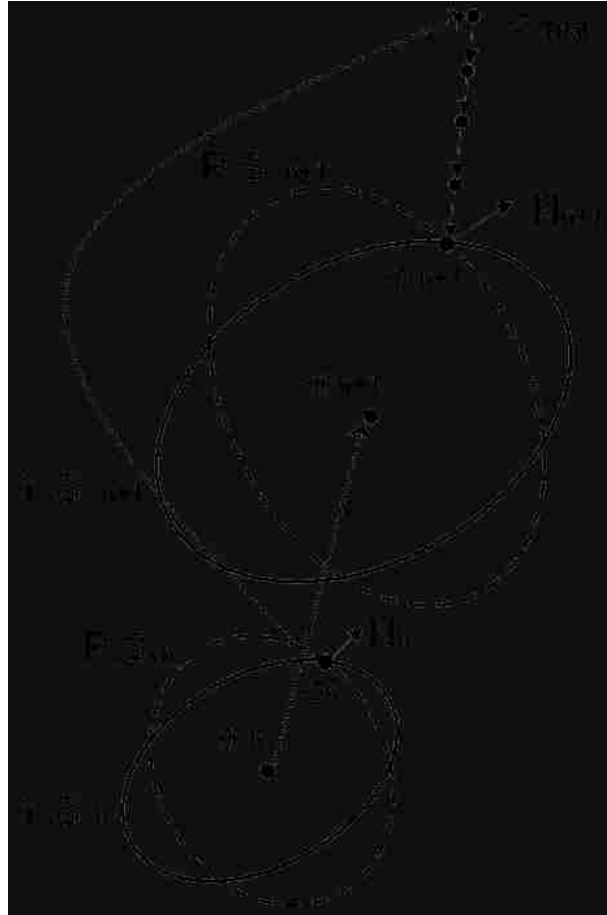
Figure 4.1. Schematic diagram showing the return mapping algorithm for the non-associated model in the 2-D stress space (Y.S.: Yield Surface, P.S.: Potential Surface, N: Normal to the Potential Surface).

4.3. Material parameters and model verification

The most common material model that is used in the simulation of sheet metal forming is Hill's 1948 anisotropic yield criterion, in which the anisotropic coefficients are defined by r-values with associated flow rule and isotropic hardening. The material model used in this investigation offers two different improvements compared to models used more commonly. Firstly, the anisotropic behaviour was modeled with Hill's quadratic function but took advantage of the NAFR: this enabled us to consider both the experimental r-values and yield stresses. Secondly, the hardening was defined by the mixed isotropic-nonlinear kinematic hardening model (NKH) which is simpler to implement than advanced single or multi-surface or multiple backstress kinematic models and sufficient to replicate the main aspects of the cyclic behaviour.

4.3.1. Cyclic hardening identification

Simple shear tests were carried out to obtain the cyclic stress-strain behaviour of three different steel sheets (DP600, AKDQ and HSLA). The explanations were given in the previous chapter (section 3.3) and also more details about the test might be found in (Thuillier and Manach, 2009). The exact same procedure explained in the previous chapter (section 3.3) was used to obtain the mixed hardening model parameters. The cyclic stress-strain data obtained experimentally were compared with those obtained by two different hardening models (Isotropic Hardening: IH and mixed Nonlinear Kinematic Hardening: NKH) and were shown in Figure 3.2 (for brevity they are not repeated here). It was evident that the NKH model can reproduce the cyclic effects, such as the transient Bauschinger effect, better than the IH model. Also, a summary of the mixed hardening parameters for the sheet materials used in the simulations was shown in Table 3.1.

4.3.2. Anisotropic yield and flow behaviour

In order to determine the anisotropic coefficients of the present NAFR model, both r-values and yield stresses are required at three different orientations with respect to the rolling direction (0˚, 45˚, and 90˚). Quasi-static tensile tests (ASTM E8 standard test method) were carried out at each of these orientations to measure these properties (Shi and Huang, 2005; Brem et al., 2005). Furthermore, the equibiaxial yield stress or the shear yield stress is also required to fully determine the parameters in the yield function and both types of tests were carried out for verification purposes. The shear yield stress was obtained from the results of the shear tests described earlier and the yield stress in equibiaxial tension was obtained by carrying out hydraulic bulge tests. Table 4.1 shows the summary of the anisotropic coefficients of different sheet materials used in the Numisheet 05 BM#3.

Table 4.1. Summary of the sheet materials anisotropic coefficients.

Material	Yield Function Coefficients				Potential Function Coefficients			
	F	G	H	N	F'	G'	H'	N'
AA6022	0.632	0.496	0.504	1.585	0.697	0.493	0.507	1.228
AKDQ	0.329	0.419	0.581	1.776	0.313	0.393	0.607	1.417
HSLA	0.417	0.567	0.433	1.983	0.363	0.633	0.367	1.658
DP600	0.438	0.465	0.535	1.822	0.465	0.549	0.451	1.435

As discussed earlier, fully anisotropic plastic behaviour with a NAFR results in an accurate simulation of the r-value distribution function and of both the uniaxial and equibiaxial yield

behaviour. When using Hill's 1948 yield function with the AFR, only one set of parameters, i.e. r-values or yield stresses, can be used at the same time. In this case, the in-plane distributions of the yield stresses and r-values can be determined with the following relationships

$$\sigma_\theta = \frac{\sigma_0}{\sqrt{(G+H)\,Cos^4\theta + (F+H)\,Sin^4\theta + (2N-2H)\,Sin^2\theta\,Cos^2\theta}} \tag{4.45}$$

$$r_\theta = \frac{H' + (2N' - F' - G' - 4H')\,Sin^2\theta\,Cos^2\theta}{F'\,Sin^2\theta + G'\,Cos^2\theta} \tag{4.46}$$

where θ is the angle of the tensile specimen with respect to the rolling direction. It should be noted that the anisotropic coefficients used in Equations (4.45) and (4.46) are different for yield stress and r-value functions. Distributions of the yield stress ratio (normalized with respect to the yield stress in the rolling direction, σ_θ/σ_0) predicted by NAFR and AFR models for different materials are shown in Figure 4.2. The AFR model is not able to predict the yield stress as well as the NAFR because the anisotropic coefficients were determined with the r-values rather than the yield stresses. In Figure 4.2d, the in-plane yield stress data for the AA6022-T43 sheet material were provided (Brem et al., 2005) in the increments of 15° from the RD (0°) to the TD (90°). And it can be seen that the prediction of yield stress with the NAFR is also in good agreement with the experimental values that were not used to define the function. Unfortunately, the additional yield stress data were not available for the other materials at the time of publication. However, it is expected that the same trend would be observed for the three grades of steel.
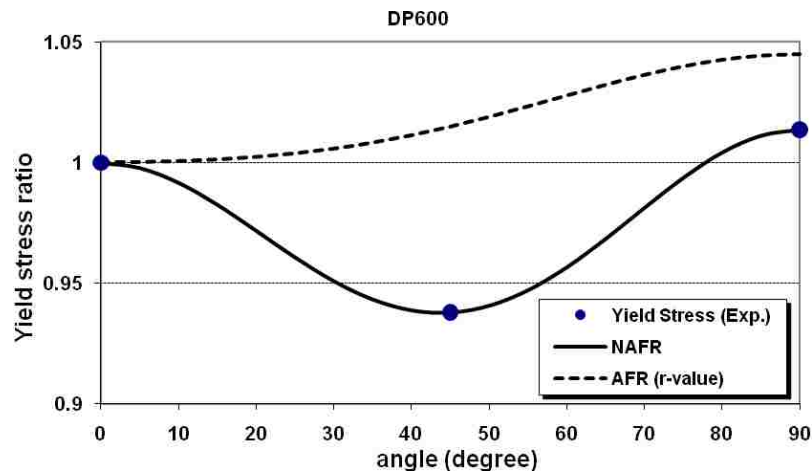
(4.2. a)
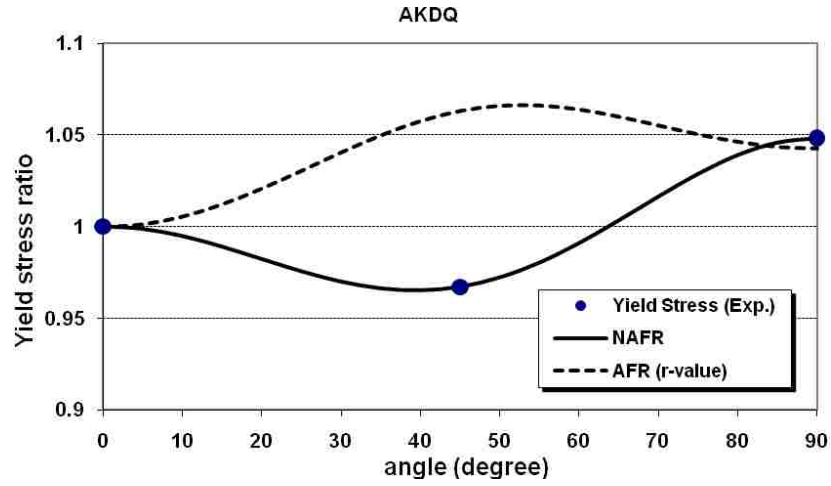
(b)
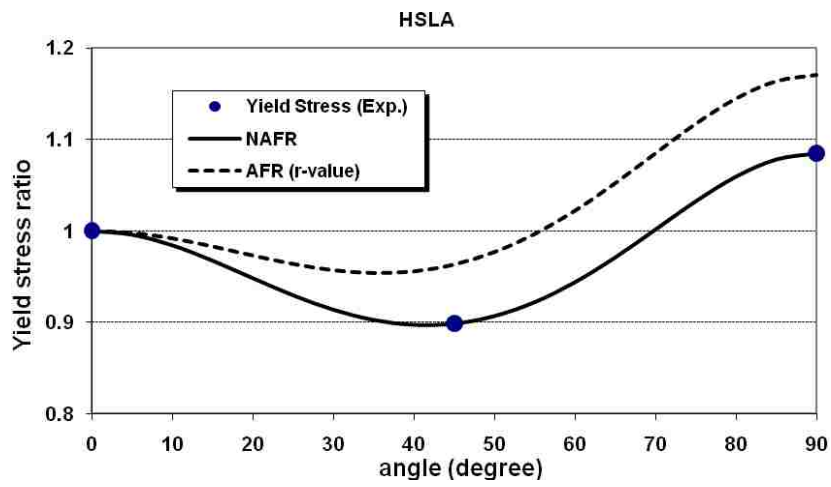
(c)
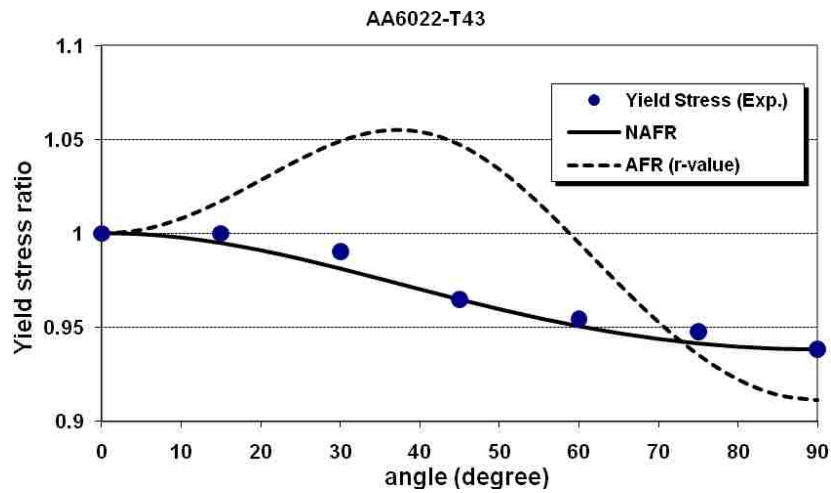
(d)

Figure 4.2. Distribution of the yield stresses at different angles to the rolling direction predicted by NAFR and AFR models for: (a) DP600, (b) AKDQ, (c) HSLA, and (d) AA6022-T43.

Distributions of the r-values for different materials are also shown in Figure 4.3. As would be expected, both the NAFR and AFR models exactly predict the three experimental r-values that were used to define the anisotropic coefficients in the models. Again, for the AA6022-T43 additional data points were available for every 15° and are shown in Figure 4.3d. Similar to the yield stresses, a close agreement is seen between the distribution curve and the experimental r-value data points.

(4.3. a)

(4.3. b)
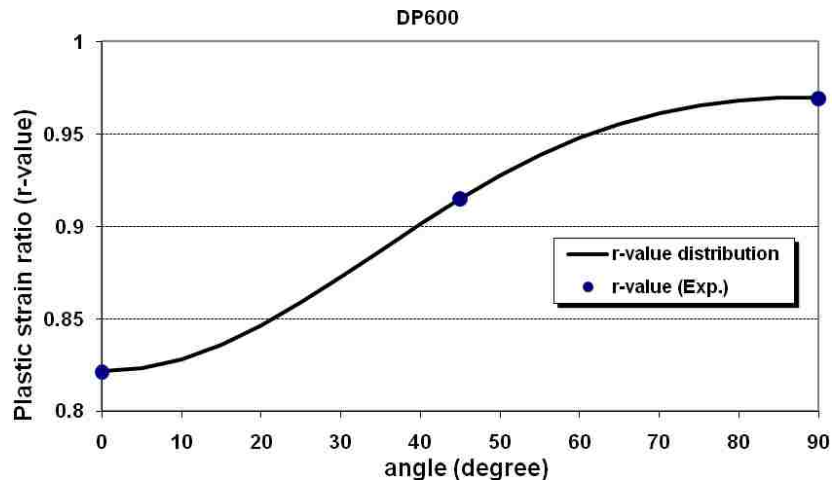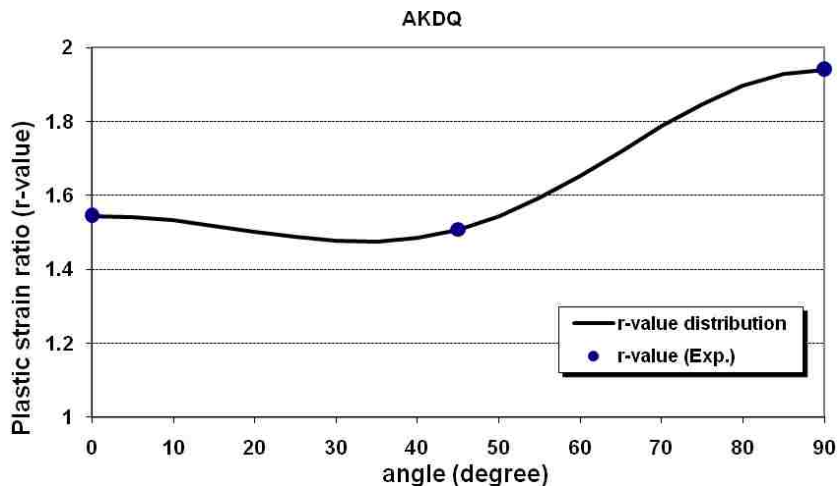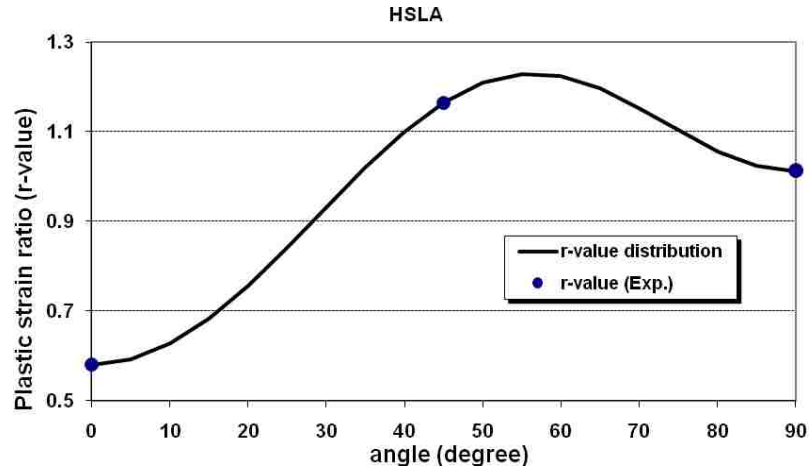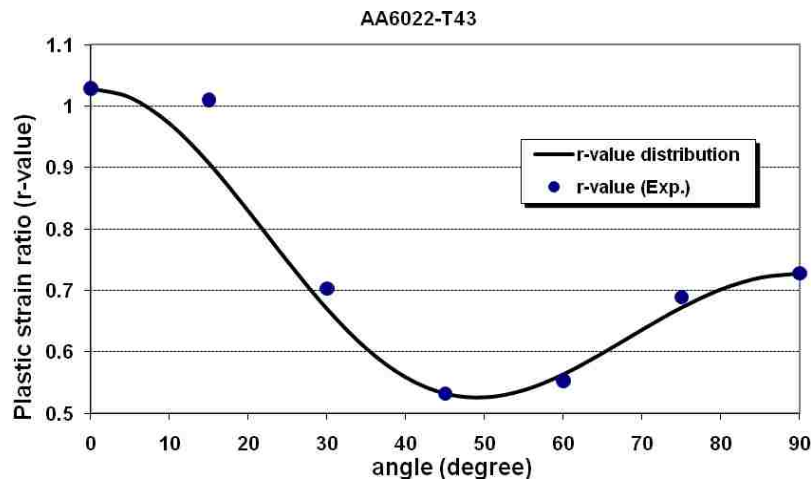
Figure 4.3. Distribution of the r-values at different angles to the rolling direction for: (a) DP600, (b) AKDQ, (c) HSLA, and (d) AA6022-T43.

For a better understanding of the difference between yield and plastic potential functions for the above materials the yield and potential loci were derived and plotted in 2-dimensional principal stress space. To consider the effect of the shear term on these surfaces the yield and potential loci were plotted for constant levels of shear stress. Figure 4.4 shows the yield and potential surfaces at 0, 0.1, and 0.2 levels of normalized shear stress with respect to the uniaxial yield stress. As can be seen, the difference between the two loci is not very significant for any of these four materials. The reason may be explained by the small difference between yield stress and r-value anisotropy in these materials. Another observation is that for all materials the difference between the two surfaces is more significant as the value of the shear stress increases, because the shear anisotropy coefficient is different depending on whether it is defined with r-values or with yield stresses. This difference between the shear coefficients will be explained and shown in the next section.
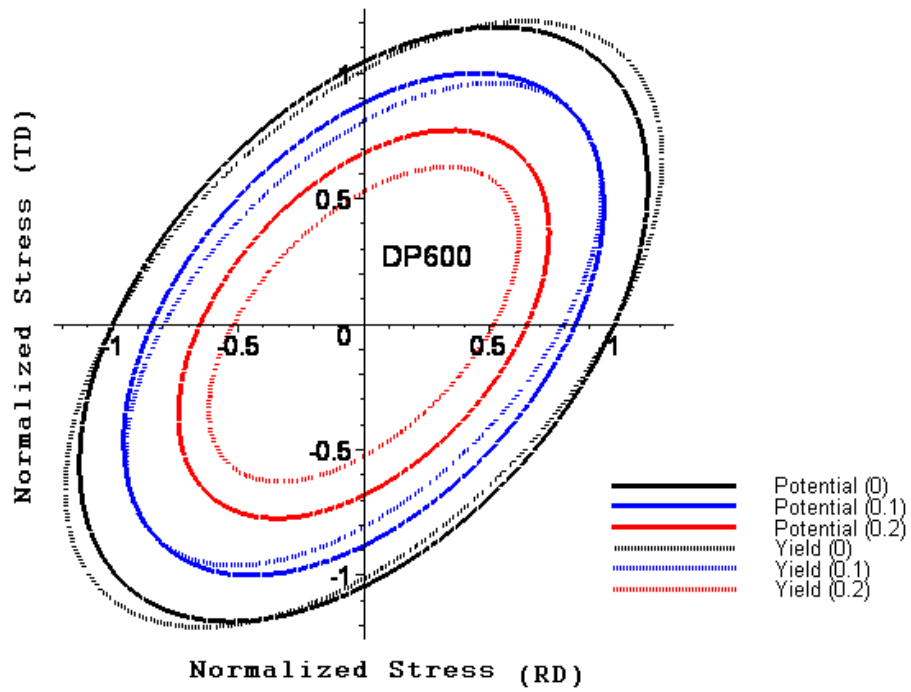
(4.4. a)
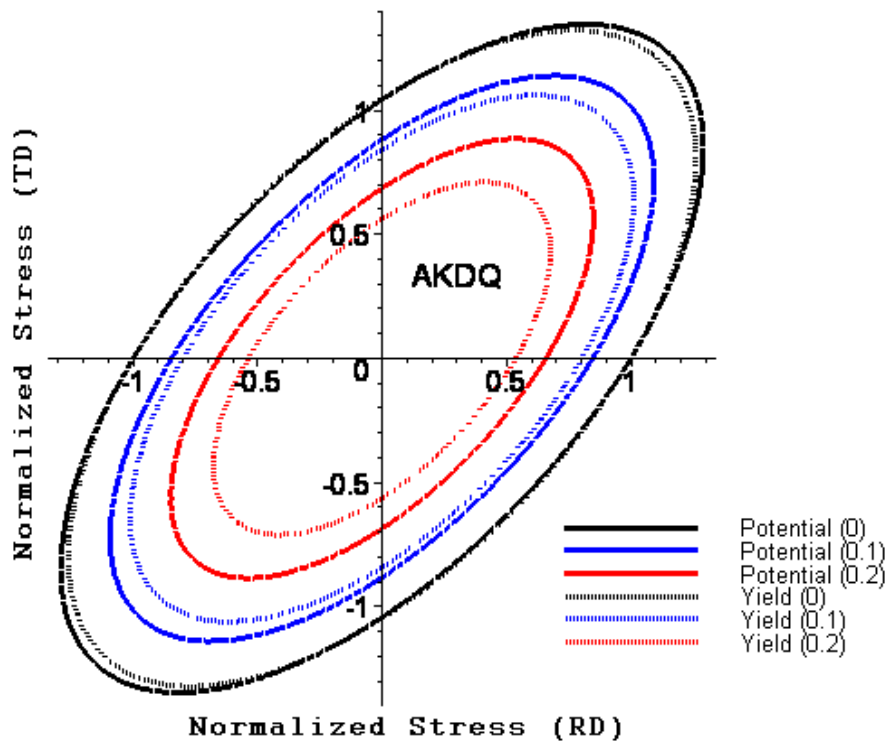
(4.4. b)
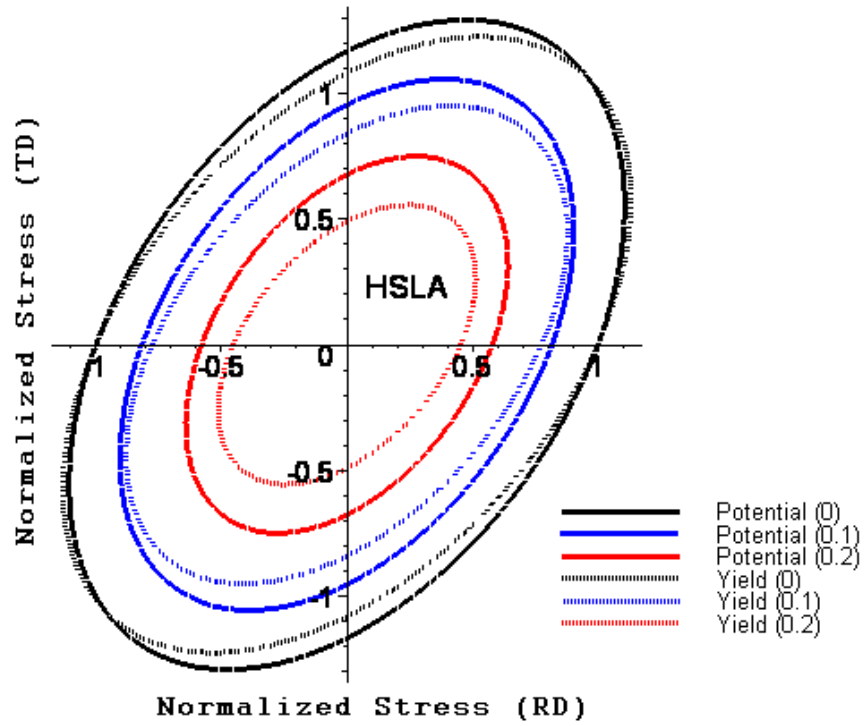
(c)
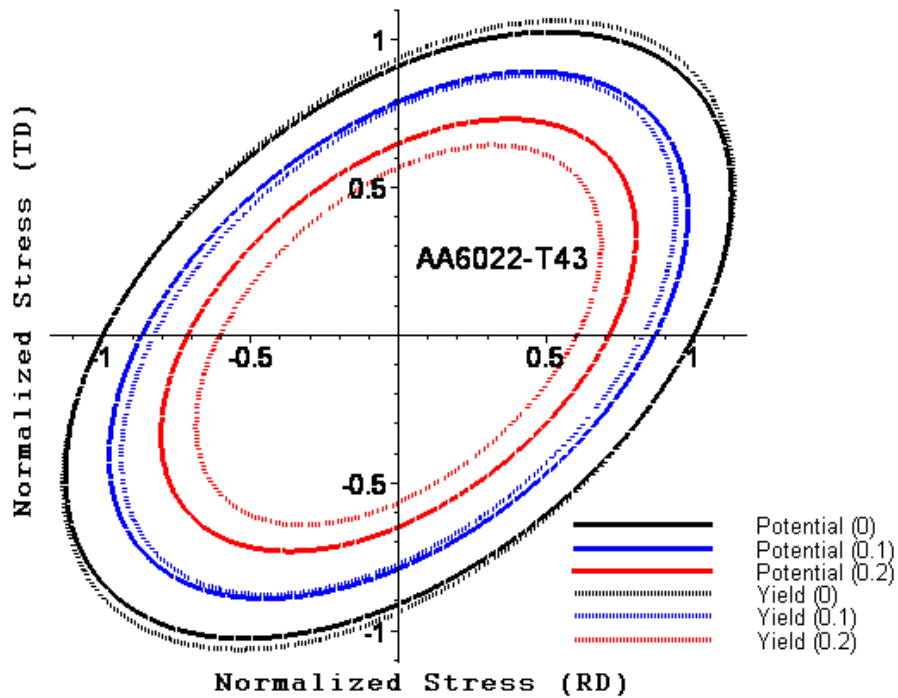
(d)

Figure 4.4. Yield and potential surfaces at different constant levels of normalized shear stress with respect to the uniaxial yield stress for: (a) DP600, (b) AKDQ, (c) HSLA, and (d) AA6022-T43.

4.3.3. Equibiaxial and shear stress predictions

One of the weaknesses of using r-values to define Hill's 1948 anisotropic coefficients is the potential for an inaccurate prediction of the equibiaxial and shear stress-strain curves when work-hardening is determined by the uniaxial stress-strain curve. When the NAFR model is used, both the r-value distribution and the stress-strain curves are satisfied at the same time. The hydraulic bulge test was also performed to measure the balanced biaxial flow behaviour. The details of the experimental procedure and tool geometry can be found in Young et al. (1981). Duplicate hydraulic bulge tests were carried out for each sheet material. The tests were conducted at a constant true strain rate = 0.005 s-1 in order to maintain a stable response under quasi-static conditions. The extensometer was oriented at 45° to the rolling direction of the sheet, which is standard test condition. As reported by Young et al. (1981), the measurement of the radius and strain from a hydraulic bulging specimen shows a slight directional discrepancy in biaxial stress-strain curves. Planar anisotropy and insufficient geometric data during the bulge test may cause this discrepancy. Another possible reason that the accuracy of the measurement may be affected is that the thickness strain distribution at the top of a bulging specimen is calculated from an extensometer based on the "averaged" radius of the bulging specimen. Although the mechanical measuring system is easy to construct and maintain, and has shown robustness in the hydraulic bulge experiments, more recent optical measuring devices for hydraulic bulge tests have been successfully developed and reported by Dziallach et al. (2007).

Both the NAFR and AFR models were used to predict the equibiaxial stress-strain curve knowing the uniaxial curve and the corresponding yield function. Once again, the r-values were used to define the anisotropic coefficients for the AFR function while the yield stress ratios were used to define the NAFR coefficients. Comparison of the experimental equibiaxial curve with the predicted curves by both NAFR and AFR models for different materials is shown in Figure 4.5. It can be seen that the appropriate extrapolation was applied for each material to extend the uniaxial curves to the same level as the equibiaxial curves. In the case of the DP600 sheet material, the NAFR model predicts the equibiaxial stress quite accurately compared to the AFR model. There is only a minor discrepancy during the initial plastic strain region (0-0.25) where the NAFR model slightly overestimates the biaxial stress. In the case of the AKDQ material, the predicted equibiaxial stress-strain curve also correlates quite well with the experimental curve. It is noticeable that in this case, the difference between the experimental uniaxial and biaxial curves is significant from the onset of yielding. All four curves (uniaxial and biaxial experimental curves predicted by the NAFR and AFR models) are practically coincident for the HSLA steel. This means the degree of anisotropy in the biaxial and uniaxial states is very small for this material.

For the aluminum alloy AA6022-T43, the biaxial stress-strain curves predicted with the NAFR and AFR models are rather similar, however the curve predicted with the NAFR is closer to the experimental one. It is worth mentioning that the normalized yield stress ratios (shown in Figure 4.2) were determined based on the minimum plastic work to fracture calculated from each of the four stress-strain curves along the 0, 45, 90 and biaxial directions (Yoon and Barlat, 2006). This was done because the initial yield point, especially for the biaxial bulge test, is not clear and sometimes shows unstable behaviour around the initial yield. By taking the stress-ratios away from the initial yielding point, it is possible to obtain stable stress ratios. Also, hardening-dependent responses such as earing during cup drawing are more accurately predicted. Therefore, in Figure 4.5, the biaxial predictions at initial yield are not quite as accurate as they are after some hardening. Nevertheless, yield stress ratios along the 0, 45, 90 and biaxial directions were all considered for NAFR, but only the r-values at 0, 45 and 90 degrees were considered for AFR. Therefore, NAFR gives a better prediction than AFR in the biaxial responses.

(4.5. a)

107
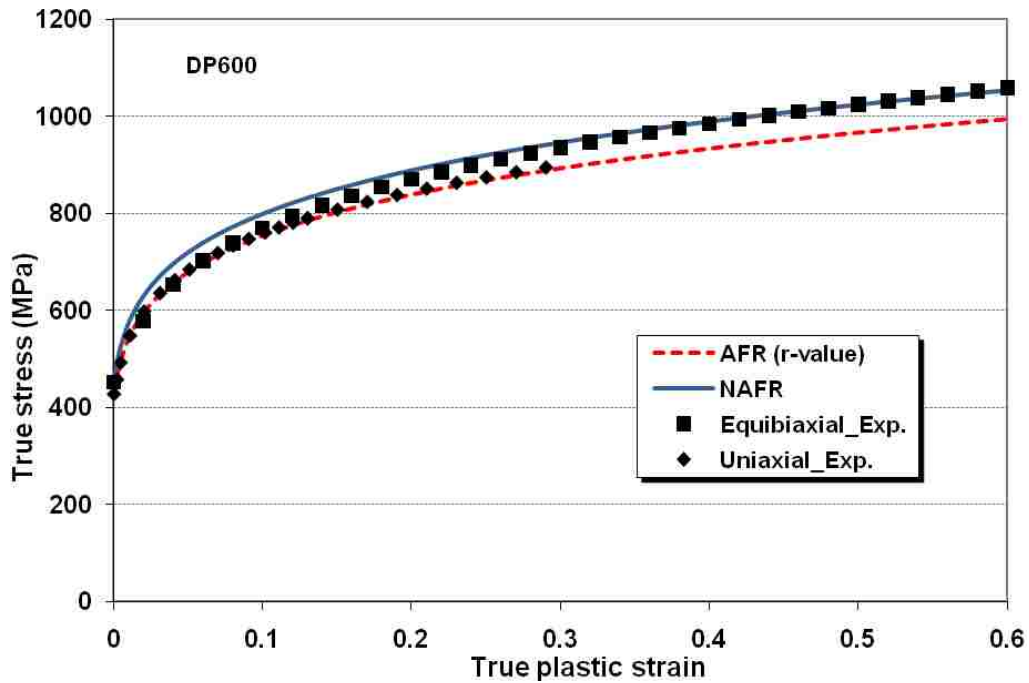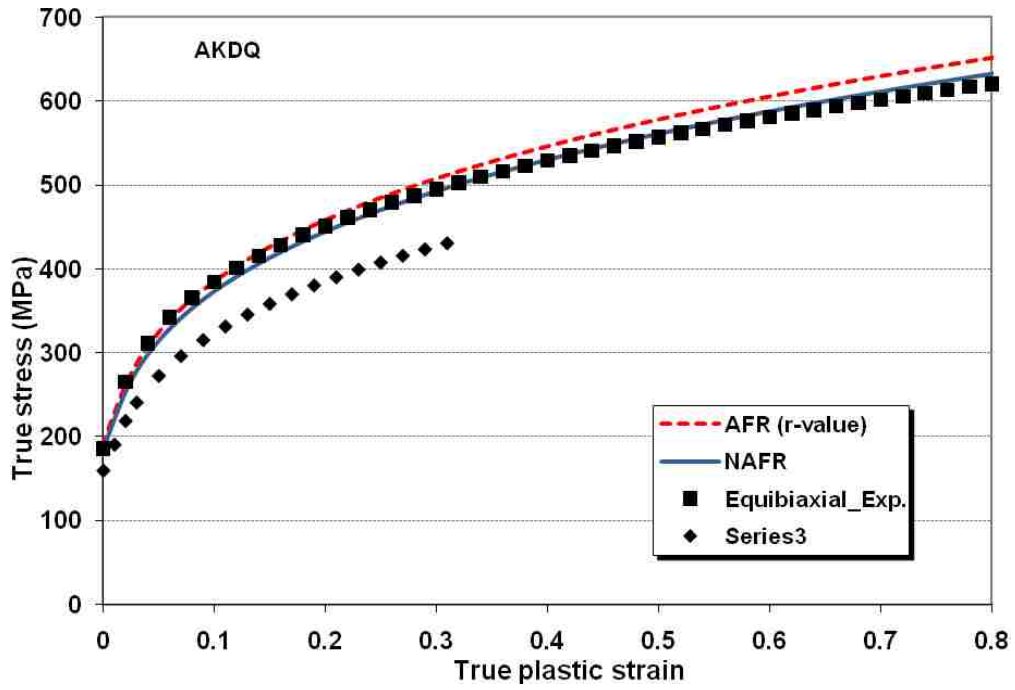
(4.5. b)
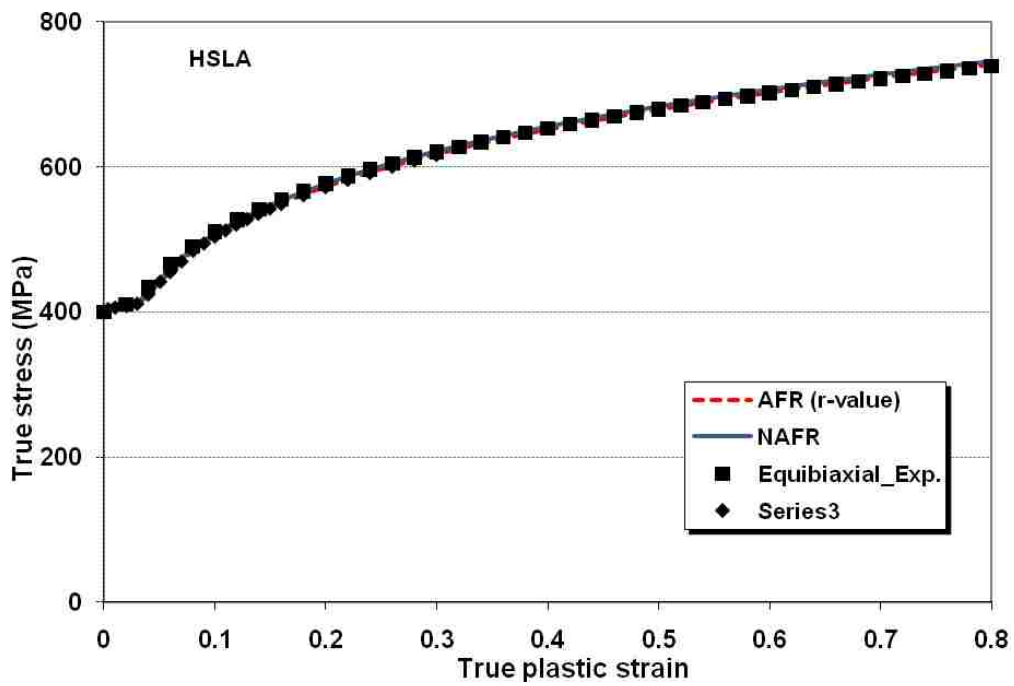
(4.5. c)
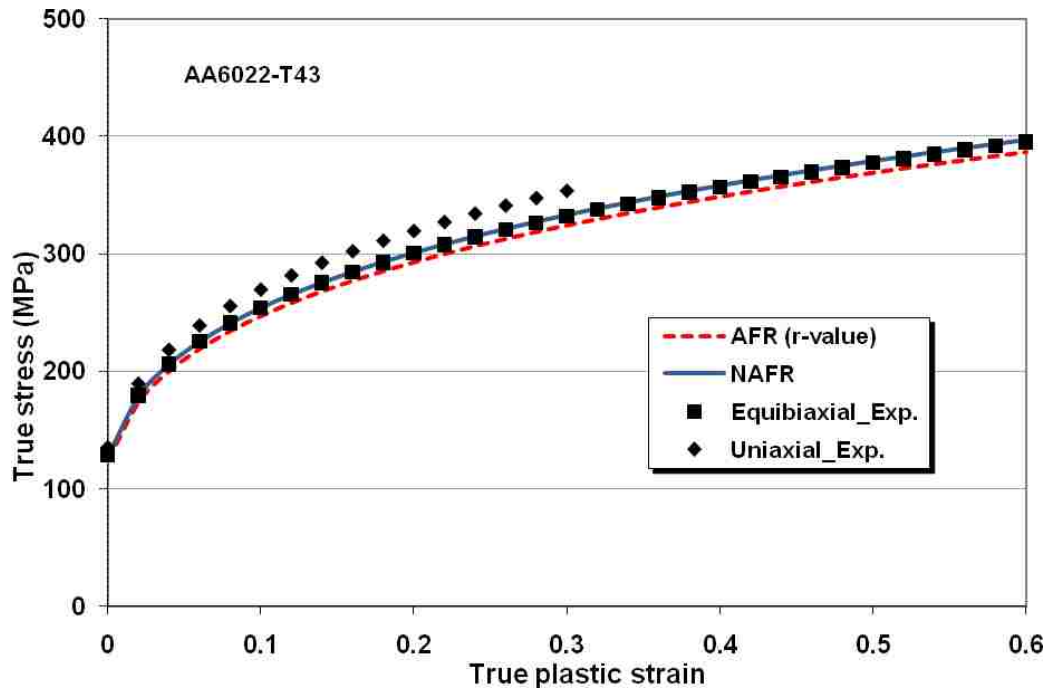
(d)

Figure 4.5. Comparison between the experimental equibiaxial curve and those predicted with the NAFR and AFR models for: (a) DP600, (b) AKDQ, (c) HSLA, and (d) AA6022-T43.

Similarly, the shear stress-strain behaviour predicted by the NAFR and AFR models was compared to the experimental shear stress-strain curve. The testing procedure for the monotonic simple shear test is the same as that described in section 3.4. Figure 4.6 shows the comparison of the experimental shear stress-strain curve with the curves predicted with NAFR and AFR models for three steel sheets. Unfortunately, the simple shear test was not carried out for the aluminum alloy, since the aluminum sheet was not available at the time. The uniaxial tensile test result is also shown in this figure for comparison. Obviously, the simple shear curves predicted with the AFR model overestimate the experiments for all materials. But for all three grades of steel the curves predicted by NAFR model are in excellent agreement with the experimental curves. One interesting point in the case of the DP600 and AKDQ steels is the slight difference in the initial yielding region between the experimental and predicted simple shear curves based on the uniaxial tensile curve. This small discrepancy may be due to some basic differences between yielding behaviour when loaded in tension and in simple shear. The yield point obtained from the shear test is not as sharp as for the tensile test, and the work hardening behaviour sometimes varies for these two different states. Hußnatter and Merklein, (2008) have proposed that these slight differences in the initial yielding behaviour may be explained by the fact that different slip systems are activated in the tensile test and in the shear test.
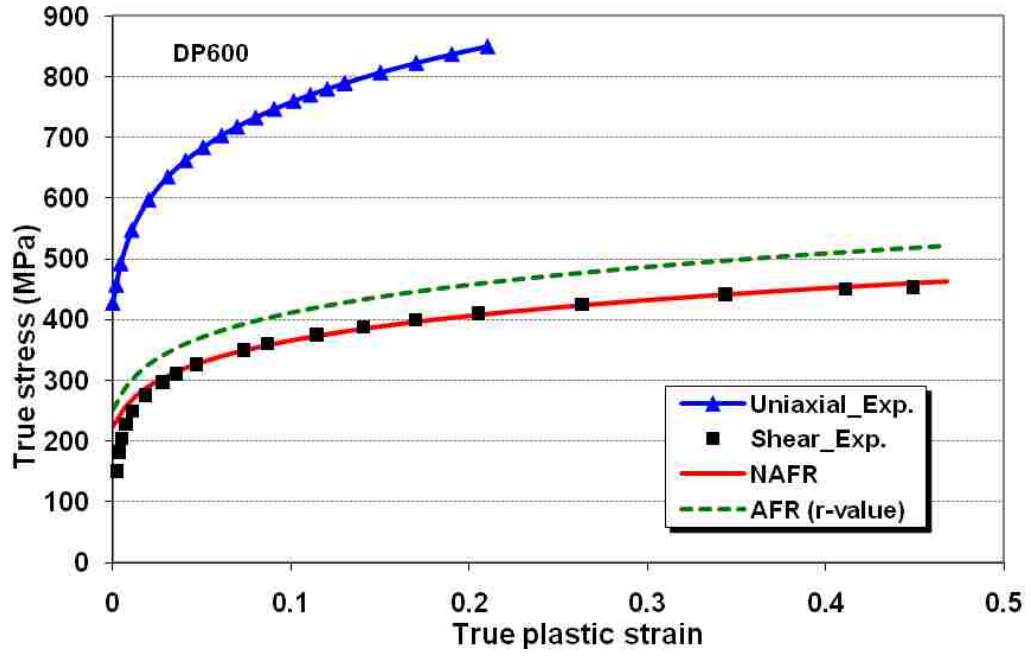
(4.6. a)
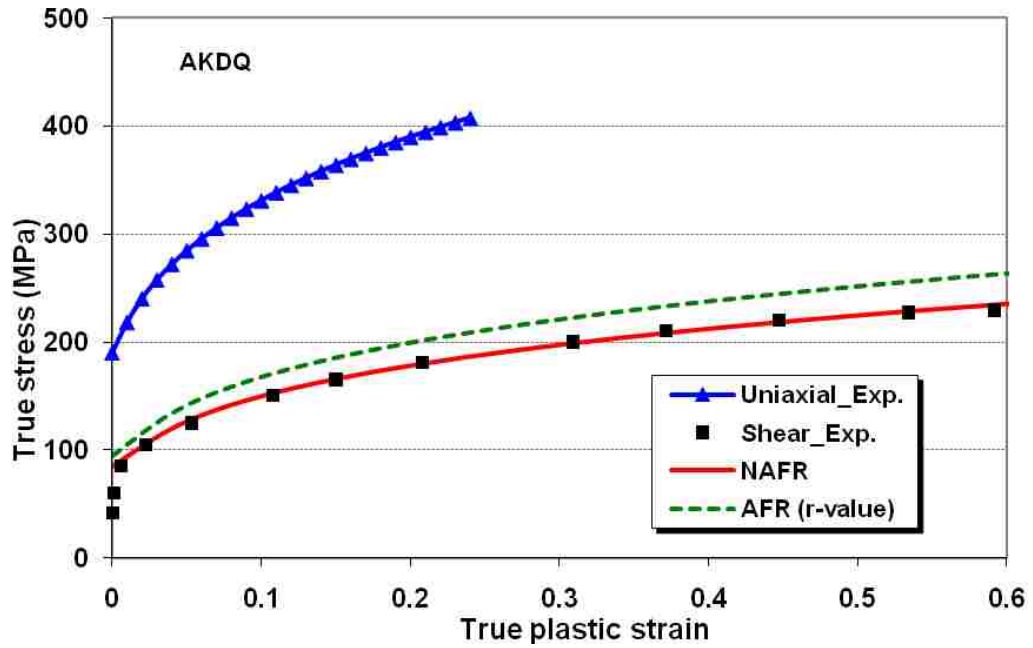
(4.6. b)
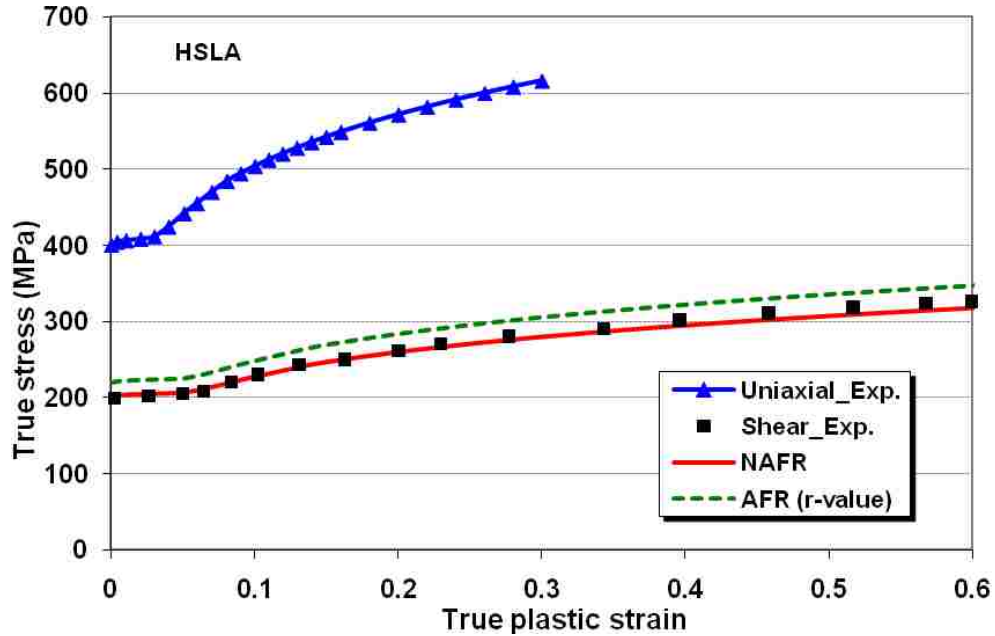
(c)

Figure 4.6. Comparison between the experimental shear stress-strain curve and those predicted with the NAFR and AFR models for: (a) DP600, (b) AKDQ, and (c) HSLA.

4.4. Simulation results and discussion

Two different sheet metal forming processes were simulated using the implemented user-defined subroutine material to evaluate the different aspects of this non-associated model. A cylindrical cup drawing process was simulated to measure the ability of the model to predict the earing profile and the effects of sheet metal anisotropy, and springback prediction of a channel draw process (with drawbead) was simulated to assess the effect of the hardening model.

4.4.1. Cylindrical cup drawing

The cup drawing test was performed with a 2090-T3 aluminum alloy sheet. The specific dimensions of the tools and process parameters were given in Yoon et al. (2000), and the material characteristic coefficients for this alloy were provided in this same paper. In order to minimize the influence of the blank-holder force and friction in this verification, a cup was formed with a minimum blank-holder force, sufficient to prevent wrinkling under well-lubricated conditions. This cylindrical cup drawing process was simulated in order to verify the ability of the non-associated model to predict more aspects of anisotropy in sheet metal forming simulations. A shell element formulation with reduced integration mode was used to model the blank and due to symmetry only one quarter of the blank was simulated.

111

The earing profile (cup height after drawing) was simulated using three different material models: Hill's 48 (r-value), Hill's 48 (yield stresses), and the NAFR model. In the first two models the Hill's 1948 yield function and associated flow rule is used where Lankford's coefficients and yield stresses are used to define the anisotropic parameters, respectively.

In Figure 4.7, the measured and predicted cup height profiles are compared. Because of the orthotropic anisotropy only the cup height profile between 0 and 90 degree is illustrated here. Based on this figure, the AFR (r-value) model overestimates the predicted earing profile amplitude while the AFR (yield stresses) model underestimates it. The earing profile predicted by the NAFR model is in better agreement with the experimental values. Both earing amplitude and location of ears are affected by the two aspects of anisotropy i.e. yield stresses and r-values, therefore the NAFR model is capable of better prediction of earing compared to the AFR model in which only one aspect can be considered. However, there is still a significant discrepancy between the experimental profile and the one predicted by the NAFR model. In this case, the use of non-quadratic yield and potential functions may improve the results but the expense of the numerical procedure and simulation should be considered.
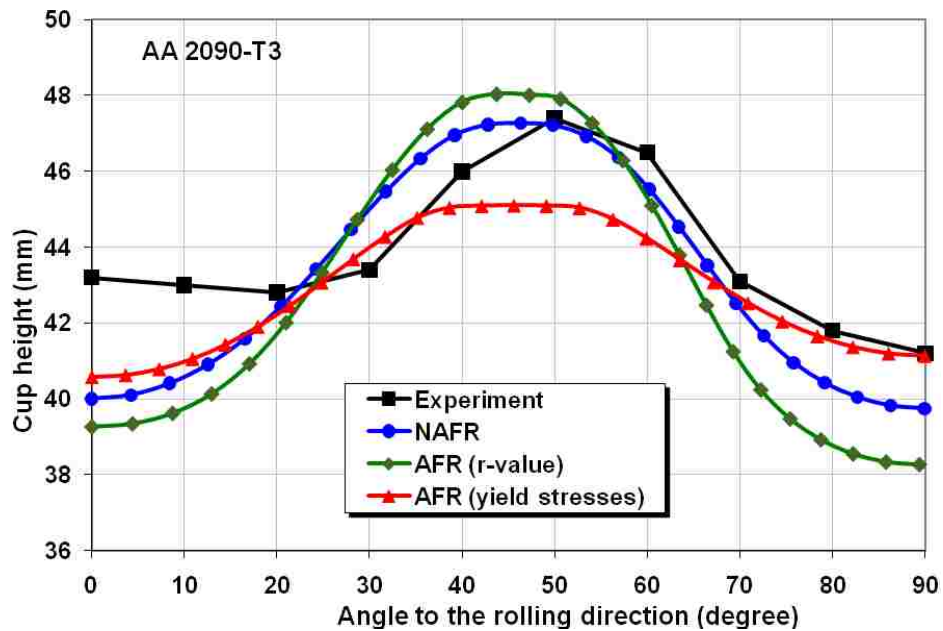
Figure 4.7. Comparison of the experimental earing profile and the profiles predicted with the NAFR and AFR models.

The thickness strain distribution along the cup height in both rolling and transverse directions predicted with the AFR and NAFR models is compared with experimentally measured values in

Figure 4.8. As it is seen in both directions (RD and TD) the NAFR model results lie between the AFR (r-value) and AFR (yield stresses) results. Furthermore, the NAFR model improved the simulations results compared to the AFR models. It is obvious that the thickness strain in the transverse direction is more significant than that in the rolling direction. Not only were the results obtained from the NAFR model improved in both cases, but in the transverse direction the strain distribution predicted by this model is practically the same as the experimental value.
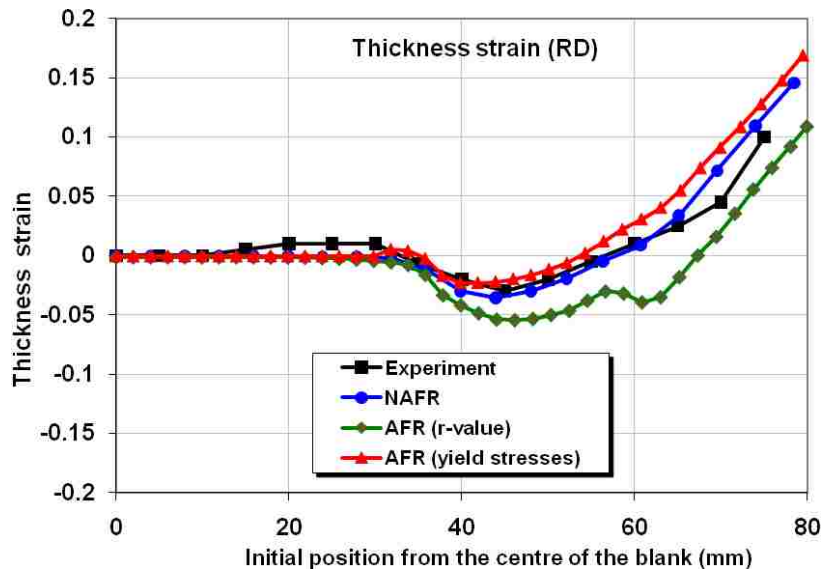
(a)
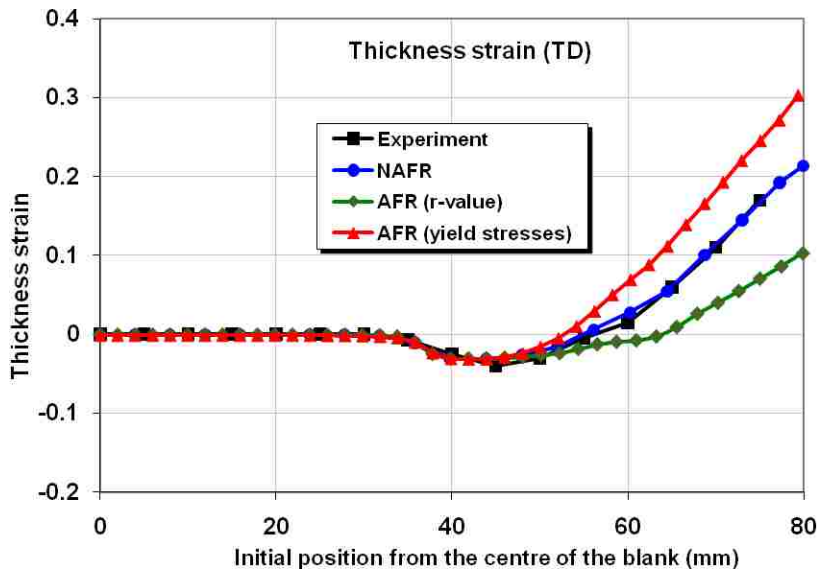
(b)

Figure 4.8. Comparison of the experimental and predicted thickness strain along the rolling direction (a) and transverse direction (b) with both NAFR and AFR models.

4.4.2. Springback of a channel draw process with drawbead

Both the forming and subsequent springback stages of the Numisheet'05 Benchmark #3 were simulated for different drawbead penetrations using the commercial code ABAQUS. Four different sheet materials (AKDQ, HSLA, DP600 and AA6022-T43) were used to evaluate the ability of material models to predict the springback in the drawn channel section. This benchmark considers four different drawbead penetrations: 25, 50, 75 and 100%, but for the sake of brevity, only the results for the deepest and shallowest penetrations will be presented: (i.e. 25 & 75% for DP600 and 25 & 100% for the other materials). The sidewall curl after springback was recorded for each sheet material and for each prestrain condition, using a 2D laser scanner (LaserQC™). Further technical details about the experimental procedure, process parameters and tooling may be found in the section 3.4 of the previous chapter or the following references: (Green, 2005; and Stoughton et al., 2005).

Plane stress shell elements with reduced integration mode were used to model the sheet (denoted by S4R in ABAQUS) where 19 integration points were used through thickness to thoroughly simulate the cyclic stresses caused by bending-unbending deformation in the drawbead and die shoulder. Only one half of the channel section was modeled due to the symmetry. A study of mesh sensitivity was conducted for different combinations of materials, penetrations, and constitutive models to find the best mesh in each case. The friction coefficient was assumed to be 0.1 for all steels and 0.12 for the aluminum alloy, and the classical Coulomb friction law with penalty algorithm was used as the contact model. Finally, the explicit-implicit scheme was used for forming and springback stages, respectively. Therefore, user-defined material subroutines were developed for both explicit and implicit time integration schemes using the above non-associated model. A series of 16 simulations, each including separate explicit and implicit stages, were carried out: 8 with isotropic hardening (NAFR-IH) and 8 with combined isotropic-nonlinear kinematic hardening (NAFR-NKH). It was observed, both experimentally and numerically, that the amount of springback decreased when the drawbead penetration depth increased. Indeed, deeper drawbead penetrations result in higher restraining force so that, the sheet metal is stretched to a greater extent in the sidewall region after passing over the die shoulder. The higher tensile stresses help to decrease the residual stress gradient through the sheet thickness. Yoshida and Uemori (2002) have recently indicated that the unloading modulus decreases with plastic deformation and they have shown that this effect must be taken into account for a thorough simulation of springback. Therefore, the decrease of the unloading elastic modulus was implemented into the UMAT to improve the accuracy of the model for springback prediction.

Figures 4.9 shows a comparison between the experimental profiles of the AKDQ channel sidewalls after springback with those predicted with the IH and NKH models at 25% and 100% drawbead penetrations. It is apparent from these figures that NKH predicts the sidewall profile better than the IH, especially at 25% drawbead penetration where the range of cyclic strain is smaller than for 100% penetration. The NKH model divides the work hardening of the material into expansion and translation of the yield surface in stress space. However, the IH model assumes only an expansion of the yield surface due to global work hardening of the material. Consequently, it does not take the Bauschinger effect into account and is expected to overestimate springback. The overestimated stress obtained by the IH model for the uniaxial condition is also evident in Figure 3.2.

(a)

(b)

Figure 4.9. Springback profile of the AKDQ channel sidewall for (a) 25% and (b) 100% drawbead penetration.

A comparison between the experimental sidewall profiles with those obtained by simulation at different drawbead penetrations for DP600 channel sections is shown in Figures 4.10. For both penetration cases the springback profiles predicted by the IH model significantly overestimate the experimental profile. The reason can be explained by referring to Figure (3.2a), where the difference between the IH and NKH models is quite large. Therefore, the level of stress calculated with the IH model is distinctly greater than the actual stress, and consequently, the predicted profile after springback is also far from the experimental sidewall profile. The NKH model slightly underestimates the springback in the middle of the sidewall for the case of 25% penetration but generally predicts the sidewall curl more accurately than the IH model. The springback in the sidewall for the 75% drawbead penetration case is quite well predicted with the NKH model although, as seen previously, a slight overestimation is seen towards the lower end.

(a)

(b)
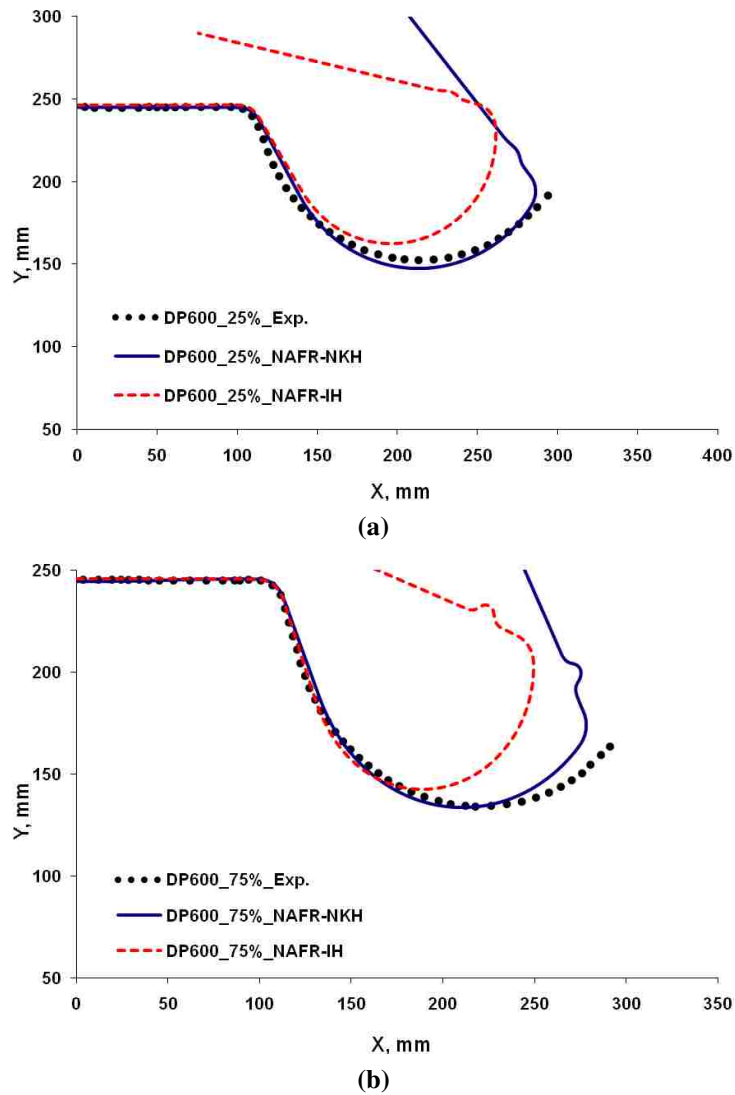
Figure 4.10. Springback profile of the DP600 channel sidewall for (a) 25% and (b) 75% drawbead penetration

In Figures 4.11, the profiles of the HSLA channel sidewalls after springback for the 25 and 100% drawbead penetration cases are shown. Again, the IH model assumption overestimates the springback. In contrast, the NKH model is capable of more accurately predicting springback both in the general shape of the sidewall and in the amount of springback, although it is slightly underestimated for both 25% and 100% drawbead penetration. The difference between the springback predictions with the two models is more significant in the 100% penetration case. The reason for this is either that the anisotropic function is inaccurate or the errors in stress prediction introduced by extrapolating the work-hardening curve increase for the deeper drawbead cases.
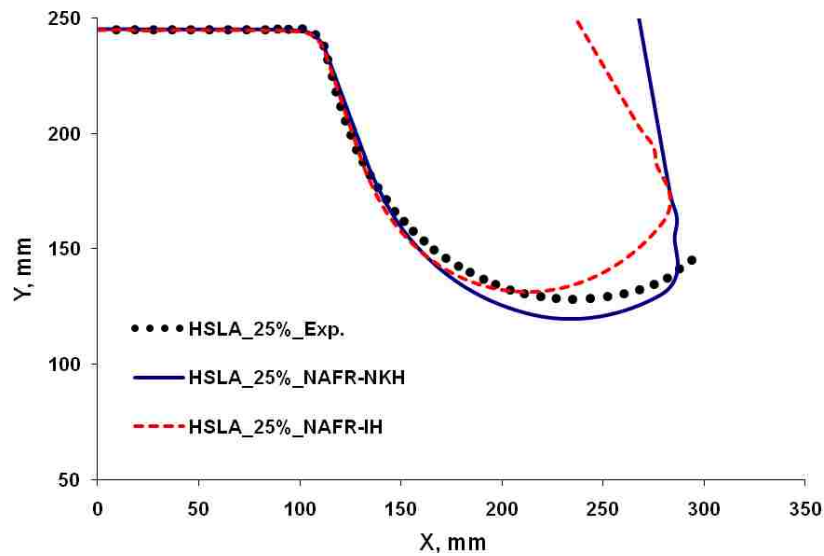
(a)
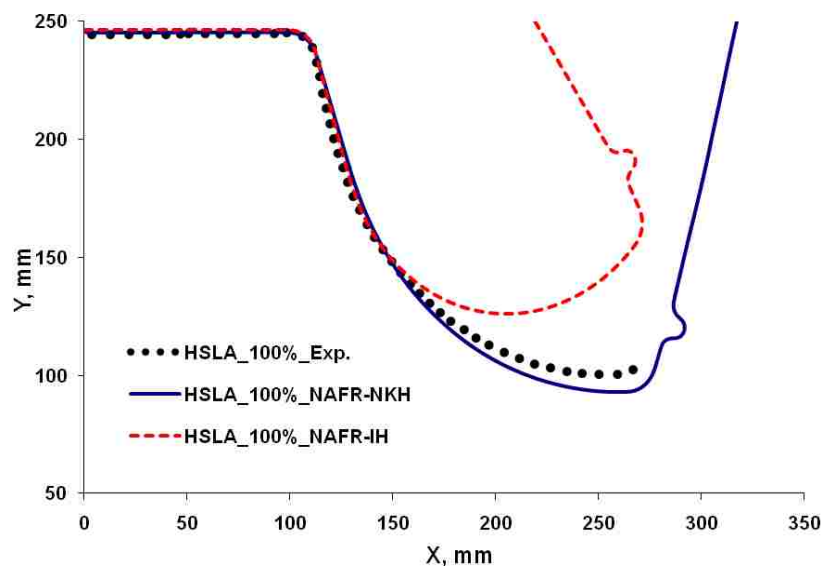
(b)

Figure 4.11. Springback profile of the HSLA channel sidewall for (a) 25% and (b) 100% drawbead penetration

117

The profile of the channel sidewall after springback for AA6022-T43 at 25% and 100% drawbead penetration is shown in Figures 4.12. In the case of 25% drawbead penetration, the IH model slightly overestimates the springback whereas the NKH slightly underestimates the springback. However, the curvature predicted by the NKH model is much more similar to that of the experimental profile than the one predicted by the IH model. With 100% drawbead penetration, the shape of the sidewall profile predicted with the NKH model is in very good agreement with the profile measured experimentally, while that obtained with the IH model overestimates the actual springback. As it was noted previously, the coefficients in the NKH model for the aluminum alloy were obtained from the uniaxial offset of the three-point bending test as explained by Zhao and Lee (2001). Moreover, it has often been pointed out that Hill's quadratic yield function is not able to represent the anisotropic behaviour of most aluminum alloys. As a consequence, numerous non-quadratic anisotropic yield functions have been proposed for aluminum alloys. It will therefore be interesting to investigate the effect of different yield criteria on the springback behaviour of aluminum alloys for forming processes that do lead to cyclic deformation due to the presence of drawbeads.
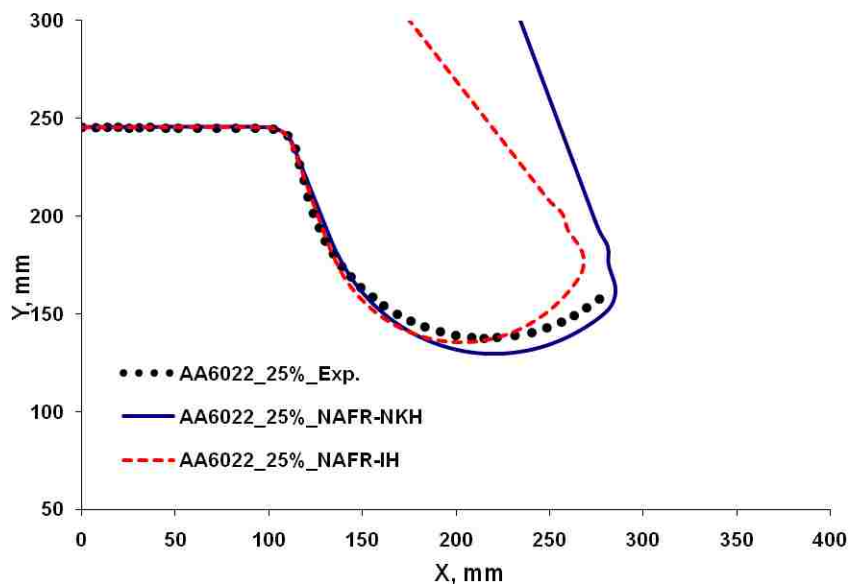
(4.12. a)
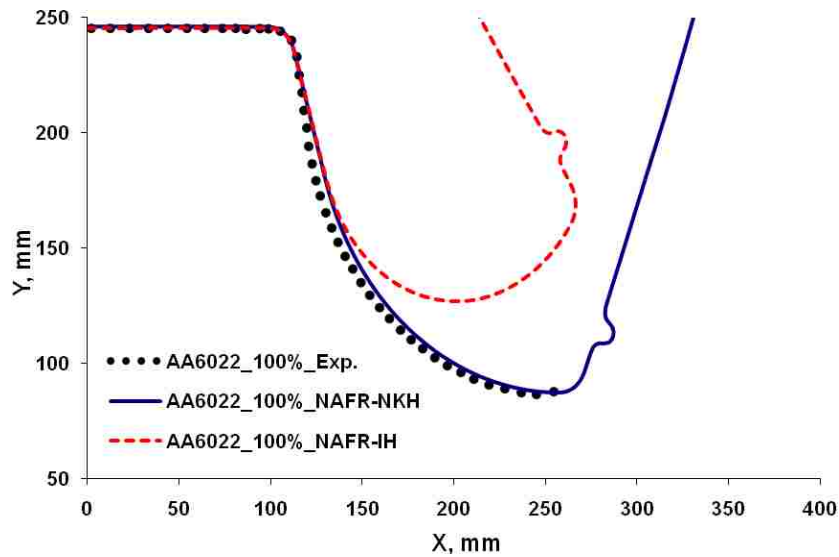
(b)

Figure 4.12. Springback profile of the AA6022-T43 channel sidewall for (a) 25% and (b) 100% drawbead penetration

4.5. Summary and concluding remarks

In this chapter an anisotropic material model based on non-associated flow rule and mixed isotropic-nonlinear kinematic hardening was developed and computationally formulated using the return mapping algorithm for implementation into the nonlinear commercial finite element code ABAQUS based on a user-defined material subroutine. Both yield and plastic potential functions were defined in the form of Hill's 1948 quadratic anisotropic function. Isotropic hardening followed a non-linear behaviour, generally in the power law form for most grades of steel and the exponential law form for aluminum alloys. Also, a nonlinear kinematic hardening law was implemented so as to account for cyclic loading effects caused mainly by the drawbead and die shoulder. The evolution of the backstress tensor was modeled based on the nonlinear kinematic hardening theory (Armstrong-Frederick formulation).

For verification, the distribution of yield stress ratios and r-values at different angles were compared with experimental values. The experimental cyclic stress-strain curves were also compared with the curves predicted by the IH and NKH models to evaluate the mixed hardening model. Yield surfaces and plastic potential surfaces were also compared and the differences became more significant with increasing levels of shear stress. Also, predicted equibiaxial and shear stress-strain curves with the proposed model were compared with the experimental curves. All comparisons show that the two aspects of the model, non-associated flow rule and mixed hardening are necessary to enhance the prediction of the material behaviour.

119

The material model implemented as a user-defined subroutine was used to simulate different sheet metal forming processes in order to assess its ability to predict earing and springback behaviours. Springback prediction of a channel draw process with drawbead and earing prediction of a cylindrical cup drawing process were simulated. Simulation results show that by using this non-associated mixed hardening material model both anisotropy and hardening descriptions are improved even though a rather simple quadratic constitutive model and a single-backstress kinematic hardening model were used.

4.6. References

ABAQUS 6.7, 2007. Documentation and Theory Manual. Hibbit, Karlsson, Sorensen, Inc.

Ahadi, A., Krenk, S., 2003. Implicit integration of plasticity models for granular materials. Comput. Methods Appl. Mech. Eng. 192, 3471-3488.

Aravas, N., 1987. On the numerical integration of a class of pressure-dependent plasticity models. Int. J. Num. Meth. Eng. 24, 1395-1416.

Armstrong, P.J., Frederick, C.O., 1966. A Mathematical representation of the multiaxial Bauschinger effect, Central Electricity Generating Board Report, Berkeley Nuclear Laboratories, RD/B/N 731.

Boger, R.K., Wagoner, R.H., Barlat, F., Lee, M.G., Chung, K., 2005. Continuous, large strain, tension/compression testing of sheet material. Int. J. Plasticity 21, 2319-2343.

Brem, J.C., Barlat, F., Dick, R.E., Yoon J.-W., 2005. Characterizations of aluminum alloy sheet materials Numisheet 2005. Proceedings of Numisheet 05, CP778 Volume B, American Institute of Physics, eds. Cao, J., Shi, M.F., Stoughton, T.B., Wang, C.T., Zhang, L., 1179-1190.

Brunet, M., Morestin, F., Godereaux, S., 2001. Nonlinear kinematic hardening identification for anisotropic sheet metals with bending-unbending tests. ASME J. Eng. Mat. Tech. 123, 378-383.

Brunig, M., Obrecht, H., 1998. Finite elastic-plastic deformation behaviour of crystalline solids based on a non-associated macroscopic flow rule. Int. J. Plasticity 14, 1189-1208.

Brunig, M., 1999. Numerical simulation of the large elastic-plastic deformation behaviour of hydrostatic stress-sensitive solids. Int. J. Plasticity 15, 1237-1264.

Brunig, M., Simone, B., Obrecht, H., 2000. Numerical simulation of localization behaviour of hydrostatic stress-sensitive metals. Int. J. Mech. Sci. 42, 2147-2166.

Cardoso, R.P.R., Yoon, J.W., 2009. Stress integration method for a nonlinear kinematic/isotropic hardening model and its characterization based on polycrystal plasticity. Int. J. of Plasticity 25, 1684-1710.

Chaboche, J.L., 1986. Time-independent constitutive theories for cyclic plasticity. Int. J. Plasticity 2, 149-188.

Chaboche, J.L., 1989. Constitutive equations for cyclic plasticity and cyclic viscoplasticity. Int. J. Plasticity 5, 247-302.

Clausen, J., Damkilde, L., Andersen, L., 2007. An efficient return algorithm for non-associated plasticity with linear yield criteria in principal stress space. Computers & Structures 85, 1795-1807.

Cvitanić, V., Vlak, F., Lozina, Z., 2008. A finite element formulation based on non-associated plasticity for sheet metal forming. Int. J. Plasticity 24, 646-678.

Dziallach, S., Bleck, W., Blumbach, M. and Hallfeldt, T., Sheet Metal Testing and Flow Curve Determination under Multiaxial Conditions. Advanced Engineering Materials, 2007, 9, 987-994.

Foster, C.D., Regueiro, R.A., Fossum, A.F., Borja, R.I, 2005. Implicit numerical integration of a three-invariant, isotropic/kinematic hardening cap plasticity model for geomaterials. Comput. Methods Appl. Mech. Eng. 194, 5109-5138.

GOM, Gesellschaft für Optische Messtechnik mbH, 2005. ARAMIS v5.4.1. User Manual.

Green, D.E., 2005. Description of Numisheet 2005 Benchmark #3 Stage-1: Channel Draw with 75% Drawbead Penetration. Proceedings of Numisheet 05, CP778 Volume B, American Institute of Physics, eds. Cao, J., Shi, M.F., Stoughton, T.B., Wang, C.T., Zhang, L., 894-904.

Hill, R., 1948. A theory of the yielding and plastic flow of anisotropic metals. Proc. Roy. Soc. Lond. A 193, 281-297.

Hjiaj, M., Fortin, J., de Saxcé, G., 2003. A complete stress update algorithm for the non-associated Drucker–Prager model including treatment of the apex. Int. J. Eng. Sci. 41, 1109-1143.

Hußnatter, W., Merklein, M., 2008. Characterization of metal behaviour under pure shear condition, Int. J. Mater. Form. 1, 233-236.

Karafillis, A.P., Boyce, M.C., 1993. A general anisotropic yield criterion using bounds and a transformation weighting tensor. J. Mech. Phys. Solids 41, 1859.

Kojic, M., 2002. Stress integration procedures for inelastic material models within finite element method. Appl. Mech. Reviews 55, 389-414.

Lei, X., Lissenden, C.J., 2007. Pressure sensitive nonassociative plasticity model for DRA composites. ASME J. Eng. Mater. Tech. 129, 255-264.

Mahnken, R., 2001. Strength difference in compression and tension and pressure dependence of yielding in elasto-plasticity. Comput. Meth. Appl. Mech. Eng. 190, 5057-5080.

Prager, W., 1956. A new method of analyzing stresses and strains in work-hardening plastic solids. ASME J. Appl. Mech. 23, 493-496.

Shi, M.F., Huang, M., 2005. Specification for benchmark materials. Proceedings of Numisheet 05, CP778 Volume B, American Institute of Physics, eds. Cao, J., Shi, M.F., Stoughton, T.B., Wang, C.T., Zhang, L., 1173-1178.

Simo, J.C., Taylor, R.L., 1985. Consistent tangent operators for rate independent elasto-plasticity. Comput. Meth. Appl. Mech. Eng. 48, 101-118.

Simo, J.C., Taylor, R.L., 1986. Return mapping algorithm for plane stress elasto-plasticity. Int. J. Num. Meth. Eng. 22, 649-670.

Simo, J.C., Meschke, G., 1993. A new class of algorithms for classical plasticity extended to finite strains. Application to Geomaterials. Comput. Mech. 11, 253-278.

Simo, J.C., Hughes, T.J.R., 1998. Computational Inelasticity. Volume 7 of Interdisciplinary Applied Mathematics. Springer-Verlag, Berlin.

Stoughton, T.B., 2002. A non-associated flow rule for sheet metal forming. Int. J. Plasticity 18, 687-714.

Stoughton, T.B., Green, D.E., Iadicola, M., 2005. Specification for BM3: two-stage channel/cup draw. Proceedings of Numisheet 05, CP778 Volume B, American Institute of Physics, eds. Cao, J., Shi, M.F., Stoughton, T.B., Wang, C.T., Zhang, L., 1157-1172.

Thuillier, S., Manach, P.Y., 2009. Comparison of the work-hardening of metallic sheets using tensile and shear strain paths. Int. J. Plasticity 25, 733-751.

Yoon, J.W., Yang, D.Y., Chung, K., 1999a. Elasto-plastic finite element method based on incremental deformation theory and continuum based shell elements for planar anisotropic sheet materials. Comput. Methods Appl. Mech. Eng. 174, 23-56.

Yoon, J.W., Yang, D.Y., Chung, K., Barlat, F., 1999b. A general elasto-plastic finite element formulation based on incremental deformation theory for planar anisotropy and its application to sheet metal forming", Int. J. of Plasticity, 15, 35-68.

Yoon, J.W., Barlat, F., Chung, K., Pourboghrat, F., Yang, D.Y., 2000. Earing prediction based on asymmetric nonquadratic yield function. Int. J. Plasticity 16, 1075-1104.

Yoon, J.W., Barlat, F., 2006. Modelling and Simulation of the Forming of Aluminum Sheet Alloys, Vol.14B, Metal Working: Sheet Forming, Article in ASM Handbook, ASM International, Materials Park (OH), 792-826 (2006).

Yoshida, F., Uemori, T., 2002. A model of large-strain cyclic plasticity describing the Bauschinger effect and work hardening stagnation. Int. J. Plasticity 18, 661-686.

Young, R.F., Bird, J.E., Duncan, J.L., 1981. An automated hydraulic bulge tester. J. Appl. Metal Working. 2, 11-18.

Zeng, L.F., Horrigmoe, G., Andersen, R., 1996. Numerical implementation of constitutive integration for rate-independent elastoplasticity. Comput. Mech. 18, 387-396.

Zhao, K., Lee, J.K., 2001. Generation of cyclic stress-strain curves for sheet metals. ASME J. Eng. Mater. Tech. 123, 391-397.

Ziegler, H., 1959. A modification of Prager's hardening rule. Quarterly of Applied Mathematics 17, 55-60.

Zienkiewicz, O.C., Taylor, R.L., 2005. The Finite Element Method for Solid and Structural Mechanics. Sixth Edition, Butterworth-Heinemann.

Chapter 5

Comparison of Two Anisotropic Models for Sheet Metal Forming: a Quadratic Non-associated and a Non-quadratic Associated

5.1. Introduction

Generally, anisotropy in sheet metals is due to the significant alignment (preferred orientation) of crystal-texture that is generated during the rolling process. In sheet metals, anisotropy is commonly evident in both plastic yielding and flow, so that any material model should consider it in both concepts for a realistic simulation. Several anisotropic yield functions have been proposed for sheet metals in order to model the experimental behaviour as accurately as possible. Hill's (1948) quadratic yield function may be noted as the most well-known yield criteria proposed as a generalization of the von Mises yield function for anisotropic materials. Although Hill's 1948 yield function has been widely used for analysis of orthotropic metals, it exhibits some limitations particularly for some aluminum alloys, as highlighted by some researchers (Mellor and Parmer, 1978; Mellor, 1981). Therefore in recent decades, much attention has been focused on developing more advanced anisotropic yield criteria. Many researchers (Hill, 1979, 1990, 1993; Barlat and Lian, 1989; Barlat et al., 1991, 1997, 2003, 2005; Karafillis and Boyce, 1993; Banabic et al., 2005 etc.) have developed different non-quadratic yield functions. A comprehensive review of some micro- and macro- anisotropic models proposed for metals can be found in Habraken (2004). Some of these recent anisotropic plasticity models are able to describe the anisotropic

behaviour of sheet metals with considerable accuracy, but they necessitate a large number of experiments to define the coefficients.

One of the novel applications of the Non-Associated Flow Rule (NAFR) in metals plasticity is to describe the anisotropic yielding and flow in a more convenient way. Therefore, in order to improve accuracy without having to define a large number of material parameters, Stoughton (2002) proposed a non-associated flow rule model. This signifies that different yield and plastic potential functions, each with simpler formulations, can be combined to describe plastic behaviour. In this model, Stoughton (2002) assumed that both yield and potential functions were based on Hill's (1948) function with isotropic hardening and reviewed the validation of the model under experiments. The generalization described by Stoughton includes realistic elastic effects and fully anisotropic plastic behaviour under a NAFR results in an accurate simulation of the r-value distribution and both uniaxial and biaxial yield behaviour. The latter behaviour is challenging for Hill's quadratic function under the associated flow rule (AFR). Cvitanic et al. (2008) implemented a NAFR anisotropic material model for simulation of sheet forming processes. They considered two different yield and potential functions: Hill's 1948 and Karafillis and Boyce with only isotropic hardening (IH). Stoughton and Yoon (2009) proposed a material model based on NAFR and anisotropic hardening to improve the prediction of different experimental results. Recently, Taherizadeh et al. (2009b) developed a NAFR model with mixed isotropic-nonlinear kinematic hardening (NKH) and implemented it in the finite element code ABAQUS. They compared the anisotropy prediction of different automotive sheets obtained by the NAFR and AFR models, and also simulated springback of a channel draw with drawbeads using the new model. The main shortcoming of their implementation (i.e. stress integration formulation) is that the proposed direct integration is only applicable to quadratic yield and potential functions, such as Hill's (1948).

In this chapter, two different approaches to analyze the anisotropic behaviour of sheet materials were compared. The first model was based on a non-associated formulation with both yield and potential functions in the form of Hill's 1948 quadratic equation. The coefficients in the yield function were determined from the yield stresses, and those of the potential function were determined from the r-values. The second model was an associated non-quadratic model so-called Yld-2000-2d, proposed by Barlat et al. (2003). The anisotropy of this model was introduced in the formulation by using two linear transformations on the Cauchy stress tensor. Seven material coefficients were required for the first model: uniaxial yield stresses and r-values at 0, 45, and 90° from the rolling direction, and the balanced biaxial yield stress. The second model required the same seven coefficients as input, as well as balanced biaxial r-value. Therefore, both models are

able to consider the effect of r-values and yield stresses on the anisotropic behaviour. The formulations of both anisotropic models were derived for two different hardening frameworks: pure isotropic that is acceptable for monotonic loadings, and mixed isotropic-nonlinear kinematic hardening that is more suitable for cyclic loadings. The constitutive formulation in the form of incremental equations that is used in the finite element analysis was also derived based on the minimum plastic work path. A general return mapping algorithm based on the backward-Euler method that is applicable to generic types of yield and potential functions (quadratic or non-quadratic) was used to computationally integrate the stress and state variables in each time increment during the nonlinear finite element analysis. Both models were implemented in the commercial finite element code ABAQUS as user-defined material subroutines. Simulations of three different cylindrical cup drawing processes based on three different Al-alloy sheets were performed with both anisotropic models. As a measurable result of the planar anisotropy, the predicted earing profiles of the formed cups were compared with experimental results to demonstrate the accuracy of each model. Also, springback of a channel draw process with drawbead was simulated, using two constitutive models for two sheet materials to evaluate the effect of anisotropic modelling on the springback prediction. Computational cost, as an important aspect of advanced models, was compared for the two models. Moreover, in order to extract the mixed hardening parameters for the springback simulations, the in-plane cyclic tension-compression tests were performed for two sheet materials (Al-alloy and DP steel).

5.2. Anisotropic models with mixed hardening

A brief description of two anisotropic models with mixed hardening for plane stress condition is presented in the following:

5.2.1. Quadratic non-associated model

A non-associated anisotropic model based on Hill 1948 quadratic yield and potential functions with combined isotropic- nonlinear kinematic hardening was developed by Taherizadeh et al. (2009). The yield function has the following form for plane stress condition

$$2F = \overline{\eta}_Y(\boldsymbol{\sigma} - \boldsymbol{\alpha}) - \sigma_u^{Y} = \left(\frac{3}{2}\boldsymbol{\eta}^T \mathbf{M}\boldsymbol{\eta}\right)^{\frac{1}{2}} - \sigma_u^{Y}(p) = 0 \qquad (5.1)$$

where $\bar{\eta}_Y$ is the equivalent value of the tensor η that is defined as $\eta = \sigma - \alpha$, α is a backstress tensor (that is used to describe the evolution of the center of the yield surface in stress space as a kinematic hardening behaviour), $\mathbf{M}$ is the yield function anisotropic tensor, σ_u^Y is the yield stress in the reference direction and scalar p is a hardening parameter (or equivalent plastic strain). The yield anisotropic tensors $\mathbf{M}$ and its dimensionless components are defined as

$$\mathbf{M} = \begin{bmatrix} M_1 + M_2 & -M_1 & 0 \\ -M_1 & M_1 + M_3 & 0 \\ 0 & 0 & M_4 \end{bmatrix}$$

and

$$M_1 = \frac{(\sigma_u^Y)^2}{3}\left(\frac{1}{(\sigma_0^Y)^2} + \frac{1}{(\sigma_{90}^Y)^2} - \frac{1}{(\sigma_B^Y)^2}\right)$$

$$M_2 = \frac{(\sigma_u^Y)^2}{3}\left(\frac{1}{(\sigma_0^Y)^2} - \frac{1}{(\sigma_{90}^Y)^2} + \frac{1}{(\sigma_B^Y)^2}\right)$$

$$M_3 = \frac{(\sigma_u^Y)^2}{3}\left(\frac{1}{(\sigma_{90}^Y)^2} - \frac{1}{(\sigma_0^Y)^2} + \frac{1}{(\sigma_B^Y)^2}\right)$$

$$M_4 = \frac{(\sigma_u^Y)^2}{3}\left(\frac{1}{(2\sigma_{45}^Y)^2} - \frac{1}{(\sigma_B^Y)^2}\right)$$

where σ_0^Y, σ_{90}^Y, and σ_{45}^Y are tensile yield stresses in the rolling, transverse and diagonal (45 degree) directions, and σ_B^Y is the equibiaxial yield stress.

To take into account the effect of r-value parameters in the anisotropic constitutive model by using the same quadratic formulation the plastic potential function in a similar way is defined as

$$\bar{\eta}_P(\sigma - \alpha) = \left(\frac{3}{2}\eta^T \mathbf{P}\eta\right)^{\frac{1}{2}} \tag{5.2}$$

where $\mathbf{P}$ is the plastic potential anisotropic tensor and with its components are defined as

$$\mathbf{P} = \begin{bmatrix} P_1 + P_2 & -P_1 & 0 \\ -P_1 & P_1 + P_3 & 0 \\ 0 & 0 & P_4 \end{bmatrix}$$

and

$$P_1 = \frac{2}{3} \frac{r_0}{1 + r_0}$$

$$P_2 = \frac{2}{3} \frac{1}{1 + r_0}$$

$$P_3 = \frac{2}{3} \frac{r_0}{(1 + r_0)r_{90}}$$

$$P_4 = \frac{(1 + 2r_{45})(r_0 + r_{90})}{3(1 + r_0)r_{90}}$$

where r_0, r_{90}, and r_{45} are plastic strain ratios (also called Lankford's coefficients) in the rolling, transverse and diagonal directions. The flow rule is used to determine the plastic part of the strain increment

$$d\varepsilon^P = d\lambda \frac{\partial \bar{\eta}_P}{\partial \boldsymbol{\eta}} \tag{5.3}$$

where $d\lambda$ is a non-negative scalar called the plastic multiplier or consistency parameter. In most cases of classical plasticity, particularly in metals plasticity, it is assumed that the potential function is identical to the yield function which is called associated flow rule (AFR). Consistency parameter is then determined to be the same as increment of the effective plastic strain by using the principle of plastic work equivalence, i.e. $d\lambda = dp$. Details for using the incremental deformation theory based on minimum plastic work path in the presence of backstress tensor and kinematic hardening were developed by Chung et al. (2005) and Cardoso and Yoon (2009).

The isotropic hardening that determines the size of the yield surface, is represented by either an exponential or power law function

$$\sigma_u^Y(p) = \sigma_0 + Q(1 - e^{-b \cdot p}) \tag{5.4a}$$

$$\sigma_u^Y(p) = K(\varepsilon_0^P + p)^n \tag{5.4b}$$

where Q and b, or K and n, are material constants associated with isotropic hardening. The evolution of the backstress tensor in this paper is modeled based on the nonlinear kinematic hardening theory or so-called AF formulation (Armstrong and Frederick, 1966)

$$d\boldsymbol{\alpha} = \left(\frac{C}{\overline{\eta}_P}\boldsymbol{\eta} - \gamma\boldsymbol{\alpha}\right)dp \qquad (5.5)$$

where parameters C and γ are material constants associated with kinematic hardening and are determined from cyclic tests. The first part of the backstress tensor increment was written based on Ziegler's method (1959). Also a fully-non-associated model was used to define the backstress formulation, since the potential function was applied in the linear term. Applications of this nonlinear approach and also modifications to increase the range of validity of the original model and to improve the quantitative description of the ratcheting effect and degree of freedom were later presented by Chaboche (1986; 1989).

It is necessary to derive the relation between the increments of stress and strain for implementation of a constitutive model in the finite element formulation. Using the consistency condition for the above formulations, the plastic multiplier is calculated. Consequently, by using the flow rule and elastic equilibrium equation, $d\boldsymbol{\sigma} = \mathbf{D}(d\boldsymbol{\varepsilon} - d\boldsymbol{\varepsilon}^p)$, the incremental relation between stress and strain in the general form is obtained

$$\frac{d\boldsymbol{\sigma}}{d\boldsymbol{\varepsilon}} = \mathbf{D}^{ep}{}_{NAFR} = \mathbf{D} - \frac{\left(\mathbf{D}:\dfrac{\partial\overline{\eta}_P}{\partial\boldsymbol{\eta}}\right)\otimes\left(\dfrac{\partial\overline{\eta}_Y}{\partial\boldsymbol{\eta}}:\mathbf{D}\right)}{\dfrac{\partial\overline{\eta}_Y}{\partial\boldsymbol{\eta}}:\mathbf{D}:\dfrac{\partial\overline{\eta}_P}{\partial\boldsymbol{\eta}} + \dfrac{C}{\overline{\eta}_P}(\dfrac{\partial\overline{\eta}_Y}{\partial\boldsymbol{\eta}}:\boldsymbol{\eta}) - \gamma(\dfrac{\partial\overline{\eta}_Y}{\partial\boldsymbol{\eta}}:\boldsymbol{\alpha}) + h} \qquad (5.6)$$

where $\mathbf{D}^{ep}$, a non-symmetric matrix for the non-associated model that is called the elasto-plastic tangent modulus, $\mathbf{D}$ is the elastic stiffness matrix and $h = d\sigma_u{}^Y / dp$. The above matrix for the current non-associated model based on Hill's 1948 functions is derived as

$$\frac{d\boldsymbol{\sigma}}{d\boldsymbol{\varepsilon}} = \mathbf{D}^{ep}{}_{NAFR} = \mathbf{D} - \frac{\dfrac{3}{2}\boldsymbol{\eta}^T\mathbf{MD}\otimes\mathbf{DP}\boldsymbol{\eta}}{\dfrac{3}{2}\boldsymbol{\eta}^T\mathbf{MDP}\boldsymbol{\eta} + C\boldsymbol{\eta}^T\mathbf{M}\boldsymbol{\eta} - \overline{\eta}_P\gamma\boldsymbol{\eta}^T\mathbf{M}\boldsymbol{\alpha} + \dfrac{2}{3}\overline{\eta}_P\sigma_u{}^Y h} \qquad (5.7)$$

5.2.2. Non-quadratic associated model

A non-quadratic yield function proposed by Barlat et al. (2003) that is so-called Yld2000-2d is briefly explained here. For plane stress condition the effective value of the tensor $\boldsymbol{\eta}$ and yield criterion are written as follows

$$\phi = \phi' + \phi'' = \underbrace{\left| X_1' - X_2' \right|^a}_{\phi'} + \underbrace{\left| 2X_2'' + X_1'' \right|^a + \left| 2X_1'' + X_2'' \right|^a}_{\phi''} = 2\overline{\eta}^{\,a}(\boldsymbol{\sigma} - \boldsymbol{\alpha}) \tag{5.8}$$

and

$$\overline{\eta} - \sigma_u^{\,Y} = 0 \tag{5.9}$$

where the exponent a is recommended as $a=8$ for FCC metals and $a=6$ for BCC metals. Components X_i' and X_j'' are the principal values of two linear transformations ($\boldsymbol{X'}$ and $\boldsymbol{X''}$) of the tensor $\boldsymbol{\eta}$ (or simply the stress tensor $\boldsymbol{\sigma}$ if no kinematic hardening is considered) as follows

$$\boldsymbol{X'} = \boldsymbol{L'}\boldsymbol{\eta} \quad \text{and} \quad \boldsymbol{X''} = \boldsymbol{L''}\boldsymbol{\eta} \tag{5.10}$$

where $\boldsymbol{L'}$ and $\boldsymbol{L''}$ are two linear higher-ranked tensors applying the transformations on the stress tensor. There are other forms of definitions applied on the stress tensor or its deviator tensor, but they are not mentioned here because the current notation is more convenience compared to the others. The above transformations in the matrix notation are written as

$$\begin{Bmatrix} X'_{xx} \\ X'_{yy} \\ X'_{xy} \end{Bmatrix} = \begin{bmatrix} L'_{11} & L'_{12} & 0 \\ L'_{21} & L'_{22} & 0 \\ 0 & 0 & L'_{33} \end{bmatrix} \begin{Bmatrix} \eta_{xx} \\ \eta_{yy} \\ \eta_{xy} \end{Bmatrix} \tag{5.11a}$$

and

$$\begin{Bmatrix} X''_{xx} \\ X''_{yy} \\ X''_{xy} \end{Bmatrix} = \begin{bmatrix} L''_{11} & L''_{12} & 0 \\ L''_{21} & L''_{22} & 0 \\ 0 & 0 & L''_{33} \end{bmatrix} \begin{Bmatrix} \eta_{xx} \\ \eta_{yy} \\ \eta_{xy} \end{Bmatrix} \tag{5.11b}$$

The principal values of these vectors used in the yield function are written as

$$X'_{1,2} = \frac{X'_{xx} + X'_{yy}}{2} \pm \sqrt{\left(\frac{X'_{xx} - X'_{yy}}{2} \right)^2 + X'^{\,2}_{xy}} \tag{5.12a}$$

and

$$X''_{1,2} = \frac{X''_{xx} + X''_{yy}}{2} \pm \sqrt{\left(\frac{X''_{xx} - X''_{yy}}{2}\right)^2 + X''^2_{xy}}$$

(5.12b)

The expressions of the anisotropy coefficients of **L'** and **L''** are given as functions of independent coefficients α_1 to α_8 which all reduce to 1 for the isotropic case

$$L'_{11} = \frac{2\alpha_1}{3} \qquad L''_{11} = \frac{8\alpha_5 - 2\alpha_3 - 2\alpha_6 + 2\alpha_4}{9}$$

$$L'_{12} = -\frac{\alpha_1}{3} \qquad L''_{12} = \frac{4\alpha_6 - 4\alpha_4 - 4\alpha_5 + \alpha_3}{9}$$

$$L'_{21} = -\frac{\alpha_2}{3} \quad \text{and} \quad L''_{21} = \frac{4\alpha_3 - 4\alpha_5 - 4\alpha_4 + \alpha_6}{9}$$

$$L'_{22} = \frac{2\alpha_2}{3} \qquad L''_{22} = \frac{8\alpha_4 - 2\alpha_6 - 2\alpha_3 + 2\alpha_5}{9}$$

$$L'_{33} = \alpha_7 \qquad L''_{33} = \alpha_8$$

(5.13)

where α_1 to α_8 are functions of eight uniaxial and biaxial test input data in different directions: σ^Y_0, σ^Y_{90}, σ^Y_{45}, σ^Y_B, r_0, r_{90}, r_{45}, and r_B are tensile yield stresses and r-values in the rolling, transverse, diagonal (45 degree), and biaxial directions, respectively. If the biaxial r-value (r_B) is not available or only seven coefficients are needed to account for seven input data, there is a possibility to eliminate one parameter by assuming $\alpha_3 = \alpha_6$ (Therefore, $L''_{12} = L''_{21}$) or $\alpha_4 = \alpha_5$ (Therefore, $L''_{11} = L''_{22}$). To determine the anisotropy coefficients, α_1 to α_8, a system of nonlinear equations must be solved generally by using the Newton-Raphson iteration method. The system of eight equations consists of four yield functions for the yield stresses and their corresponding derivatives for the r-values in different test states. These equations can be found in the Appendix 5.6.1.

Using the same fundamental equations in the previous sub-section and modifying them for the non-quadratic associated case we have

$$\frac{d\sigma}{d\varepsilon} = \mathbf{D}^{ep}_{AFR} = \mathbf{D} - \frac{(\mathbf{D} : m) \otimes (m : \mathbf{D})}{m : \mathbf{D} : m + \frac{C}{\eta}(m : \eta) - \gamma(m : \alpha) + h}$$

(5.14)

130

where **m** is the derivative of the effective value $\overline{\eta}$

$$m = \frac{\partial \overline{\eta}}{\partial \eta} \qquad\qquad (5.15)$$

Unlike the concise derivative of Hill's 1948 function, the derivative of the Yld2000-2d is lengthy but straightforward. The explicit forms of the first and the second derivatives of this equivalent stress function are available by Yoon et al. (2003) for isotropic hardening; however, the same procedure can be followed for the current model in the presence of the backstress tensor (presented in Appendix 5.6.2).

5.3. Stress integration algorithm

In nonlinear finite element analysis the implementation of a constitutive model involves the integration of the state of the material at an integration point over a time increment. Different approaches have been proposed in order to numerically integrate the stress and other state variables over an increment. The radial return-mapping algorithm is a particular case of elastic predictor-plastic corrector algorithms when a purely elastic trial stress is followed by a plastic corrector phase (Simo and Hughes, 1998). The purpose of the latter is to enforce consistency at the end of a step in a manner consistent with the prescribed flow rule.

It is assumed that the stresses and all state variables are known at the beginning of the time step based on the converged values of the last time increment and the system is in the global equilibrium. First, the trial stress tensor is computed based on the gradient of the displacement field increment (or total strain increment tensor) over the time increment $[t_n, t_{n+1}]$. Then, the radial return mapping algorithm (elastic predictor - plastic corrector) was used to numerically enforce the stress state on the subsequent yield surface. In the following formulation, subscript n represents values at the beginning of the time step and subscript n+1 is omitted for the sake of simplicity.

5.3.1. Forward-Euler stress integration

In fact, the above-mentioned straightforward formulation might be used in the numerical procedure to integrate the stress over the time increment as first-order forward Euler integration scheme, also called the explicit stress integration because the stress at the end of time step t_{n+1} is calculated as a function of all variables at the beginning of time step t_n:

$$\boldsymbol{\sigma}_{n+1} = \boldsymbol{\sigma}_n + \mathbf{D}_n{}^{ep} \Delta\boldsymbol{\varepsilon} \tag{5.16}$$

In this method, the normal to the yield or potential surface is known and is evaluated at the previous or trial configuration. Since the direction is known, there is only one unknown variable during the return mapping procedure, the plastic multiplier, which can be extracted from the consistency condition. However, it has been shown that this method has significant disadvantages when compared to the implicit integration scheme, primarily because it is conditionally stable and only accurate for small time steps (Kojic, 2002; Cardoso and Yoon, 2009).

5.3.2. Backward-Euler stress integration

In the backward-Euler method, the normal to the yield or potential surface is evaluated at the current (unknown) configuration. As a result, the variation of the normal to the yield surface must be taken into consideration during the return mapping procedure, resulting in a more complex method, but also in a more accurate scheme. There are some nonlinear equations to be solved for Δp at each time increment which enable the resulting stresses to stay on the hardening surface as expressed in Equation (5.17)

$$\overline{\eta}_Y(\boldsymbol{\eta}_n + \Delta\boldsymbol{\eta}) - \sigma_u{}^Y(p_n + \Delta p) = 0 \tag{5.17}$$

This Equation is a nonlinear function of the plastic multiplier, so that, a predictor-corrector algorithm based on the Newton-Raphson method is generally used to solve it. Different terms in the above equation are written as

$$\Delta\boldsymbol{\eta} = \Delta\boldsymbol{\sigma} - \Delta\boldsymbol{\alpha} \tag{5.18a}$$

$$\Delta\boldsymbol{\sigma} = \mathbf{D}^e \, \Delta\boldsymbol{\varepsilon}^e \tag{5.18b}$$

$$\Delta\boldsymbol{\varepsilon} = \Delta\boldsymbol{\varepsilon}^e + \Delta\boldsymbol{\varepsilon}^p \tag{5.18c}$$

$$\Delta\boldsymbol{\varepsilon}^p = \Delta p \frac{\partial\overline{\eta}_P}{\partial\boldsymbol{\eta}} \tag{5.18d}$$

$$\Delta\boldsymbol{\alpha} = (\frac{C}{\overline{\eta}_P}\boldsymbol{\eta} - \gamma\boldsymbol{\alpha})\Delta p \tag{5.18e}$$

If the strain increment is not small enough, it is difficult to obtain the solution of Equation (5.17) numerically, even though it has a mathematical solution. Therefore, a multi-stage return mapping procedure, which utilizes the control of the potential residual suggested by Yoon et al. (1999a) was employed. The proposed method is applicable to a non-quadratic yield function and a general hardening law without the need of a line search algorithm, even for a relatively large strain increment. For sub-step k, the nonlinear equation is modified with the given residual as follows

$$\Phi(\Delta p_k) = \overline{\eta}_Y(\boldsymbol{\eta}_n + \Delta\boldsymbol{\eta}_k) - \sigma_u^{Y}(p_n + \Delta p_k) = F_k \tag{5.19}$$

where $F_{k=1-N-1}$, is a residual for each sub-step and is a prescribed value. Suppose we need N sub-steps to achieve the final answer of the nonlinear equation. In that case we have $F_0 > F_1 > ... > F_k > ... F_N (F_N \approx 0)$ and $\Delta F_k < \sigma_u^{Y}{}_k$. This procedure ends when $F = F_N(\approx 0)$.

To explain the procedure briefly, using the above Equations (5.18a-5.18e) the following auxiliary functions or residuals (g_1, g_2, and g_3) can be written for a sub-step (k)

(i) $\quad g_1(\Delta p_k) = \overline{\eta}_Y(\boldsymbol{\eta}_k) - \sigma_u^{Y}(p_n + \Delta p_k) - F_k = 0 \tag{5.20}$

(ii) $\quad \boldsymbol{g}_2(\Delta p_k) = \mathbf{D}^{-1}(\boldsymbol{\sigma}_k - \boldsymbol{\sigma}^T) + \Delta p_k.\boldsymbol{n}_k = 0 \tag{5.21}$

(iii) $\quad \boldsymbol{g}_3(\Delta p_k) = \boldsymbol{\alpha}_k - \boldsymbol{\alpha}_n - \dfrac{C}{\overline{\eta}_P(\boldsymbol{\eta}_k)} \Delta p_k \, \boldsymbol{\eta}_k + \gamma \Delta p_k \, \boldsymbol{\alpha}_k = 0 \tag{5.22}$

The above residuals should be approximately zero (within a convergence tolerance) when convergence is achieved. In Equation (5.21) $\boldsymbol{\sigma}^T$ is the trial stress and $\boldsymbol{n}$ is the current normal to the potential surface

$$\boldsymbol{n}_k = \frac{\partial \overline{\eta}_P(\boldsymbol{\eta}_k)}{\partial \boldsymbol{\eta}_k} \tag{5.23}$$

Also, p_n and $\boldsymbol{\alpha}_n$ stand for the equivalent plastic strain and the back stress tensor for the last converged configuration, respectively. The residuals, $g_1(\Delta p_k)$, $\boldsymbol{g}_2(\Delta p_k)$, and $\boldsymbol{g}_3(\Delta p_k)$ are nonlinear functions of plastic multiplier (Δp_k). At each iteration three nonlinear functions are linearized around the current values of the state variables to obtain the increment of the plastic multiplier

and consequently the backstress and stress tensors. By applying a Taylor's series expansion at the current configuration and by considering only the linear terms, we obtain the following linear residuals for each iteration of the current sub-step (k)

(i) $g_1(\Delta p_k) + \boldsymbol{m}_k : \Delta \boldsymbol{\sigma}_k - \boldsymbol{m}_k : \Delta \boldsymbol{\alpha}_k - H.d\Delta p_k = 0$ (5.24)

(ii) $g_2(\Delta p_k) + \left(\mathbf{D}^{-1} + \Delta p_k \dfrac{\partial \boldsymbol{n}_k}{\partial \boldsymbol{\eta}_k} \right) \Delta \boldsymbol{\sigma}_k - \left(\Delta p_k \dfrac{\partial \boldsymbol{n}_k}{\partial \boldsymbol{\eta}_k} \right) \Delta \boldsymbol{\alpha}_k + \boldsymbol{n}_k .d\Delta p_k = 0$ (5.25)

(iii) $g_3(\Delta p_k) + \Delta \boldsymbol{\alpha}_k - \dfrac{C}{\bar{\eta}_P(\boldsymbol{\eta}_k)} . \boldsymbol{\eta}_k .d\Delta p_k - \dfrac{C\Delta p_k}{\bar{\eta}_P(\boldsymbol{\eta}_k)} \left(1 - \dfrac{(\boldsymbol{n}_k : \boldsymbol{\eta}_k)}{\bar{\eta}_P(\boldsymbol{\eta}_k)} \right).(\Delta \boldsymbol{\sigma}_k - \Delta \boldsymbol{\alpha}_k) +$

$\gamma \Delta p_k . \Delta \boldsymbol{\alpha}_k + \gamma . \boldsymbol{\alpha}_k .d\Delta p_k = 0$ (5.26)

In Equation (5.24) $\boldsymbol{m}$ is the current normal to the yield surface and H is the derivative of the isotropic hardening function

$$\boldsymbol{m}_k = \frac{\partial \bar{\eta}_Y(\boldsymbol{\eta}_k)}{\partial \boldsymbol{\eta}_k}$$ (5.27)

After some mathematical arrangements, the evolution equations for the backstress tensor ($\Delta \boldsymbol{\alpha}_k$) is obtained by using Equation (5.26). Then, by using this relation for the backstress tensor increment and substitution in the Equation (5.25) the evolution equation for the stress tensor ($\Delta \boldsymbol{\sigma}_k$) is obtained. Finally, by substituting these two evolution equations into Equation (5.24) the plastic multiplier increment ($d\Delta p_k$) will be obtained.

$$\Delta \boldsymbol{\alpha}_k = \frac{1}{A_2} \left[-g_3(\Delta p_k) + \frac{C}{\bar{\eta}_P(\boldsymbol{\eta}_k)} . \boldsymbol{\eta}_k .d\Delta p_k + \frac{CA_1\Delta p_k}{\bar{\eta}_P(\boldsymbol{\eta}_k)} . \Delta \boldsymbol{\sigma}_k - \gamma . \boldsymbol{\alpha}_k .d\Delta p_k \right]$$ (5.28)

$$\Delta \boldsymbol{\sigma}_k = -\boldsymbol{\Xi} . \left[\left(g_2(\Delta p_k) + \frac{\Delta p_k}{A_2} . \left(\frac{\partial \boldsymbol{n}_k}{\partial \boldsymbol{\eta}_k} \right) \right) \left(g_3(\Delta p_k) - \frac{C}{\bar{\eta}_P(\boldsymbol{\eta}_k)} . \boldsymbol{\eta}_k .d\Delta p_k - \gamma . \boldsymbol{\alpha}_k .d\Delta p \right) + \boldsymbol{n}_k .d\Delta p_k \right]$$ (5.29)

134

$$d\Delta p_k = \frac{g_1(\Delta p_k) - A_3(m_k : \Xi : B_1) + \frac{1}{A_2}(m_k : g_3(\Delta p_k))}{A_3\left(m_k : \Xi : \frac{\partial n_k}{\partial \eta_k} : B_2\right) + \frac{C}{A_2\overline{\eta}_P(\eta_k)}(m_k : \eta_k) - \frac{\gamma}{A_2}(m_k : \alpha_k) + H}$$

(5.30)

where the parameters used in Equations (5.28) to (5.30) are defined as following

$$A_1 = 1 - \frac{(n_k : \eta_k)}{\overline{\eta}_P(\eta_k)}$$

(5.31)

$$A_2 = 1 + \frac{CA_1\Delta p_k}{\overline{\eta}_P(\eta_k)} + \gamma\Delta p_k$$

(5.32)

$$A_3 = 1 - \frac{CA_1\Delta p_k}{A_2\overline{\eta}_P(\eta_k)}$$

(5.33)

$$\Xi = \left[D^{-1} + \Delta p_k A_3 \cdot \frac{\partial n_k}{\partial \eta_k}\right]^{-1}$$

(5.34)

$$B_1 = g_2(\Delta p_k) + \frac{\Delta p_k}{A_2}\cdot\left(\frac{\partial n_k}{\partial \eta_k} : g_3(\Delta p_k)\right)$$

(5.35)

$$B_2 = n_k - \frac{C\Delta p_k}{A_2\overline{\eta}_P(\eta_k)}\cdot\eta_k - \frac{\gamma\Delta p_k}{A_2}\cdot\alpha_k$$

(5.36)

The plastic multiplier is then updated for step (k) as follows

$$\Delta p^{i+1}{}_k = \Delta p^i{}_k + d\Delta p_k$$

(5.37)

The stress tensor, the backstress tensor and the isotropic hardening function are also updated based on the new values of the plastic multiplier and other state variables as follows

$$\sigma^{i+1}{}_k = \sigma^i{}_k + \Delta\sigma_k$$

(5.38)

$$\alpha^{i+1}{}_k = \alpha^i{}_k + \Delta\alpha_k$$

(5.39)

$$\sigma^{i+1}{}_u{}^Y = \sigma_u{}^Y\left(p_n + \Delta p\right) \tag{5.40}$$

The Newton iterative cycle continues until the residuals $g_1(\Delta p_k)$, $g_2(\Delta p_k)$, and $g_3(\Delta p_k)$ are smaller than a prescribed tolerance (Figure 5.1).
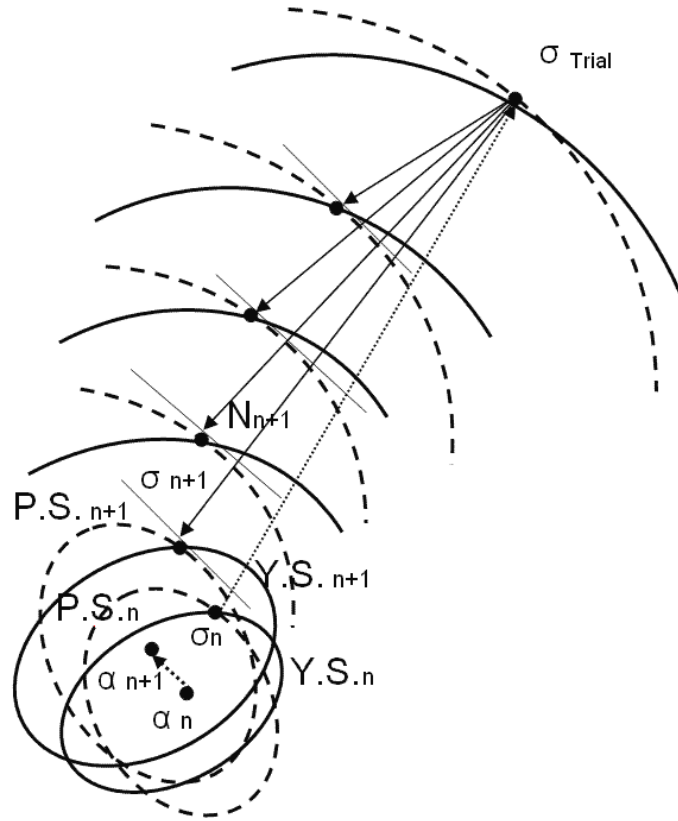
Figure 5.1. Multi-stage return mapping method to improve convergence in backward-Euler integration of NAFR-NKH model.

5.3.3. Consistent tangent modulus

To preserve the quadratic rate of asymptotic convergence for the Newton-Raphson algorithm of the global finite element equilibrium equations, the consistent elasto-plastic tangent modulus has to be derived for the specific stress integration algorithm (Simo and Hughes, 1998). The elasto-plastic tangent modulus should be returned to the global finite element solver after getting the local stress integration equations converged. Therefore, in its derivation it should be assumed that all stress integration equations are numerically solved. It was verified that the following parameters will reach a specific value after convergence is achieved during the return mapping procedure

$$A_1 = \left(1 - \frac{(\boldsymbol{n}_k : \boldsymbol{\eta}_k)}{\overline{\eta}_P(\boldsymbol{\eta}_k)} \right) \rightarrow 0 \tag{5.41}$$

$$A_2 = \left(1 + \frac{CA_1 \Delta p_k}{\overline{\eta}_P(\boldsymbol{\eta}_k)} + \gamma \Delta p_k \right) \rightarrow 1 + \gamma \Delta p \tag{5.42}$$

$$A_3 = \left(1 - \frac{CA_1 \Delta p_k}{A_2 \overline{\eta}_P(\boldsymbol{\eta}_k)} \right) \rightarrow 1 \tag{5.43}$$

$$\Xi = \left[\mathbf{D}^{-1} + \Delta p_k A_3 . \frac{\partial \boldsymbol{n}_k}{\partial \boldsymbol{\eta}_k} \right]^{-1} \rightarrow \left[\mathbf{D}^{-1} + \Delta p \frac{\partial \boldsymbol{n}}{\partial \boldsymbol{\eta}} \right]^{-1} \tag{5.44}$$

Knowing the residuals g_1, g_2, and g_3 are numerically zero after convergence, the following evolution equations can be written for the backstress tensor's increment

$$\Delta \boldsymbol{\alpha} = \frac{1}{1 + \gamma \Delta p} \left[\frac{C}{\overline{\eta}_P(\boldsymbol{\eta})} . \boldsymbol{\eta} - \gamma . \boldsymbol{\alpha} \right] d\Delta p \tag{5.45}$$

The stress tensor's increment also can be written as

$$\Delta \boldsymbol{\sigma} = \mathbf{D} . (\Delta \boldsymbol{\varepsilon} - \Delta \boldsymbol{\varepsilon}^p) = \Xi . [\Delta \boldsymbol{\varepsilon} - \boldsymbol{n} . d\Delta p] \tag{5.46}$$

Since the increment of the plastic strain tensor by using the backward-Euler method is given by

$$\Delta \boldsymbol{\varepsilon}^p = \boldsymbol{n} . d\Delta p + \Delta p \frac{\partial \boldsymbol{n}}{\partial \boldsymbol{\eta}} . \Delta \boldsymbol{\sigma} \tag{5.47}$$

By substituting the above equations in the consistency condition we have

$$\boldsymbol{m} : \Xi : [\Delta \boldsymbol{\varepsilon} - \boldsymbol{n} . d\Delta p] - \boldsymbol{m} : \frac{1}{1 + \gamma \Delta p} \left[\frac{C}{\overline{\eta}_P(\boldsymbol{\eta})} . \boldsymbol{\eta}_k - \gamma . \boldsymbol{\alpha} \right] d\Delta p - H . d\Delta p = 0 \tag{5.48}$$

This gives the following equation for the plastic multiplier increment

$$d\Delta p = \frac{m : \Xi : \Delta\varepsilon}{m : \Xi : n + \dfrac{C}{\overline{\eta}_P(\eta)(1 + \gamma\Delta p)}(m : \eta) - \dfrac{\gamma}{1 + \gamma\Delta p}(m : \alpha) + H} \tag{5.49}$$

Substituting the above relation in the (5.46) and solve it for the incremental relation of the stress and strain tensors, the following elasto-plastic tangent modulus is derived

$$\tilde{\mathbf{D}}^{\mathbf{ep}} = \Xi - \frac{\Xi.n \otimes \Xi.m}{m : \Xi : n + \dfrac{C}{\overline{\eta}_P(\eta)(1 + \gamma\Delta p)}(m : \eta) - \dfrac{\gamma}{1 + \gamma\Delta p}(m : \alpha) + H} \tag{5.50}$$

Of course, the above relations are written for the general non-associated case, so that for the NAFR model this modulus is non-symmetric. But they can easily be retrieved for the associated case by assuming the equality of the yield and potential functions. In the AFR case the higher-ranked elasto-plastic tensor (5.50) will be symmetric.

5.4. Results and discussion

Two types of sheet forming processes were simulated using the above anisotropic models. In the first category three different cylindrical cup drawing processes with three different aluminum alloys were simulated to evaluate the ability of each model to predict the earing profile of the formed cups as a measure of anisotropy. In the second category, two channel draw processes with different drawbead penetrations were performed with two different materials (DP steel and aluminum alloy) to evaluate the effect of anisotropic models on the prediction of springback.

5.4.1. Cylindrical cup drawing tests

5.4.1.1. Experimental parameters

Three different cup drawing processes all producing cylindrical shapes with different drawing ratios were simulated using the above-mentioned anisotropic models. For each drawing process different aluminum alloy sheets were used as follows: AA2008-T4 (Case a), AA2090-T3 (Case b), and Al-5%wt Mg (Case c). A schematic view of the cup drawing process with detailed dimensions of the tooling and the blank is shown in Figure 5.2.
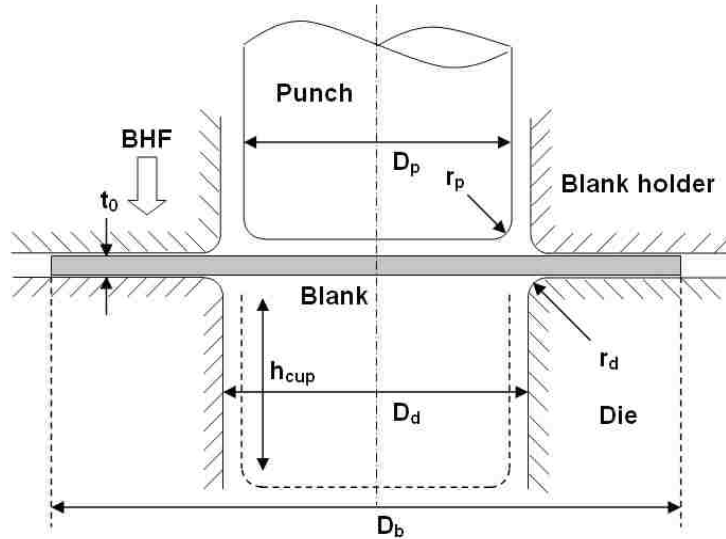
Figure 5.2. Schematic of cup drawing process.

For each case of sheet material, different process parameters were assigned according to the associated references. The process parameters for different cases are provided in Table 5.1.

Table 5.1. Cup drawing process parameters based on Figure 5.2 (all dimensions are in mm).

Material	D_p	r_p	D_d	r_d	D_b	t_0	h	BHF(kN)	COF
AA2008-T4 a	97.18	4.78	100.08	6.35	162	1.24	40-45	22.2	0.1&0.2
AA2090-T3 b	97.46	12.7	101.48	12.7	158.76	1.6	35-48	22.2	0.1
Al-5%Mg c	50	5	52.8	5	100	1	34-40	4.9	0.02

Chung and Shah (1992) implemented the Yld91 and simulated the cup drawing Case a. Yoon et al. (1999a; 1999b) also compared the results obtained by using Yld91 and Hill's48 simulations with the experimental measurements for this Case. In another work Yoon et al. (2000) implemented Yld96 and simulated the earing of the Case b by using Yld91 and Yld96. By adopting the work done by Yoon et al., Cvitanic et al. (2008) simulated the earing of Case a and Case b by using NAFR and K-B models. Yoon et al. (2006) simulated the earing of Case b by using the advanced model Yld2004-18p and an analytical approach. Finally, Yoon et al. (2004) modeled the earing of Case c by using the Yld91, Yld94, Yld96, and Yld2000-2d.

5.4.1.2. Material characterization

Seven material inputs were required for the NAFR model: uniaxial yield stresses and r-values at 0, 45, and 90° from the rolling direction, and the balanced biaxial yield stress. The Yld2000-2d model required the same seven parameters as input, as well as balanced biaxial r-value (r_{EB}). If

r_{EB} is not available the second model also can work with the same seven parameters by assuming an appropriate simplification. Therefore, both models are able to consider the effect of r-values and yield stresses on the anisotropic behaviour. Anisotropic material characterizations of different Al-alloy cases are shown in Table 5.2. Also the isotropic hardening parameters are shown for each case in this table.

Table 5.2. Yield stresses and r-values of the Al-alloy sheets in different directions and the isotropic hardening parameters.

Material	Direction	0	45	90	EB	Hardening	σ0	Q	b
AA2008-T4 a	σY/ σu	1	0.945	0.904	0.875	Isotropic	164	234	8.5
	r-values	0.878	0.498	0.534	-	Mixed	-	-	-
AA2090-T3 b	σY/ σu	1	0.811	0.910	1.035	Isotropic	280	353	3.65
	r-values	0.211	1.577	0.692	0.67	Mixed	-	-	-
Al-5% Mg c	σY/ σu	1	1.04	1.075	0.95	Isotropic	85.4	250.8	6.24
	r-values	0.27	0.58	0.29	-	Mixed	-	-	-

Each anisotropic model needs 8 coefficients based on the theoretical definitions. These coefficients obtained from material parameters for different Al-alloy cases are shown in Table 5.3.

Table 5.3. Anisotropic coefficients for different sheet materials based on two anisotropic models.

NAFR	AA2008-T4	AA2090-T3	Al-5% Mg	Yld20002d	AA2008-T4	AA2090-T3	Al-5% Mg
M1	0.306	0.424	0.253	$\alpha 1$	0.915	0.486	0.959
M2	0.361	0.243	0.414	$\alpha 2$	1.155	1.378	0.806
M3	0.509	0.380	0.325	$\alpha 3$	1.211	0.754	1.107
M4	1.056	1.691	0.863	$\alpha 4$	1.152	1.025	1.010
P1	0.312	0.116	0.142	$\alpha 5$	1.056	1.036	1.059
P 2	0.355	0.550	0.525	$\alpha 6$	1.211	0.904	1.069
P 3	0.578	0.168	0.489	$\alpha 7$	1.016	1.232	0.938
P 4	0.937	1.492	1.095	$\alpha 8$	1.041	1.486	0.911

Using the obtained anisotropic coefficients, yield and potential surfaces in 2D stress space were predicted by NAFR and Yld2000-2d models (at zero shear stress) for different Al-alloys and are shown in Figure 5.3.
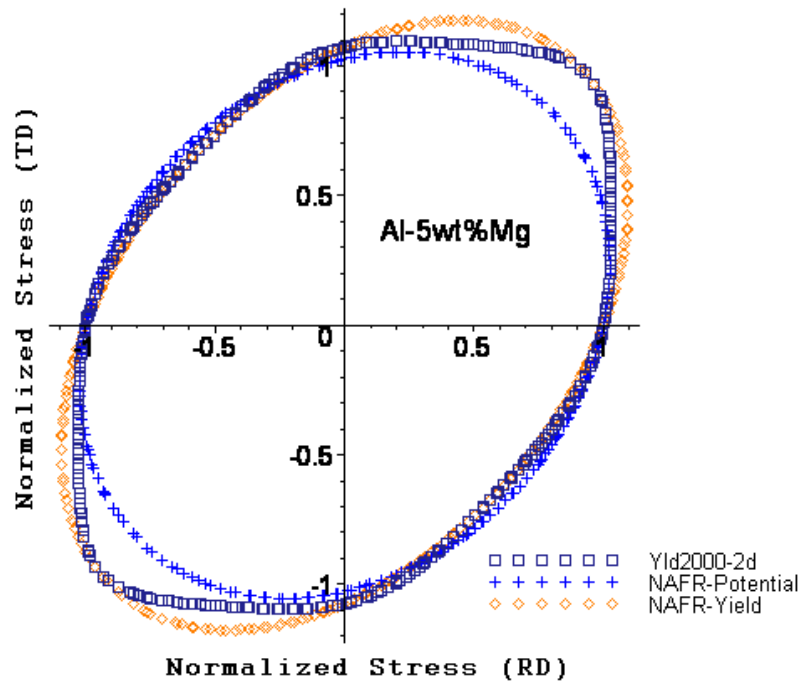
(5.3. a)
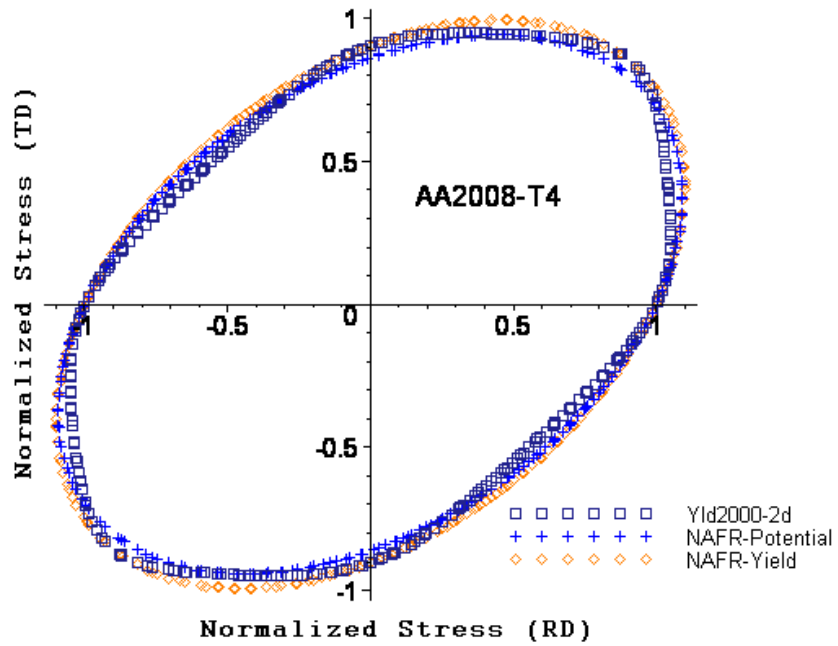
(5.3. b)
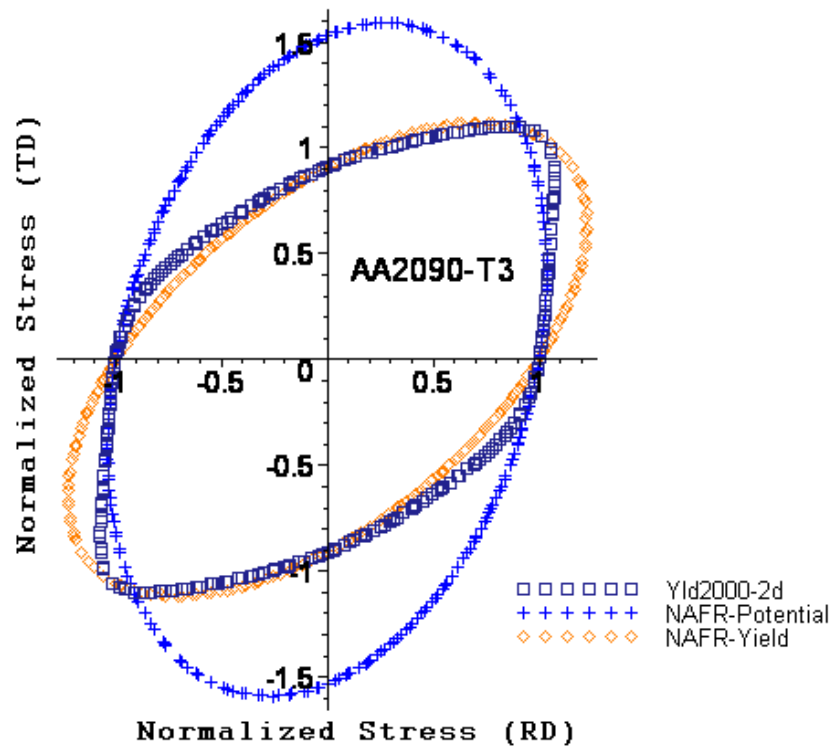
(c)

Figure 5.3. Yield and potential surfaces in 2D stress space predicted by different models (at zero shear stress) for Al-5%Mg (a), AA2008-T4 (b) and AA2090-T3 (c).

5.4.1.3. Finite element models

All tools were modelled as rigid bodies. A shell element formulation with reduced integration mode was used to model the blank, and due to symmetry only one quarter of the blank was simulated. Typical parts defined and assembled for the FE simulations are shown in Figure 5.4. To evaluate the mesh sensitivity of the earing simulations three different mesh systems were used to model the blank: Mesh1 that is a very coarse mesh consisting of mostly quadrilateral with a few triangular elements, Mesh2 that is a uniform fine mesh with all quadrilateral elements, and Mesh3 that is a very fine mesh with all triangular elements. These different mesh systems are shown in Figure 5.5.

 All cup drawing processes were simulated in the implicit time integration scheme, so that a UMAT (user-defined material for ABAQUS/Standard, ABAQUS, 2007) was needed for the material models. It should be noted that special attention might be needed for the convergence issue due to the severe deformation and contact discontinuities arising during the simulations.
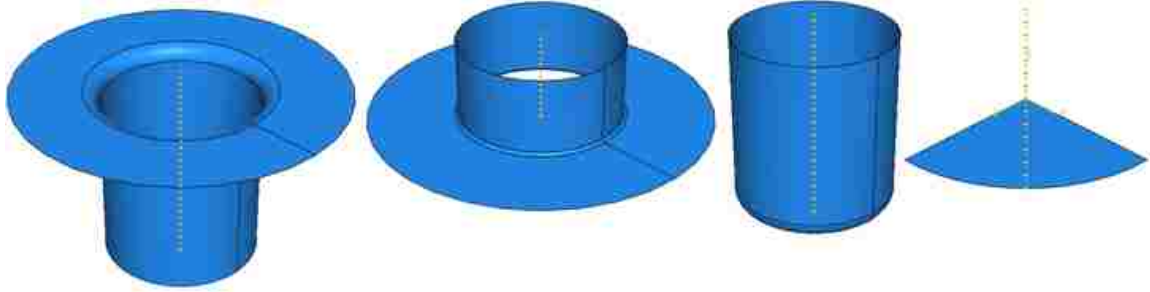
Figure 5.4. Typical parts in the FE model: Die, Holder, Punch, and Blank.

| (a) | (b) | (c) |
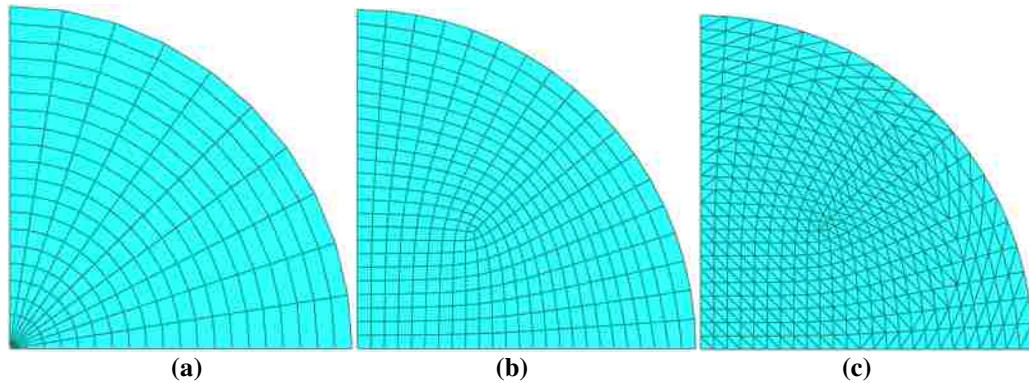
Figure 5.5. Different mesh systems for the blank: (a) Mesh1, (b) Mesh2, and (c) Mesh3.

5.4.1.4. Cup drawing simulation results

Typical deep drawing and earing formation of a cylindrical cup at different stages of the simulation with counters of the effective stress is shown in Figure 5.6. This example is for the case of Al-5%Mg alloy simulated with NAFR model and Mesh2. In total, 18 simulations were performed to get the earing profiles (cup height after drawing) of three different cases using two different material models (NAFR and Yld2000-2d) and three different mesh systems. It should be noted that the earing results obtained by both models with different hardening regimes (pure isotropic and mixed isotropic-nonlinear kinematic hardening) are almost identical, i.e. the hardening does not affect the earing prediction. Hence, only one set of results (obtained by pure isotropic hardening) are presented here.
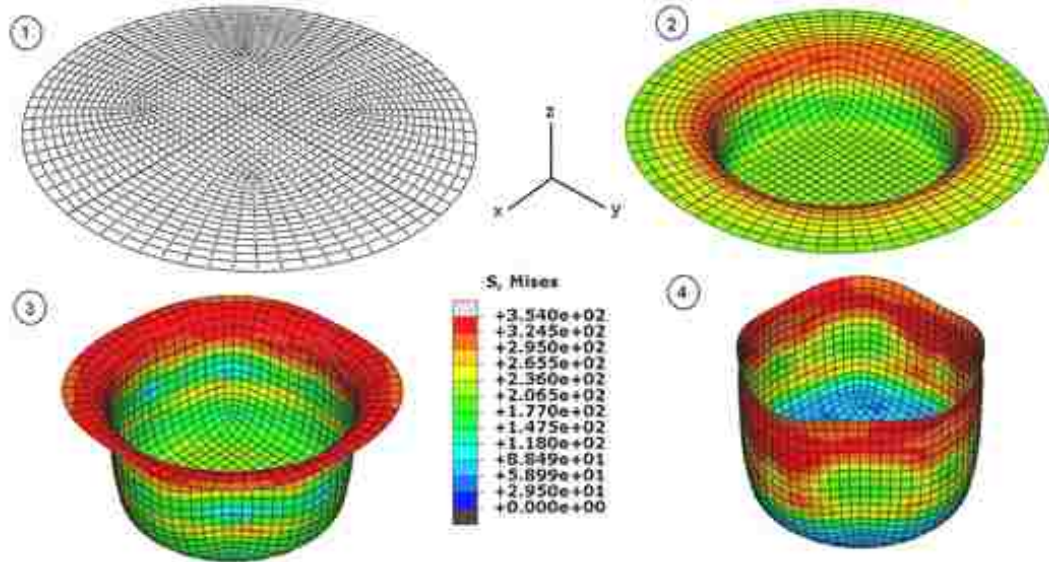
Figure 5.6. Typical deep drawing and earing formation of a cylindrical cup at different stages of the simulation with counters of the effective stress (this example is for Al-5%Mg alloy simulated with NAFR model and Mesh2).

The earing predictions using two different anisotropic models for Al-5%Mg alloy are shown in Figure 5.7. Obviously for this case the earing result predicted by NAFR model is closer to the experimental measurements than that predicted by the Yld2000-2d both in trend and accuracy. The earing profile predicted by NAFR model is in good agreement with the experimental values over the entire region except in the vicinity of 45 degree. On the other hand, the earing profile predicted by Yld2000-2d underestimates the experimental measurements in the region near 45 degrees while it overestimates the measurements in the regions near 0 and 90 degrees. Regarding the mesh sensitivity, the results obtained by using Mesh2 and Mesh3 are very similar for both material models while the results obtained with Mesh1 are slightly different from the others. In fact the simulations performed with the finer mesh system (Mesh2 and Mesh3) predict the earing slightly better than those performed with the coarser mesh system (Mesh1).

144
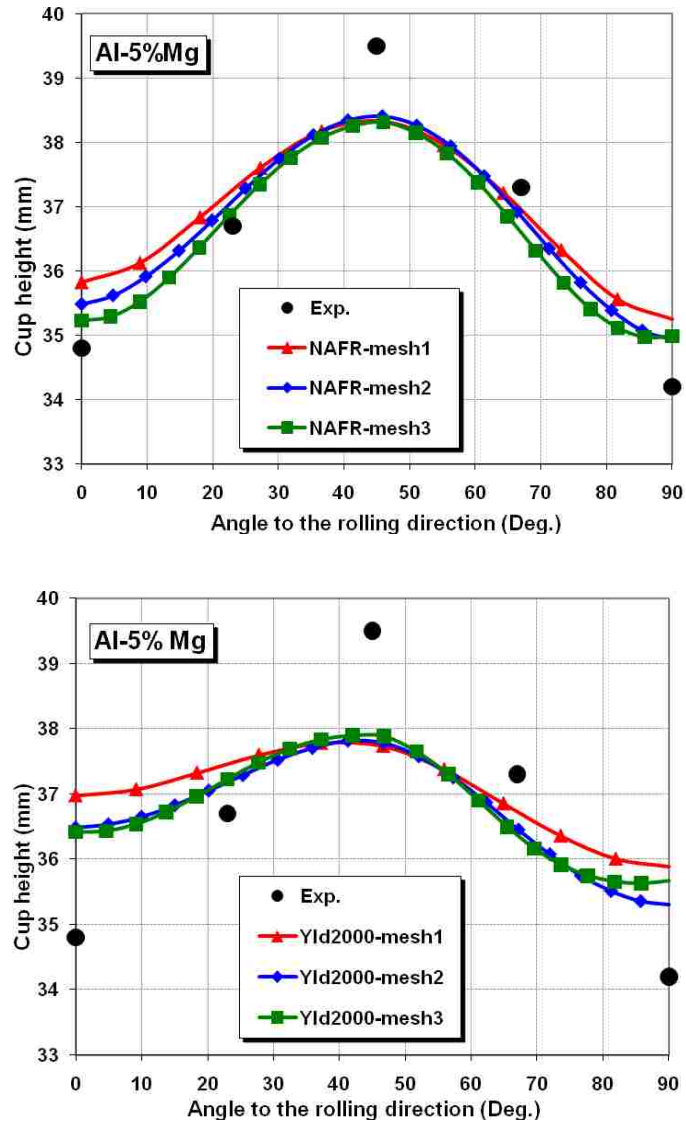
Figure 5.7. Comparison of earing profiles for Al-5%Mg calculated using NAFR (top) and Yld2000-2d (bottom) with measured values.

The earing prediction using two different anisotropic models for AA2008-T4 alloy is shown in Figure 5.8. In this case both models underestimate the experimental values over almost the entire region. It can be seen that the earing profile obtained by NAFR model predicts the earing trend better than that obtained by Yld2000-2d model. However, the earing profile predicted by Yld2000-2d model is in better agreement with the experimental values in terms of the absolute cup height. Even so, the differences between height values predicted by NAFR model and experimental measurements are less than 1mm in most of the region. Again, the results obtained by using different mesh systems are very similar for finer meshes while a small difference is noticeable for the results obtained with Mesh1.
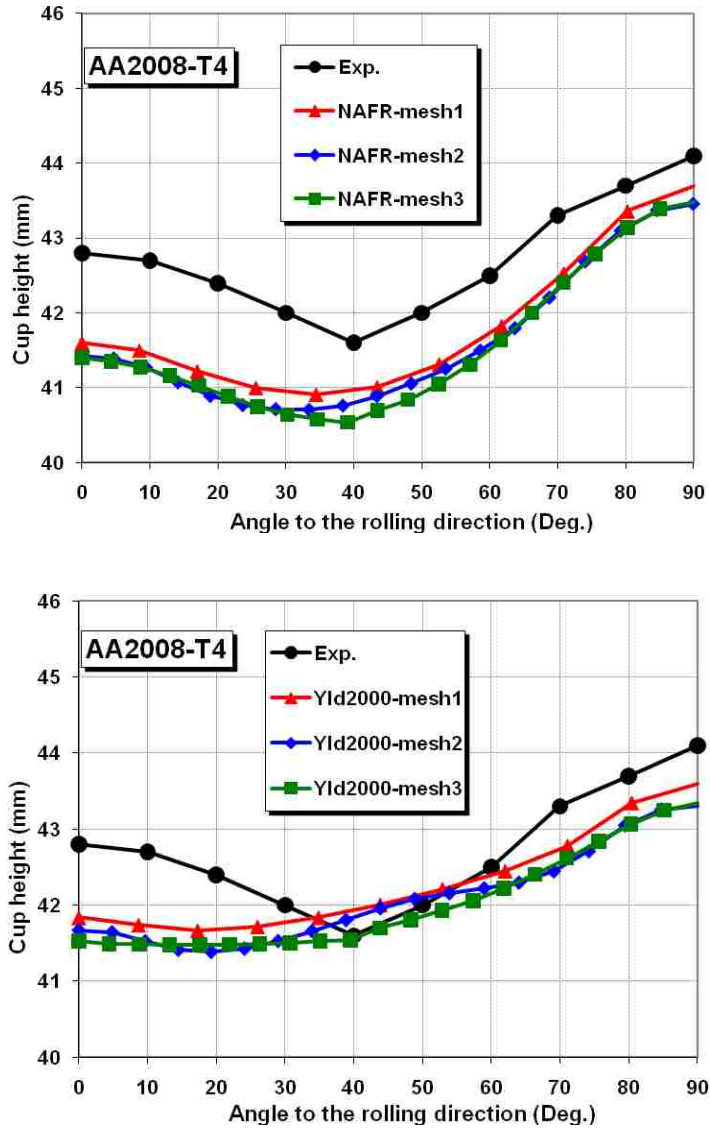
Figure 5.8. Comparison of earing profiles for AA2008-T4 calculated using NAFR (top) and Yld2000-2d (bottom) with measured values.

The earing prediction using two different anisotropic models for AA2090-T3 alloy is shown in Figure 5.9. Both models predict the earing trend well, while the NAFR shows better agreement with the fact that the cup height is a bit smaller in the 90 degree point than the 0 degree point. However, the earing predicted by Yld2000-2d model is in better agreement in regions near the 0 and 90 degrees in terms of the absolute cup height. But in the region near 45 degrees (around the peak point) the values for the absolute cup height predicted by NAFR model are closer to the experiments than those predicted by Yld2000-2d model. Also, it can be seen that the earing profile predicted by Yld2000-2d model with Mesh1 is significantly different from the results with finer meshes.
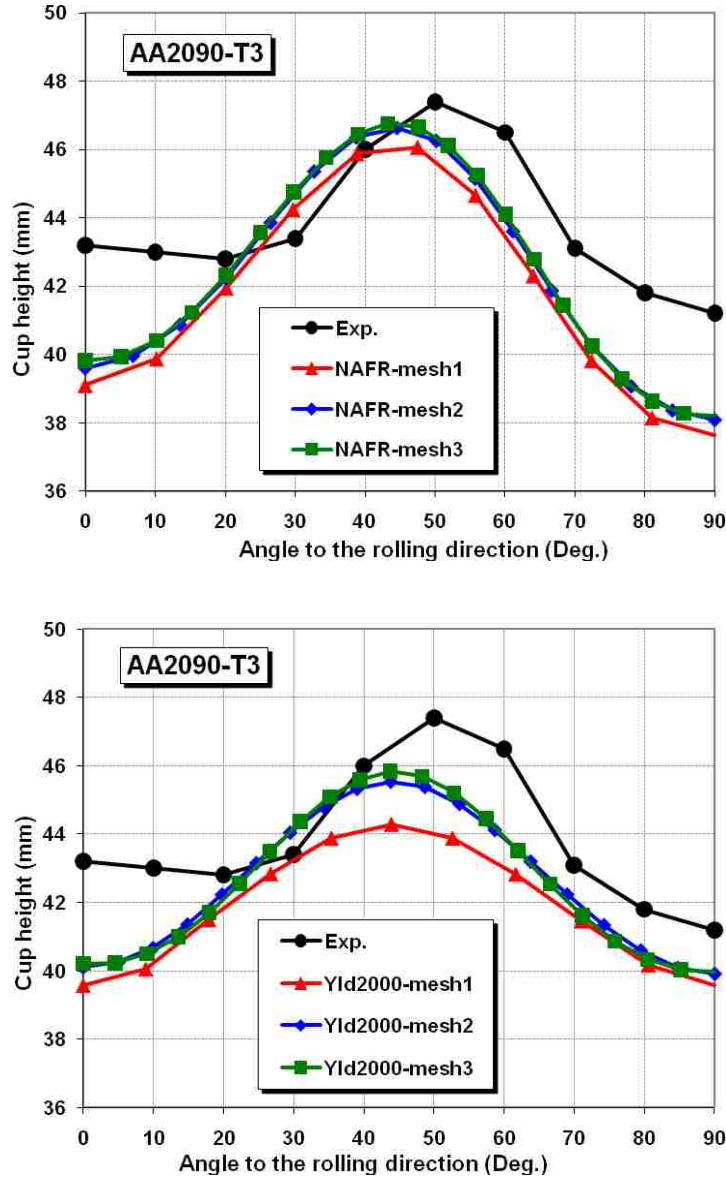
Figure 5.9. Comparison of earing profiles for AA2090-T3 calculated using NAFR (top) and Yld2000-2d (bottom) with measured values.

One important aspect of the advanced material models developed for more effective simulations of sheet metal forming is computation time. In fact, some advanced micro- and macro-constitutive models have been developed which are able to predict the elasto-plastic behaviour of sheet metals very well, but the expensive computation time is a significant disadvantage for these models. Computation times for different cup drawing processes with different anisotropic models and mesh systems are shown in Figure 5.10. All simulations were performed under the same conditions with the same machine (HP-DL585) with 4 CPUs (AMD-Opteron, 2.6 GHz, dual core) and 32 GB of RAM memory working on a Linux platform. For all cases the computation time of

147

NAFR model simulations is less than that of Yld2000-2d model. Although, two independent functions used in NAFR model as yield and potential and also a non-symmetric material Jacobian are clear reasons for more expensive simulations, but the non-quadratic nature of Yld2000-2d model and huge volume of the first and the second derivatives (required for the Euler-backward method) significantly increase the computation time compared to NAFR. Computation times for NAFR model simulations varied between a minimum 32% to maximum 82% of Yld2000-2d model simulations. In average, simulation time by using NAFR model was about 34% less than that for the Yld2000-2d model.
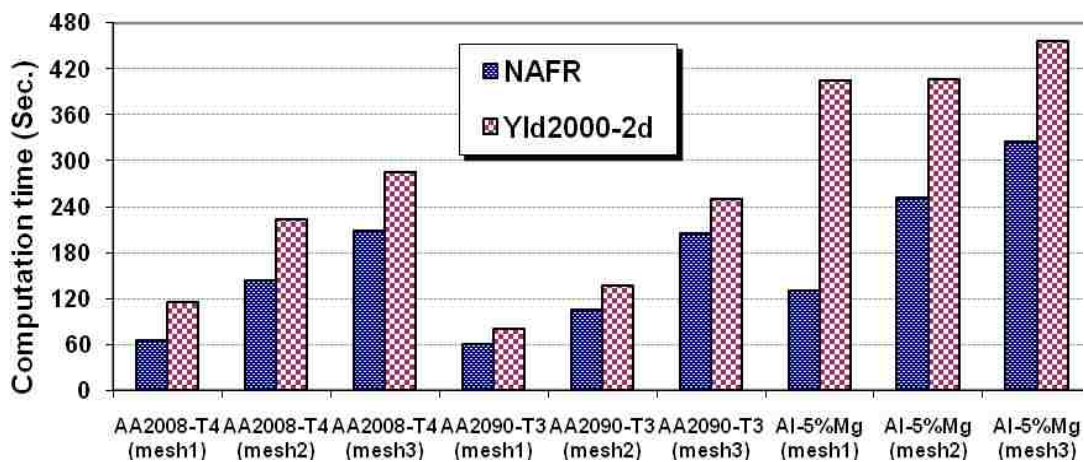
Figure 5.10. Computation times for different cup drawing cases with different models and meshes.

5.4.2. Channel draw with drawbead

5.4.2.1. Experimental parameters

Both the forming and subsequent springback stages of the Numisheet'05 Benchmark #3 were simulated for different drawbead penetrations using the commercial code ABAQUS. Two different sheet materials (DP600 and AA-6022-T43) were used to evaluate the ability of material models to predict the springback in the drawn channel section. The results for the deepest and shallowest penetrations will be presented: (i.e. 25 & 75% for DP600 and 25 & 100% for AA6022-T43). The sidewall curl after springback was recorded for each sheet material and for each prestrain condition, using a 2D laser scanner (LaserQC™). Further technical details about the experimental procedure, process parameters and tooling may be found in the Section 3.4 of the dissertation or the following references: (Green, 2005; and Stoughton et al., 2005).

5.4.2.2. Material characterization

Tension-Compression test

In-plane cyclic tension-compression (T-C) tests were carried out to obtain the cyclic stress-strain behaviour of the different sheets (DP600 and AA6022-T43). In order to avoid the limitations of existing designs for in-plane compression, a new approach was developed at Ohio State University by Boger et al. (2005). Solid, flat plates were used for buckling constraint, and a special specimen design was developed to minimize buckling outside of the constrained region (Figure 5.11). The solid plates offer several advantages over fork designs including better self-alignment, much easier machining, and better durability. The Enerpac^{TM} P141 hand pump and RWH200 hydraulic cylinder were used to apply a restraining force to the sample through four sets of hardened steel rollers. The hydraulic clamping system is a significant improvement over the other methods discussed earlier. Control of the supporting force at a specific value allows for more robust biaxial and friction corrections than in systems where the support is provided by plates connected by bolts or springs, where the actual supporting force is unknown or uncontrolled. The experimental conditions were optimized to achieve two competing goals: maximize the attainable compressive strains, and maximize the uniformity of strain and stress in the gage length of the specimen. The clamping force was optimized through FEA simulations, and the optimum side force is between 5-10 kN (depending on the material and the thickness), where the side forces are sufficient to prevent buckling, yet the frictional effects are minimized. Current tests configurations use a non-contact, EIR^{TM} laser extensometer, which enables the plates to cover the entire surface of the specimen that is an effective way to eliminate buckling along the edge. In all of the experiments a constant crosshead speed of 0.03 mm/s was used. The deforming length of the sample is approximately 30 mm, so the strain rate is 0.001/s. More details about the tests conditions might be found in Boger et al. (2005).
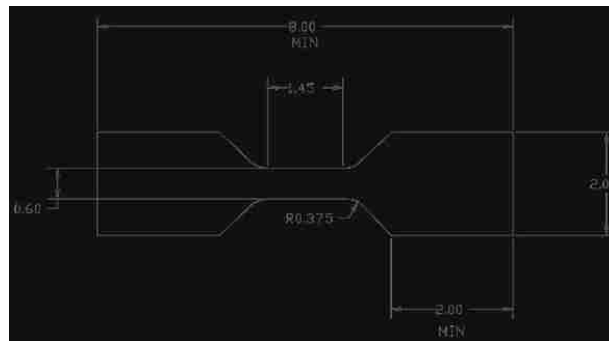
Figure 5.11. Geometry of the tension-compression test specimen (dimensions, in).

Data correction for T-C tests

Because of the need to constrain the sample in the thickness direction to prevent buckling, all raw stress-strain results require corrections for frictional and biaxial effects arising from this supporting force (Boger et al., 2005). The addition of a constraining force creates a readily calculated through-thickness stress. Knowing this value, and by using the von Mises or Hill's 48 effective stress the corrected value can be obtained. However, the biaxial effect is small and the friction correction is more significant and more complex because the direction of the friction force reverses when the loading direction changes. To reduce friction, the side supports were covered with a 0.35 mm Teflon sheet, and the supporting force was transmitted from the hydraulic pump to the supports through a series of rollers that allowed the plates to move with the sample along the loading axis. The actual force deforming the sample is the value measured from the load cell with the additional frictional force subtracted. The frictional behaviour is represented by a Coulomb friction law (with a friction coefficient). It was found that the difference of friction coefficients between the tension and compression is very small, so an averaged number for both was used. The friction coefficient was found using repeated tests with different side forces. The slope of the best fit straight line for the "biaxiality-adjusted axial load vs. side force" is 2 times the friction coefficient (because the friction force is generated by the sliding of 2 contact surfaces). For comparing loads, a strain of +/- 0.02 was used during the first leg of the first cycle. In all cases the friction coefficient was quite small and reasonably consistent. Specific values that were found and used: DP600-0.036 and AA6022-T43-0.04. After both friction and biaxial corrections, the flow curve of the supported sample agrees well with the unsupported uniaxial tension test.

The exact same procedure explained in the Sections (3.3) and (4.3.1) was used to extract the mixed hardening material model parameters, i.e. the customized optimization of the least-squares method to fit the integrated curves to the experimental data points. After analytical stress integration, the mixed constitutive model for the uniaxial condition can be rewritten as

$$\sigma_t^{\,1} = \sigma_0 + Q(\,1 - e^{-b.p}\,) + \frac{C}{\gamma}(\,1 - e^{-\gamma.p}\,) \tag{5.51a}$$

$$\sigma_c^{\,1} = -\sigma_0 - Q(\,1 - e^{-b.p}\,) - 2\frac{C}{\gamma}(\,1 - e^{-\gamma.(p-p1)}\,) + \frac{C}{\gamma}(\,1 - e^{-\gamma.p1}\,) \tag{5.51b}$$

where subscripts t and c stand for tensile and compressive loading and $\sigma_t^{\,1}$ and $\sigma_c^{\,1}$ are stress in loading and reverse loading, respectively. Parameter p_1 is the amount of plastic strain at the end of the loading cycle. This is shown schematically in Figure 5.12. Again, for each material the

optimum combination of hardening parameters was found for one cyclic and one tensile curve in a way that they fitted to the experimental data points so as to obtain the best agreement for all curves. The cyclic tension-compression stress-strain data obtained experimentally was compared with that obtained by the mixed hardening model (NKH) and is shown in Figure 5.13. Table 5.4 shows the summary of the hardening parameters used in the simulations.
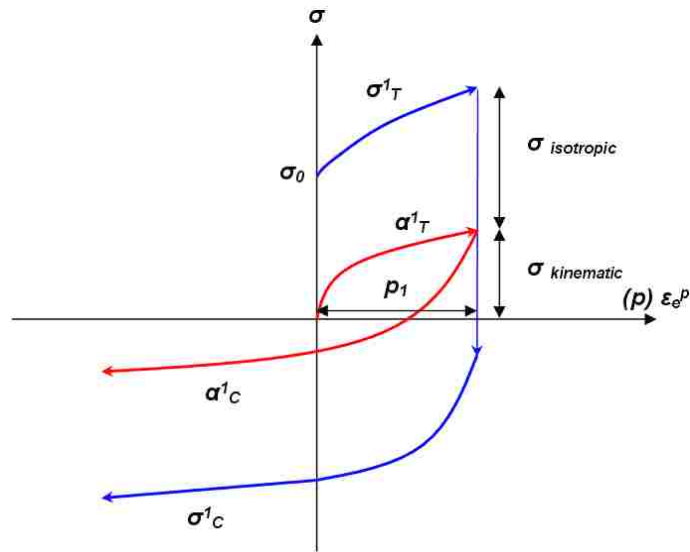
Figure 5.12. Illustration of cyclic hardening behaviour in different cycles using the mixed NKH model.

Table 5.4. Summary of the sheet materials mixed hardening parameters.

Material	Initial Yield Stress	Mixed Nonlinear Hardening			
	σ_0 (MPa)	C (MPa)	γ	Q (MPa)	b
AA6022-T43	135	2000	85	230	5
DP600	400	11000	80	350	7
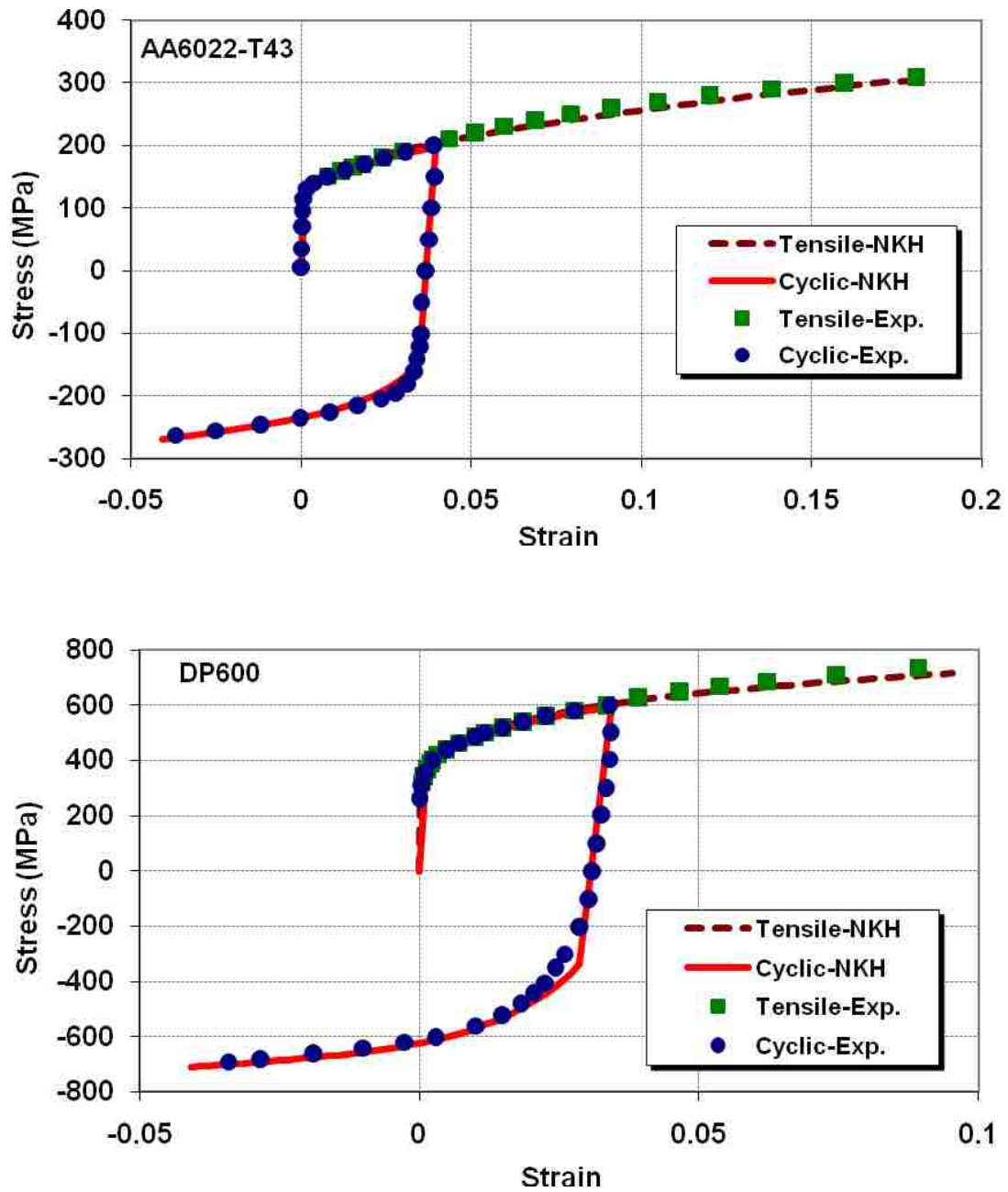
Figure 5. 13. Experimental cyclic stress-strain data (T-C test) compared with the NKH model for aluminum alloy AA6022-T43 (top) and DP600 (bottom) steel sheets.

As it is clear, the main difference between the stress-strain cycles obtained by two different test methods (cyclic shear and T-C tests) is that the level of strain in which the reverse loading is applied in the tension-compression tests is significantly lower than that in the cyclic shear tests. The reason is obvious: since the buckling is a major issue in the T-C tests the direction of loading

should be reversed at a much smaller amount of strain. Also, the difference between mixed hardening parameters extracted from different tests is evident by comparing Table 5.4 and 3.1.

Anisotropy tests

Each model needs 8 anisotropic coefficients as explained above: α_1 to α_8 for Yld2000-2d model and M_1-M_4 plus P_1-P_4 for NAFR model. These are functions of r-values and yield stress ratios of uniaxial tests in different directions plus equibiaxial test. Therefore, the anisotropic measurements (r-values and yield stress ratios) were obtained by carrying out quasi-static tensile tests (ASTM E8 standard test method) at different orientations (0, 45, and 90 degrees) with respect to the rolling direction (Shi and Huang, 2005; Brem et al., 2005). Furthermore, the duplicate hydraulic bulge tests were conducted for each material to obtain the equal biaxial stress-strain behaviours. Also, the biaxial r-value of each sheet metal was evaluated using the disk compression test. In this test, a nominal 0.500-inch diameter full thickness specimen was heavily lubricated in order to minimize/maintain constant friction characteristics and subjected to incremental compressive loading/unloading cycles. After each load increment, the dimensional changes in the longitudinal (L) and transverse (T) diameters were measured in order to calculate strains (ε_L and ε_T) in the two directions. A regression analysis was conducted using the strain data in order to calculate a biaxial r-value (r_{EB}). Using the above test results the anisotropic coefficients for two models are found and presented in Table 5.5.

Table 5.5. Anisotropic coefficients for different sheet materials based on two anisotropic models.

NAFR	AA6022-T43	DP600	Yld20002d	AA6022-T43	DP600
M1	0.336	0.357	$\alpha 1$	0.966	0.968
M2	0.330	0.310	$\alpha 2$	1.083	0.985
M3	0.421	0.292	$\alpha 3$	1.034	0.916
M4	1.057	1.215	$\alpha 4$	1.072	0.973
P1	0.338	0.301	$\alpha 5$	1.030	0.984
P 2	0.328	0.366	$\alpha 6$	1.136	0.871
P 3	0.464	0.310	$\alpha 7$	0.989	0.970
P 4	0.818	0.956	$\alpha 8$	1.087	1.034

Using the above anisotropic coefficients, the yield and potential surfaces based on two anisotropic models can be drawn in 2D stress space (Figure 5.14).
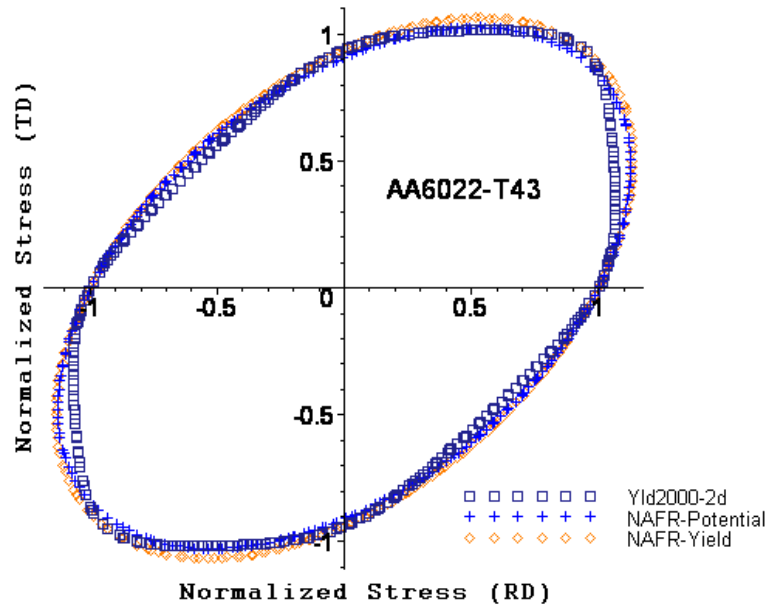
(a)
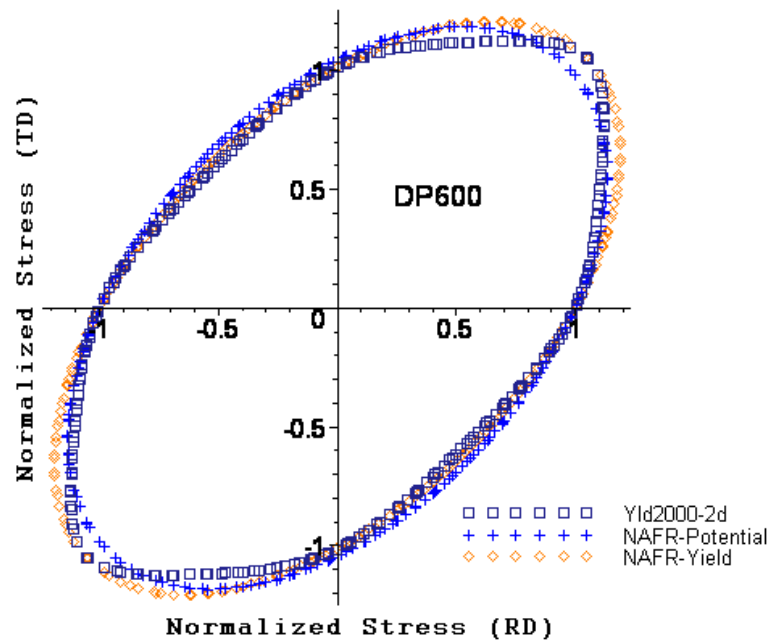
(b)

Figure 5.14. Yield and potential surfaces in the stress space predicted by different models (at zero shear stress) for AA6022-T43 (a) and DP600 (b).

5.4.2.3. Finite element models

Plane stress shell elements with reduced integration mode were used to model the sheet (denoted by S4R in ABAQUS) where 19 integration points were used through thickness to thoroughly simulate the cyclic stresses caused by bending-unbending deformation in the drawbead and die

shoulder. Only one half of the channel section was modeled due to the symmetry. A study of mesh sensitivity was conducted for different combinations of materials, penetrations, and constitutive models to find the best mesh in each case. The friction coefficient was assumed to be 0.12 for DP600 and 0.15 for AA6022-T43, and the classical Coulomb friction law with penalty algorithm was used as the contact model. Finally, the explicit-implicit scheme was used for forming and springback stages, respectively. User-defined material subroutines were developed for both explicit and implicit time integration schemes using the above non-associated and non-quadratic models.

5.4.2.4. Springback simulation results

A series of 8 simulations, each including separate explicit and implicit stages, were carried out: 4 with NAFR-NKH and 4 with Yld2000-2d-NKH. Also, the decrease of the unloading elastic modulus was implemented into the UMAT to improve the accuracy of the springback predictions. The profile of the channel sidewall after springback for AA6022-T43 at 25% and 100% drawbead penetration is shown in Figures 5.15. In the case of 25% drawbead penetration, both models predict the springback very well. However, the springback profile predicted by NAFR model is slightly higher than that predicted by Yld2000-2d model. In the case of 100% drawbead penetration, again, two models predict the springback well. But it seems that the prediction by Yld2000-2d model is slightly better than that by NAFR model. However, the difference is very insignificant and also similar to the 25% case the springback profile predicted by NAFR model is slightly higher than that predicted by Yld2000-2d model. It has often been pointed out that Hill's quadratic yield function is not able to represent the anisotropic behaviour of most aluminum alloys. But in this case the difference between the results of the non-quadratic Yld2000-2d and the quadratic NAFR (based on Hill's quadratic) models is very minor. To answer the paradox two reasons can be named: firstly, based on the numerical simulations and the experience of the authors, the prediction of springback is more sensitive to the hardening models than the yield descriptions. And secondly, this particular aluminum alloy does not show very strong anisotropy in its mechanical properties, therefore the role of anisotropic yield models is less important in springback simulations.
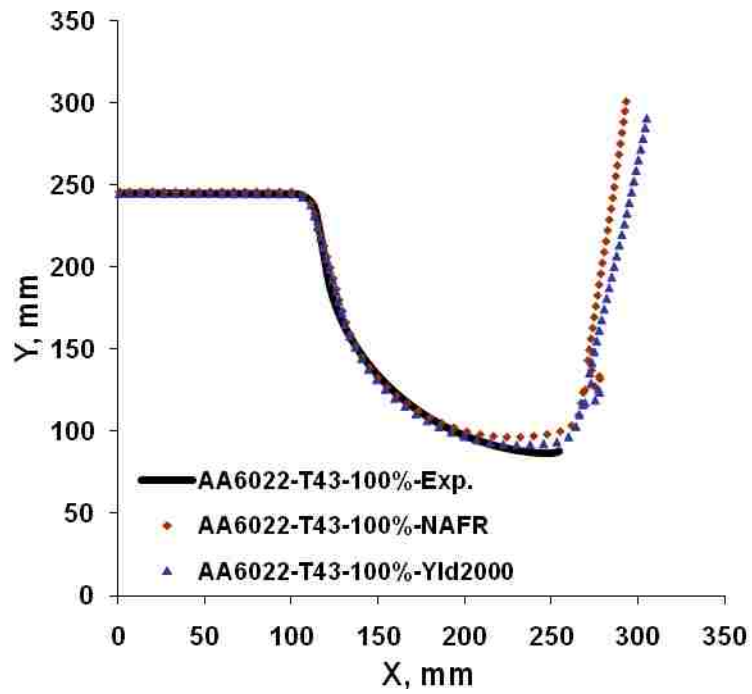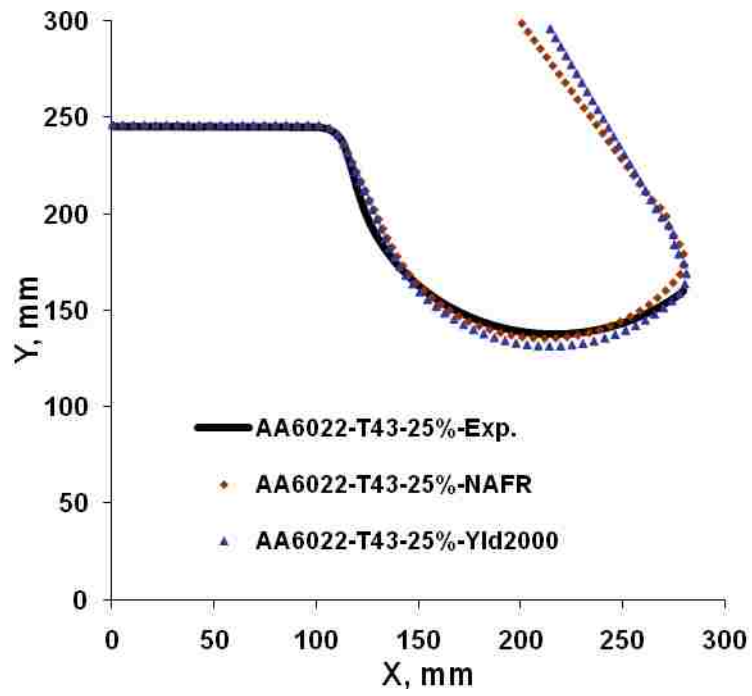
Figure 5.15. Springback profile of the AA6022-T43 channel sidewall for 25% (top) and 100% (bottom) drawbead penetration.

A comparison between the experimental sidewall profiles with those obtained by simulation at different drawbead penetrations for DP600 channel sections is shown in Figures 5.16. For both penetration cases the springback profiles predicted by two anisotropic models (Yld2000-2d and NAFR) are very similar. However, similar to the aluminum alloy case, the springback profiles predicted by the NAFR model are insignificantly higher than those predicted by the Yld2000-2d model. Also, it is clear that the shape and amount of springback profiles predicted by both models are a bit different from the experiments in the side wall of the channel. In fact, the simulation predictions for the aluminum alloy case are more accurate than those for DP600 steel. One reason to explain this is the fact that the hardening parameters for these simulations were identified from the cyclic T-C tests in which the amount of reverse strain is very small compared to the amount of the plastic strain that the sheet metal undergoes during the channel forming. And we know that the larger the amount of the reverse strain in the cyclic test is, the more realistic the extracted hardening parameters are. It is also well-known that the reverse loading behaviour of DP steel is more complicated than that of aluminum alloy (phenomenon such as work hardening stagnation is more severe for steels). Therefore, the predicted springback profiles for DP600 using cyclic shear tests (Taherizadeh et al., 2009a; b), with larger range of reverse strain, are slightly more accurate than those predicted by using the cyclic T-C tests.
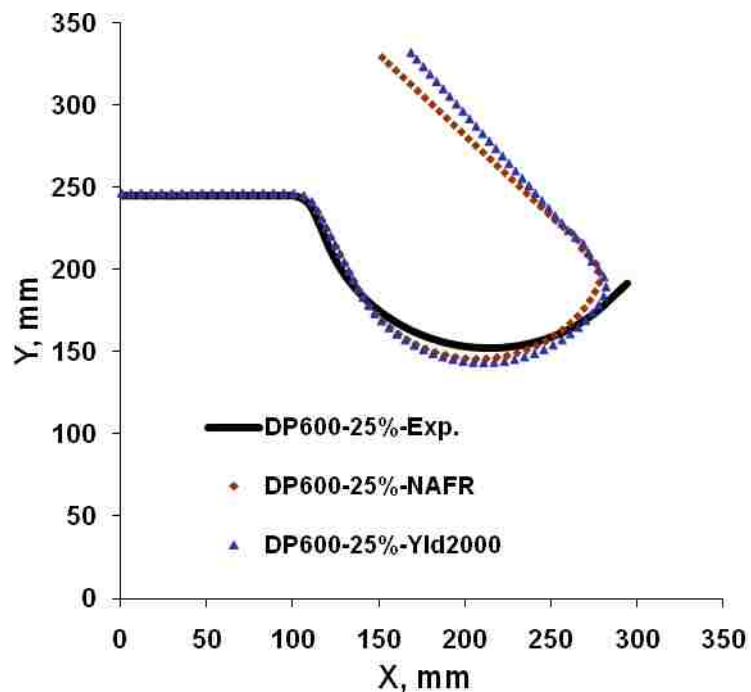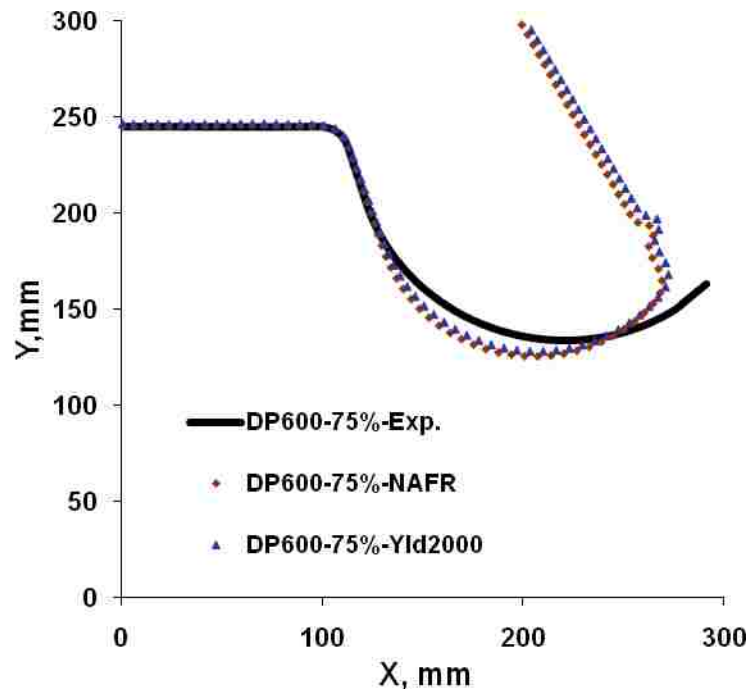
Figure 5.16. Springback profile of the DP600 channel sidewall for 25% (top) and 75% (bottom) drawbead penetration.

Once again, computation times for different channel draw processes with different anisotropic models are shown in Figure 5.17. All simulations were performed under the same conditions with the same machine (HP-DL585) with 4 CPUs (AMD-Opteron, 2.6 GHz, dual core) and 32 GB of RAM memory working on a Linux platform. For all cases the computation time of NAFR-NKH model simulations is less than that of Yld2000-2d-NKH model. The same reasons explained before significantly increase the computation time of Yld2000-2d-NKH model compared to NAFR model. The differences between computation times of the NAFR and Yld2000-2d models for these simulations are even larger than the differences for the cup drawing processes. In average, simulation time by using NAFR-NKH model was about 60% less than that for the Yld2000-2d-NKH model.
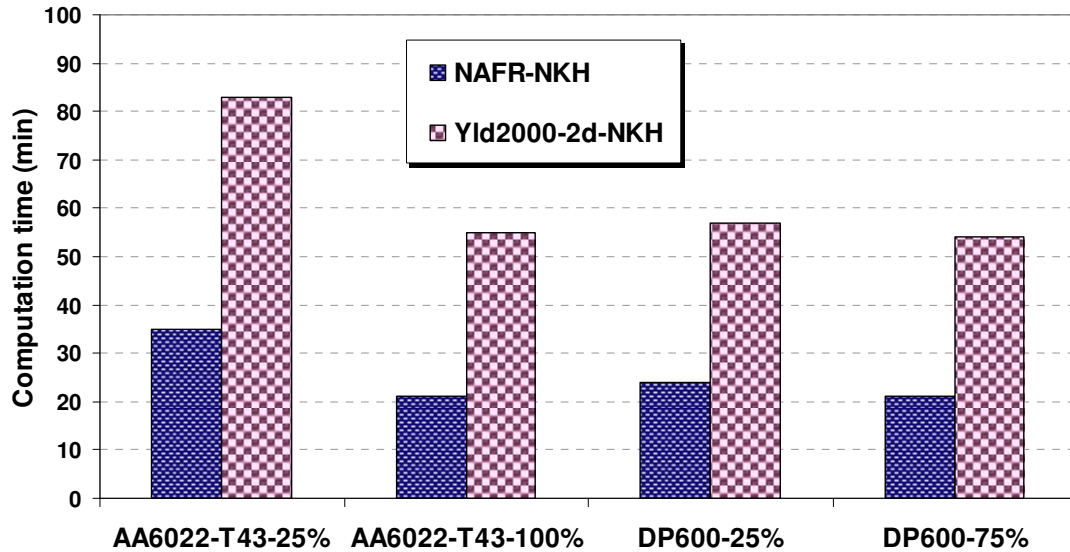
Figure 5.17. Computation times for different channel draw processes with different models.

5.5. Summary and Conclusions

Two anisotropic models for simulation of sheet metal forming processes were compared in this work. The first model was based on a non-associated formulation with both yield and potential functions in the form of Hill's 1948 quadratic function. The second model was a non-quadratic yield function based on two linear transformations of the stress tensor originally developed by Barlat et al. for isotropic hardening (so-called Yld2000-2d). Both models were implemented based on two frameworks of pure isotropic hardening and mixed isotropic-nonlinear kinematics hardening as user-defined material subroutines into the commercial nonlinear finite element code ABAQUS. Backward- Euler method was used to integrate the stress and other state variables over each time increment. Cyclic tension-compression tests were performed to generate the stress-strain curves. Mixed hardening parameters were also extracted from these tests and used for the finite element simulations. For demonstration, three different cup drawing processes were simulated using the above anisotropic models and the results were presented. It was shown that, in general the quadratic NAFR predicted the cup height trend better than the associated non-quadratic model, while in some cases the non-quadratic model predicted the cup height value slightly better than NAFR. Also, these two models were used to simulate the springback of a channel draw process with different drawbead penetrations. The results show that the springback profiles predicted by two anisotropic models are very similar. Finally, the quadratic NAFR model required significantly less computation time and was somewhat less sensitive to mesh density.

5.6. Appendices

5.6.1. Anisotropy parameter calculation of Yld2000-2d (Barlat et al., 2003)

Three stress states, namely uniaxial tension along the rolling and the transverse directions, and the balanced biaxial stress state, provide six data points, σ_0, σ_{90}, σ_B, r_0, r_{90}, and r_B. r_B defines the slope of the yield surface at the balanced biaxial stress state ($r_B = d\varepsilon_{yy} / d\varepsilon_{xx}$). This ratio can be evaluated by performing compression of circular disks in the sheet normal direction and measuring the aspect ratio of the specimen after deformation as discussed above. r_B can also be estimated by calculations using either a polycrystal model or the yield function Yld96. The loading for each stress state can be characterized by the two deviatoric components, $s_x = \gamma\sigma$ and $s_y = \delta\sigma$. There are two equations to solve per stress state, one for the yield stress and the other for the r-value (Barlat et al., 2003).

$$F = \phi - 2\left(\overline{\sigma}/\sigma\right)^a = 0 \text{ satisfies the yield stresses } (F_0, F_{90}, \text{ and } F_{EB}) \tag{5.51}$$

$$G = q_x \frac{\partial \phi}{\partial s_{xx}} - q_y \frac{\partial \phi}{\partial s_{yy}} = 0 \text{ satisfies the r-values } (G_0, G_{90}, \text{ and } G_{EB}) \tag{5.52}$$

where the function Φ can be written as

$$\phi = |\alpha_1\gamma - \alpha_2\delta|^a + |\alpha_3\gamma + 2\alpha_4\delta|^a + |2\alpha_5\gamma + \alpha_6\delta|^a - 2\left(\overline{\sigma}/\sigma\right)^a = 0 \tag{5.53}$$

where γ, δ, q_x, and q_y for the tests mentioned above are given in the Table 5.6. The 6 coefficients α_1 to α_6 can be computed by solving the two Equations (5.51) and (5.52) expressed in the three stress states. These equations were obtained using the linear transformations with the L_{ij}' and L_{ij}'' (prime and double prime) coefficients, which are related to the α_k coefficients.

Table 5.6. Parameters for identifying the anisotropic coefficients of Yld2000-2d.

	γ	δ	q_x	q_y
R.D. (0)	2/3	-1/3	$1-r_0$	$2+r_0$
T.D. (90)	-1/3	2/3	$2+r_{90}$	$1-r_{90}$
Equibiaxial	-1/3	-1/3	$1+2r_{EB}$	$2+r_{EB}$

Uniaxial tension tests loaded at 45 degree to the rolling direction give two data points, σ_{45} and r_{45}. The stress state is on the yield surface if the following equation is satisfied

$$F = \left| \frac{\sqrt{k_2'^2 + 4\alpha_7^2}}{2} \right|^a + \left| \frac{3k_1'' - \sqrt{k_2''^2 + 4\alpha_8^2}}{4} \right|^a + \left| \frac{3k_1'' + \sqrt{k_2''^2 + 4\alpha_8^2}}{4} \right|^a \quad \text{gives } (F_{45})$$
$$- 2\left(\bar{\sigma} \middle/ \sigma_{45} \right)^a = 0$$

(5.54)

where

$$k_2' = \frac{\alpha_1 - \alpha_2}{3}$$

$$k_1'' = \frac{2\alpha_5 + \alpha_6 + \alpha_3 + 2\alpha_4}{9}$$

(5.55)

$$k_2'' = \frac{2\alpha_5 + \alpha_6 - \alpha_3 - 2\alpha_4}{3}$$

Using the associated flow rule the final equation for the r-value can be expressed

$$G = \frac{\partial \phi}{\partial \sigma_{xx}} + \frac{\partial \phi}{\partial \sigma_{yy}} - \frac{2a}{(1 + r_{45})} \left(\frac{\bar{\sigma}}{\sigma_{45}} \right)^a = 0 \quad \text{gives } (G_{45})$$

(5.56)

The eighth equation (G_{45}) is very huge when calculated and expanded. Although this equation was successfully derived and solved, it is not presented here for the sake of brevity. The Newton-Raphson numerical procedure was used to solve eight equations (F_0, F_{90}, F_{45}, F_{EB}, G_0, G_{90}, G_{45}, and G_{EB}) for the eight coefficients α_1 to α_8 simultaneously. The two matrices **L'** and **L''** are completely defined with these eight coefficients.

5.6.2. The first and the second derivatives of Hill's 1948 and Yld2000-2d

Hill's 1948 derivatives

For plane stress conditions, the effective stress based on Hill's 1948 function is defined as

$$\overline{\eta}(\boldsymbol{\eta}) = \left(\frac{3}{2} \boldsymbol{\eta}^T \mathbf{H} \boldsymbol{\eta} \right)^{\frac{1}{2}} \tag{5.57}$$

where $\mathbf{H}$ is a higher ranked anisotropic tensor. The derivatives of this stress function are easily found as

$$\frac{\partial \overline{\eta}}{\partial \boldsymbol{\eta}} = \frac{3}{2} \frac{\mathbf{H}.\boldsymbol{\eta}}{\overline{\eta}} \tag{5.58}$$

And

$$\frac{\partial^2 \overline{\eta}}{\partial \boldsymbol{\eta} \partial \boldsymbol{\eta}} = \frac{3}{2} \frac{\mathbf{H}}{\overline{\eta}} - \frac{\dfrac{\partial \overline{\eta}}{\partial \boldsymbol{\eta}} \otimes \dfrac{\partial \overline{\eta}}{\partial \boldsymbol{\eta}}}{\overline{\eta}} \tag{5.59}$$

Barlat's Yld2000-2d derivatives (based on Yoon et al. (2004) for isotropic hardening)

For plane stress conditions, the effective stress Yld2000-2d function is defined as

$$\overline{\eta}(\boldsymbol{\eta}) = \left\{ \frac{1}{2} \Psi \right\}^{\frac{1}{a}} = \left\{ \frac{1}{2} \left(\left| X_1' - X_2' \right|^a + \left| 2X_2'' + X_1'' \right|^a + \left| 2X_1'' + X_2'' \right|^a \right) \right\}^{\frac{1}{a}} \tag{5.60}$$

Components $X'i$ and $X''j$ are the principal values of two linear transformations (X' and X'') of the tensor $\boldsymbol{\eta}$ as follows

$$\tilde{\boldsymbol{\eta}}' = \{ \tilde{\eta}_k \} = \begin{Bmatrix} \eta_{xx} \\ \eta_{yy} \\ \eta_{xy} \end{Bmatrix} \tag{5.61}$$

And

$$\tilde{X}' = \{ \tilde{X}_k' \} = \begin{Bmatrix} X_{xx}' \\ X_{yy}' \\ X_{xy}' \end{Bmatrix} = \begin{Bmatrix} L_{11}' \eta_{xx} + L_{12}' \eta_{yy} \\ L_{21}' \eta_{xx} + L_{22}' \eta_{yy} \\ L_{33}' \eta_{xy} \end{Bmatrix} \tag{5.62a}$$

and (5.62b)

$$\tilde{X}'' = \{\tilde{X}''_k\} = \begin{Bmatrix} X''_{xx} \\ X''_{yy} \\ X''_{xy} \end{Bmatrix} = \begin{Bmatrix} L''_{11}\eta_{xx} + L''_{12}\eta_{yy} \\ L''_{21}\eta_{xx} + L''_{22}\eta_{yy} \\ L''_{33}\eta_{xy} \end{Bmatrix}$$

And

$$\tilde{\beta}' = \{\tilde{\beta}'_k\} = \begin{Bmatrix} X'_1 \\ X'_2 \end{Bmatrix} = \begin{Bmatrix} \dfrac{X'_{xx} + X'_{yy}}{2} + \sqrt{\left(\dfrac{X'_{xx} - X'_{yy}}{2}\right)^2 + X'^2_{xy}} \\ \dfrac{X'_{xx} + X'_{yy}}{2} - \sqrt{\left(\dfrac{X'_{xx} - X'_{yy}}{2}\right)^2 + X'^2_{xy}} \end{Bmatrix}$$

(5.63a)

and

$$\tilde{\beta}'' = \{\tilde{\beta}''_k\} = \begin{Bmatrix} X''_1 \\ X''_2 \end{Bmatrix} = \begin{Bmatrix} \dfrac{X''_{xx} + X''_{yy}}{2} + \sqrt{\left(\dfrac{X''_{xx} - X''_{yy}}{2}\right)^2 + X''^2_{xy}} \\ \dfrac{X''_{xx} + X''_{yy}}{2} - \sqrt{\left(\dfrac{X''_{xx} - X''_{yy}}{2}\right)^2 + X''^2_{xy}} \end{Bmatrix}$$

(5.63b)

The quantity $\dfrac{\partial \overline{\eta}}{\partial \boldsymbol{\eta}}$ is obtained by applying the chain rules; i.e.

$$\frac{\partial \overline{\eta}}{\partial \eta_k} = \left\{2a\overline{\eta}^{(a-1)}\right\}^{-1} \frac{\partial \Psi}{\partial \eta_k}$$

$$= \left\{2a\overline{\eta}^{(a-1)}\right\}^{-1} \sum_a^2 \sum_b^3 \left(\frac{\partial \Psi}{\partial \tilde{\beta}'_a} \frac{\partial \tilde{\beta}'_a}{\partial \tilde{X}'_b} \frac{\partial \tilde{X}'_b}{\partial \tilde{\eta}_k} + \frac{\partial \Psi}{\partial \tilde{\beta}''_a} \frac{\partial \tilde{\beta}''_a}{\partial \tilde{X}''_b} \frac{\partial \tilde{X}''_b}{\partial \tilde{\eta}_k} \right)^{(k=1\sim3)}$$

(5.64)

Where

$$\left\{\frac{\partial \Psi}{\partial \tilde{\beta}'_i}\right\} = \begin{Bmatrix} a\left[(X'_1 - X'_2)|X'_1 - X'_2|^{a-2}\right] \\ -a\left[(X'_1 - X'_2)|X'_1 - X'_2|^{a-2}\right] \end{Bmatrix}$$

(5.65a)

and

163

$$\left\{\frac{\partial \Psi}{\partial \tilde{\beta}''_i}\right\} = \left\{\begin{array}{l} a\left[(2X''_2 + X''_1)|2X''_2 + X''_1|^{a-2} + 2(2X''_1 + X''_2)|2X''_1 + X''_2|^{a-2}\right] \\ a\left[2(2X''_2 + X''_1)|2X''_2 + X''_1|^{a-2} + (2X''_1 + X''_2)|2X''_1 + X''_2|^{a-2}\right] \end{array}\right\}$$

(5.65b)

And

$$\left[\frac{\partial \tilde{\beta}'_i}{\partial \tilde{X}'_j}\right] = \begin{bmatrix} \dfrac{1}{2} + \dfrac{(X'_{xx} - X'_{yy})}{4r'} & \dfrac{1}{2} - \dfrac{(X'_{xx} - X'_{yy})}{4r'} & \dfrac{X'_{xy}}{r'} \\ \dfrac{1}{2} - \dfrac{(X'_{xx} - X'_{yy})}{4r'} & \dfrac{1}{2} + \dfrac{(X'_{xx} - X'_{yy})}{4r'} & -\dfrac{X'_{xy}}{r'} \end{bmatrix}$$

(5.66a)

and

$$\left[\frac{\partial \tilde{\beta}''_i}{\partial \tilde{X}''_j}\right] = \begin{bmatrix} \dfrac{1}{2} + \dfrac{(X''_{xx} - X''_{yy})}{4r''} & \dfrac{1}{2} - \dfrac{(X''_{xx} - X''_{yy})}{4r''} & \dfrac{X''_{xy}}{r''} \\ \dfrac{1}{2} - \dfrac{(X''_{xx} - X''_{yy})}{4r''} & \dfrac{1}{2} + \dfrac{(X''_{xx} - X''_{yy})}{4r''} & -\dfrac{X''_{xy}}{r''} \end{bmatrix}$$

(5.66b)

Where $r' = \sqrt{\left(\dfrac{X'_{xx} - X'_{yy}}{2}\right)^2 + X'^2_{xy}}$ and $r'' = \sqrt{\left(\dfrac{X''_{xx} - X''_{yy}}{2}\right)^2 + X''^2_{xy}}$.

And

$$\left[\frac{\partial \tilde{X}'_i}{\partial \tilde{\eta}_j}\right] = \begin{bmatrix} L'_{11} & L'_{12} & 0 \\ L'_{21} & L'_{22} & 0 \\ 0 & 0 & L'_{33} \end{bmatrix}$$

(5.67a)

and

$$\left[\frac{\partial \tilde{X}''_i}{\partial \tilde{\eta}_j}\right] = \begin{bmatrix} L''_{11} & L''_{12} & 0 \\ L''_{21} & L''_{22} & 0 \\ 0 & 0 & L''_{33} \end{bmatrix}$$

(5.67b)

Where L'_{ij} and L''_{ij} are defined in Equation (5.13).

The quantity $\dfrac{\partial^2 \overline{\eta}}{\partial \eta \partial \eta}$ is obtained by applying the following chain rules; i.e.

$$\frac{\partial^2 \overline{\eta}}{\partial \eta_i \partial \eta_j} = \frac{\overline{\eta}^{(1-a)}}{2a} \frac{\partial^2 \Psi}{\partial \eta_i \partial \eta_j} - \frac{(a-1)}{\overline{\eta}} \frac{\partial \overline{\eta}}{\partial \eta_i} \frac{\partial \overline{\eta}}{\partial \eta_j} \quad (i,j=1\sim3)$$

(5.68)

Now

$$\frac{\partial^2 \Psi}{\partial \eta_i \partial \eta_j} =$$

$$\sum_r^2 \sum_s^3 \sum_a^2 \sum_b^3 \left\{ \frac{\partial^2 \Psi}{\partial \tilde{\beta}'_r \partial \tilde{\beta}'_a} \left(\frac{\partial \tilde{\beta}'_r}{\partial \tilde{X}'_s} \frac{\partial \tilde{X}'_s}{\partial \tilde{\eta}_i} \right) \left(\frac{\partial \tilde{\beta}'_a}{\partial \tilde{X}'_b} \frac{\partial \tilde{X}'_b}{\partial \tilde{\eta}_j} \right) + \frac{\partial^2 \Psi}{\partial \tilde{\beta}''_r \partial \tilde{\beta}''_a} \left(\frac{\partial \tilde{\beta}''_r}{\partial \tilde{X}''_s} \frac{\partial \tilde{X}''_s}{\partial \tilde{\eta}_i} \right) \left(\frac{\partial \tilde{\beta}''_a}{\partial \tilde{X}''_b} \frac{\partial \tilde{X}''_b}{\partial \tilde{\eta}_j} \right) \right\}$$

$$+ \sum_a^2 \sum_r^3 \sum_b^3 \left\{ \frac{\partial \Psi}{\partial \tilde{\beta}'_a} \frac{\partial^2 \tilde{\beta}'_a}{\partial \tilde{X}'_r \partial \tilde{X}'_b} \left(\frac{\partial \tilde{X}'_r}{\partial \tilde{\eta}_i} \right) \left(\frac{\partial \tilde{X}'_b}{\partial \tilde{\eta}_j} \right) + \frac{\partial \Psi}{\partial \tilde{\beta}''_a} \frac{\partial^2 \tilde{\beta}''_a}{\partial \tilde{X}''_r \partial \tilde{X}''_b} \left(\frac{\partial \tilde{X}''_r}{\partial \tilde{\eta}_i} \right) \left(\frac{\partial \tilde{X}''_b}{\partial \tilde{\eta}_j} \right) \right\}$$

(5.69)

$$+ \sum_a^2 \sum_b^3 \left\{ \frac{\partial \Psi}{\partial \tilde{\beta}'_a} \frac{\partial \tilde{\beta}'_a}{\partial \tilde{X}'_b} \left(\frac{\partial^2 \tilde{X}'_b}{\partial \tilde{\eta}_i \partial \tilde{\eta}_j} \right) + \frac{\partial \Psi}{\partial \tilde{\beta}''_a} \frac{\partial \tilde{\beta}''_a}{\partial \tilde{X}''_b} \left(\frac{\partial^2 \tilde{X}''_b}{\partial \tilde{\eta}_i \partial \tilde{\eta}_j} \right) \right\}$$

Note that $\left(\dfrac{\partial^2 \tilde{X}'_b}{\partial \tilde{\eta}_i \partial \tilde{\eta}_j} \right)$ and $\left(\dfrac{\partial^2 \tilde{X}''_b}{\partial \tilde{\eta}_i \partial \tilde{\eta}_j} \right)$ vanish.

Where

$$\left[\frac{\partial^2 \Psi}{\partial \tilde{\beta}'_i \partial \tilde{\beta}'_j} \right] = a(a-1) \begin{bmatrix} \left| X'_1 - X'_2 \right|^{a-2} & -\left| X'_1 - X'_2 \right|^{a-2} \\ -\left| X'_1 - X'_2 \right|^{a-2} & \left| X'_1 - X'_2 \right|^{a-2} \end{bmatrix}$$

(5.70a)

and

$$\left[\frac{\partial^2 \Psi}{\partial \tilde{\beta}_i \partial \tilde{\beta}''_j} \right] = a(a-1) \times$$

$$\begin{bmatrix} \left| 2X''_2 + X''_1 \right|^{a-2} + 4\left| 2X''_1 + X''_2 \right|^{a-2} & 2\left| 2X''_2 + X''_1 \right|^{a-2} + 2\left| 2X''_1 + X''_2 \right|^{a-2} \\ 2\left| 2X''_2 + X''_1 \right|^{a-2} + 2\left| 2X''_1 + X''_2 \right|^{a-2} & 4\left| 2X''_2 + X''_1 \right|^{a-2} + \left| 2X''_1 + X''_2 \right|^{a-2} \end{bmatrix}$$

(5.70b)

Also

$$\left[\frac{\partial^2 \tilde{\beta}'_1}{\partial \tilde{X}'_i \partial \tilde{X}'_j}\right] = \begin{bmatrix} \dfrac{1}{4r'} - \dfrac{(X'_{xx} - X'_{yy})^2}{16r'^3} & -\dfrac{1}{4r'} + \dfrac{(X'_{xx} - X'_{yy})^2}{16r'^3} & -\dfrac{(X'_{xx} - X'_{yy})X'_{xy}}{4r'^3} \\[3mm] -\dfrac{1}{4r'} + \dfrac{(X'_{xx} - X'_{yy})^2}{16r'^3} & \dfrac{1}{4r'} - \dfrac{(X'_{xx} - X'_{yy})^2}{16r'^3} & \dfrac{(X'_{xx} - X'_{yy})X'_{xy}}{4r'^3} \\[3mm] -\dfrac{(X'_{xx} - X'_{yy})X'_{xy}}{4r'^3} & \dfrac{(X'_{xx} - X'_{yy})X'_{xy}}{4r'^3} & \dfrac{1}{r'} - \dfrac{X'^2_{xy}}{r'^3} \end{bmatrix} \quad (5.71a)$$

and

$$\left[\frac{\partial^2 \tilde{\beta}''_1}{\partial \tilde{X}''_i \partial \tilde{X}''_j}\right] = \begin{bmatrix} \dfrac{1}{4r''} - \dfrac{(X''_{xx} - X''_{yy})^2}{16r''^3} & -\dfrac{1}{4r''} + \dfrac{(X''_{xx} - X''_{yy})^2}{16r''^3} & -\dfrac{(X''_{xx} - X''_{yy})X''_{xy}}{4r'^3} \\[3mm] -\dfrac{1}{4r''} + \dfrac{(X''_{xx} - X''_{yy})^2}{16r''^3} & \dfrac{1}{4r''} - \dfrac{(X''_{xx} - X''_{yy})^2}{16r''^3} & \dfrac{(X''_{xx} - X''_{yy})X'_{xy}}{4r'^3} \\[3mm] -\dfrac{(X''_{xx} - X''_{yy})X''_{xy}}{4r''^3} & \dfrac{(X''_{xx} - X''_{yy})X''_{xy}}{4r''^3} & \dfrac{1}{r''} - \dfrac{X''^2_{xy}}{r''^3} \end{bmatrix} \quad (5.71b)$$

Note that $\left[\dfrac{\partial^2 \tilde{\beta}'_1}{\partial \tilde{X}'_i \partial \tilde{X}'_j}\right] = -\left[\dfrac{\partial^2 \tilde{\beta}'_2}{\partial \tilde{X}'_i \partial \tilde{X}'_j}\right]$ and $\left[\dfrac{\partial^2 \tilde{\beta}''_1}{\partial \tilde{X}''_i \partial \tilde{X}''_j}\right] = -\left[\dfrac{\partial^2 \tilde{\beta}''_2}{\partial \tilde{X}''_i \partial \tilde{X}''_j}\right]$.

5.7. References

ABAQUS 6.7, 2007. Documentation and Theory Manual. Hibbit, Karlsson, Sorensen, Inc.

Armstrong, P.J., Frederick, C.O., 1966. A Mathematical representation of the multiaxial Bauschinger effect, Central Electricity Generating Board Report, Berkeley Nuclear Laboratories, RD/B/N 731.

Banabic, D., Aretz, H., Comsa, D.S., Paraianu, L., 2005. An improved analytical description of orthotropy in metallic sheets. Int. J. Plasticity 21, 493-512.

Barlat, F., Lian, J., 1989. Plastic behaviour and stretchability of sheet metals, Part I: a yield function for orthotropic sheets under plane stress conditions. Int. J. Plasticity 5, 51-56.

Barlat, F., Lege, D.J., Brem, J.C., 1991. A six-component yield function for anisotropic materials. Int. J. Plasticity 7, 693-712.

Barlat, F., Becker, R.C., Hayashida, Y., Maeda, Y., Yanagawa, M., Chung, K., Brem, J.C., Lege, D.J., Matsui, K., Murtha, S.J., Hattori, S., 1997. Yielding description for solution strengthened aluminum alloys. Int. J. Plasticity 13, 385-401.

Barlat, F., Brem, J.C., Yoon, J.W., Chung, K., Dick, R.E., Choi, S.H., Pourboghrat, F., Chu, E., Lege, D.J., 2003. Plane stress yield function for aluminum alloy sheets. Int. J. Plasticity 19, 1297-1319.

Barlat, F., Aretz, H., Yoon, J.W., Karabin, M.E., Brem, J.C., Dick, R.E., 2005. Linear transformation based anisotropic yield functions. Int. J. Plasticity 21, 1009-1039.

Boger, R.K., Wagoner, R.H., Barlat, F., Lee, M.G., Chung, K., 2005. Continuous, large strain, tension/compression testing of sheet material. Int. J. Plasticity 21, 2319-2343.

Brem, J.C., Barlat, F., Dick, R.E., Yoon J.-W., 2005. Characterizations of aluminum alloy sheet materials Numisheet 2005. Proceedings of Numisheet 05, CP778 Volume B, American

Institute of Physics, eds. Cao, J., Shi, M.F., Stoughton, T.B., Wang, C.T., Zhang, L., 1179-1190.

Cardoso, R.P.R., Yoon, J.W., 2009, Stress integration method for a nonlinear kinematic/isotropic hardening model and its characterization based on polycrystal plasticity. Int. J. of Plasticity 25, 1684-1710.

Chaboche, J.L., 1986. Time-independent constitutive theories for cyclic plasticity. Int. J. Plasticity 2, 149-188.

Chaboche, J.L., 1989. Constitutive equations for cyclic plasticity and cyclic viscoplasticity. Int. J. Plasticity 5, 247-302.

Chung K., Shah K. Finite element simulation of sheet metal forming for planar anisotropic metals, Int. J. Plasticity 8 (1992) 453-476.

Chung, K., Lee, M.G., Kim, D., Kim, C., Wenner, M.L., Barlat, F., 2005. Spring-back evaluation of automotive sheets based on isotropic–kinematic hardening laws and non-quadratic anisotropic yield functions, Part I: theory and formulation. Int. J. Plasticity 21, 861-882.

Cvitanić, V., Vlak, F., Lozina, Z., 2008. A finite element formulation based on non-associated plasticity for sheet metal forming. Int. J. Plasticity 24, 646-678.

Green, D.E., 2005. Description of Numisheet 2005 Benchmark #3 Stage-1: Channel Draw with 75% Drawbead Penetration. Proceedings of Numisheet 05, CP778 Volume B, American Institute of Physics, eds. Cao, J., Shi, M.F., Stoughton, T.B., Wang, C.T., Zhang, L., 894-904.

Habraken A.M., 2004. Modelling the plastic anisotropy of metals, Arch. Comput. Meth. Eng. 11, 3-96.

Hill, R., 1948. A theory of the yielding and plastic flow of anisotropic metals. Proc. Roy. Soc. Lond. A 193, 281-297.

Hill, R., 1979. Theoretical plasticity of textured aggregates. Math. Proc. Cambridge Philos. Soc. 85, 179-191.

Hill, R., 1990. Constitutive modelling of orthotropic plasticity in sheet metals. J. Mech. Phys. Solids 38, 405-417.

Hill, R., 1993. A user-friendly theory of orthotropic plasticity in sheet metals. Int. J. Mech. Sci. 35, 19–25.

Karafillis, A.P., Boyce, M.C., 1993. A general anisotropic yield criterion using bounds and a transformation weighting tensor. J. Mech. Phys. Solids 41, 1859-1886.

Kojic, M., 2002. Stress integration procedures for inelastic material models within finite element method. Appl. Mech. Reviews 55, 389-414.

Mellor, P.B., 1981. Sheet metal forming. Int. Metals. Rev. 26, 1-20.

Mellor, P.B., Parmer, A., 1978. Plasticity of sheet metal forming. In: Koistinen, D.P., Wang, N.M., (Eds.), Mechanics of Sheet Metal Forming, Plenum Press, New York, 53-74.

Shi, M.F., Huang, M., 2005. Specification for benchmark materials. Proceedings of Numisheet 05, CP778 Volume B, American Institute of Physics, eds. Cao, J., Shi, M.F., Stoughton, T.B., Wang, C.T., Zhang, L., 1173-1178.

Simo, J.C., Hughes, T.J.R., 1998. Computational Inelasticity. Volume 7 of Interdisciplinary Applied Mathematics. Springer-Verlag, Berlin.

Stoughton, T.B., 2002. A non-associated flow rule for sheet metal forming. Int. J. Plasticity 18, 687-714.

Stoughton, T.B., Green, D.E., Iadicola, M., 2005. Specification for BM3: two-stage channel/cup draw. Proceedings of Numisheet 05, CP778 Volume B, American Institute of Physics, eds. Cao, J., Shi, M.F., Stoughton, T.B., Wang, C.T., Zhang, L., 1157-1172.

Stoughton, T.B., Yoon J.W., 2009. Anisotropic hardening and non-associated flow in proportional loading of sheet metals. Int. J. Plasticity 25, 1777-1817.

Taherizadeh A., Ghaei A., Green D.E., Altenhof W.J., 2009a. Finite element simulation of springback for a channel draw process with drawbead using different hardening models. Int. J. Mech. Scie. 51, 314-325.

Taherizadeh A., Green D.E., Ghaei A., Yoon J.W., 2009b. A non-associated constitutive model with mixed iso-kinematic hardening for finite element simulation of sheet metal forming. Int. J. Plasticity, In press, Accepted Manuscripts.

Yoon, J.W., Yang, D.Y., Chung, K., 1999a. Elasto-plastic finite element method based on incremental deformation theory and continuum based shell elements for planar anisotropic sheet materials. Comput. Methods Appl. Mech. Eng. 174, 23-56.

Yoon, J.W., Yang, D.Y., Chung, K., Barlat, F., 1999b. A general elasto-plastic finite element formulation based on incremental deformation theory for planar anisotropy and its application to sheet metal forming", Int. J. of Plasticity, 15, 35-68.

Yoon, J.W., Barlat, F., Chung, K., Pourboghrat, F., Yang, D.Y., 2000. Earing prediction based on asymmetric nonquadratic yield function. Int. J. Plasticity 16, 1075-1104.

Yoon J.W., Barlat F., Dick R.E., Chung K., Kang T.J. Plane stress yield function for aluminum alloy sheet-Part II: FE Formulation and its implementation, Int. J. Plasticity 20 (2004) 495-522.

Yoon J.W., Barlat F., Dick R.E., Karabin M.E. Prediction of six or eight ears in a drawn cup based on a new anisotropic yield function, Int. J. Plasticity 22 (2006) 174-193.

Ziegler, H., 1959. A modification of Prager's hardening rule. Quarterly of Applied Mathematics 17, 55-60.

Chapter 6

Conclusions

6.1. Summary

The work that was done in this research can be summarized in different categories. First, the effect of drawbead penetration and hardening model on the springback prediction of a channel draw process was investigated. User-defined material subroutines based on Hill's quadratic function and mixed isotropic nonlinear kinematic hardening (NKH) for both ABAQUS/Explicit and ABAQUS/Standard were developed. Both forming and springback stages of the Numisheet'05 Benchmark #3 were simulated for different sheet materials (AKDQ-HDG, HSLA-HDG, DP600-HDG and AA-6022-T43) and four different drawbead penetrations (25%, 50%, 75% and 100%). Also, cyclic simple shear tests were carried out to generate the cyclic stress-strain curves, and in order to study the Bauschinger effect, and the mixed hardening parameters were extracted from these experiments. Then, a phenomenological plane stress elasto-plastic constitutive model based on quadratic anisotropic non-associated flow rule with combined isotropic-nonlinear kinematic hardening was developed. The material model was implemented to user-defined subroutines (UMAT and VUMAT) and used to simulate different sheet metal forming processes to assess its ability to improve the results of finite element simulations. For verification, the mixed hardening model under uniaxial stress-strain curves, and the anisotropic flow rule theory under uniaxial, biaxial, and shear stress-strain curves were compared to the experiments. In the final part of the project, two anisotropic models were compared: the proposed non-associated formulation and a non-quadratic anisotropic function based on two linear transformations of the stress tensor originally developed by Barlat et al. (so-called Yld2000-2d).

To implement these two functions, a general return mapping algorithm was proposed to computationally integrate the stress that is applicable for both models with mixed nonlinear hardening. Simulations of different cylindrical cup drawing and springback of channel draw processes based on various sheet materials were performed with both anisotropic models. The simulation results and the computational costs for all cases were compared for the two models. Also, cyclic tension-compression tests were performed, as alternatives to cyclic shear tests, to generate the stress-strain curves.

6.2. Concluding remarks

Based on the studies done in the course of the project the following conclusions were drawn:

- The hardening model is a critical parameter in simulation of springback, especially for the processes in which the sheet undergoes cyclic deformation such as cases with drawbead.

- Other factors such as the mesh density of the finite element model and the evolution of unloading elastic modulus are very important factors in simulation of springback.

- For the case of Numisheet 2005 BM#3, the mixed isotropic-nonlinear kinematic hardening (NKH) model is able to predict both the sidewall curl and the sidewall angle of the profile after springback significantly more accurately than the pure isotropic (IH) hardening. In other words, it can be concluded that IH model cannot accurately predict springback of sheet metal parts when the forming process leads to cyclic deformations.

- The experimental cyclic stress-strain curves can be theoretically reproduced in a more accurate manner by NKH model rather than IH model. However, the NKH model is not able to capture some cyclic effects such as work hardening stagnation or permanent softening.

- Also, the predicted punch force, major and thickness strains after the forming of the channel (and before the springback) by NKH model are in a better agreement with the experimental results compared with the results predicted by IH model.

- Comparison of residual internal stresses before and after springback shows the effect of drawbead penetration on the springback results, i.e. deeper drawbead penetrations result in less springback.

- Although the NKH model is quite enough for the engineering applications, the prediction of springback can be further improved by accounting for observed material behaviour such as the work hardening stagnation, and by implementing more advanced constitutive models into the numerical simulation code.

- Hill's 1948 quadratic anisotropic function is not able to predict the variations of r-values and yield stress ratios at the same time.

- The proposed non-associated model with mixed hardening (NAFR) based on the same Hill's quadratic function and nonlinear kinematic hardening theory maintains the theoretical simplicity while it is able to predict both the anisotropic and cyclic behaviour of sheet metals more accurately than the conventional constitutive models.

- In more detail, the NAFR model can predict the r-values and yield stress ratios in different directions better than the conventional quadratic AFR models. Also the cyclic, equi-biaxial and shear stress-strain curves of different anisotropic materials can be reproduced by the NAFR model in a more accurate way.

- By comparing the yield and potential surfaces of different materials it can be shown that the difference between these two surfaces is very dependent on the anisotropic properties. In fact, sometimes this difference is very significant so that ignoring it when using conventional anisotropic models can strongly affect the simulation results.

- Simulation results showed that this non-associated mixed hardening model improves the prediction of both anisotropy and hardening behaviour, even though a rather simple quadratic constitutive model was used. In fact, it was shown that the simulation results of both cup drawing and channel draw processes were significantly improved by using the NAFR model.

- All comparisons show that the two aspects of the model, non-associated flow rule and mixed hardening are necessary to enhance the prediction of the material behaviour.

- It was shown that the numerical procedure based on the multi-stage general return mapping algorithm that was proposed by Yoon et al. for associated model and isotropic hardening can successfully be developed for non-associated model with mixed nonlinear hardening regime (applicable for different types of yield and potential functions).

- Comparison of the proposed quadratic NAFR model with the Yld2000-2d non-quadratic model shows that both models are able to take the both aspects of the material anisotropy into account.

- By performing the simulations of different cup drawing processes, it was shown that, in general the quadratic NAFR predicted the cup height trend better than the associated non-quadratic model, while in some cases the non-quadratic model predicted the cup height value slightly better than NAFR.

- Based on the channel draw simulation results, the springback predictions by two anisotropic models are quite similar, i.e., the hardening model is much more effective on the springback results than the yield function.

- It seems the larger strain ranges in the cyclic tests may result in better material parameters, which in turn is closer to the realistic behaviour, and will improve the simulation results (for example, the springback results based on the cyclic shear tests were insignificantly better than those based on the cyclic T-C tests)

- Finally, the quadratic NAFR model required significantly less computation time than the non-quadratic Yld2000-2d model and was somewhat less sensitive to mesh density.

Almost all comparisons were represented in the qualitative style. In fact, quantifying the error in some of the comparisons is a quite challenging job that might need a substantial research.

6.3. Future work

Different aspects of the current work have the potential to be continued, modified, and/or more investigated in the future work. The current quadratic non-associated (NAFR) model can be further generalized for the combinations of different quadratic and non-quadratic (and also pressure sensitive or insensitive) yield and potential functions. The effect of using different backstress evolution theories for the yield and potential functions can be investigated. The current NAFR model can be combined with more advanced kinematic hardening rules such as two-surface or multiple-backstress theories. The proposed NAFR model can be generalized to take into account the anisotropic hardening (or directional hardening) for both isotropic and kinematic parts. This NAFR model can also be generalized for temperature sensitive simulations (such as warm or hot forming) by adding the viscous effects to the current rate independent model. Further investigations can be conducted on the comparison of different cyclic tests of sheet metals and their effects on the springback simulations. Finally, quantifying the error in some comparisons such as prediction of springback profiles or stress-strain curves can be further studied.

VITA AUCTORIS

Name: Aboozar Taherizadeh

Date and Place of Birth: 1980, Isfahan, Iran

Education:

B.Sc. (Honours)

Materials Science and Engineering

Isfahan University of Technology, Isfahan, Iran, 1998-2002

M.Sc.

Materials Science and Engineering

Sharif University of Technology, Tehran, Iran, 2002-2004

Ph.D.

Mechanical Engineering

University of Windsor, Windsor, ON, Canada, 2006-2009